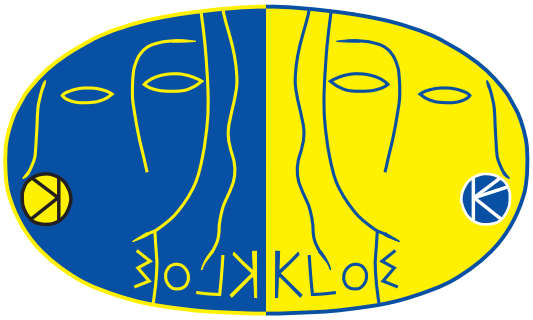

Measurement of the pion form factor via Radiative Return for data taken at $\sqrt{s} = 1$ GeV with the KLOE detector

Zur Erlangung des akademischen Grades eines
DOKTORS DER NATURWISSENSCHAFTEN
von der Fakultät für Physik
der Universität Karlsruhe (TH)

genehmigte
DISSERTATION
von

Dott. **Paolo Beltrame** (Laurea)
aus Rom (Italien)

Tag der mündlichen Prüfung 13.02.2009
Referent Prof. Dr. Thomas Müller
Korreferent Prof. Dr. Achim Denig

To Mario, Ugo and Tartanicchia.

CONTENTS

1. SUMMARY

The hadronic cross section and $(g-2)_\mu$

On one side, high energy physics experiments are searching at the highest achievable energies for new particles as extensions of the Standard Model (SM) of particle physics. On the other side, high precision measurements are setting more and more stringent tests on the Standard Model. The Standard Model theory has been describing, so far, with many successes what we understand about the basic constituents of the Universe. However the Standard Model is not a complete theory; therefore, where is it possible to search for New Physics beyond it?

One of the most precise tests of the Standard Model consists in the *anomaly of the magnetic moment of the muon*, a_μ, defined as

$$a_\mu = \frac{g_\mu - 2}{2},$$

where g_μ is the gyromagnetic factor of the muon, which, according to Dirac theory, is predicted to be $g_\mu = 2$. This "anomaly" can be predicted theoretically and measured directly with an extremely high precision.
The most precise direct measurement of a_μ comes from the E821 experiment at the Brookhaven National Laboratory.[1] The present world average value is

$$a_\mu^{\rm exp} = (11659208.0 \pm 6.3) \times 10^{-10}.$$

The precision of ca. 0.5 ppm is remarkable.
The Standard Model prediction of the muon anomaly, $a_\mu^{\rm theo(SM)}$ includes quantum corrections from all known fundamental interactions:

$$a_\mu^{\rm theo(SM)} = a_\mu^{\rm QED} + a_\mu^{\rm Weak} + a_\mu^{\rm had},$$

i.e. Quantum Electrodynamics (QED), Weak (W) and Strong (had) interactions. For the time being the discrepancy between the experimental value of a_μ and the theoretical one corresponds to more than 3 standard deviations. This discrepancy could be due to a New Physics contribution not accounted for in the Standard Model.
The hadronic contribution, $a_\mu^{\rm had}$, is the second largest contribution, after QED, and its uncertainty is dominating the total error of $a_\mu^{\rm theo(SM)}$. Therefore its precise determination can significantly improve the accuracy of the theoretical prediction and provide a significant contribution to one of the most relevant tests of the Standard Model.

[1] G.W. Bennet et al., (Muon (g-2) Coll.), *Phys. Rev. Lett. D* **73**, 072003 (2006).

The hadronic contribution of a_μ can be related to the hadronic cross section $\sigma(e^+e^- \to \text{hadrons})$, by means of the *Optical Theorem*, which leads to the dispersion integral, where $K(s)$ is a well-known analytical function behaving like $1/s$:

$$a_\mu^{\text{had}} = \frac{1}{4\pi^3} \int_{4m_\pi^2}^{\infty} \sigma_{e^+e^- \to \text{had}}(s) K(s) ds.$$

The integral is carried out over the invariant mass squared of the hadronic system, s. Low energy cross sections therefore strongly contribute to a_μ^{had}. Since perturbative QCD (pQCD) is not applicable for s smaller than ca. 5 GeV, experimental measurements of hadron production via e^+e^- collisions are needed.
The channel $e^+e^- \to \pi^+\pi^-$ is of utmost importance, since it contributes to ca. 70% to a_μ^{had}, and a precision at the level of at least 1% is needed in order have an error on $a_\mu^{\text{theo(SM)}}$ comparable to the one of the direct measurement. An alternative way to provide the experimental input for the dispersion integral is measuring the hadronic decays of the τ lepton, corrected for isospin violating effects. A considerable difference was found between e^+e^- and τ based spectra, and, if the latter is used in the evaluation of a_μ^{had}, the discrepancy between the theoretical prediction and the direct measurement shows a smaller deviation ($\sim 0.7\sigma$). However, several effects entering the hadronic τ-decay are probably not completely under control, and as a consequence τ-data are not considered in the evaluation of $(g-2)_\mu$ at the moment. This work presents a new precise determination of the pion form factor, $|F_\pi(s)|^2$, and of $a_\mu^{\pi\pi}$, i.e. the contribution to a_μ given by the the $\pi^+\pi^-$-channel.

The standard approach to measure hadronic cross sections consists in the so-called energy scan, i.e. in changing the energy of the colliding beams to the desired value s. In the case of "particle-factories", the collider operates at a fixed energy. In these kind of facilities, the radiative process $e^+e^- \to \text{hadrons} + \gamma$ is used, where the photon has been radiated in the initial state (*initial state radiation, ISR*) by electrons or positrons of the incoming beams. In such a way the colliding energy is lowered and the hadronic system at final state can be produced with different invariant mass values.[2] This method has been called *Radiative Return* because by means of the *radiation* the Center-of-Mass energy of the colliding beams goes down, i.e. *returns*, to lower resonances with respect to the resonance for which the collider has been set. DAΦNE, the ϕ-factory at LNF, was designed to run at the fixed $\sqrt{s}$ equal to the mass of the ϕ meson (1019.48 MeV) with high luminosity; thus, by means of ISR events radiative return down to the $\rho(\omega)$ resonance is possible.
In the assumption that the radiative photon does not derive from the final state process, the cross section $\sigma(e^+e^- \to \pi^+\pi^-)$ can be expressed as a function of the differential cross section $d\sigma(e^+e^- \to \pi^+\pi^-\gamma)/ds_\pi$ and the two quantities are related by the *radiator function* $H(s_\pi, s)$:

$$\frac{d\sigma(e^+e^- \to \pi^+\pi^- + \gamma_{\text{ISR}})}{ds_\pi} \cdot s = \sigma(e^+e^- \to \pi^+\pi^-, s_\pi) \times H(s_\pi, s),$$

where s is the collider energy and s_π is the invariant mass squared of the hadronic system after initial state radiation. The following energy relation holds for one ISR-photon only:

$$s_\pi = s - 2E_{\gamma_{\text{ISR}}}\sqrt{s},$$

[2] S. Binner, J.H. Kühn and K. Melnikov, *Phys. Lett. B* **459**, 279 (1999)

where s is the fixed energy of the collider.
The radiator function $H(s_\pi, s)$ is a theoretical function inserted in the Monte Carlo (MC) generator PHOKHARA.[3] This generator includes hard, soft and virtual radiative corrections to the process $e^+e^- \to \pi^+\pi^-\gamma$ at Next-to-Leading Order (NLO) and includes also *final state radiation* (*FSR*) from the pions, described by the point-like approximation (scalar QED, sQED). An accuracy at the permil level is needed for H, in order to perform a precision measurement.

KLOE so far has been the only experiment publishing the cross section $\sigma(e^+e^- \to \pi^+\pi^-)$ exploiting ISR events. The first result, based on data sample collected in 2001, was published in 2005,[4] and a second more precise analysis, using data collected in 2002, was published in 2009.[5] The University of Karlsruhe and, successively, the University of Mainz have played a fundamental role in developing the Radiative Return method and in performing the hadronic cross section measurements at KLOE.
An accuracy at the level of percent, or better, is required for $a_\mu^{\pi\pi}$, to get an uncertainty of the theoretical prediction of the muon anomaly comparable to the one of the direct measurement.
In the published analyses mentioned above the events selected have ISR-photon emitted at *small polar angle* with respect to the beam line, $|90^\circ - \theta_\gamma| > 75^\circ$. The extracted pion form factor results show a disagreement with respect to the energy scan experiments, SND and CMD-2 at VEPP-2M in Novosibirsk,[6] of up to ca. 5%, while the calculated $a_\mu^{\pi\pi}$ values are consistent among all the collaborations.

Analysis	$a_\mu^{\pi\pi}(0.630 < \sqrt{s} < 0.958\ \text{GeV}) \times 10^{-10}$
Small Angle 2002	$356.7 \pm 0.4_{\text{stat}} \pm 3.0_{\text{sys}}$
SND	$361.5 \pm 1.7_{\text{stat}} \pm 2.9_{\text{sys}}$
CMD-2	$361.0 \pm 2.0_{\text{stat}} \pm 4.7_{\text{sys}}$

Including the KLOE Small Angle result based on 2002 data in the computation of $a_\mu^{\text{theo(SM)}}$ confirms the discrepancy of more than 3σ between the predicted value and the direct measurement of $(g-2)_\mu$.
The "small angle" geometrical acceptance enhances the statistics of ISR events and reduces the background contamination from the decay of the ϕ but kinematically forbids energies below 0.35 GeV^2, which is indeed an important energy region, since it contributes to ca. 20% to the total value of a_μ^{had}.
In order to cross check the published result and to cover the energy region below 0.35 GeV^2, for which most precise measurements come from the SND and CMD-2 collaborations, KLOE has performed a first analysis, selecting events with the ISR-photon emitted at *large polar angle*, $|90^\circ - \theta_\gamma| < 40^\circ$, using data collected in 2002. This analysis is very close to be finalized, but irreducible background from ϕ-decay into scalar mesons, as well as the background from $\phi \to \rho\pi$, makes a precision measurement of the $\sigma(e^+e^- \to \pi^+\pi^-)$ cross section impossible for low energies. This has lead to the decision that a major data sample needs to be taken off the ϕ resonance, i.e.

[3] G. Rodrigo and J.H. Kühn, *Eur. Phys. Jour. C* **25**, 215 (2002), and newer versions.
[4] A. Aloisio et al. (KLOE Coll.), *Phys. Lett. B* **606**, 12 (2005).
[5] F. Ambrosino et al. (KLOE Coll.), *Phys. Lett. B* **670**, 285 (2009).
[6] M.N. Achasov et al. (SND Coll.), *Jour. Exp. Theor. Phys.* **103** (2006); R. R. Akhmetshin et al. (CMD2 Collaboration), *Phys. Lett. B* **648**, 28 (2007).

at $\sqrt{s} = 1$ GeV, providing a data sample free from background processes from ϕ-decays.[7] This "off-peak" data sample (collected in 2006), which has been used in the analysis presented in this thesis, can give the most accurate measurement of the $\sigma(e^+e^- \to \pi^+\pi^-)$ cross section at KLOE.

The *Large Angle off-peak analysis*, selecting events with ISR-photon emitted at large polar angle, represents the first pion form factor measurement performed by KLOE which covers the $2m_\pi$-threshold region with high precision.
All the selection cuts and all the related efficiencies have been evaluated. A preliminary result on the pion form factor is obtained. The systematic uncertainties have been estimated and a precision better than 0.9% is obtained in the region above 0.2 GeV^2. At the very $2m_\pi$-threshold the systematic uncertainty is about 5%, which is competitive with the results of the scan-experiment, SND and CMD-2. On the ρ-peak the systematic uncertainty is 0.6%.
The pion form factor evaluated in this analysis is in good agreement with the KLOE analysis using 2002 data, confirming the discrepancy with SND and CMD-2, especially at energies above 0.6 GeV^2, see Fig. 1.1. This discrepancy still represents an open question.
The agreement between the KLOE Small Angle and Large Angle analyses, which are based on different phase space selections and on different data sets, provides a solid cross check of the KLOE results.
The theoretical uncertainty associated to H is of the order of permil, making it a very robust instrument for ISR measurements. Moreover, the `PHOKHARA` Monte Carlo generator, which is used by KLOE and includes this theoretical function, has been compared to other Monte Carlo generators, and a very good agreement has been found. A further test on the radiator function $H(s)$ can be performed experimentally by measuring the $\sigma(e^+e^- \to \mu^+\mu^-\gamma)$ cross section. This measurement has been started. Therefore, it is very unlikely that the reason of the discrepancy can be attributed to the radiator function.
A possible explanation for the difference in $|F_\pi(s)|^2$ between KLOE and the Novosibirsk experiments could come from the description of FSR events, which depends on the model inserted in the Monte Carlo generator. In the `PHOKHARA` generator the FSR events are treated within the sQED approach. The reliability of the simulation has been tested comparing the data-Monte Carlo agreement in the Forward-Backward asymmetry, which arises from the interference between ISR-LO and FSR-LO events. An agreement better than 5% has been found, which, multiplied for the amount of FSR events in the data spectrum, gives an uncertainty of few permil. Higher radiative corrections (Next-to-Next-to-Leading Order) for FSR events, which are not present in the Monte Carlo generators and may be needed at the achieved experimental accuracy, could represent a possible source of discrepancy between the pion form factor results. However, higher order effects should cause a minimal impact on $|F_\pi(s)|^2$, and a-priori can not modify the spectra of some percent.

This analysis represents so far the most precise ISR measurement at KLOE: it is almost background free from ϕ-decays, especially from the irreducible background from ϕ-decays into scalar mesons. The large photon polar angle selection has given the possibility, for the first time at KLOE, to measure the $\sigma(e^+e^- \to \pi^+\pi^-)$ cross section down to the $\pi^+\pi^-$-threshold with high precision and to significantly contribute to the a_μ determination, also below 0.35 GeV^2.
Since at the very threshold the systematic uncertainty gets large, reaching about 5%,[8] and further cross check are under study we decided to compute the dispersion integral in the range between

[7] Even if the energy of the beams have been lowered, it is not possible to use DAΦNE for an energy scan at $\sqrt{s} \ll m_\phi$, i.e. for measuring the ρ-meson region.
[8] The systematic uncertainty could be in principle better kept under control if more statistics was available at

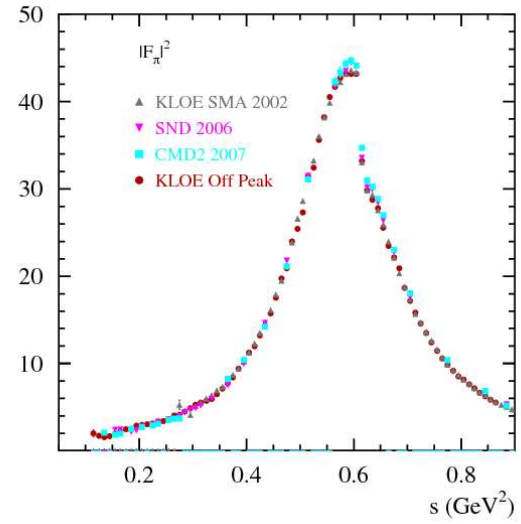

(a)

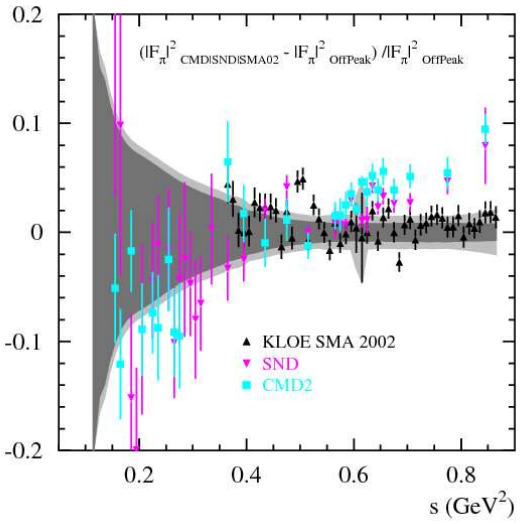

(b)

Fig. 1.1: The comparison among $|F_\pi(s)|^2$ results from KLOE, SND and CMD-2 is shown. The pion form factor result based on 2006 KLOE data is still preliminary. (b): the relative difference among the different pion factor evaluations with respect to the one obtained by the KLOE Large Angle analysis with off peak data presented in this work. The dark grey band gives the statistical error for KLOE, the light grey band combines the statistical and systematic error (added in quadrature).

low energies.

0.25 and 0.85 GeV^2. The obtained preliminary value is:

$$a_\mu^{\pi\pi}(0.25 < s < 0.85\ \mathrm{GeV}^2) = (426.7 \pm 0.9_{\mathrm{stat}} \pm 2.8_{\mathrm{exp}} \pm 2.5_{\mathrm{theo}}) \times 10^{-10}$$

To illustrate the relevance of this measurement we point out that this result contributes to more than 80% of the total value of $a_\mu^{\pi\pi}$ and corresponds to ca. 60% of the total contribution to a_μ^{had}. The precision achieved is 0.9%.
Evaluating $a_\mu^{\pi\pi}$ in the range between 0.35 and 0.85 GeV^2 allows to compare our preliminary result to the published KLOE result, based on small angle acceptance using 2002 data:

KLOE Analysis	$a_\mu^{\pi\pi}(0.35 < s < 0.85\ \mathrm{GeV}^2) \times 10^{-10}$
LA 2006	$375.0 \pm 0.7_{\mathrm{stat}} \pm 2.3_{\mathrm{exp}} \pm 2.2_{\mathrm{theo}}$
SA 2002	$379.6 \pm 0.4_{\mathrm{stat}} \pm 2.4_{\mathrm{exp}} \pm 2.2_{\mathrm{theo}}$

The two results are in agreement within errors (0.7σ). This represents a further test of the consistency of the KLOE analyses.

To estimate the impact of the off-peak result on the $(g-2)_\mu$ discrepancy, we use our new result presented above in the range $[0.25 - 0.85]$ GeV^2, combine it with the world data set elsewhere.[9] The total contribution given by the $\pi^+\pi^-$-channel to a_μ results to be:

$$a_\mu^{\pi\pi} = (504.04 \pm 3.9) \times 10^{-10}.$$

Including all the other hadronic contributions, the ones from QED and from Weak interaction,[10] one obtains:

$$a_\mu^{\mathrm{theo(SM)}} = (11\,659\,178.6 \pm 6.0) \times 10^{-10}.$$

Comparing this value to the world average experimental value, one gets: $a_\mu^{\mathrm{exp}} - a_\mu^{\mathrm{theo(SM)}} = (29.4 \pm 8.7)$, which corresponds to ca. 3.4σ, confirming the discrepancy between the Standard Model prediction and the direct measurement of $(g-2)_\mu$.

The KLOE collaboration is also going to perform an analysis using the off-peak data sample selecting events with ISR-photons at small polar angle. The measurement of $R(s)$ ratio

$$R(s) = \frac{\sigma(e^+e^- \to \pi^+\pi^-)(s)}{\sigma(e^+e^- \to \mu^+\mu^-)(s)},$$

is also in progress, with both on-peak and off-peak samples. These analyses will provide other high precision evaluations of the hadronic contribution to the anomaly of the muon magnetic moment.

If future measurements will keep sustaining the difference between the Standard Model predicted value and the direct measurement of $(g-2)_\mu$, the anomaly of the muon magnetic moment could represent a "narrow open window" where to peer for New Physics.

[9] M. Davier, *Nucl. Phys. Proc. Suppl.* **169**, 288-296 (2007)
[10] Values for a_μ^{had}(for the other hadronic channels and for the higher order), a_μ^{QED} and a_μ^{Weak} have been taken from: K. Hagiwara et al, *Phys. Rev. B* **649**, 173 (2007), M. Passera, *Phys. Rev. D* **75**, 013002 (2007) and A. Czarnecki, W.J. Marciano and A. Vainshtein, *Phys. Lett. D* **73**, 11901 (2006).

2. THE HADRONIC CORRECTION TO a_μ AND ITS IMPACT ON THE STANDARD MODEL AND BEYOND

Modern particle physics experiments are moving into two different and complementary directions. On one side, colliders are trying to reach higher and higher energies to measure particles, which have never been seen before.[1] On the other side, at lower energies, measurements are achieving higher and higher precision. Focusing on the latter, accurate knowledge of theory and of physics parameters become more and more relevant. Moreover, precision tests of the *Standard Model* (*SM*) of particle physics, or testing the existence of new theoretical frameworks, as for instance *SuperSymmetry* (*SUSY*), necessitate the evaluation of higher order quantum corrections and precise knowledge of theory-defining input parameters, like coupling constants.
In the case of the *anomalous magnetic moment of the muon*, a_μ, which is very sensitive to radiative corrections, as well as in the case of the *running QED coupling constant*, $\alpha_{\rm em}(s)$, the determination within the Standard Model is limited by the uncertainty on the photon vacuum polarization . Perturbative Quantum Chromodynamics (pQCD) fails to calculate this contribution due to the low energies involved. Unitarity and analyticity provide a way out in relating the hadronic vacuum polarization amplitude $\Pi(s)$ to the total hadronic cross sections

$$\gamma^* \to q\overline{q} \to \text{hadrons}.$$

Therefore precise measurements of *hadronic cross sections* are necessary to improve the predictions on both a_μ and $\alpha_{\rm em}(s)$, and to probably give some light on the existence of *New Physics* (*NP*) beyond the Standard Model, which can be resolved if the measurement and the Standard Model prediction of certain quantities differ significantly.

In the following we will concentrate on how the hadronic cross section enter the determination of the anomaly of the muon magnetic moment, defined as

$$a_\mu = \frac{g_\mu - 2}{2}.$$

It is worth to state that recent $(g-2)$ experiments at Brookhaven National Laboratory (BNL) have reached the precision of 0.5 parts per million [2], making this quantity one of the most precise measurements in particle physics and setting severe limits on deviations from the Standard Model and giving the possibility to open a window to New Physics.
We will also give a brief overview on the contribution that the hadronic cross section can give to $\alpha_{\rm em}(s)$.

[1] LHC, the Large Hadron Collider at CERN in Geneva, has started is commissioning phase while these lines were written.

2.1 The muon anomalous magnetic moment

To get an idea of what makes the muon and its magnetic moment so special, let us consider the leptons in general. Leptons (electrons, e^-, muons, μ^-, and tau, τ^-) are elementary spin 1/2 fermions of electric charge -1 in units of the positron charge e, and, as free relativistic one particle states, are described by the Dirac equation. Of course the charged leptons are never really free, they interact electromagnetically, with the photon, and weakly, via the heavy gauge bosons W and Z, as well as very much weaker also with the Higgs boson. The three leptons have identical properties, but they have very different masses ($m_e = 0.511$ MeV, $m_\mu = 105.658$ MeV and $m_\tau = 1776.99$ MeV). This fact causes very different lifetimes: while the electron is stable, the muon lifetime, τ_μ, results to be equal to 2.2×10^{-6} s and the tau lifetime, τ_τ, to 2.9×10^{-9} s. Since the muon is much more sensitive to physics beyond the Standard Model than the electron itself, it is much more suitable to give hints about New Physics. The reason lies in the fact that effects from New Physics scale with powers of m_ℓ^2.
Besides charge, spin, masses and lifetime, leptons have other interesting properties like the *magnetic dipole moment*. Its operator can be expressed as

$$\vec{\mu}_{\rm m} = \pm qg\mu_0 \frac{\vec{\sigma}}{2}, \tag{2.1}$$

where $\sigma_i (i = 1, 2, 3)$ are the Pauli spin matrices, q is the electrical charge in unit of e (with positive sign for positive charged particle and negative sign for the negative ones) and g is the *gyromagnetic factor*. The quantity μ_0 indicates the Bohr magneton:

$$\mu_0 = \frac{e\hbar}{2mc}. \tag{2.2}$$

The Dirac equation predicts [3] that $g = 2$ for a free lepton. Through the measurement of the electron's magnetic moment, the first evidence of an "anomalous" contribution was observed, resulting in a value which is about 0.12% larger than 2 [4, 5]. This deviation from Dirac's prediction, the so-called *anomaly of the magnetic moment*,[2] is usually formulated as

$$a_\ell = \frac{g_\ell - 2}{2}, \tag{2.3}$$

where ($\ell = e, \mu, \tau$).
The first explanation of the reason of the existence of a_ℓ came from Quantum Electrodynamics (QED), which at its leading contribution (one-loop diagram) adds to the classical quantity the value

$$a_\ell^{\rm QED(1)} = \frac{\alpha}{2\pi}, \tag{2.4}$$

evaluated by Schwinger [6].
Experiments – the first precision determination of the magnetic moment of the electron, by Kusch and Foley [10], whose result stated $g_e = 2.00238(10)$ – arrived bit earlier than the theoretical explanation. Together with the Schwinger's result, this provided one of the first test of the virtual quantum corrections, usually called *radiative corrections*, predicted by a relativistic Quantum Field Theory (QFT).

[2] The magnetic moment is named "anomalous" for historical reasons, as a deviation from the classical result.

Today it is known that – within the Standard Model – the contributions to the magnetic moment anomaly are due to the radiative corrections coming from QED, Weak interaction (W) and Strong (hadronic) interaction.[3] The most important condition for the anomalous magnetic moment to be a useful monitor for testing a theory is its unambiguous predictability within that theory. This predictability depends on the following properties: the theory

1. must be a local relativistic QFT;
2. must be renormalizable.

This implies that g cannot be an adjustable parameter but, in turn, it is a calculable quantity and its predicted value can be compared with experiments. Moreover, since high precision has been reached both in computations and in experiments, $(g-2)$ represents a very stringent test for the theory and a good indicator of its possible limitations.

As mentioned above, the sensitivity of a_ℓ to short distance physics scales like

$$\frac{\delta a_\ell}{a_\ell} \simeq \frac{m_\ell^2}{\Delta^2} \propto \frac{m_\ell^2}{M^2}, \tag{2.5}$$

where Δ is the ultraviolet cut-off characterizing the scale on which New Physics occurs, and M may be the mass of a heavier Standard Model particle, or the mass of a hypothetical heavy state beyond the Standard Model.[4] On one side, this means that the heavier the new state or scale is, the more difficult is to detect it. But, on the other side, the sensitivity to New Physics grows quadratically with the mass of the lepton, which means that the interesting effects are amplified in a_μ relatively to a_e by a factor

$$(m_\mu/m_e)^2 \simeq 4 \times 10^4,$$

and this is what makes the anomalous magnetic moment of the muon a special place where to get hints of New Physics. The best would be to exploit the sensitivity of a_τ, but present experimental precision are not sufficient due to the short the τ lifetime.
Thus, in the following, we refer essentially to the anomaly of the muon magnetic moment, presenting the status of the measurements and of its theoretical prediction.

2.2 Direct measurement of a_μ

A particle of mass m, charge q and momentum p in an uniform magnetic field $\vec{B}$ possesses a cyclotron frequency equal to

$$\omega_c = \frac{eB}{m}, \tag{2.6}$$

while the spin precession is:

$$\omega_s = g\frac{eB}{2m}. \tag{2.7}$$

The proportionality with the gyromagnetic factor g comes from the relation between the spin and the magnetic moment. This opens a possibility to perform direct measurements of $(g-2)$. For high momenta, Eq. 2.6 and Eq. 2.7 become:

$$\omega_c = \frac{eB}{\gamma m} \quad \text{and} \quad \omega_s = \frac{eB}{\gamma m} + a\frac{eB}{m}, \tag{2.8}$$

[3] More details on the contributions to a_μ will be given in Sec. 2.3.
[4] This was already known at the end of the '50, when a_e was already well measured [11, 12, 13].

and the difference between the two is:

$$\omega_a = \omega_c - \omega_s = a\frac{eB}{m} = a\gamma\omega_c, \tag{2.9}$$

which means that, e.g. for $a = 0.1$ the spin rotates with respect to the momentum by $1/10$ turn by turn.
First experiments, based on muon storage ring, were set up at CERN in 1961 [14] and, with successive upgrades, were operating until 1968 [15, 16, 17].[5] To overcome systematic difficulties a second muon storage ring was built (1969-1976). The new experimental set up – together with new software tools – allowed to determine a_μ with a precision of 7 ppm [18, 19] and for the first time m_μ^2/m_e^2-enhanced contribution came into play.

The most recent experiment is E821, at Brookhaven National Laboratory (BNL). The latest published result, based on data collected in 2001, has been released in 2004. The experimental technique is based on high relativistic pions (obtained from protons hitting a target) decaying in muons. Forward decay muons are highly polarized (therefore the direction of their spin is known). The muons are accumulated in a storage ring, where they decay into electrons ($\mu^\pm \to e^\pm \nu_e \nu_\tau$). The key point stays in the fact that favored directions of the electron momentum is opposite to the direction of the spin of the muon, because of the *Vector-Axial* (*V-A*) nature of the Weak interaction. This means that measuring the direction of the electron momentum, one knows (in average) the direction of the muon spin. This correlation is increased if one cuts on the minimum energy of the detected electron. At BNL [2] the measurement of the negative muon anomalous magnetic moment has been performed by counting the number of decay electrons above an energy threshold of ca. 2 GeV as a function of time, which is modulated with the frequency ω_a of Eq. 2.9:

$$N(t) = N_0(E)e^{-t/\gamma\tau}\left[1 + A(E)\sin(\omega_a t + \phi_a(E))\right]. \tag{2.10}$$

In Eq. 2.10 the normalization N_0, the asymmetry A and the phase ϕ_a vary with the energy E. An electrical quadrupole field is applied for vertical focusing purpose; the presence of such a field modifies Eq. 2.9, and $\vec{\omega}_a$ becomes:

$$\vec{\omega}_a = \frac{e}{mc}\left[a_\mu \vec{B} - \left(a_\mu - \frac{1}{\gamma^2 - 1}\right)\vec{\beta} \times \vec{E}\right]. \tag{2.11}$$

The dependence of $\vec{\omega}_a$ on the electric field is removed by storing muons with the "magic" value of $\gamma = 29.3$, corresponding to muons of momentum $p = 3.09$ GeV. In Fig. 2.1 the time spectrum for positrons with energy above 2 GeV is shown. Each line refers to a period of 100 μs. The value of ω_a is extracted from a fit of the curves shown and is used, together with a very precise measurement of the magnetic field $\vec{B}$, to determine a_μ according to:

$$a_\mu = \frac{m_\mu}{e}\frac{\omega_a}{B}. \tag{2.12}$$

The new world average value using positive and negative muon is [2]

$$a_\mu = (11659208.0 \pm 6.3) \times 10^{-10}. \tag{2.13}$$

In Fig. 2.2 the four measurements performed at BNL are shown together with the previous values obtained at CERN.

[5] Experimental results agreed well within the errors. An accuracy of 270 ppm was reached and a deviation of 1.7σ from theory was found.

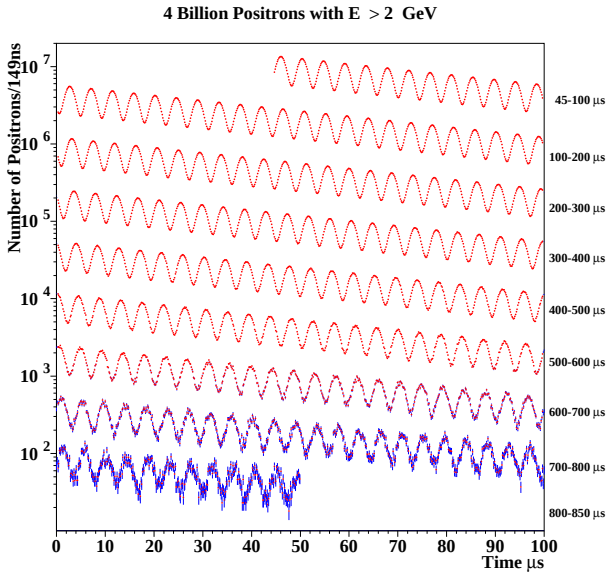

Fig. 2.1: Time spectrum for positrons with energy above 2 GeV collected from January to March 2000 at BNL. Data points are shown in red, error bars in blue.

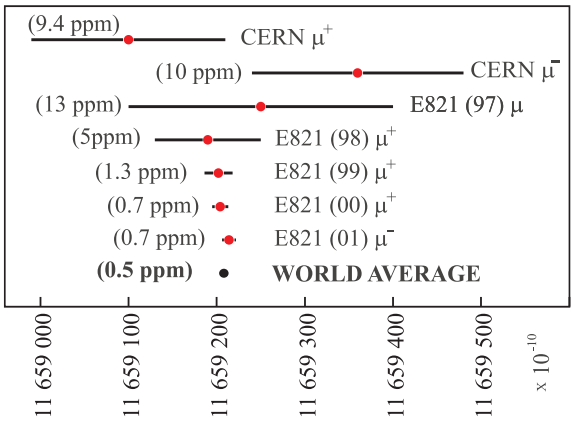

Fig. 2.2: Results for a_{μ^+} and a_{μ^-} from CERN and E821 experiments.

2.3 Theoretical prediction of a_μ

As mentioned above, in the Standard Model, a_μ is expected to include three contributions, coming from the quantum corrections of all the known fundamental interactions of the Standard Model:

$$a_\mu^{\text{theo(SM)}} = a_\mu^{\text{QED}} + a_\mu^{\text{Weak}} + a_\mu^{\text{had}}. \tag{2.14}$$

In Fig. 2.3 the interaction between a muon and an external electromagnetic field is drawn: here it is possible to see examples of how the coupling is modified by the QED, the Weak and the Strong interactions.

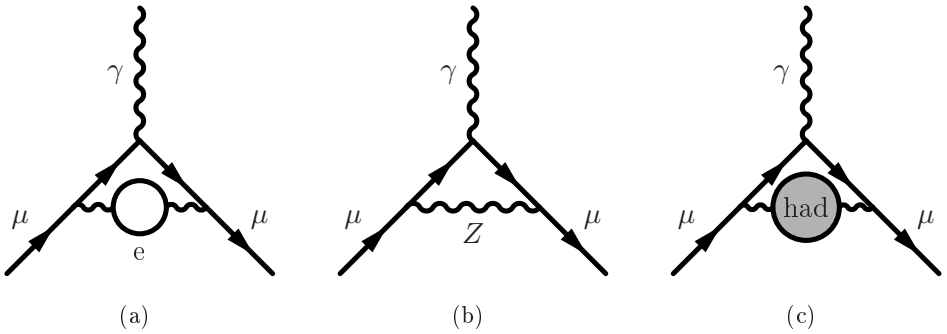

Fig. 2.3: Different examples of vertex modifications from QED (a), Weak (b) and hadronic effects (c).

The *QED contribution* is defined as the contribution arising from all the diagrams containing only leptons and photons. It can be expressed in the general form:

$$a_\mu^{\mathrm{QED}} = \Sigma C_i \left(\frac{\alpha}{\pi}\right)^i, \tag{2.15}$$

where the coefficients C_i are functions of the different lepton masses and i indicates the number of loops considered in the computation.[6] Two- and three-loop contributions are known analytically,[7] while most of the four-loop diagrams are known only numerically. The five-loop contribution, which is now an active field of research [29], is still dominating the total error on the QED prediction. The most recent value for the QED contribution on a_μ is [20]

$$a_\mu^{\mathrm{QED}} = (11658471.81 \pm 0.016) \times 10^{-10}. \tag{2.16}$$

The *Weak contribution* is suppressed by a factor $(m_\mu/m_W)^2$ with respect to the QED one. The one loop part was computed by several authors and it is known analytically since 1972. Recent calculations of the the two-loops part are presented in [30, 31]. The total value is[8]

$$a_\mu^{\mathrm{Weak}} = (15.4 \pm 0.2) \times 10^{-10}. \tag{2.17}$$

The third Standard Model contribution comes from the *Strong interaction*, and gives the second largest contribution, though dominating the theoretical error. It consists of three terms:

$$a_\mu^{\mathrm{had}} = a_\mu^{\mathrm{had,LO}} + a_\mu^{\mathrm{had,HO}} + a_\mu^{\mathrm{had,LbL}}, \tag{2.18}$$

[6] A more detailed explanation of Eq. 2.15 can be found in [20].

[7] See [21, 22, 23, 24] concerning the two-loop and [25, 26, 27, 28] for the three-loop contribution.

[8] In the error have been taken into account the hadronic loop uncertainties in the two-loop corrections, the unknown Higgs mass the current top mass uncertainty and the neglected three-loops effects have been taken into account. The mass range for the Higgs boson has been considered between 114 and 250 GeV.

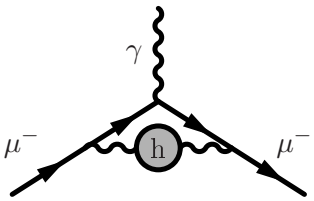

Fig. 2.4: Leading Order hadronic contribution, $a_\mu^{\mathrm{had,LO}}$.

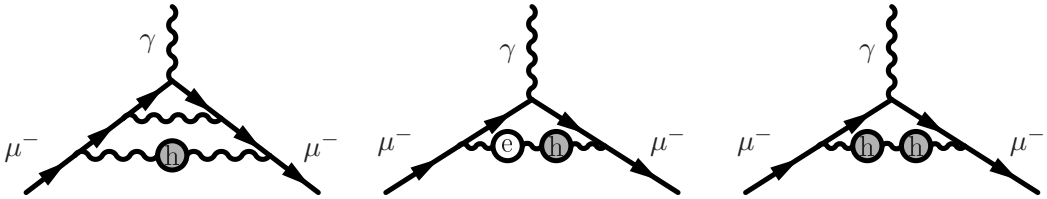

Fig. 2.5: Examples of Higher Order contributions, $a_\mu^{\mathrm{had,HO}}$.

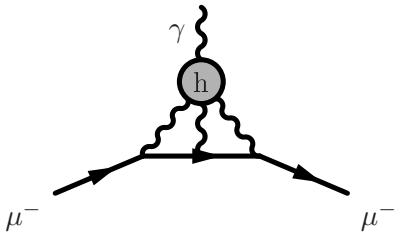

Fig. 2.6: Light-by-light scattering contribution, $a_\mu^{\mathrm{had,LbL}}$.

the leading order contribution, $a_\mu^{\mathrm{had,LO}}$ (Fig. 2.4), is the dominant one and can be calculated via a dispersion integral, Eq. 2.23, using hadronic cross section (or the hadronic decays of τ) data as inputs; higher order contribution $a_\mu^{\mathrm{had,HO}}$ (Fig. 2.5) has less impact to a_μ^{had}; the so-called "Light-by-Light" contribution, $a_\mu^{\mathrm{had,LbL}}$ (Fig. 2.6), heavily relies on effective field theories and model and is still poorly known.
A description of these three terms, concentrating especially on the first one, will be given in the next section.

Hadronic contribution to a_μ

Considering the *vacuum polarization* in the photon propagator introduces the following modification:

$$\frac{-ig_{\mu\nu}}{s} \rightarrow \frac{-ig_{\mu\nu}}{s}\frac{1}{1+e^2\Pi_\gamma(s)} \tag{2.19}$$

where s is the momentum transferred and $\Pi_\gamma(s)$ is the vacuum polarization amplitude containing both the leptonic and the hadronic part.[9] In this section, we will consider only the latter. In Fig. 2.7 the leading order of the hadronic contribution to a_μ and of the electromagnetic coupling constant, $\alpha_{\rm em}$, in the process $e^+e^- \to \mu^+\mu^-$, are drown in (a) and in (b), respectively. One can see the modification of the photon propagator due to the polarization of the vacuum. The

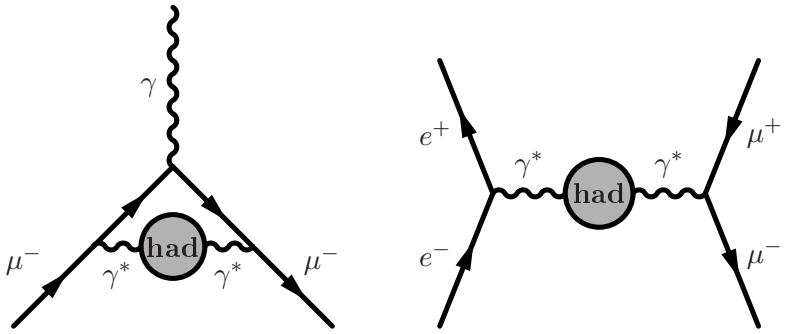

Fig. 2.7: Leading order of the hadronic vacuum polarization modifying the anomalous magnetic moment of the muon a_μ, (a), and the electromagnetic coupling constant $\alpha_{\rm em}$ in the process $e^+e^- \to \mu^+\mu^-$, (b).

unitarity of the scattering matrix leads to the *Optical Theorem*. This theorem states that the imaginary part of the hadronic vacuum polarization amplitude, $\Im m\Pi_\gamma(s)$, can be written as the sum over all the possible hadronic final states generated from the photon, see Fig. 2.8. The photon vacuum polarization amplitude $\Pi_\gamma(s)$ can be expressed as following:

$$\Im m(\Pi_\gamma(s)) = \frac{s}{e^2}\sigma(e^+e^- \to \gamma^* \to \text{hadrons}) = \frac{1}{12\pi}R(s), \tag{2.20}$$

where γ^* is the virtual photon and $R(s)$ represents the ratio of $e^+e^- \to$ hadrons over $e^+e^- \to \mu^+\mu^-$

$$R(s) = \frac{\sigma(e^+e^- \to \text{hadrons})(s)}{\sigma(e^+e^- \to \mu^+\mu^-)(s)} \approx \frac{\sigma^{\rm had}(s)}{4\pi\alpha^2/3s}. \tag{2.21}$$

Exploiting also the analyticity of the photon propagator one obtains the dispersion relation:

$$\Im m(\Pi_\gamma(s)) - \Im m(\Pi_\gamma(0)) = \frac{s}{\pi}\int_0^\infty ds' \frac{\Im m\Pi_\gamma(s')}{s'(s'-s-i\epsilon)} \tag{2.22}$$

Eq. 2.20 and Eq. 2.22 are the basis for the evaluation of the hadronic vacuum polarization in terms of the measured quantity $\sigma(e^+e^- \to \text{hadrons})$.
It is possible to write down the relation which connects $a_\mu^{\rm had,LO}$ to the process $e^+e^- \to \gamma^* \to q\bar{q} \to$ hadrons:

$$a_\mu^{\rm had,LO} = \frac{1}{4\pi^3}\int_{4m_\pi^2}^\infty ds\, \sigma_{\rm had}(s)K(s) = \left(\frac{\alpha m_\mu}{3\pi}\right)^2 \int_{4m_\pi^2}^\infty ds\, \frac{R(s)\hat{K}(s)}{s^2}. \tag{2.23}$$

[9] The contribution from the Weak interaction is actually suppressed. What is indicated as "hadronic" contains basically the five lightest quarks, since top quark is too heavy to hadronize and it is usually considered as an additional contribution.

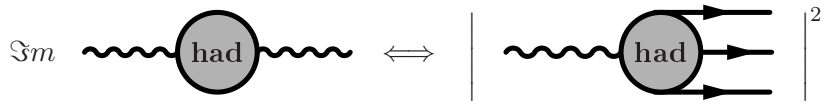

Fig. 2.8: The optical theorem relating the hadronic vacuum polarization to the cross section for $\gamma^* \rightarrow$ hadrons.

Eq. 2.23 describe the role of the hadronic cross section for the determination of $a_\mu^{\rm had,LO}$ and subsequently of a_μ. It represents the *master formula* of the relation between the hadronic cross section and its contribution to the anomaly of the muon magnetic moment. Two aspects need to be pointed out:

1. the low energy region, close to the two pion threshold, $(2m_\pi)^2$, represents the most important part. Since both the kernel function, $K(s)$,[10] and $\sigma_{\rm had}(s)$ behave like $1/s$, the contribution to a_μ by the low energy region of the spectrum dominates by far. More than 75% comes from the region $4m_\pi^2 < s < m_\phi^2$ (see Fig. 2.10), ca. 73% from the $\pi^+\pi^-$ channel;

2. the integration variable s runs from the threshold, $4m_\pi^2$, to infinity. While at sufficiently high energies (above 4-10 GeV), $\sigma_{\rm had}(s)$ can be safely calculated within the framework of *perturbative QCD* (*pQCD*), at lower energies – because of resonances in $\sigma_{\rm had}(s)$ – one has to rely on experimental data for $R(s)$, or $\sigma_{\rm had}(s)$, and to use them as input in Eq. 2.23.[11] In Fig. 2.9 the behaviour of $R(s)$ as a function of the energy is shown.

These two points, indicates the relevance to have an extremely precise measurement of the hadronic cross section. It comes out that a precision of ca. 1% or better is needed for the most important channel $e^+e^- \rightarrow \pi^+\pi^-$in order to be competitive with the direct measurement of $(g-2)_\mu$.
In Sec. 2.4 the experimental techniques to obtain the $\sigma(e^+e^- \rightarrow$ hadrons) cross section, or $R(s)$, will be briefly described. In Tab. 2.1 the values of $a_\mu^{\rm had,LO}$ evaluated in different energy ranges based on e^+e^--data are reported.

For the complete computation of $a_\mu^{\rm had}$ the other two hadronic contributions have to be included, that is $a_\mu^{\rm had,HO}$, which contains all the additional fermionic loops or photonic corrections to the vacuum polarization (see Fig. 2.5), and $a_\mu^{\rm had,LbL}$, i.e the Light-by-Light contribution (see Fig. 2.6).

[10] The kernel function $K(s)$ can be written in terms of the variables [40, 41]

$$x = \frac{1-\beta_\mu}{1+\beta_\mu} \quad , \quad \beta_\mu = \sqrt{1-4m_\mu^2/s}$$

as

$$K(s) = \frac{x^2}{2}(2-x^2) + \frac{(1+x^2)(1+x)^2}{x^2}\left(\ln(1+x) - x + \frac{x^2}{2}\right) + \frac{(1+x)}{(1-x)}x^2\ln(x),$$

and the kernel function to be used when taking $R(s)$ in the dispersion integral is

$$\hat{K}(s) = \left(\frac{3s}{m_\mu^2}\right)K(s),$$

which is an bounded function between 0.63 at m_π^2 and 1 at infinity.

[11] Accurate and clear demonstrations of the optical theorem and of the dispersion integral can be found in [32] and [33].

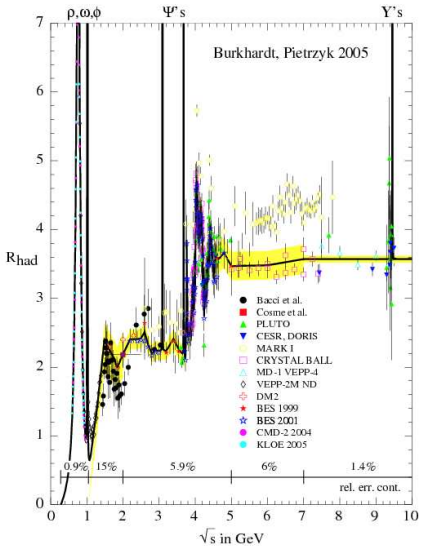

Fig. 2.9: Ratio of hadronic cross section over the pointlike, born-level muon-cross section as a function of the energy $\sqrt{s}$ below 5 GeV [39]. Plotted is a compilation of data points together with the prediction from pQCD.

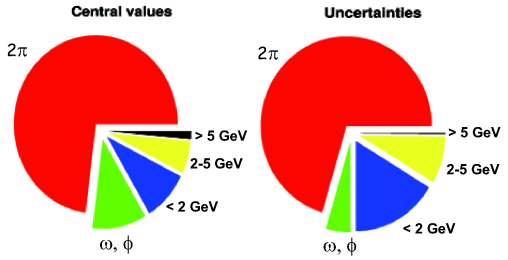

Fig. 2.10: Fractions of the total contributions (a) and errors (b) to $a_\mu^{\mathrm{had,LO}}$ coming from various energy intervals. Plot taken from [42].

The *Higher Order* hadronic vacuum polarization can be calculated in terms of dispersion integrals, like

$$a_\mu^{\mathrm{had,HLO}} \propto \int ds \, \frac{R(s)G(s)}{s^2},$$

where $G(s)$ is a smooth function of s. However, as already written above, they have much smaller contribution to a_μ^{had}, due to higher order, than $a_\mu^{\mathrm{had,LO}}$. An update value of $a_\mu^{\mathrm{had,HO}}$ is [45]

$$a_\mu^{\mathrm{had,HO}} = (-9.8 \pm 0.1) \times 10^{-10}. \tag{2.24}$$

The *Light-by-Light* term cannot be expressed in terms of experimental quantities: its evaluation has to rely solely on theoretical considerations. Several calculations have been performed and the updated ones are in agreement; we report one of most recent [46]

$$a_\mu^{\mathrm{had,LbL}} = (11.0 \pm 4.0) \times 10^{-10}. \tag{2.25}$$

channel, $\sqrt{s}$ (GeV)	$a_\mu^{\mathrm{had,LO}} \times 10^{10}$	$\delta a_\mu^{\mathrm{had,LO}}(\%)$
$\pi^+\pi^-$	$505.6 \pm 3.1 \pm 1.0$	73.0
ω	$38.0 \pm 1.0 \pm 0.3$	5.5
ϕ	$35.7 \pm 0.8 \pm 0.2$	5.2
$0.6 - 1.8$	$54.2 \pm 1.9 \pm 0.4$	7.8
$1.8 - 5.0$	$41.6 \pm 0.6 \pm 0.0$	6.0
$J/\Psi, \Psi'$	$7.4 \pm 0.4 \pm 0.0$	1.0
> 50	$9.9 \pm 0.2 \pm 0.0$	1.4
Total	$690.9 \pm 3.9_{\mathrm{exp}} \pm 1.9_{\mathrm{rad}} \pm 0.7_{\mathrm{QCD}}$	100.0

Tab. 2.1: Contributions from different energy ranges to the leading order to $a_\mu^{\mathrm{had,LO}}$ are reported, [44]. Looking at the percentage contribution, on the third column, one can realize the important role that the $e^+e^- \to \pi^+\pi^-$ channel takes in the $a_\mu^{\mathrm{had,LO}}$.

Contribution	$a_\mu \times 10^{10}$
Experiment	11659208.0 ± 6.3
QED [20]	11658471.810 ± 0.016
Weak [31]	15.4 ± 0.2
Hadronic [44]	691.4 ± 4.4
Theory [47]	11659177.8 ± 6.1
Exp. - Theory	30.2 ± 8.8 (3.4σ)

Tab. 2.2: Standard Model contributions to a_μ are reported and compared to the world average of the experimental value. A difference of 3.4 σ is found.

The error is due to the model dependence in the theoretical description.

Summing up all the Standard Model contributions reported so far, one gets theoretical value

$$a_\mu^{\mathrm{theo(SM)}} = (11\,659\,177.8 \pm 6.1) \times 10^{-10},$$

which has to be compared with the world average experimental value

$$a_\mu^{\mathrm{exp}} = (11\,659\,208.0 \pm 6.3) \times 10^{-10}.$$

Performing the difference between the two results one gets

$$\Delta a_\mu = a_\mu^{\mathrm{exp}} - a_\mu^{\mathrm{theo(SM)}} = (30.2 \pm 8.8) \times 10^{-10},$$

that correspond to 3.4σ discrepancy. This gap must be investigated.
In Tab. 2.2 the comparison between the experimental and theoretical value is listed. In Tab. 2.3, comparisons between different $a_\mu^{\mathrm{theo(SM)}}$ evaluations and the average of the experimental results are listed. The discrepancy between the Standard Model prediction and the experimental result

References	$a_\mu \times 10^{10}$	σ
e^+e^--data		
Jegerlehner [49], 2004	11659186.0 ± 9.0	2.0
de Trocóniz & Yndurain [50], 2005	11659185.6 ± 5.5	2.7
Hagiwara et al. [51], 2006	11659180.4 ± 5.1	2.7
Davier et al. [44], 2006	11659180.3 ± 5.6	3.3
Jegerlehner [33], 2008	11659181.3 ± 7.2	2.0
Passera et al. [47], 2008	116591778 ± 61	3.4
τ-data		
Davier [44]	11659202.2 ± 6.3	0.7
de Trocóniz & Yndurain [50]	11659193.9 ± 5.4	1.7

Tab. 2.3: Standard Model predictions for a_μ performed by different groups. The difference between the average of the experimental values and the theoretical prediction in terms of standard deviations is reported in the last column. Both evaluations based on e^+e^-- and on τ-data are reported.

spans from 2.0 to 3.4σ, if e^+e^--data are used as experimental input to Eq. 2.23, but it becomes smaller, 0.7 - 1.2σ, if only τ-data are considered for the evaluations.
The connection between $e^+e^- \to \pi^+\pi^-$ and $\tau^\pm \to \pi^\mp\pi^0\nu_\tau$ is due to *Charged Vector Current conservation* (*CVC*). The use of the hadronic decay of the τ will be briefly described in Sec. 2.4. However since τ-data require several corrections (probably not completely under control) to obtain $\sigma(e^+e^- \to \pi^+\pi^-)$ they provide a less direct measurement of this quantity, which is included in the dispersion integral. As a result, many groups are not taking τ-data into account for the $a_\mu^{\rm had}$ evaluation.
In Fig. 2.11 a graphical view of the comparison between predictions based on different inputs for $a_\mu^{\rm had}$ and the experimental world average value is shown. To be notice that the only value close to the experimental result is the one based on τ-data.

The existence of Δa_μ and its non negligible value ($\sim 3\sigma$) could be an indication of New Physics beyond the Standard Model. More details on the investigation of this possibility will be given in Sec. 2.6 and Sec. 2.6.2. On the other side, in order to understand whether such a discrepancy is really a hint of New Physics or just a possible error in some experimental or theoretical inputs, more precise measurement of the hadronic cross section (whose uncertainty is dominating the error of $a_\mu^{\rm theo(SM)}$) are needed, especially for the channel $e^+e^- \to \pi^+\pi^-$. The aim of this work is indeed to improve the knowledge of the contribution to a_μ given by the $e^+e^- \to \pi^+\pi^-$channel, named $a_\mu^{\pi\pi}$.

2.4 Experimental inputs to $a_\mu^{\rm had}$

As pointed out in the previous section, particularly in Eq. 2.23, the cross section of $e^+e^- \to$ hadrons represent the necessary experimental input for the evaluation of a_μ, especially at low energy. Low energies hadronic cross sections have been measured by experiments at the e^+e^- colliders (OLYA [52], TOF [53], ND [54], CMD [55], CMD-2 [56, 57], SND [58, 59], DM1 [60],

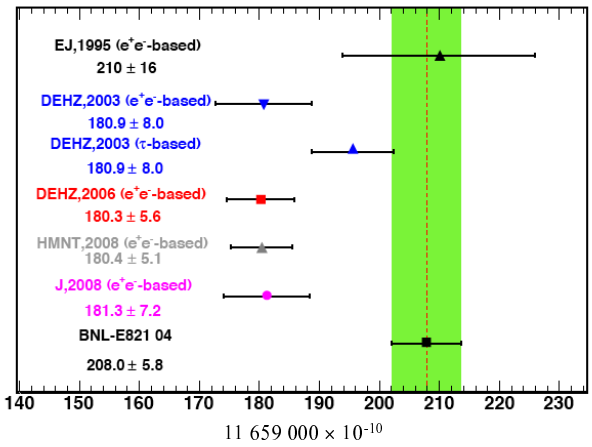

Fig. 2.11: The world average for the experimental value of a_μ (greed shaded area) and several theoretical predictions, based on different $a_\mu^{\rm had}$ inputs, [43].

DM2 [61], KLOE [62, 63] and BaBar [66, 67, 68, 69, 70]).

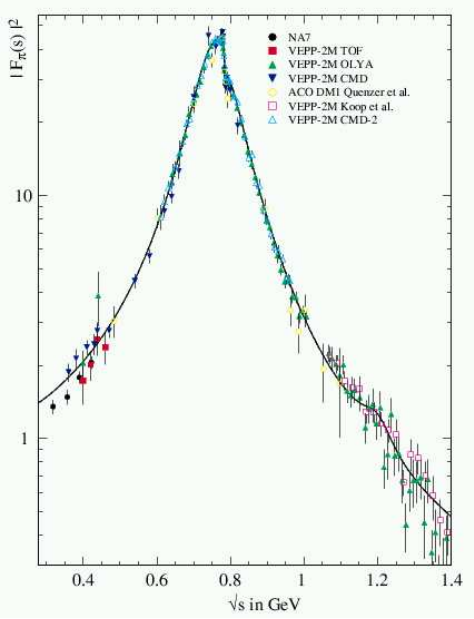

Fig. 2.12: The pion form factor as measured by the experiments NA7, TOF, OLYA, CMD and CMD-2, [39].

At low masses, where the reaction $e^+e^- \to \pi^+\pi^-$ is dominant, so far the most precise measurements are coming from CMD-2 and SND, both running at the VEPP-2M collider in Novosibirsk, and from KLOE, running at the DAΦNE collider at Frascati. CMD-2 and SND claim for $\sqrt{s} > 420$ MeV a systematic error of 0.6% ([56, 57]) and of 1.3%, respectively, and of 3.2% for $\sqrt{s} < 420$ MeV ([58, 59]). KLOE states a systematic error of 1.3% [62] and of 0.9% [63], for the

results published in 2004 and 2009 respectively. In the region close to the threshold ($\sqrt{s} \sim 2m_\pi$) the data from CMD-2 are the most recent, so far.
This work presents the result, still preliminary, based on KLOE data, in the range from 0.85 Gev^2 down to the 0.1 GeV^2, with a competitive precision with respect to the values from SND and CMD-2. This works represents the first KLOE measurement, more generally the first ISR measurement, which has reached the $\pi^+\pi^-$-threshold.
The CMD-2 experiment has provided also precise measurements of other important cross section channels such as $\sigma(e^+e^- \to \pi^+\pi^-\pi^0)$, $\sigma(e^+e^- \to \pi^+\pi^-\pi^0\pi^0)$ and $\sigma(e^+e^- \to \pi^+\pi^-\pi^+\pi^-)$ [65].
The construction of a new machine, VEPP-2000, is in advanced state and it will be able to provide more accurate results, thanks to the extended energy range, with respect to VEPP-2M, covering from 0.4 to 2 GeV and thanks to the 10 times bigger statistics, which is expected to be collected.
Improvement on the knowledge of the hadronic cross section above 1 GeV comes also from the BaBar experiment (running at the B-factory PEP-II at $\sqrt{s} = 10.6$ GeV). The BaBar collaboration has already published results [66, 67, 68] of several analysis with three and four hadrons in the final state ($e^+e^- \to \pi^+\pi^-\pi^0$, $\pi^+\pi^-\pi^+\pi^-$, $K^+K^-\pi^+\pi^-$, $K^+K^-K^+K^-$, $2(\pi^+\pi^-)\pi^0$, $2(\pi^+\pi^-)\eta$, $K^+K^-\pi^+\pi^-\pi^0$, $K^+K^-\pi^+\pi^-\eta$) with the systematic accuracy of 5% in the mass region between 1 and 4.5 GeV. Results have been obtained also in the five hadrons channel ($e^+e^- \to K^+K^-\pi^+\pi^-$, $K^+K^-\pi^0\pi^0$,$K^+K^-K^+K^-$) [69] and in the six hadrons channels ($e^+e^- \to 3(\pi^+\pi^-)$, $2(\pi^+\pi^-\pi^0)$, $2(\pi^+\pi^-)K^+K^-$) [70], improving largely the existing measurements. Also the analysis to determine the most important two pion channel cross section $\sigma(e^+e^- \to \pi^+\pi^-)$ is on the way at BaBar [73]. This last analysis could provide a relevant check to the KLOE, SND and CMD-2 results.

At e^+e^- experiments there are essentially two possible ways that can be used to perform $\sigma_{\text{had}}(s)$ measurements:

1. changing the energy of the crossing beams. This is the "standard approach" and experiments using this technique are usually named as *scan experiments*. The VEPP-2M collider covering the energies below 1.4 GeV, where CMD-2 and SND are set, and BES-C, operating at energy above 2 GeV, are using this approach. To be noticed the gap between the energy ranges of two colliders, which will be covered by the VEP-2000 machine;

2. an alternative way consists in looking at events where one of the incoming beams radiate a photon in the initial state (*Initial State Radiation, ISR*). This technique, called *Radiative Return*, is used in colliders where the center of mass energy of the beams is fixed and can not be easily varied over a wide range, like in *particle-factories*, such as PEP-II, KEKB and DAΦNE, where the BaBar, Belle and KLOE detectors are based respectively.

A detailed explanation of the Radiative Return method will be given in Sec. 4.1.

To get access to cross section data precise measurement of the spectral function from τ hadronic decays can be used, as suggested in [71]. Assuming CVC, the isovector part of the cross section for e^+e^- into hadrons can be derived from τ-decay spectra by an isospin rotation.[12] However, sophisticated corrections have to be applied [72]. $SU(2)$ symmetry breaking effects, due to mass differences of the neutral and the charged pions, as well as a possible difference between the neutral and the charged ρ mass, have to be precisely controlled in order to use τ-data to extract $e^+e^- \to$ hadrons.

[12] Since the W has isospin 1, it can only couple to a ϱ, not to an ω. For the photon, both processes are possible.

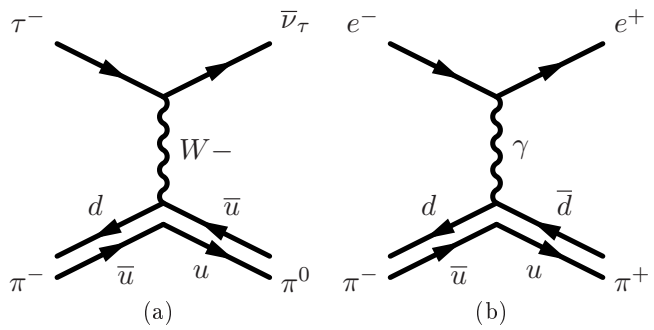

Fig. 2.13: The decay $\tau^- \to \overline{\nu}_\tau \pi^- \pi^0$ (a) can be seen as the isospin rotation of the isovector part of the process $e^+e^- \to \pi^+\pi^-$ (b), assuming that CVC holds.

In Fig. 2.13 the decay $\tau^- \to \nu_\tau \pi^- \pi^0$, related to the reaction $e^+e^- \to \pi^+\pi^-$ is shown. Since in the τ decay only Weak interactions are involved, any effects from vacuum polarization are excluded. Thus what is really related to the $e^+e^- \to \pi^+\pi^-$ cross section is the τ spectral function $v_{\pi^-\pi^0}(s)$ that can be extracted directly from the corresponding invariant mass spectra of the final state $\pi^-\pi^0$, through the relation:

$$v_{\pi^-\pi^0}(s) = \frac{m_\tau^2}{6|V_{ud}|^2 S_{\rm EW}} \frac{B(\tau^- \to \nu_\tau \pi^- \pi^0)}{B(\tau^- \to \nu_\tau e^- \bar{\nu_e})} \frac{1}{N_{\pi^-\pi^0}} \frac{dN_{\pi^-\pi^0}}{ds} \left[\left(1 - \frac{s}{m_\tau^2}\right)^2 \left(1 - \frac{2s}{m_\tau^2}\right) \right]^{-1}, \quad (2.26)$$

where $|V_{ud}|$ is the CKM weak mixing matrix element and $S_{\rm EW}$ accounts for ElectroWeak quantum corrections. The cross section $\sigma(e^+e^- \to \pi^+\pi^-)$ can then be extracted from $v_{\pi^-\pi^0}(s)$ via the relation

$$\sigma^{I=1}_{\pi^+\pi^-} = \frac{4\pi\alpha^2}{s} v_{\pi^-\pi^0}. \quad (2.27)$$

However this equation holds only in the limit of exact isospin invariance. So breaking of isospin due to electromagnetic effects and *up-down* quark mass splitting must be properly taken into account (see [72]).

Once the τ is corrected for the isospin breaking corrections, τ spectral function can be compared directly to the corresponding e^+e^- hadronic cross section, as it is done in Fig. 2.14, [43], for the $\pi^+\pi^-$ channel. Although the latest CMD-2 data are basically consistent with τ-data for the energy region below 850 MeV (0.72 GeV^2 in the plot), there is a clear discrepancy for larger energies. The most recent result from KLOE strongly confirms the discrepancy.[13] Due to the several corrections to be applied, the hadronic decays of the τ represent, as stated above, a more indirect measurement of $e^+e^- \to$ hadrons.

The puzzle concerning the e^+e^-- and τ-data disagreement is still not solved, and many computations for $a_\mu^{\rm had}$ do not rely on τ-data any more.[14]

[13] Recent preliminary BaBar results on $\sigma(e^+e^- \to \pi^+\pi^-)$ via radiative return claims to be in agreement with τ-data from CLEO and Belle, see [73]. However the BaBar preliminary result is still under control studies.

[14] More complete $SU(2)$ breaking effects have been considered in [74]. They tend to provide better agreement.

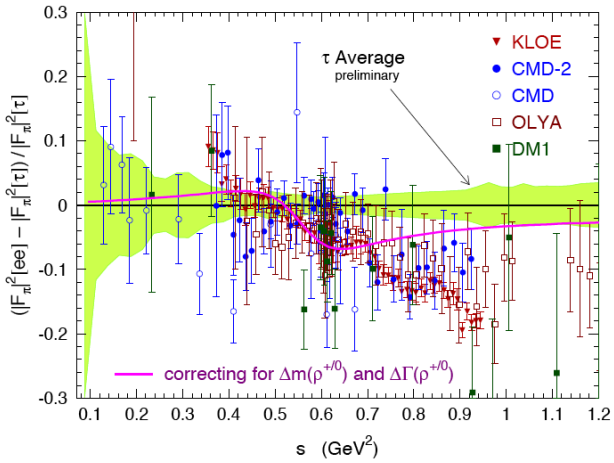

Fig. 2.14: Relative comparison among $\pi^+\pi^-$ spectral functions from e^+e^- experiments and isospin breaking corrected τ-data, averaged from ALEPH and CLEO. The green band shows the uncertainty in the τ spectral function.

The pion form factor

A *form factor* describes the interaction between a photon and the observable hadrons. For the two pion final state, $F_\pi(s)$ parametrizes the coupling between the photon and the $q\bar{q}$ pair hadronizing into a resonant state, that subsequently decays into two pions. It contains thus all the parameters of the corresponding resonance and can be directly related to the cross section $\sigma(e^+e^- \to \pi^+\pi^-)$ via the relation:

$$\sigma_{e^+e^-\to\pi^+\pi^-}(s) = \frac{\pi\alpha^2}{3s}\beta^3|F_\pi(s)|^2, \tag{2.28}$$

with s being the virtual photon, γ^*, Center-of-Mass (CM) energy squared, m_π the charged pion mass and $\beta_\pi = \sqrt{1-4m_\pi^2/s}$ the pion velocity in the e^+e^- CM-frame.

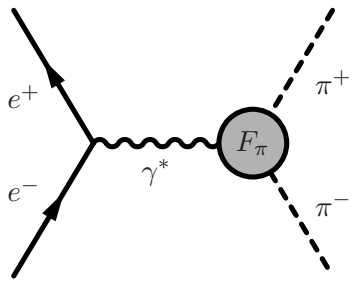

Fig. 2.15: pion form factor sketched within the process $e^+e^- \to \pi^+\pi^-$.

In the form factor all the possible effects, which are represented in the blob of Fig. 2.15 are included. Therefore its measurement can be used to determine all the properties of the underlying

hadrons, where the reaction proceeds to. Particularly interesting are the parameters for isospin violating effects, like the ρ-ω interference, which creates an observable effect in the data spectrum at $s = m_\omega^2$. Several theoretical parametrizations for the pion form form factor exist.[15]

2.5 The running of $\alpha_{\rm em}$

In Fig. 2.7(b) the modification of $\alpha_{\rm em}$ due to the hadronic vacuum polarization is shown. This *fine structure constant* is a fundamental input parameter of the ElectroWeak Standard Model. Moreover it can also set boundary conditions on the value of the Higgs boson mass, as the LEP ElectroWeak Working Group (LEP EWWG) fit results show.
The EWWG combines the measurements of the four LEP experiments ALEPH, DELPHI, L3 and OPAL on ElectroWeak observables, such as cross sections, masses and various couplings of the heavy ElectroWeak gauge bosons, properly taking into account the common systematic uncertainties. These combined precision ElectroWeak results are then publicised as the "best" LEP averages. Also ElectroWeak results from other experiments, notably NuTeV, CDF, DØ and SLD are compared or combined with LEP results.
Particular attention is dedicated to the constraint on the mass of the Higgs boson, because this ingredient of the Standard Model has not been observed yet. Fig. 2.16 shows he $\Delta\chi^2 = \chi^2 - \chi^2_{\rm min}$ curve derive from high-Q^2 precision ElectroWeak measurements, performed at LEP and by SLD, CDF, and D0, as a function of the Higgs boson mass, assuming the Standard Model to be the correct theory. The preferred value for its mass, corresponding to the minimum of the curve, is at 84^{+34}_{-26} GeV (at 68 percent confidence level derived from $\Delta\chi^2 = 1$ for the black line, thus not taking into account the theoretical uncertainty shown as the blue band). The precision ElectroWeak measurements tell that the mass of the Standard Model Higgs boson is lower than about 154 GeV (one-sided 95% CL upper limit derived from $\Delta\chi^2 = 2.7$ for the blue band, thus including both the experimental and the theoretical uncertainties). This limit increases to 185 GeV, when the LEP-2 direct search limit of 114 GeV shown in yellow is included. The dashed curve is the result obtained using the evaluation of $\Delta\alpha_{\rm em}^{\rm had(5)}(m_Z^2)$.[16]

Vacuum polarization by virtual pairs of particles tend to screen partially the electrical charge, modifying the value of the *bare charge* e. The charge screening effects determine a redefinition of the classical charge e^2, which is replaced by a *running charge* depending on the energy scale s as:

$$e^2 \to e^2(s) = \frac{e^2 Z}{1 + \prod_\gamma'(s)}, \tag{2.29}$$

where Z is a renormalization factor fixed by the condition that $e^2(s)$ equals the classical charge in the limit $q^2 \to 0$ and $\prod_\gamma'(s)$ is again the photon vacuum polarization amplitude. The electrical charge screening is less effective at low momentum transfer, while the strength of the interaction grows with the energy scale involved. This is the reason why the value for the coupling constant at m_Z^2 is significantly larger than the one in the limit at $s \sim 0$. As for the muon anomalous magnetic moment, the limited knowledge of the hadronic vacuum polarization dominates the

[15] Tow parametrizations for the pion form factor are mostly used: one by Gounaris and Sakurai [34] and another by by Kühn and Santamaria [35].
[16] The number 5 indicates that in the hadronic contribution only the 5 lightest quark are considered.

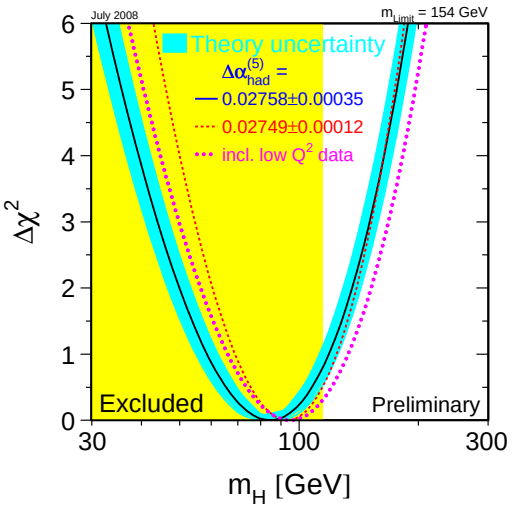

Fig. 2.16: Boundary conditions on Higgs boson mass set by $\alpha_{\rm em}$ [80].

uncertainty for $\alpha(m_Z^2)$. The "running" of $\alpha_{\rm em}$ is usually written as:

$$\alpha_{\rm em}(s) = \frac{\alpha_{\rm em}(0)}{1 - \Delta\alpha_{\rm em}(s)}, \tag{2.30}$$

where $\Delta\alpha_{\rm em}$ is composed of different contributions:

$$\Delta\alpha_{\rm em}(s) = \Delta\alpha_{\rm em}^{\rm lep}(s) + \Delta\alpha_{\rm em}^{\rm had(5)}(s) + \Delta\alpha_{\rm em}^{\rm top}(s). \tag{2.31}$$

The leptonic contribution is directly calculated and it is known up to three-loops [75] at $s = m_Z^2$ and equal to

$$\Delta\alpha_{\rm em}^{lep}(m_Z^2) = 314.98 \times 10^{-4} \tag{2.32}$$

The contribution from the top quark is very small [76]:

$$\Delta\alpha_{\rm em}^{top}(m_Z^2) = -0.7 \times 10^{-4} \tag{2.33}$$

As for the hadronic contribution to the muon magnetic moment, the hadronic contribution to $\Delta\alpha_{\rm em}^{\rm had(5)}(s)$ can be expressed via a dispersion integral:

$$\Delta\alpha_{\rm em}^{\rm had(5)}(s) = \frac{-e^2 s}{12\pi^2}\, \Re e \int_{4m_\pi^2}^{\infty} ds^{'}\, \frac{R(s^{'})}{s^{'} - s - i\epsilon}, \tag{2.34}$$

and again R is an experimental input for the low mass region, see Eq. 2.21 and Fig. 2.9. Assuming pQCD to be applicable above some energy E_{cut}, Eq. 2.34 can be written as:

$$\Delta\alpha_{\rm em}^{\rm had(5)}(s) = \frac{-e^2 s}{12\pi^2} \left(\Re e \int_{4m_\pi^2}^{E_{cut}} ds^{'}\, \frac{R(s^{'})}{s^{'} - s - i\epsilon} + \Re e \int_{E_{cut}}^{\infty} ds^{'}\, \frac{R(s^{'})}{s^{'} - s - i\epsilon} \right) \tag{2.35}$$

Eq. 2.34 can be equivalently expressed at the Z boson mass pole as

$$\Delta\alpha_{\rm em}^{\rm had(5)}(m_Z) = \frac{m_Z^2}{4\alpha\pi^2}\, P \int_{4m_\pi^2}^{\infty} ds\, \frac{\sigma(s)}{m_Z^2 - s} \tag{2.36}$$

where P is Cauchy's principal value.
Different theoretical approaches have been used to evaluate $\Delta\alpha_{\rm em}^{\rm had(5)}(s)$: they differ for (i) the choice of $E_{\rm cut}$ in the dispersion integral, (ii) in the way different data sets are combined and (iii) in using different technique, like Adler-function approach. Moreover some authors assume the validity of pQCD already above 1.8-2.5 GeV, while others prefer to use experimental data up to 12 GeV. All these different evaluations are in a reasonable agreement among each other (see Fig. 2.17).

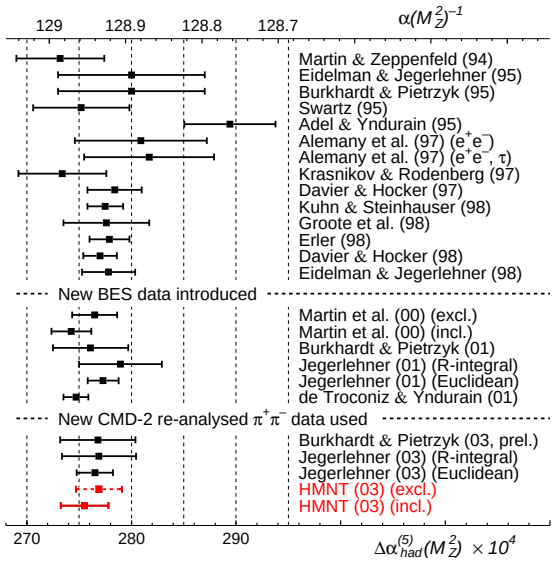

Fig. 2.17: Recent evaluations of $\Delta\alpha_{\rm em}^{\rm had(5)}$ (lower scale) with the corresponding value of $\Delta\alpha_{\rm em}(m_Z^2)^{-1}$ at the Z boson mass shown in the upper scale [45].

The τ spectral function has been also used: the difference between e^+e^-- and τ-data based approach has been calculated in [44] and yields

$$\Delta\alpha_{\rm em}(e^+e^-) - \Delta\alpha_{\rm em}(\tau) = (-2.37 \pm 0.62) \times 10^{-4}, \tag{2.37}$$

which is larger than the uncertainties of the mean value for $\alpha_{\rm em}$ itself.

In order to obtain more precise estimates for $\alpha_{\rm em}$ more accurate measurements of hadronic cross section are needed. Fig. 2.18 shows the relative contributions of different energy regions to the magnitude and uncertainty of $\Delta\alpha_{\rm em}^{\rm had(5)}(m_Z^2)$. Using the $R(s)$ ratio as experimental input up to 12 GeV, the largest contribution to $\Delta\alpha_{\rm em}^{\rm had(5)}$ comes from the 1-2 GeV and 2-5 GeV energy regions. However, if pQCD is used already for $\sqrt{s}$ >1.8 GeV, a precise measurement of the hadronic cross section below 1 GeV plays a more important role in the reduction of the uncertainty of $\Delta\alpha_{\rm em}$.

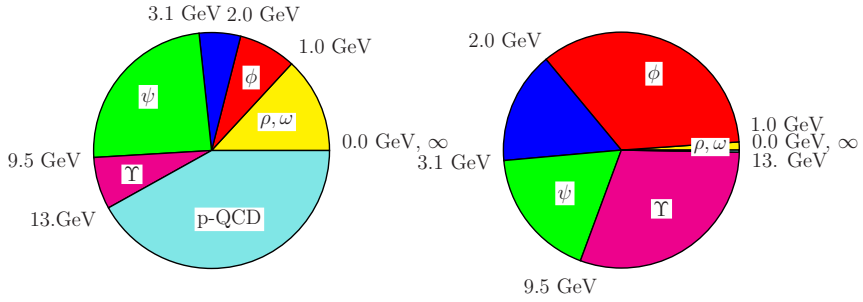

Fig. 2.18: Fractions of the total contributions (on the left) and errors squared (on the right) to $\Delta\alpha_{\rm em}^{\rm had(5)}(m_Z^2)$ coming from different energy intervals. The plot is taken from [77]

2.6 Hints for New Physics in $(g-2)_\mu$?

2.6.1 Errors or Physics beyond the Standard Model?

The $\sim 3\sigma$ discrepancy between the theoretical Standard Model prediction and the experimental value of $(g-2)_\mu$ can be explained in several ways.[17]
The $a_\mu^{\rm theo(SM)}$-$a_\mu^{\rm exp}$ discrepancy could be due to an error in the Light-by-Light hadronic contribution. However if this was the only cause, $a_\mu^{\rm had,LbL}$ should move of about eight standard deviations, using the value computed in [46]. Even if the errors on this contribution are not well established, such a large shift seems to be rather unlikely.
Another possibility would be to employ the QED, Weak and hadronic Higher Order vacuum polarization contributions.[18] But also this hypothesis looks improbable, just considering their values and errors, see Tab. 2.2.

Assuming the $g-2$ experiment E821 is correct, there are two options left: possible contributions from New Physics beyond the Standard Model, or an erroneous determination of the hadronic Leading Order, $a_\mu^{\rm had,LO}$. A possible explanation coming from physics beyond the Standard Model will be briefly described in Sec. 2.6.2.
If $\sigma_{\rm had}(s)$ is the only responsible of the discrepancy $a_\mu^{\rm theo(SM)}$-$a_\mu^{\rm exp}$, one has to increase the contribution from $a_\mu^{\rm had,LO}$ in order to reduce Δa_μ.[19] An increase of the hadronic contribution also affects the effective fine structure constant at m_Z: it is easy to see the similarities between Eq. 2.23 ($a_\mu^{\rm had,LO}$) and Eq. 2.36 ($\Delta\alpha_{\rm em}^{\rm had(5)}$), and the fact that $\sigma_{\rm had}(s)$ enters both.
The global fit of the LEP ElectroWeak Working Group gives a Higgs boson mass $m_H = 84^{+34}_{-26} GeV$ and, at 95% confidence level, an upper bound $m_H^{\rm UB} \simeq 154$ GeV.[20] The LEP direct-search lower bound is $m_H^{LB} = 114.4$ GeV at 95% Confidence Level (CL) [79]. $m_H^{\rm UB}$ is strongly driven by the comparison of the theoretical predictions of the W boson mass and the effective ElectroWeak mixing angle $\sin^2\theta_{\rm eff}^{\rm lept}$. Combining these two predictions via a numerical χ^2-analysis and using the

[17] Several papers have been focused on the $(g-2)_\mu$-puzzle. The Main arguments presented in this section have been explored in [47, 48].

[18] By hadronic higher-order vacuum polarization we mean $a_\mu^{\rm had,HO}$, indicated also as $a_\mu^{\rm HO(vp)}$, in order to better distinguish it from the light-by-light one.

[19] We have defined $\Delta a_\mu = a_\mu^{\rm exp} - a_\mu^{\rm theo(SM)}$.

[20] This result is based on new preliminary top quark mass $m_t = 172.4 \pm 1.2$ GeV [78] and the value of $\Delta\alpha_{\rm em}^{\rm had}(m_Z^2) = 0.02758 \pm 0.0035$ [39].

present world average values $m_W = 80.399 \pm 0.0025$ GeV [81], $\sin^2\theta_{\rm eff}^{\rm lept} = 0.23153 \pm 0.00016$ [82], $m_t = 172.4 \pm 1.2$ GeV [83], $\alpha_s(m_Z) = 0.118 \pm 0.002$ [1], and the determination $\Delta\alpha_{\rm em}^{\rm had(5)}(m_Z) = 0.02758 \pm 0.00035$ [39], on gets $m_H = 89^{+37}_{-27}$ GeV and $m_H^{UB} = 156$ GeV. See Fig. 2.16.

Considering the most recent value $\Delta\alpha_{\rm em}^{\rm had(5)} = 0.02768 \pm 0.0022$ [45] and shifting it by the required quantity to adjust the muon $(g-2)$ discrepancy, a new value of $m_H^{\rm UB}$, via the combined χ^2-analysis, can be evaluated. The work in [47] shows that an increase $\epsilon\sigma_{\rm had}(s)$ of hadronic cross section data decreases $m_H^{\rm UB}$ further, restricting the already narrow allowed region for m_H. The conclusion is that these hypothetical shifts conflict with the lower limit $m_H^{\rm LB}$ when the increasing of $\sigma_{\rm had}(s)$ is applied in a range of few hundered MeV in a region above 1.2 GeV.

It has been already been noticed that if τ-data are considered in the evaluation of the anomaly of the magnetic moment of the muon the $a_\mu^{\rm theo(SM)}$-$a_\mu^{\rm exp}$ discrepancy reduces down to 1.7σ (or even less), see Sec. 2.4. Using τ-data, from one side, almost solves the Δa_μ discrepancy but, on the other sides, increases $\Delta\alpha_{\rm em}^{\rm had(5)}$ to 0.02782 ± 0.0016 [84]. In [84] it is also shown that the increasing leads to a low m_H prediction which is almost in conflict with $m_H^{\rm LB}$, leaving only a narrow window. Indeed with this value of $\Delta\alpha_{\rm em}^{\rm had(5)}$, and the same input used above for the χ^2-analysis, $m_H^{\rm UB}$ results to be equal to 133 GeV, a value that difficultly fits with the boundary conditions put by the LEP EWWG χ^2-analysis.

New computations ([85] for details) of isospin-breaking violations, on long-distance radiative corrections to the decay $\tau^- \to \pi^-\pi^0\nu_\tau$, and differentiation of the neutral and charged ρ properties, reduces the difference between τ- and e^+e^--data, lowering the τ-based determinations of $a_\mu^{\rm had,LO}$. Moreover, a recent analysis of the pion form factor below 1 GeV claims that τ-data are consistent with e^+e^--data after isospin violation effects and vector meson mixings are considered [86]. In this case one could use the e^+e^- data below ~ 1 GeV, confirmed by the τ ones, and assume that Δa_μ is accommodated by hypothetical errors occurring above ~ 1 GeV, where disagreement persists between these two data sets. However the work is still in progress, and, in any case, using τ-data above ~ 1GeV would lead to $m_H^{\rm UB}$ values inconsistent with $m_H^{\rm LB}$.

Moreover reducing $m_H^{\rm UB}$ to be smaller than ca. 130 GeV causing tension with the lower bound on m_H, which is required to be bigger than ca. 120 GeV at 95% CL, enters also in conflict with the vacuum stability in the assumption that the Standard Model is valid up to the Planck scale.

It has been suggested [88] that a P-wave electromagnetic bound state of $\pi^+\pi^-$, "pionium", could enter the dispersion relations through 1% mixing with the ρ in a way that significantly increases $a_\mu^{\rm had}$. If so, such a state would give little change to the Higgs boson mass determination. However, this hypothesis is not established. And most likely the required mixing is 0.1, and not 0.01 as claimed in [88], which is too large to be possible. The effect of pionium on a_μ is actually negligible.

If the Δa_μ discrepancy is real, it points to New Physics, like low energy SuperSymmetry where Δa_μ is reconciled by the additional contributions of supersymmetric partners and one expects m_H 135 GeV for the mass of the lightest scalar. If, instead, the deviation is caused by an incorrect $a_\mu^{\rm had,LO}$ contribution, it leads to reduced $m_H^{\rm UB}$ values. This reduction, together with the LEP lower bound, leaves a too much narrow window for the mass of this fundamental particle.

2.6.2 A possible contribution from New Physics: $a_\mu^{\rm SUSY}$

Considering the possibility of having a *supersymmetric* contribution to a_μ, we want to describe only one of the possible New Physics scenarios. This supersymmetric contribution would corre-

spond to

$$a_\mu^{\text{theo}} = a_\mu^{\text{theo(SM)}} + a_\mu^{\text{SUSY}}, \tag{2.38}$$

where $a_\mu^{\text{theo(SM)}}$ represents the part coming from Standard Model and a_μ^{SUSY} the contribution from SUSY.

Main features of SUSY

The main theoretical motivation for a supersymmetric extension of the Standard Model is the *hierarchy* or *naturalness* problem: chiral symmetry requires fermions to be massless, local gauge symmetries require the gauge bosons to be massless, so the only Standard Model particle which is not required to be massless, before the spontaneous symmetry breaking by the Higgs mechanism, is the scalar Higgs boson. As a consequence, one would expect the Higgs boson to be much heavier than all other Standard Model particles, which acquire a mass proportional to the Higgs vacuum expectation value $v = 1/\left(\sqrt{2}G_\mu\right) = 246.221 \pm 0.001$ GeV. As already mentioned above, indirect Higgs boson mass bounds from LEP require the Higgs boson to be relatively light ($m_H < 200$ GeV), i.e., not heavier than the other Standard Model particles, including the heaviest ones. Therefore a symmetry should protect the Higgs particle from being much heavier than other Standard Model states. The only known symmetry which requires scalar particles to be massless is SuperSymmetry. Simply because a scalar is always a supersymmetric partner of a fermion, which is required to be massless by chiral symmetry. And in a supersymmetric theory it becomes natural to have a "light" Higgs, which, in a SUSY extension of the Standard Model, the lightest scalar h^0 corresponds to the Standard Model Higgs.
Supersymmetric extensions of the Standard Model, in particular the *Minimal Supersymmetric Standard Model (MSSM)*, implement a symmetry mapping

$$\text{boson} \overset{Q}{\longleftrightarrow} \text{fermion}$$

between bosons and fermions, by changing the spin by $\pm 1/2$ units [89].[21] The SUSY algebra

$$\{Q_\alpha, \bar{Q}_\beta\} = -2\left(\gamma^\mu\right) P_\mu; P_\mu = (H, P)$$

where P_μ are the generators of space-time translations, Q_α the four component Majorana (neutral) spinors and $\bar{Q}_\alpha = (Q^+\gamma^0)_\alpha$ the Pauli adjoint, represents the only possible non trivial unification of internal and space-time symmetry in a Quantum Field Theory. The Dirac matrices in the Majorana representation play the role of the structure constants. The SUSY extension of the Standard Model associates to each Standard Model state X a supersymmetric "s-state" $\tilde{X}$, where sfermions are bosons and sbosons are fermions, see Tab. 2.4. SUSY, being a global symmetry imposed on Standard Model, leaves the Standard Model group unchanged and there are not new gauge bosons. Also the matter fields remain the same. SUSY and gauge invariance are compatible only after the introduction of a second Higgs doublet in which H_1 induces the masses of all *down* fermions and H_2 the masses of all *up* fermions. And a second complex Higgs doublet is also required for the anomaly cancellation of the fermionic *sboson* sector. This means that in SUSY four additional scalars $(H^0, A^0, H^\pm)$ and their supersymmetric partners are introduced. The lightest neutral scalar, denoted by h^0, corresponds to the Standard Model Higgs

[21] Several publications describing the feature of SUSY Physics can be found in literature, e.g. lectures of the school held in Karlsruhe before the SUSY07 conference [90].

MSSM particles ($R_p = +1$)	SUSY partners ($R_p = -1$)	
$\begin{pmatrix}\nu_e\\ e^-\end{pmatrix}_L, \begin{pmatrix}\nu_\mu\\ \mu^-\end{pmatrix}_L, \begin{pmatrix}\nu_\tau\\ \tau^-\end{pmatrix}_L$	$\begin{pmatrix}\tilde{\nu}_e\\ \tilde{e}^-\end{pmatrix}_L, \begin{pmatrix}\tilde{\nu}_\mu\\ \tilde{\mu}^-\end{pmatrix}_L, \begin{pmatrix}\tilde{\nu}_\tau\\ \tilde{\tau}^-\end{pmatrix}_L$	sneutrinos, sleptons
$\nu_{e_R}, e^-_R, \nu_{\mu_R}, \mu^-_R, \nu_{\tau_R}, \tau^-_R$	$\tilde{\nu}_{e_R}, \tilde{e}^-_R, \tilde{\nu}_{\mu_R}, \tilde{\mu}^-_R, \tilde{\nu}_{\tau_R}, \tilde{\tau}^-_R$	
$\begin{pmatrix}u\\ d\end{pmatrix}_L, \begin{pmatrix}c\\ s\end{pmatrix}_L, \begin{pmatrix}t\\ b\end{pmatrix}_L$	$\begin{pmatrix}\tilde{u}\\ \tilde{d}\end{pmatrix}_L, \begin{pmatrix}\tilde{c}\\ \tilde{s}\end{pmatrix}_L, \begin{pmatrix}\tilde{t}\\ \tilde{b}\end{pmatrix}_L$	squarks
$u_R, d_R, c_R, s_R, t_R, b_R$	$\tilde{u}_R, \tilde{d}_R, \tilde{c}_R, \tilde{s}_R, \tilde{t}_R, \tilde{b}_R$	
$W^\pm, H^\pm$	$\tilde{W}^\pm, \tilde{H}^\pm \rightarrow \tilde{\chi}^\pm_{1,2}$	charginos
γ, Z, h^0, H^0, A^0	$\tilde{\gamma}, \tilde{Z}, \tilde{h}^0, \tilde{H}^0, \tilde{A}^0 \rightarrow \tilde{\chi}^0_{1,2,3,4}$	neutralinos
g, G	$\tilde{g}, \tilde{G}$	gluino, gravitino

Tab. 2.4: The particle spectrum of a MSSM.

boson. Both Higgs fields exhibit a neutral scalar, which acquire the vacuum expectation values v_1 and v_2. The parameter $\tan\beta = v_2/v_1$ is one of the basic parameters in SUSY theories. As $m_t \propto v_2$ and $m_b \propto v_1$ in such a scenario the large mass splitting $m_t/m_b \sim 40$ can be explained by a large ratio v_2/v_1, which means a large $tan\beta$, i.e. values $\tan\beta \sim 40$ GeV look natural.
While extending the Standard Model by means of SUSY fixes all gauge and Yukawa couplings of the sparticles, there are a lot of free parameters to fix the SUSY breaking and masses, such that mixings of the sparticles, which remain quite arbitrary. In fact, a SUSY extension of the Standard Model in general exhibits more than 100 parameters, while the Standard Model has only 28 (including neutrino masses and mixings). Moreover, a SUSY extension of the Standard Model leads to *Flavor Changing Neutral Currents* (*FCNC*) and unsuppressed CP-violation, which are absent or small, respectively, in the Standard Model and known to be suppressed in nature. Actually, just a SUSY extension of the Standard Model, while solving the naturalness problem of the Standard Model Higgs sector, creates its own naturalness problem as it leads to proton decay and the evaporation of baryonic matter in general. An elegant way to get rid of the latter problem is to impose the so called *R-parity*, which assigns $R_p = +1$ to all normal particles and $R_p = -1$ to all sparticles. If R-parity is conserved, sparticles can only be produced in pairs and there must exist a stable *Lightest Supersymmetric Particle (LSP)*, the lightest neutralino. Thus all sparticles at the end decay into the LSP plus normal matter.[22]

The contribution a_μ^{SUSY}

In an supersymmetric theory the anomalous magnetic moment must vanish, as already observed in 1974 by Ferrara and Remiddi [92], that is

$$a_\mu^{\mathrm{theo}} = a_\mu^{\mathrm{theo(SM)}} + a_\mu^{\mathrm{SUSY}} = 0.$$

[22] The LSP is a *Cold Dark Matter* (*CDM*) candidate [91] if it is neutral and colorless.

Thus, since $a_\mu^{\text{theo(SM)}} > 0$, in the unbroken SUSY limit, it must be

$$a_\mu^{\text{SUSY}} < 0.$$

However, SUSY must be drastically broken, as not a single supersymmetric partner has been observed so far and all super-partners of existing particles seem to be too heavy to be produced up to now. Thus since SUSY is broken, a_μ may have both signs. In fact, the ca. 3σ discrepancy in $(g-2)_\mu$ requires $a_\mu^{\text{SUSY}} > 0$, the same sign as the Standard Model contribution and at least the size of the Weak contribution, $\sim 20 \times 10^{-10}$, see Fig. 2.3(b) . The leading SUSY contributions,

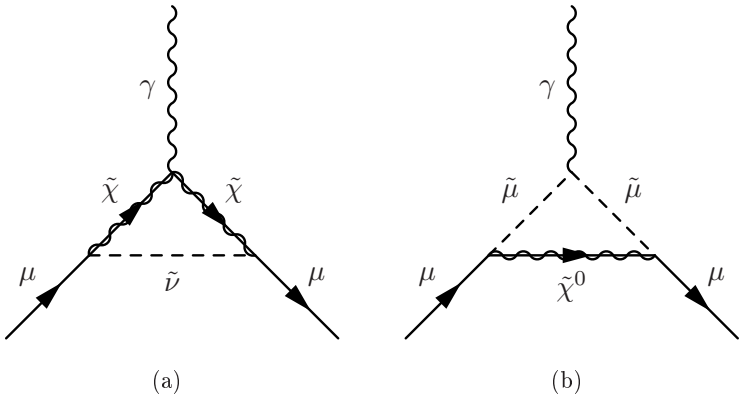

Fig. 2.19: Leding SUSY contributions: (a) sneutrino-chargino and (b) smuon-neutralino.

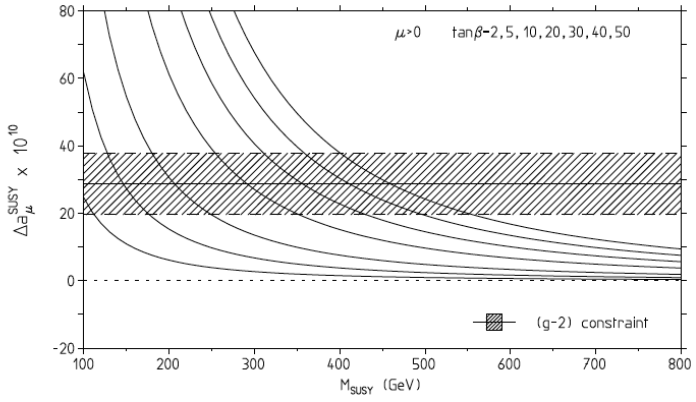

Fig. 2.20: Constraint on large tanβ SUSY contribution as a function of m_{SUSY}.

like the ElectroWeak Standard Model contributions, are due to one-loop diagrams. The most interesting ones are the ones get enhanced for large tanβ. Such supersymmetric contributions to

a_μ stem from *sneutrino-chargino* loops, see Fig. 2.19(a), and *smuon-neutralino*, see Fig. 2.19(b), and yield [93, 94, 95]

$$a_\mu^{\mathrm{SUSY,LO}} = a_\mu^{\chi^\pm} + a_\mu^{\chi^0}. \tag{2.39}$$

Since the SUSY contributions to a_μ are enhanced by large $\tan\beta$, the anomalous magnetic moment may be used to constrain the SUSY parameter space. Expansions in $1/\tan\beta$ and m_W/m_{SUSY} lead to the approximation

$$a_\mu^{\mathrm{SUSY}} \simeq \mathrm{sign}(\mu)\frac{\alpha_{\mathrm{em}}(m_Z)}{8\pi\sin^2\theta_W}\frac{5+tan^2\theta_W}{6}\frac{m_\mu^2}{\tilde{m}^2}\tan\beta\left(1-\frac{4\alpha_{\mathrm{em}}}{\pi}\ln\frac{\tilde{m}}{m_\mu}\right), \tag{2.40}$$

where $\tilde{m} = m_{\mathrm{SUSY}}$ is a typical SUSY loop mass and μ is the Higgsino mass term. In Fig. 2.20, the SUSY contributions are shown for different values of $\tan\beta$.
Above $\tan\beta \sim 5$ and $\mu > 0$ the SUSY contributions from the diagrams Fig. 2.19 could explain easily the observed deviation in a_μ with SUSY states of masses in the interesting range from 100 to 500 GeV.
In large $\tan\beta$, it is possible to write the approximate expression

$$|a_\mu^{\mathrm{SUSY}}| \simeq 12.3\times10^{-10}\left(\frac{100\ \mathrm{GeV}}{\tilde{m}}\right)^2\tan\beta, \tag{2.41}$$

with a_μ^{SUSY} having the same sign of the μ-parameter. Therefore, to cover the gap between $a_\mu^{\mathrm{theo(SM)}}$ and a_μ^{exp}, a positive $\mathrm{sign}(\mu)$ is required. If the Δa_μ is caused by SUSY, then

$$\tilde{m} = (65.5\ \mathrm{GeV})\sqrt{\tan\beta}, \tag{2.42}$$

and, for $\tan\beta$ in the range 2 - 40, a typical SUSY mass becomes

$$\tilde{m} \simeq 93 - 414\ \mathrm{GeV}, \tag{2.43}$$

which exactly fit with the expectation for SUSY particles.[23]

[23] For more detailed discussion and references, see [96] and [95].

3. THE KLOE EXPERIMENT

3.1 The DAΦNE accelerator

The *DAΦNE* (*Double Annular Φ-factory for Nice Experiments*) ϕ-factory belongs to the generation of e^+e^--colliders running at a fixed Center-of-Mass energy (CM-energy) with high luminosity (the so-called meson factories). Operating at a CM-energy equal to the mass of the ϕ-meson (1019.48 MeV), DAΦNE is optimally suited for kaon physics, due to the fact that the ϕ-decay fraction into kaon pairs (charged and neutral) is $\sim 83\%$ [1].
Therefore the physics program of *KLOE* (*K LOng Experiment*) contains the measurement of all kinds of kaon decay branching ratios.[1]
Apart from kaon physics the KLOE physics program contains a variety of interesting hadronic issues like the study of η and η'-decays, the study of the nature of scalar mesons (from $\phi \to f_0\gamma$, $\phi \to a_0\gamma$ decays) and the measurement of the hadronic cross section, which is discussed in Chap. 4.
In addition, DAΦNE is also a very good laboratory for synchrotron radiation due to the high currents stored in its two storage rings. Fig. 3.1 shows the layout of the DAΦNE complex. In

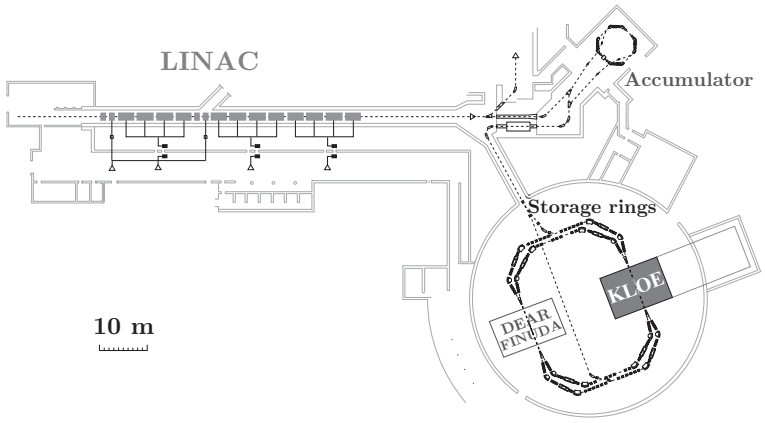

Fig. 3.1: The DAΦNE ϕ-factory in Frascati.

the linear accelerator (LINAC), which has a length of ca. 60 m, electrons are injected by a triode gun. The electron beam is then accelerated to 250 MeV and focused to a spot of 1 mm radius. To produce the positrons, the electron beam hits a removable target made of tungsten. The

[1] The other detector set at DAΦNE are DEAR and FINUDA. *DEAR* (*DAΦNE Exotic Atoms Research*) investigates kaonic hydrogen which is produced by stopping a K^- in a gaseous hydrogen target. The nuclear physics is covered by *FINUDA* (*FIsica NUcleare a DAΦNE*): by stopping low energetic K^- particles in a thin target hypernuclei are produced via the reaction $K^- + n \to \Lambda + \pi^-$, in which a neutron is replaced by a Λ hyperon.

positrons are separated by the electrons by means of magnetic dipoles and can be accelerated up to a maximum energy of 550 MeV. Electrons can be accelerated up to an energy of 800 MeV. The particles coming from the LINAC are injected into the accumulator ring, which has a circumference of 32.6 m. The accumulator minimizes the number of particle injections into the main rings and thus reduces the number of electrons or positrons which are lost during the injections. Due to the lowered high frequency with respect to the main rings in the accumulator, a higher longitudinal acceptance is achieved by the prolongation in time of the particle bunches, which allows to accept all particles coming from the LINAC. Furthermore, the particle beams are damped in the accumulator, making the injection into the main rings more easy and lowering the requirements on the main ring magnets. The accumulator contains only one particle type (electrons or positrons) at a time.
After a bunch in the accumulator has reached the desired number of particles and damping, it is injected into one of the two main rings. This can be done while beams are circulating without interrupting the data taking process (*topping up*). The main rings have a circumference of 97.7 m and are coplanar to each other. The particles collide in one of the two interaction regions of 10 m length each, in which the detectors KLOE and FINUDA are located. The fact that there are two separate rings forces the beams to meet at a crossing angle of ca. 25 mrad, which creates a small transverse momentum of -12.75 MeV/c when the particles collide in the KLOE detector. [2] The decision to have two separate rings for electrons and positrons was made to minimize the beam-beam interactions occuring at the high currents in the rings needed to achieve the desired luminosity. Since the damping due to synchrotron radiation is too small at the low energy of DAΦNE, the emission of synchrotron radiation has been doubled by the use of 8 conventional electromagnets (wigglers). DAΦNE is in operation since 1999. In the period of data takings (for

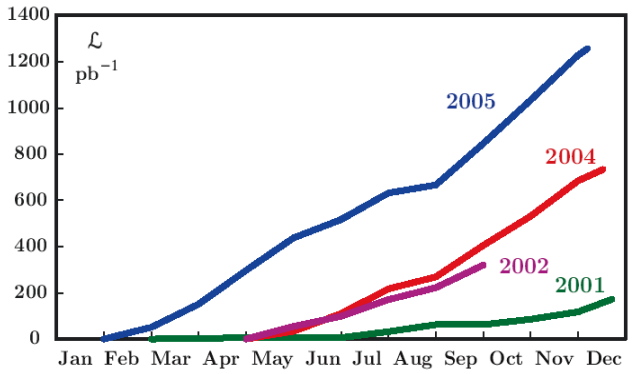

Fig. 3.2: Integrated Luminosity collected by the KLOE detector on the ϕ mass in the years 2001-2005. The total integrated luminosity collected by KLOE corresponds to 2.5 fb^{-1}. From January 2006 to April 2006 other ca. 230 pb^{-1} have been stored at a CM-energy equal to 1 GeV.

which the integrated luminosity accumulated in different years is shown in Fig. 3.2) from 2001 to

[2] For the 2006 set up of the collider, with CM-energy equal to 1000 MeV, the transversal momentum has been changed to -16 MeV/c

2005 ca. 2500 pb^{-1} have been accumulated. The improvement in performance over the years is clearly visible. In 2006, for the *Physics off-peak* program ca. 230 pb^{-1} of data with a CM-energy of 1000 MeV have been collected.

DAΦNE Parameters	
LINAC	
Number of accelerator sections e^+/e^-:	10/5
Max. beam energy e^+/e^- (MeV):	550/800
ACCUMULATOR	
Energy (MeV):	510
R. F. frequency (MHz):	73.65
Average bunch current (mA):	150
Bunch length (cm):	3.8
Synchrotron radiation loss (KeV per turn):	5.2
MAIN RINGS	
Energy (MeV):	510
Max. luminosity Design/achieved ($cm^{-2}s^{-1}$):	$5 \cdot 10^{32}/1 \cdot 10^{32}$
R. F. frequency (MHz):	368.25
Max. numbers of bunches Design/achieved:	120/49
Min. bunch distance (cm/ns)	81.4/2.7
average bunch length (mm)	30 (rms)
average bunch height (mm)	0.02 (rms)
average bunch width (mm)	2.0 (rms)
Horizontal crossing angle (mrad):	25
Synchrotron radiation loss (keV per turn):	9.3

Tab. 3.1: DAΦNE Parameters in 2002.

3.2 The KLOE detector

The KLOE detector, situated in one of the two interaction regions of DAΦNE, essentially consists of a cylindrical drift chamber (DC), to detect charged particles, and an electromagnetic calorimeter (EMC), allowing the detection of photons with energies down to 10 MeV, which surrounds the drift chamber almost hermetically (see Fig. 3.3). The dimensions of the detector (2 m radius and 3.2 m length) are motivated by the decay length of the K_L, which at the DAΦNE energy is ca. 3.4 m. The KLOE drift chamber can thus detect about 25% of the occurring K_L-decays. Both drift chamber and calorimeter are placed in a superconducting coil creating a longitudinal magnetic field with a field strength of 0.52 T.

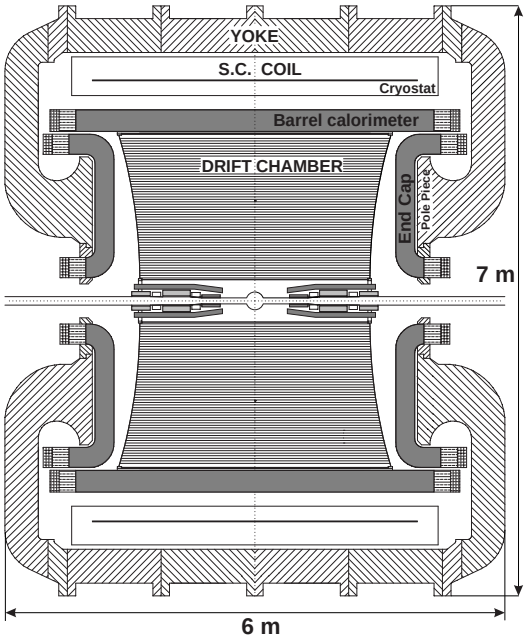

Fig. 3.3: Section of the KLOE detector.

3.2.1 The drift chamber

The basic requirements for the drift chamber [97] were: (*i*) the high homogeneity and isotropy, (*ii*) an optimal resolution for tracks of particles with low momenta and (*iii*) the best possible reduction of multiple scattering inside the chamber. Furthermore, the volume of the chamber should be big enough that a sufficient part of the K_L particles produced at DAΦNE decays inside the chamber volume. Together with technical and economical considerations, these requirements lead to the construction of a cylindrical chamber with a radius of 2 m and a length of 4 m, with an inner cylinder containing the beam-line with a radius of 25 cm. The mechanical structure of the chamber is made out of carbon fibre in order to minimize the K_L regeneration, which could mimic CP-violating decays, and to maximize stability and transparency for photons. It consists of two end plates of 8 mm thickness which are connected by 12 struts. The inner cylinder with a thickness of only 0.7 mm closes the chamber volume towards the beam pipe, while 12 covering plates make the outer wall.

The requirement of three-dimensional track reconstruction led to almost rectangular drift cells arranged in coaxial layers. All the wires belonging to the same layer are parallel to each other and have the same stereo angle with the line parallel to the z-axis, see Fig. 3.4(a). The stereo angles change from one layer to the next, and their magnitudes vary from $\pm$ 60 to $\pm$ 150 mrad. These values assure a good resolution of the measurement of the z-coordinate: being $\sigma_z = \sigma_{r\phi}/\tan(\epsilon)$, with an average $r\phi$ resolution of 200 μm, the z resolution is about 2 mm across the whole chamber volume. The ratio between field and sense wires is 3:1. Field wires are also disposed in concentric layers following the stereo angles of the sense wires layer above them. Since the track density is much higher at small radii due to the small momenta of charged particles produced in the ϕ-decay and since vertexing capabilities for $K_S \to \pi^+\pi^-$ are required, the innermost layers have cells of smaller size (see Fig. 3.4(b)), with a dimensions of 2×2 cm^2 (to be compared with the 3×3 cm^2 of the larger cells). There are 58 layers, of which 12 consist of small cells

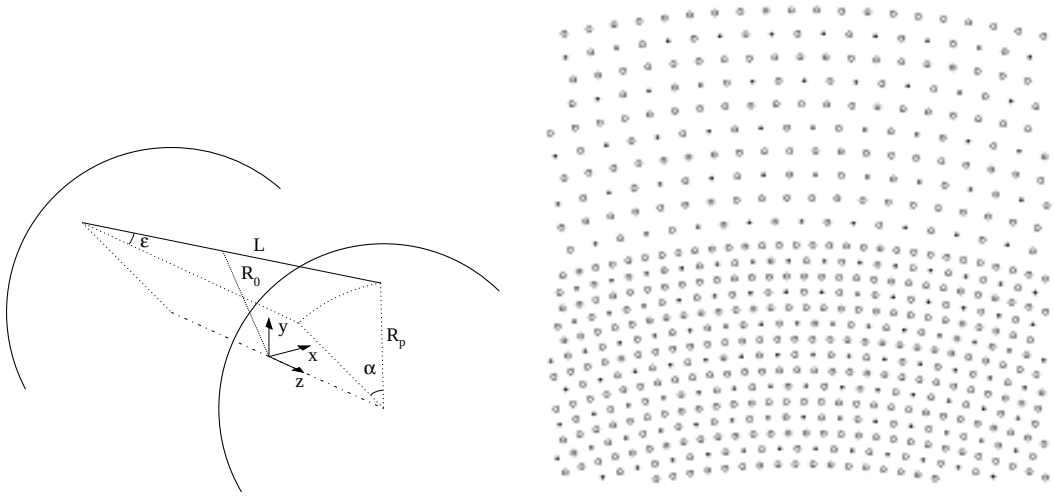

(a) (b)

Fig. 3.4: (a) Sketch of the stereo angles of the cells. (b) Drift cells configuration at z=0; a portion of the chamber at the boundary between small cells in the inner layers and large cells in the outer cells is shown. Full dots indicate the sense wires while the circles indicate the fields wires.

and 46 of big ones. The total number of the drift cells is 12585, corresponding to about 52000 field plus sense wires. Simulation studies have shown that good efficiency and spatial resolution are achieved using a helium-based gas mixture with a gain of $\sim 10^5$ together with gold-plated tungsten sense wires (25 μm thickness) and silver-plated aluminium field wires (80 μm thickness) at a voltage of 1800-2000 V. The gas mixture is composed of 90% helium and 10% isobutane. The low atomic mass of helium minimizes multiple scattering and regeneration. The isobutane absorbs UV photons produced in recombination processes (in order to avoid the production of discharge in the chamber). The mixture has a radiation length $X_o \simeq$1300 m; taking into account also the presence of the wires, the average radiation length in the whole chamber volume is about 900 m.

Since the number of cells is a multiple of six for each layer, connections to the wires are grouped by six. The bulk of ionization in the chamber is due to beam background and decreases with radius. For this reason the number of sense wires connected to one high voltage line increases with the radius. The preamplifier outputs are sent to an amplifier-discriminator-shaping circuit (ADS). This circuit provides a discriminated signal for the TDC (for drift time measurement) and the ADC (for dE/dx measurements), plus a further signal sent to the trigger module, which will be described below.[3]

The momentum resolution for electrons with 510 MeV energy and polar angles (respect to the beam line) $50^\circ < \theta < 130^\circ$ is $\sigma_p \simeq 1.3$ MeV (relative resolution σ_p/p=2.5×10^{-3}, as shown in Fig. 3.5).

[3] ADC stays for *Analogical Digital Converter*. TDC for *Time Digital Counter*.

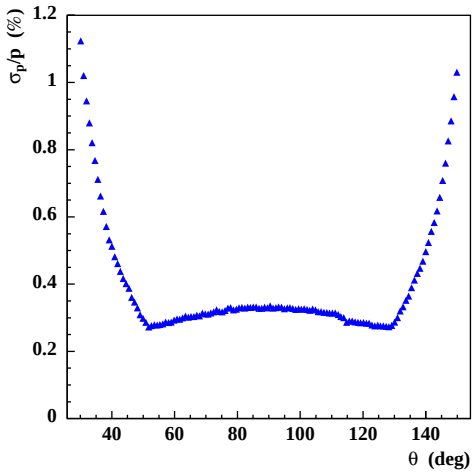

Fig. 3.5: Momentum resolution σ_p/p as a function of the polar angle θ for Bhabha events.

3.2.2 The electromagnetic calorimeter

The design of the EMC was driven by the needs to detect photons with high acceptance and good spatial, energy and time resolutions down to energies of 10 MeV [98]. To minimize the loss of photons, the calorimeter surrounds the drift chamber almost completely and is fully immersed in the magnetic field. The barrel calorimeter, built by 24 modules with 4.3 m length which form a cylinder enclosure with ca. 2 m radius due to their trapezoidal shape, is parallel to the beam axis. The cylinder is closed by the two endcap calorimeters, which consist of 26 C-shaped modules of varying sizes. This shape has the advantage that it improves the full enclosure of the DC, and it also reduces the effect of the magnetic field on the photo-multipliers mounted at both ends of the modules. In total, there are 4880 photo-multipliers. Fig. 3.6 shows a front view of the calorimeter.

Thanks to the large overlap between barrel and endcap calorimeters, there is no gap at the intersection of the three calorimeters. The central endcap modules are vertically divided into two halves to allow the passage of the beam pipe.

The modules consist of scintillating fibres of 1 mm thickness glued on 0.5 mm thick lead foils (see Fig. 3.7), which have grooves to accommodate the fibres. This structure results in a ratio for Fibres:Lead:Epoxy(glue) of 48:42:10, yielding a high amount of active material. The module thickness of 23 cm corresponds to ca. 15 radiation lengths. The read-out at both sides of each module is connected via light pipes of Plexiglas to the photomultipliers. The whole calorimeter is divided into five planes from the inside to the outside of the detector, of which the outermost one is slightly thicker with respect to the other four. In the transverse direction of the modules, each plane is subdivided into cells 4.4 cm wide. The photomultipliers work in a magnetic field of 0.56 T; the outer parts of the endcaps have been designed to minimize the transverse component of the field acting on the photomultipliers axis, reducing the dangerous field component to less than 0.4 kG. Since the time resolution depends also on the efficiency of the light collection, this quantity has been maximized, up to a value of $\sim 80 - 90\%$.

The signal coming out from the photomultipliers passes a preamplifier before being fed into three different circuits: a first part goes to the trigger, the other two parts to the ADCs and the TDCs

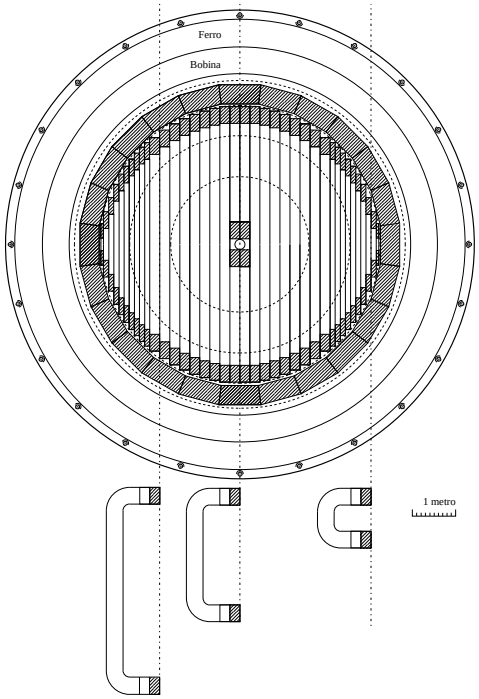

Fig. 3.6: Front view of the KLOE calorimeter and side view of endcap modules. The modules of the barrel calorimeter form a ring around the end cap calorimeters.

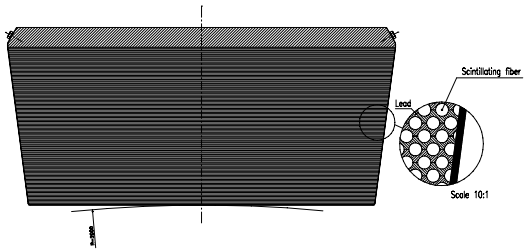

Fig. 3.7: Fiber-lead sampling structure of the KLOE calorimeter.

respectively. The energy deposit in each cell is obtained by the charge measured at each side of the modules by the ADCs. The time of arrival of a particle is derived from the time intervals measured at each side of the modules by the TDCs. The difference between the arrival time at the two ends of the fiber allows to reconstruct the coordinate along the fiber. The resolution of the longitudinal z coordinate is $\sigma_z \sim 9\ \mathrm{mm}/\sqrt{E(\mathrm{GeV})}$.

The energy resolution and the linearity of the calorimeter are determined using radiative Bhabha events, fore which the photons cover a wide energy and angular range. Including also drift chamber information and closing the kinematics, one can obtain the photon direction and the photon energy E_γ with good accuracy. Matching the photon direction obtained from the drift chamber information with the position of the fired cluster in the calorimeter, the distribution $E_{\mathrm{cl}} - E_\gamma$ is fitted with a gaussian to find its central value. This is done in energy intervals

of 10 MeV in E_γ. The plot of Fig. 3.8(a) shows the results of this procedure for the whole energy range E_γ: the linearity is better than 1% for E_γ >75 MeV. Deviations of the order of 4-5% are observed at low energies, mainly due to the loss of parts of the shower in the cluster reconstruction. The energy resolution, dominated by sampling fluctuations, can be parametrized as $5.7\%/\sqrt{E(\mathrm{GeV})}$ (see Fig. 3.8(b)). The photon detection efficiency is defined as the number

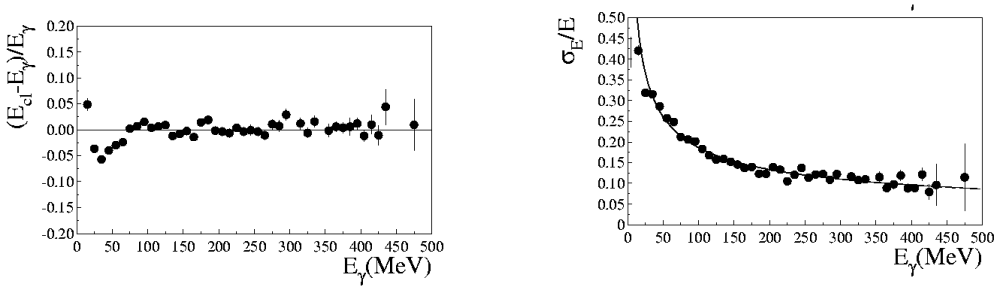

(a) (b)

Fig. 3.8: Calorimeter linearity (a) and resolution (b) for photons as a function of the photon energy E_γ. The resolution is parametrized with $5.7\%/\sqrt{E(\mathrm{GeV})}$.

of detected clusters divided by the number of produced photons. It has been measured with different samples: here we report the result obtained with radiative Bhabha events (where $e^\pm$ direction and energy are measured with the drift chamber), with the decays $\phi \to \pi^+\pi^-\pi^0$ and $K_L \to \pi^+\pi^-\pi^0$ (where energy and direction of one of the two photons from the π^0 is deduced from the tracking information and the energy and direction of the other photon) (see Fig. 3.9(a)). The results obtained with the different channels are in reasonable agreement with each other, and for energies larger than 100 MeV a constant value of more than 98% is observed.
The time resolution is given in Fig. 3.9(b) for photons from different radiative ϕ-decays. Good agreement among the different measurements is observed down to 100 MeV. The curve in the plot gives the resolution of the calorimeter: $\sigma_t = 54\ \mathrm{ps}/\sqrt{E(\mathrm{GeV})} \oplus 140$ ps.

3.2.3 The trigger system

The main purpose of the KLOE trigger system is to discriminate among events from ϕ-decays and Bhabha events, cosmic rays and machine background. The time between two bunch crossings at DAΦNE is 2.7 ns; this is too short to generate a trigger. Therefore the trigger operates continuously, and a physics event is synchronized to a bunch crossing at a later stage. Due to the fact that the *Data Acquisition* (*DAQ*) can handle a total rate up to $\sim$ 10 kHz, while the total rate (physical events plus background) correspond to ca. 90 kHz, the trigger must provide good background rejection in order not to overload the DAQ, without losing efficiency of the physical events.
Both the EMC and the DC can be used to generate the trigger [99], since they both allow to get information about the topology of the different reactions, which is crucial to separate the different events. For example, low angle Bhabha events are concentrated in the two endcaps of the calorimeter as well as the machine background. Both produce a low multiplicity in the drift chamber, in contrast to the ϕ-decay events. Cosmic rays behave differently from the these two background sources: $\sim$ 85% of them deposit their energy in the barrel, and their multiplicity in

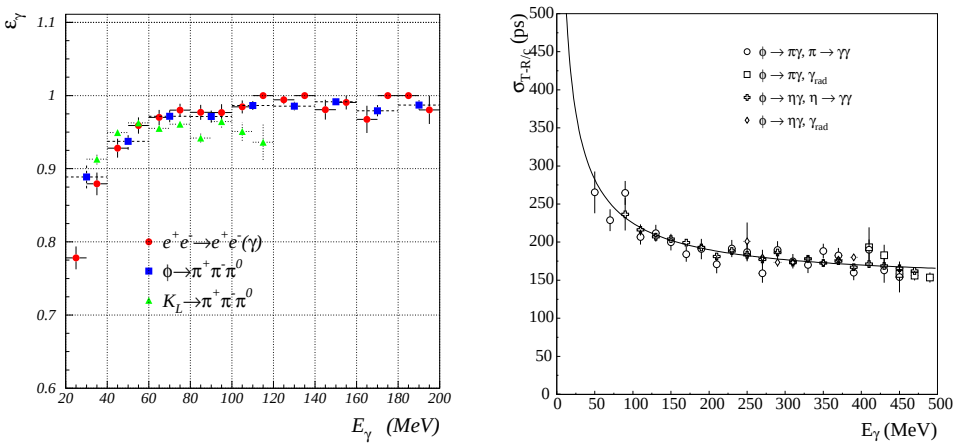

(a) (b)

Fig. 3.9: (a) Calorimeter efficiency for different ϕ-decays and (b) time resolution for ϕ radiative decays, both as a function of E_γ.

the chamber is similar to the one of physical events.

The trigger is based on the local energy deposit in the calorimeter and multiplicity information from the drift chamber. It works in two levels (see Fig. 3.10). A *first level trigger T1* with fast timing dedicated for starting the front-end electronic read-out, uses as much information as possible from the chamber. After this, additional information collected from the DC is used, together with the information from the EMC, to constrain the first level and start the DAQ. The EMC triggers if the energy deposit is larger than 50 MeV, to trigger low energetic particles from ϕ-decays or larger than 350 MeV. This second threshold is used to recognize Bhabha, which either will be rejected or collected in a downscaled sample to calibrate the calorimeter. The signals from the wires of the chamber, after being preamplified, are sent to a TDC and the trigger signal is formed with a gate of 250 ns. The first level trigger also sets a 2 μs long signal, which vetoes the other first level trigger and allows signal formation from the drift chamber cells.

Before being passed to the front-end electronics of the calorimeter, the first level trigger is synchronized with the DAΦNE radio-frequency (RF). Therefore the calorimeter TDCs measure the time with respect to a bunch crossing coming n periods after the collision which has originated the event, where n is then determined at offline reconstruction level.

At the end of the dead time (2 μs) the trigger system asks for the confirmation of the level 1 decision. In this *second level T2* two conditions, similar to those of the first level, are required, with the difference that thresholds are now chosen to be equal to the energy average released in a cell by a minimum ionizing particle (MIP) ($40 \div 50$ MeV). Once two sectors are above threshold, the cosmic ray bit is activated and the event is flagged as cosmic ray. The cosmic ray flag requires two energy releases above threshold on the outermost plane of the calorimeter in barrel-barrel or barrel-endcap configuration. The second level trigger produces the stop signal for the chamber TDCs and starts the data acquisition.

To avoid the rejection of $\mu^+\mu^-(\gamma)$ and $\pi^+\pi^-(\gamma)$ events due to this cosmic veto, which easily reach the outer planes of the calorimeter, a *third level trigger T3* has been developed. Each event

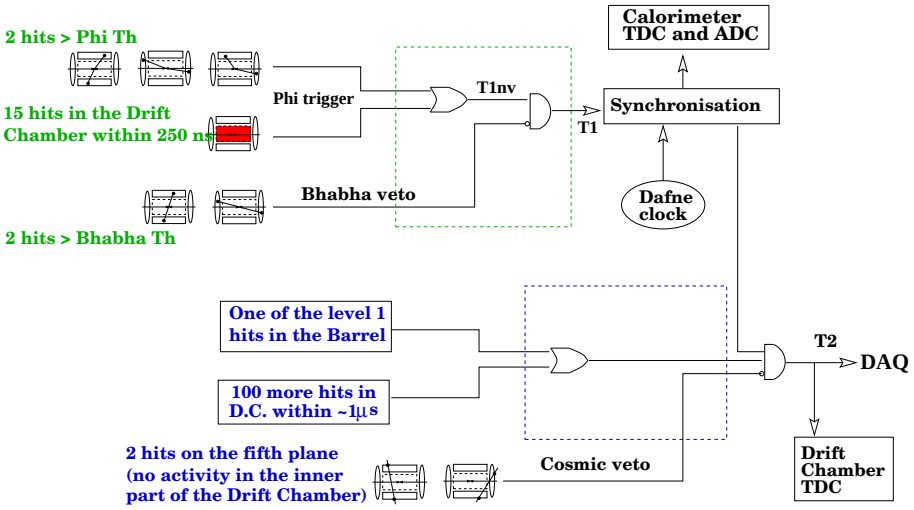

Fig. 3.10: KLOE trigger logic.

flagged by T2, will pass the T3 filter before being written on tape or rejected. The T3 filter performs a fast preliminary pattern recognition looking for tracks coming from the interaction point. If it finds no tracks from the IP, the event is rejected. The insertion of the T3 filter from beginning of the year 2002 was very important for the measurement of the $\pi^+\pi^-\gamma$ channel, reported in this thesis, since it increased significantly the efficiency of signal events with respect the 2001.

EMC trigger

For the trigger purpose the full granularity of the calorimeter is not needed and the 5000 readout channels are grouped in ca. 200 summed signals. The barrel is divided into three groups of 47 trigger channels, named *normal*, *overlap* and *cosmic* series. Each sector in the normal and overlap series is made of 5×6 columns (see Fig. 3.11), while the cosmic series (used for the cosmic ray flag) consists only of the cells of the fifth plane of the calorimeter. In total there are 48×3 sectors. The geometry of the trigger sectors in the endcaps is more complicated, and, like for the barrel, it consists of the normal and overlap series. Since the multiplicity is higher in the forward region, mostly due to machine background, the two series are segmented in groups of 4 columns in the zone close to the beam pipe, and 5 or 6 elsewhere. The signals from the cells forming a column are summed up, followed by the sums of the six columns of a given trigger sector. The analog signal of each trigger sector is read at both sides (labeled A and B in the following) and it is compared to a high and a low threshold value, which is fixed during the DAQ initialization. The four logical signals $T_A^{\rm low}, T_A^{\rm high}, T_B^{\rm low}$ and $T_B^{\rm high}$ generate the signal T for each sector according to the logical equation: $T = (T_A^{\rm low} \cap T_B^{\rm low})$ and $(T_A^{\rm high} \cup T_B^{\rm high})$. This two-threshold scheme is applied in order to obtain an as much as possible uniform response as a function of the coordinate along the fibers of the energy deposit, minimizing thus the effect of the light attenuation along the fibers.

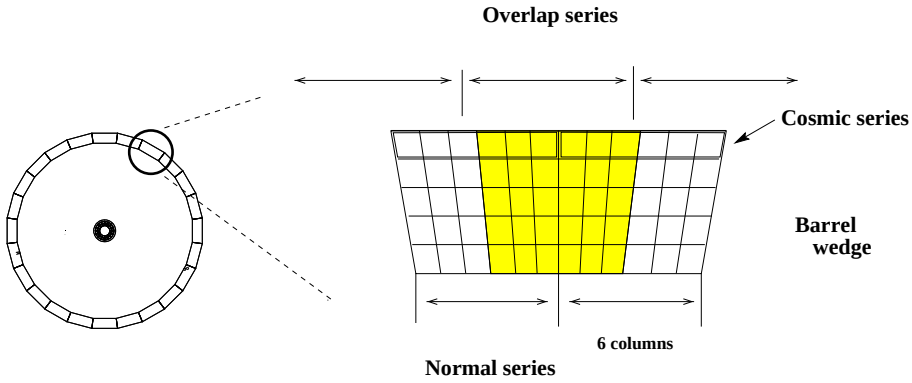

Fig. 3.11: Trigger sector in the barrel. The *normal* and the *overlap* series are shown.

3.3 Data reconstruction and event classification

3.3.1 The data samples

KLOE started its data taking for physics events in 2000. Between the years 2000 and 2006 (with a long interruption in 2003) an integrated luminosity of 2.5 fb^{-1} has been collected and the data taking has been stopped in April 2006.[4] In the last three months of data taking the CM-energy of DAΦNE was reduced to $\sqrt{s}$=1000 MeV (*off-resonance*) in order to allow a background-free measurement of the hadronic cross section via the Radiative Return method. In this work the 2006 data sample has been analyzed. Results from 2002 *on-resonance* data, corresponding to ca. 240 pb^{-1}, will be also presented.[5]

3.3.2 Data reconstruction

The data acquisition system [119] handles about 23000 front-end channels from the DC, the EMC and the trigger. It can manage a readout of 10 MB/s. For a typical peak luminosity, the trigger rate was 1.6 kHz and the average event size 2.7 kB, leading to a data acquisition of 4.3 MB/s. The on-line server writes raw data in 1-GB files. Data taking is divided into runs of approximately the same integrated luminosity (ca. 200 nb^{-1}) and to each run number the machine parameters, the calibration constants and all the relevant quantities of the detector related to that specific run are associated. Raw data are kept on disk until calibration and reconstruction processes are completed. The reconstruction process starts immediately after the completion of the calibration processes for the run. The data then is processed in parallel by separate reconstruction processes. The reconstruction program consists of several modules performing the following tasks:

- to load the drift chamber and the calorimeter calibration constants;
- the reconstruction of calorimeter clusters and the determination of the Time-of-Flight (ToF) and energy deposition;
- the determination of the current bunch crossing;

[4] It is forseen that KLOE will start data taking again in fall 2009 with a DAΦNE luminosity at least twice as high as in 2005.

[5] In the following the 2002 data will be also simply called *on-peak* while the 2006 ones, *off-peak*.

- the rejection of machine background and cosmic ray events;
- the patter-recognition and track fitting of the charged particles;
- the vertex reconstruction for charged particles;
- the association of drift chamber tracks with the calorimeter clusters for charged particles hitting the calorimeter;
- the event classification into several physics stream.

Since the tracking procedure is the most CPU-intensive reconstruction task, machine background and cosmic rays events are filtered out before. The filter algorithm (`FILFO`) is based only on information from the EMC. The last step of the reconstruction procedure is the classification of events on the basis of topological information into different streams. Streams are divided into five categories:

- Bhabha scattering events;
- ϕ-decays into charged kaons;
- ϕ-decays into neutral kaons;
- $\phi \to \pi^+\pi^-\pi^0$;
- radiative ϕ-decays

Apart from the Bhabha stream, a further sub-division is done, in order to keep only the information needed for the physics analysis. The resulting set of data-summary tapes (`DST`s) is six times smaller in size than the corresponding reconstruction output files and can be kept on disk for an easy access.

3.3.3 Clustering

The first step in the event reconstruction is the processing of the calorimeter information.
A *cell* is defined as the smallest part of calorimeter seen by two photomultipliers at its ends. The photomultiplier outputs are preamplified and sent with a delay of 220 ns (the time necessary for the trigger to decide whether to start the acquisition or not) to the ADCs and to the TDCs. Considering the two ends of a cell (A and B) two time signals, $t^{A,B}$, and two amplitude signals, $S^{A,B}$, are recorded from the corresponding photomultiplier outputs. They are used to get the position and the energy of the particle point of impact on the EMC.
To get the spatial position of the energy release in the calorimeter, the arrival time of the signal is considered. Defining the time at the ends of the cell as

$$t^{A,B} = c^{A,B} \times T^{A,B},$$

where $c^{A,B}$ (in ns/counts) are the TDCs calibration constants and $T^{A,B}$ are the counts in the TDCs. The position of the energy release along the fiber direction is obtained from the time

difference $t^A - t^B$. The particle time arrival t and the position along the fiber direction is (choosing as "0" the mid of the fibre length):

$$\begin{aligned} t(\text{ns}) &= \frac{t^A + t^B}{2} - \frac{t_0^A + t_0^B}{2} - \frac{L}{2v} - t_0^G, \\ s(\text{cm}) &= \frac{v}{2}(t^A - t^B - t_0^A + t_0^B), \end{aligned}$$

where L is the length of the cell and v the speed of light velocity inside the fiber, $t_0^{A,B}$ and t_0^G are overall time offset and the event global time offset, respectively. The two coordinates orthogonal to the fiber direction are given by the center of the cells according to the measured geometry. The constants c^A and c^B of every TDC channels have been measured in test (as well as the length L of the cells), before the installation of the experiment. They provide the conversion from TDC counts to ns (average value is 53 ps/counts). The measurement of the global time of the event, t_0^G, is needed since the time spread of the event (which can reach $30 \div 40$ ns for $K_S K_L$ events) is bigger than the time interval between two consecutive bunch crossing. The DAΦNE machine clock has a period T_{RF} of 2.7 ns and the time between one bunch crossing and the next is $n \times 2.7$ ns. The event reconstruction has to find the true bunch crossing for each event, which is then subtracted from the absolute time measured in each event. This procedure takes into account several effects: the ToF of the particles, the delay between trigger and calorimeter due to electronics and cables and the fact that the trigger signal is synchronised with the DAΦNE radio frequency. In order to determine t_0^G a calibration of the delay and of T_{RF} is performed using $\gamma\gamma$ events, which provide the easiest time signature. The expected time of such a sample is given by R/c, where R is calculated assuming a neutral particle coming from the interaction point and c is the speed of light. Delay due to cables and electronics and the synchronization RF are obtained from the difference of the measured time t and expected time of flight R/c. The time between peaks in Fig. 3.12 is the inter-bunch time and it is a multiple of the RF period. The delay is obtained by selecting one peak; any peak is in principle equivalent as a reference time.

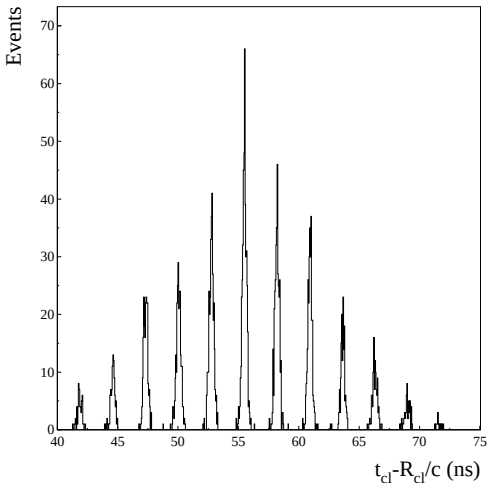

Fig. 3.12: t-R/c distribution for $\gamma\gamma$ events before any corrections.

To obtain the energy release E on each side of the cell, the ADCs' counting S is taking into account:

$$E^{A,B}(\text{MeV}) = \frac{S^{A,B} - S_0^{A,B}}{S_M} \times \kappa_E, \tag{3.1}$$

where $S_0^{A,B}$ represent the zero offsets of the amplitude scale, S_M is the signal for a minimum ionizing particle crossing the calorimeter centre and κ_E is the energy scale factor (in MeV/counts). $S_0^{A,B}$ are obtained from cosmic ray runs without circulating beam, i.e. with very low occupancy of the detector. In the S_M factor, the response of the photomultipliers, the fiber light yield and the electronic gain are considered. Cosmic rays are also used to measure this quantity: during a typical cosmic ray run (18 hours of data taking), ∼1000 events per cell are collected. The mean values of the Gaussian used to fit the amplitude spectra are by definition the S_M (for each cell) which enter in Eq. 3.1. Finally, in order to be independent from the position, a correction factor $A^{A,B}(s)$, due to the attenuation along the fiber length, is applied, and the energy of the cell becomes:

$$E\,(MeV) = (E^A \cdot A^A + E^B \cdot A^B)/2. \tag{3.2}$$

Once the cells have been reconstructed, the *clustering algorithm* merges together groups of adjacent cells. A cell becomes part of the cluster if times and amplitudes are available from both sides of the fiber. If one of these four inputs is missing (incomplete cell), the cell belonging to the barrel is recovered on the basis of the difference $\Delta\phi$ between its azimuth angle and the one of the closest cluster. Incomplete cells are assigned to a cluster if $|\Delta\phi| < 3°$. An analogous procedure is repeated in the two endcaps using the z-coordinate. The cluster energy E_{cl} is simply the sum of the energies of the cells making the cluster, while the cluster positions and time ($x_{\text{cl}}, y_{\text{cl}}, z_{\text{cl}}$ and t_{cl}) are computed as energy-weighted averages of the cell variables.

3.3.4 Tracking

Due to the large cell dimensions, to the variation of the electric field along the wires and mostly due to the gas mixture of $\text{He} - \text{iC}_4\text{H}_{10}$, the drift velocity is not saturated. These effects produce space-time (s-t) relations depending on the spatial coordinates of the cell and on the incident direction of the track. The s-t relations have been parametrised according to β and $\tilde{\phi}$ variables, see in Fig. 3.13(a). Six cells with β varying between 65° and 125° are chosen as reference cells. In each of these cells the $\tilde{\phi}$ angle is divided into 36 intervals of 10°. Since only the upper part of the cell is deformed by the stereo geometry, in 20 bins of $\tilde{\phi}$, the s-t relation is the same for all the six reference cells. This results in a total of $16 \times 6 + 20 = 116$ parametrisation (to be doubled once one considers both small and big cells). In one single cell, the drift distance is related to the drift time in terms of a 5^{th} order Chebychev polynomial

$$t_{\text{drift}} = P(C_i^k, d),$$

where t_{drift} is the measured time, d is the impact parameter and the 6×232 coefficients C_i^k ($k = 1, ..., 232$ and $i = 1, ..., t$) account for the cell type, track orientation and cell shape, as described above. An automatic calibration procedure checks the validity of the current s-t relations at the beginning of each run and calculates new C_i^k values using cosmic ray events, if necessary. For more details see [119].

The event reconstruction in the drift chamber starts with the *pattern recognition*. It searches for candidate tracks, first in the x-y plane, then looks for their projection in the z plane. Due to the

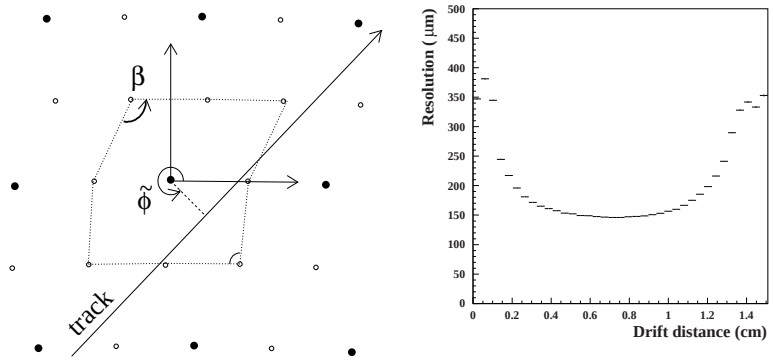

(a) (b)

Fig. 3.13: (a) Definition of the variables used in the *s-t* relations classification. Sense-wires are represented by the full black points, while the field-wires by the empty circles. (b) Spatial resolution as a function of drift distance over all big cells for a single $\tilde{\phi}$ value.

stereo setting of the wires, a track in the chamber is seen as two distinct curves. In each stereo view, hits close in space are associated to form a chain, on the basis of their curvature, and the left-right ambiguity is solved requiring the single-view candidate track to have a minimum of four hits in at least two layers. At this stage the magnetic field is assumed to be homogeneous, multiple scattering and energy loss are not treated, and rough *s-t* relations are used. The track fitting minimizes iteratively a χ^2 function based on the comparison between the measured (as obtained by the *s-t* relations) and expected (from the fit) drift distance for each hit (see Fig. 3.13(b)). The drift distance is corrected using more accurate *s-t* relations which depend on the track parameters and all the effects neglected in the pattern recognition (local variation of the magnetic filed, multiple scattering and energy loss) are now properly taken into account. After a first iteration, dedicated procedures recover missed or wrongly assigned hits by the pattern recognition, merge split tracks having a kink. The tracks from the fitting procedures are then used to look for primary and secondary vertices. In order to reduce the number of combinations, the tracks are first extrapolated in the x-y plane and primary vertices are searched for using tracks whose impact parameters are smaller than 10% of their radius of curvature. The remaining tracks are then connected to secondary vertices. For tracks crossing the beam-pipe or the walls of the chamber, the momentum is corrected for energy loss and multiple scattering. The minimization of a χ^2 function based on the distance of the closest approach between two tracks is used to assign the two tracks to a *vertex*. For a vertex inside the beam-pipe the spatial resolution is about 2 mm. For each track pair, a χ^2 function is evaluated from the distances of closest approach between tracks. For more details on the vertex fitting procedure see [101].

4. HADRONIC CROSS SECTION MEASUREMENTS AT KLOE

The KLOE experiment, applying the Radiative Return, has measured the $\sigma(e^+e^- \to \pi^+\pi^-)$ cross section, with an accuracy better than 1%. An explanation of this new method and an overview of the main features of the KLOE analyses will be given.
KLOE has already published two articles on this measurement. These published results will be compared to those one from CMD-2 and SND, operating at the VEPP-2M collider situated in Novosibirsk. A discrepancy of about 5% between the KLOE results and those from the scan experiments is found, enforcing the needs of new precise measurements. This work has the goal to give the ultimate KLOE high precision measurement on $\sigma(e^+e^- \to \pi^+\pi^-)$ and to compute the contribution from the two pion channel to the anomaly of the muon magnetic moment, $a_\mu^{\pi\pi}$, cross checking the other KLOE analyses and reaching the $2m_\pi$-threshold, for the first time in our collaboration.
Some tools are shared by the different KLOE hadronic cross section analyses. They will be introduced in this chapter and explained, with more details, in Chap. 5 and Chap. 6.

4.1 The Radiative Return method

As mentioned in Sec. 2.4 the standard approach to measure hadronic cross section is the so-called energy scan, in which the energy of the colliding beams is changed to the desired value of the Center-of-Mass (CM) energy. In the case of "particle-factories",[1] the collider is set to operate at a fixed energy. DAΦNE, the ϕ-factory at LNF, was designed to run at the fixed $\sqrt{s}$ equal to the ϕ resonance peak (1019.48 MeV) with high luminosity. For this work DAΦNE was operating, for the first time, off-resonance, only 20 MeV below the standard CM-energy of $\sqrt{s} = m_\phi$. It is not possible to use DAΦNE for an energy scan at $\sqrt{s} \ll m_\phi$, i.e. for measuring the ρ-meson region. As a consequence of this, the idea which has been worked out to obtain $\sigma(e^+e^- \to \text{hadrons})$ at DAΦNE is to use the radiative process $e^+e^- \to \text{hadrons} + \gamma$, where the photon has been radiated in the initial state (*Initial State Radiation, ISR*) by electrons or positrons of the incoming beams, lowering, in such a way, the colliding energy and producing an hadronic system at different invariant mass [133, 103]. By looking at this ISR process the hadronic cross sections become accessible from the ϕ mass down to the two-pion threshold. This method has been called *Radiative Return* because, by means of the radiation, the CM energy of the beams goes down, i.e. "returns", to a lower resonance with respect to the resonances which the collider has been set up for. In the case of DAΦNE the resonance coupling to the virtual photon is not the ϕ meson but the ρ-ω resonance.

[1] Collider designed to produce large amount of mesons. Main particle factories are: PEP-II and KEK-B for B meson and DAΦNE for K meson.

In the assumption that the radiative photon does not derive from the final state process, the cross section $\sigma(e^+e^- \to \pi^+\pi^-)$ can be expressed as a function of the differential cross section $d\sigma(e^+e^- \to \pi^+\pi^-\gamma)/ds_\pi$ and the two quantities are related by the *radiator function* $H(s_\pi, s)$:

$$\frac{d\sigma(\pi^+\pi^- + \gamma_{\rm ISR})}{ds_\pi} \cdot s = \sigma(\pi^+\pi^-, s_\pi) \times H(s_\pi, s), \tag{4.1}$$

where s is the machine energy and s_π is the invariant mass squared of the hadronic system after initial state radiation, i.e. the Q^2. We stress again that Eq. 4.1 is only valid for ISR events (Fig. 4.1). An accuracy at the per mill level is needed for H in order to perform a precision measurement. The following energy relation also holds for one ISR-photon only:

$$s_\pi = M^2_{\pi^+\pi^-} = s - 2E_{\gamma_{\rm ISR}}\sqrt{s}, \tag{4.2}$$

where s is the fixed energy of the collider.[2]

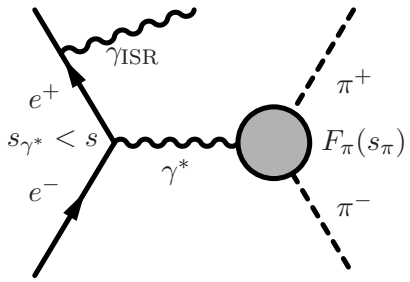

Fig. 4.1: Initial State radiation process $e^+e^- \to \pi^+\pi^-\gamma$. In the figure s_{γ^*} represents the energy of the virtual photon, equal to the center-of-mass energy of the beams, $F_\pi(s_\pi)$ is the pion form factor and s_π is the invariant mass of the two-pion system. Notice that $s_\pi = s_{\gamma^*}$ only in absence of final state radiation. The Radiative Return method performs measurements looking for events where the energy of the collision, $\sqrt{s_{\gamma^*}}$, is lower than the fixed energy of the collider, $\sqrt{s}$.

The radiator function $H(s_\pi, s)$ is a theoretical function inserted in the Monte Carlo (MC) generator `PHOKHARA`, [36, 37, 38]. It includes hard, soft and virtual radiative corrections to the process $e^+e^- \to \pi^+\pi^-\gamma$ at Next-to-Leading Order (NLO) and includes also final state radiation from the pions described by the point-like approximation (*scalar QED, sQED*).
Particular attention must be taken for events with a photon radiated in the final state (*Final State Radiation, FSR*). These processes are drawn in Fig. 4.2: (a) for Leading Order Final State Radiation (LO-FSR), (b) and (c) for Next-to-Leading Order Final State Radiation (NLO-FSR). In this case Eq. 4.1 is not valid anymore, as a wrong energy value would be associated to the two-pion system, since $s_{\gamma^*} \neq s_\pi$, i.e. the two-pion invariant mass is different from the invariant mass of the virtual photon. This kind of process needs to be well understood to perform precision measurements, and it will be described in the following.
We want to summarize below the main differences between the energy scan and Radiative Return methods.

[2] In the following we will use the notation s_{γ^*} for the energy squared transferred by the virtual photon and s_π for the two-pion invariant mass. Sometimes it may happen that those quantities can be indicated with a different notation, as $M^2_{\pi\pi}$, but in any case the meaning of the variable will be explicitly clarified.

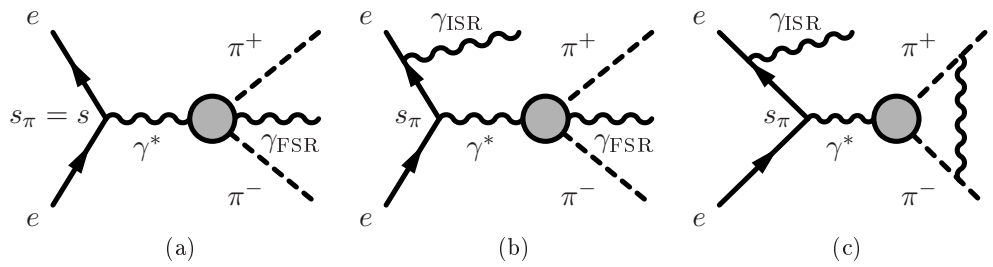

Fig. 4.2: (a) Leading order final state radiation. (b) and (c) Next-to-leading order final state radiation.

1. Energy scan method (CMD-2 and SND at VEPP-2M, Beijing)
   - the colliding energy of the beams is changed to the desired value;
   - one can perform "direct" measurements of cross sections;
   - a dedicated accelerator/physics program is required;
   - the luminosity and systematic uncertainty has to be determined for each data point.
2. Radiative Return method (KLOE at DAΦNE, BABAR at PEP-II and BELLE at KEK-B)
   - the technique works at fixed-energy collider (particle-factory);
   - the initial state radiation process is used to access lower lying energies or resonances are used;
   - the standard physics program of the experiment does not have to be modified, since ISR events are produced in any case;
   - the measurement requires precise theoretical calculation of the radiator function, H;
   - the luminosity and beam energy determination enters only once for all the data points;
   - a larger, with respect to scan experiments, integrated luminosity is needed;
   - radiative corrections have to be evaluated very precisely up to higher order (NLO or NNLO).

Even in case that the ISR-photon is measured (tagged) in a Radiative Return measurement, the invariant mass of the virtual photon, s_{γ^*}, is not known with the required precision, due to the limited energy resolution of the calorimeter. This makes an accurate measurement of the hadronic system invariant mass, s_π, unavoidable.

4.1.1 Photon polar angle

In Fig. 4.3 a cross section of the KLOE detector is drawn. Two polar angle regions for the ISR-photon are shown. Conventionally the zone in green is named *Large Angle* (*LA*) and that one in blue *Small Angle* (*SA*). Since FSR events can not be distinguished from ISR one experimentally, one has to relay on the Monte Carlo generator is use, which describes these events using the sQED approximation. However choosing appropriate angular cuts the FSR events can be significantly reduced. The preferred emission direction of the photons are displayed in Fig. 4.4(a) and in Fig. 4.4(b) for the cases of ISR and FSR, respectively, where the distribution (in the two pion

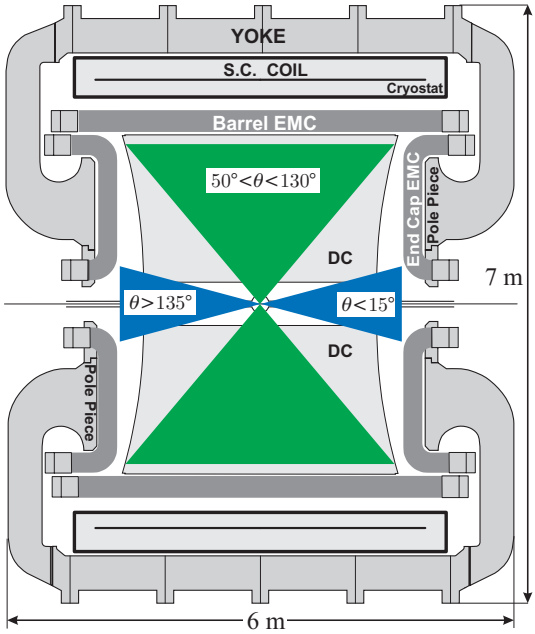

Fig. 4.3: Vertical cross section of the KLOE detector, showing the small (in blue) and large (in green) angle regions where photons and pions are accepted.

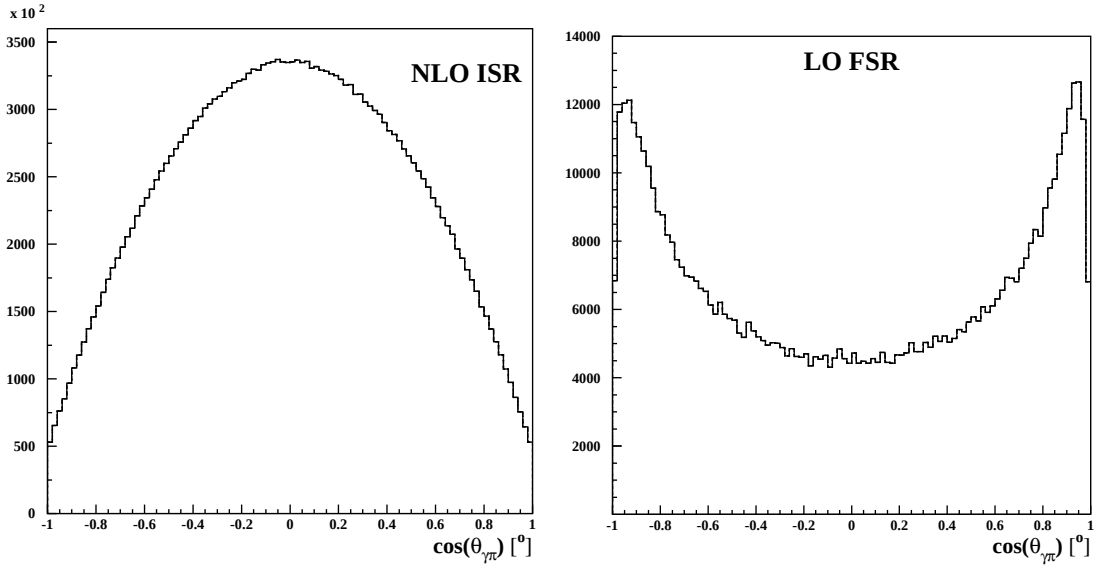

(a) (b)

Fig. 4.4: Distribution of the minimum angle between the photon and one of the two pions, in the pion rest frame, for the cases of ISR (a) and FSR (b), respectively.

rest frame) of the cosine of the minimum angle between the photon and one of the two pions is plotted. The ISR-photons tend to be emitted preferably parallel to the beam direction, i.e. at small polar angle. The opposite occurs for FSR-photons, which are preferably emitted at large polar angle, i.e. parallel to the pion direction.

Asking for pions at large polar angles and photons at small polar angles, allows to minimize the relative amount of FSR events in the data spectrum. If the event consists of two pions and only one photon (LO-event), the polar angle of the photon equals the angle of the missing momentum of the event: $\theta_\gamma = 180^\circ - \theta_{\rm miss}$, where the missing momentum is $\vec{p}_{\rm miss} = \vec{p}_{\pi^+} + \vec{p}_{\pi^-}$. The so-called *Small Angle analysis* is based on the following acceptance regions selection

$$50^\circ < \theta_\pi < 130^\circ, \tag{4.3}$$

for pions, and

$$0^\circ < \theta_{\rm miss} < 15^\circ \text{ or } 165^\circ < \theta_{\rm miss} < 180^\circ. \tag{4.4}$$

This phase space excludes the very low energy regions, i.e. $s_\pi < 0.35$ GeV^2 is kinematically forbidden. In fact, at small hadron invariant mass (high photon energy) the two-pion system, recoiling against the photon emitted at the small polar angle will force the pions to be produced at small polar angle as well, and this kind of events are excluded by the condition in Eq. 4.3. KLOE has already performed two measurements selecting events with photon at small polar angle. The two published analyses are based on data collected in the years 2001 and 2002, respectively. These will be described in Sec. 4.2.1 and Sec. 4.2.2.

In this thesis a complementary analysis is presented, in which the photon is measured (tagged) at large polar angle with the electromagnetic calorimeter:

$$50^\circ < \theta_\gamma < 130^\circ. \tag{4.5}$$

In this so-called *Large Angle analysis* the threshold region $4m_\pi^2 < s_\pi < 0.35$ GeV^2 becomes accessible. In Fig. 4.5 the $\pi^+\pi^-\gamma$ spectrum from Monte Carlo simulation for $\theta_{\rm miss} < 15^\circ (> 165^\circ)$ and $50^\circ < \theta_{\rm miss} < 130^\circ$ is shown. It is possible to see that while the spectrum towards low s_π rapidly decreases in the case of $\theta_{\rm miss} < 15^\circ (> 165^\circ)$, it extends down to the $2m_\pi$-threshold when the photon(s) are required to be at large polar angles. It is worth to state the relevance of having precise measurements at the low energy region, since the range $4m_\pi^2 < s_\pi < 0.35$ GeV^2 contributes for ca. 20% to $a_\mu^{\pi\pi}$.

The Large Angle analysis presented in this work, using off-peak 2006 data, is not the first analysis of KLOE with tagged photon. In fact 2002 data has been already used for a similar approach. We will see however in the following that the on-peak data ($\sqrt{s} = m_\phi$) suffers from large background from ϕ-decay, which makes this new analysis necessary.

The Large Angle 2002 analysis will be described in Sec. 4.3.1, while the analysis based on 2006 data, which was performed solely within this thesis, will be explained in Chap. 5 and Chap. 6. A preliminary result will be presented in Chap. 7.

The hadronic cross section measurements performed at KLOE are listed in Tab. 4.1. We stress the point that Small Angle and the Large Angle analyses cover different energy ranges, and the $\pi^+\pi^-$-threshold can be reached only by the latter. However, since for the on-peak data sample the presence of background from ϕ-decay at small energies gives a large systematic uncertainty, the analysis based on data collected at $\sqrt{s} = 1$ GeV is the only KLOE measurement which can cover energies below 0.35 GeV^2 with a percent level precision.

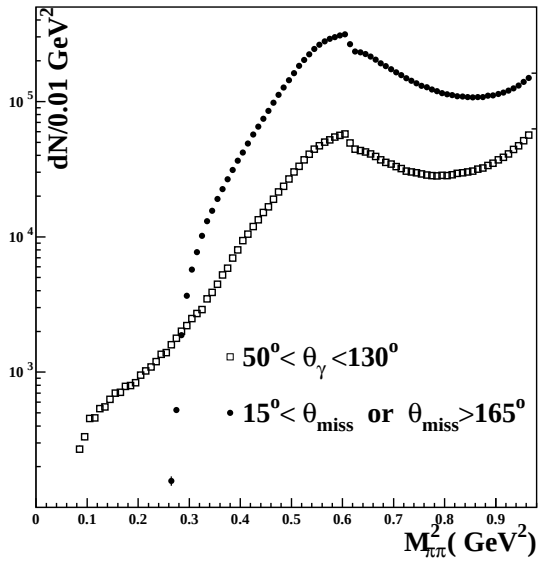

Fig. 4.5: Monte Carlo spectra of s_π as axis label in bins of 0.001 GeV^2 for different angular cuts. Both plots correspond to an integrated luminosity of $\sim$ 800 pb^{-1}. It is possible to see that the threshold region can be reached when the photon is required to be at Large Angles.

	data sample	L (pb^{-1})	$\sigma_{\rm syst}$ $s_\pi < 0.35$ GeV^2	$\sigma_{\rm syst}$ $s_\pi > 0.35$ GeV^2
Small Angle	on-peak 2001	140	not covered	1.3%
	on-peak 2002	240	not covered	0.8%
	data sample	L (pb^{-1})	$\sigma_{\rm syst}$ $s_\pi < 0.35$ GeV^2	$\sigma_{\rm syst}$ $s_\pi > 0.35$ GeV^2
Large Angle	on-peak 2002	240	dominated by f_0 model	0.9% (w/o f_0 contr.)
	off-peak 2006	230	1.5%	0.6%

Tab. 4.1: Large Angle hadronic cross section measurements performed at KLOE. "On-peak" means that the data sample has been collected at $\sqrt{s} = 1.01948$ GeV, while for the "off-peak" data sample DAΦNE was operating at $\sqrt{s} = 1$ GeV. To be notice that for the Large Angle analysis based on 2002 data, the threshold is kinematically achievable, but it suffers from the presence of ϕ-decay, which gives an extremely large systematic uncertainty in the region below 0.5 GeV^2 (see Sec. 4.3.1). The Large Angle analysis based on 2006 off-peak data is then the only KLOE analysis covering the $\pi^+\pi^-$-threshold with high precision.

4.2 Analysis with photons emitted at small polar angle

4.2.1 2001 data sample

KLOE has been so far the only experiment to publish the cross section $\sigma(e^+e^- \to \pi^+\pi^-)$ exploiting ISR events [62, 63]. Due to the reasons explained above, the first acceptance choice

was to select photons in the forward-backward region, enhancing in this way the ISR contribution. The main analysis cuts of the Small Angle analysis will be briefly described in the following:

- the *acceptance cuts* consist in requiring pions to be at large polar angle and photon(s) at small one, as described in Eq. 4.3 and Eq. 4.4;
- a *Particle identification (PID) method* based on a likelihood estimator, using the value and the position of the cluster energy release in the calorimeter as well as the Time-of-Flight (ToF) to separate pions from electrons (for a detailed explanation see [106, 107]);
- a kinematic variable called *trackmass*, $M_{\rm trk}$, is used to reject $\pi^+\pi^-\pi^0$ events and $\mu^+\mu^-\gamma$ events. This variable is obtained by imposing the four-momentum conservation on events consisting of two charged particles with the same mass and one photon, $e^+e^- \to x^+x^-\gamma$, via the relation

$$(m_\phi - \sqrt{|\vec{p}_+|^2 + M_{\rm trk}} - \sqrt{|\vec{p}_-|^2 + M_{\rm trk}})^2 - |\vec{p}_+ + \vec{p}_-|^2 = 0. \tag{4.6}$$

  For events where $x^\pm$ are equal to $\pi^\pm$ or $\mu^\pm$, $M_{\rm trk}$ is peaked at m_π or m_μ respectively. In Fig. 4.6 the trackmass peaks for different processes ($\pi^+\pi^-\gamma$, $\mu^+\mu^-\gamma$ and $\pi^+\pi^-\pi^0$) are well visible.

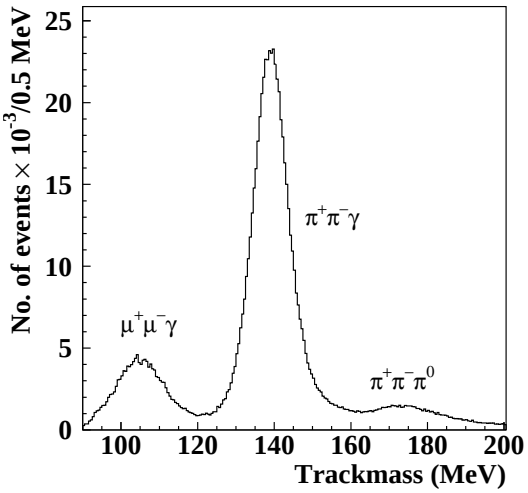

Fig. 4.6: Trackmass distribution for $\pi^+\pi^-\gamma$, $\mu^+\mu^-\gamma$ and $\pi^+\pi^-\pi^0$, after requiring PID as pion for at least one of the two tracks and acceptance. The particle ID does not effect the $\mu^+\mu^-\gamma$ region and the $\pi^+\pi^-\pi^0$ peak is lower than the $\pi^+\pi^-\gamma$ because of the acceptance, i.e. request of the photon to be at small polar angle.

The spectrum $\Delta N/\Delta s_\pi$ obtained after signal selection and residual background subtraction $\Delta N_{\rm bkg}/\Delta s_\pi$, is then normalized to the integrated luminosity $\int \mathcal{L}\, dt$ (corresponding to ca. 140 pb^{-1} for data taken in 2001), corrected for selection efficiencies and acceptance ε and divided by the radiator function H.

$$\frac{d\sigma_{\pi\pi}}{ds_\pi} = \frac{\Delta N_{\rm obs} - \Delta N_{\rm bkg}}{\Delta s_\pi} \cdot \frac{1}{\varepsilon} \cdot \frac{1}{\int \mathcal{L}\, dt} \cdot \frac{1}{H(s_\pi)}. \tag{4.7}$$

Effects from final state radiation have been treated by means of the PHOKHARA Monte Carlo code, and the spectrum has been corrected for these effects. The combined total efficiency is almost flat and around 60%. In Tab. 4.2 the systematics errors associated to the individual efficiencies are reported. A detailed description of the evaluation of each of them can be found in [104].

Experimental sources	
Acceptance	0.3 %
Trigger	0.3 %
Reconstruction Filter	0.6 %
Tracking	0.3 %
Vertex	0.3 %
Particle ID	0.1 %
Trackmass	0.2 %
Background subtraction	0.3 %
Unfolding	0.2 %
Total experimental systematics	0.9 %

Tab. 4.2: List of experimental systematic errors in the *Small Angle* analysis based on 2001 data [104].

The cross section $\sigma(e^+e^- \to \pi^+\pi^-)$ is presented in Fig. 4.7(a), as a function s_{γ^*}. It covers the full angular range in θ_π and θ_{miss} and includes final state radiation and vacuum polarization (*dressed cross section*). The pion form factor, obtained from Eq. 2.28, is show in Fig. 4.7(b).

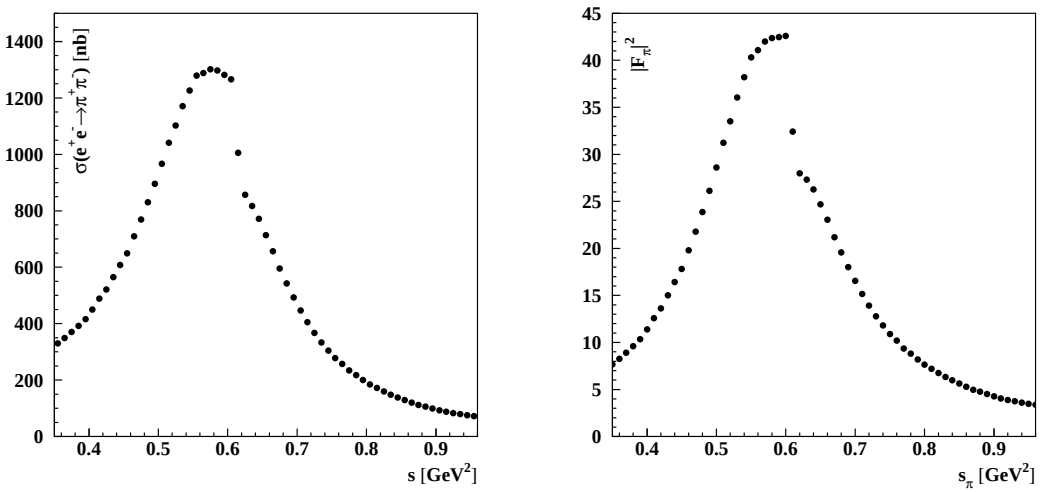

(a) (b)

Fig. 4.7: Final result of (a) "dressed" hadronic cross section $\sigma(e^+e^- \to \pi^+\pi^-)$ and of (b) pion form factor from $|F_\pi(s)|^2$ from the Small Angle analysis based on 2001 data [62]. For kinematical reason the 2π-threshold is not cover by the spectra.

To evaluate $a_\mu^{\pi\pi}$ in the dispersion integral, Eq. 2.23, one has to insert the *bare cross section* inclusive of FSR, $\sigma^{bare}(e^+e^- \to \pi^+\pi^-(\gamma_{\rm FSR}))$. By σ^{bare} one means the cross section corrected for *vacuum polarization* (*VP*) of the virtual photon [105]. The dispersion integral has been evaluated in the energy range $0.35 < s_\pi < 0.95$ GeV^2, and the result is:

$$a_\mu^{\pi\pi}(0.35 - 0.95) = (388.7 \pm 0.8_{\rm stat} \pm 3.5_{\rm syst} \pm 3.5_{\rm th}) \times 10^{-10} \tag{4.8}$$

It is worth to notice that the statistical error is almost negligible and the theoretical error is as big as the experimental one. The theoretical error gets three contributions:

- the knowledge of the Bhabha cross section needed for the luminosity determination;
- the precision of the radiator function;
- the dependence of the FSR and the vacuum polarization corrections on the model inserted in the Monte Carlo and on the theoretical calculation.

More details are given later, when the off-peak analysis will be presented.

4.2.2 2002 data sample

After the publication of the Small Angle analysis result based on data collected in 2001, KLOE has performed a new and more accurate analysis, exploiting the same acceptance region, with data collected in 2002. The analysis has been recently published [63].
The 2002 data sample, apart from having an higher integrated luminosity (ca. 240 pb^{-1}), contains improvements concerning the lower machine background and more stable DAΦNE running conditions. Further improvements include:

1. the new L3 trigger (see Sec. 3.2.3), which reduces a 30% loss of events, due to the cosmic veto in 2001, to only 0.2%;
2. the offline background filter resulted in a large systematic uncertainty in 2001 data, due to a strong dependence on the actual machine conditions. A new filter with 98.5% efficiency and negligible systematic uncertainty has been implemented;
3. the vertexing of the two fitted tracks is not required anymore. This removes the corresponding uncertainty due to the efficiency evaluation, which was a leading systematic in the analysis of the 2001 data.

Finally, the Bhabha cross section, used for evaluation of the luminosity, is known theoretically [108] with a smaller uncertainty than in the previous measurement.
The signal selection has been essentially based cutting on the same variables as in the previous analysis with the main difference of the exclusion of the vertexing. To distinguish $e^+e^-\gamma$ background from the signal events the same PID method has been used, rejecting events where both of the tracks have been identified as an electron.
In Fig. 4.8 the trackmass distribution as a function of the pion system invariant mass is shown. The black lines represent the analysis cut: $M_{\rm trk} > 130$ MeV, applied in order to reject $\mu^+\mu^-\gamma$, and the $M^2_{\pi\pi}$ dependent curve, for $\pi^+\pi^-\pi^0$ rejection.
The residual $e^+e^-\gamma$, $\mu^+\mu^-\gamma$ and $\pi^+\pi^-\pi^0$ background contamination is evaluated and subtracted fitting the $M_{\rm trk}$ spectrum of the selected data sample with a superposition of the Monte Carlo

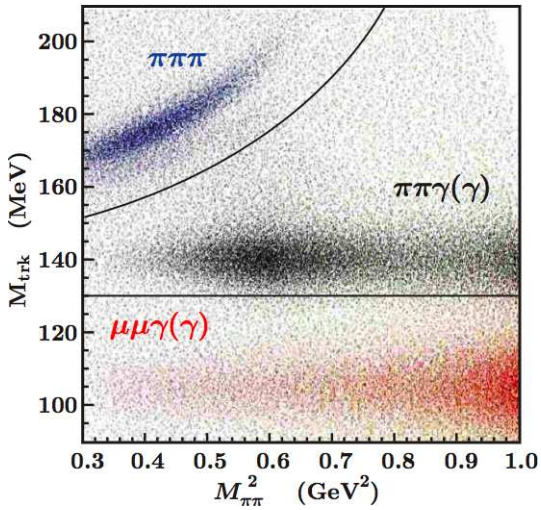

Fig. 4.8: Trackmass distribution as a function of the pion system invariant mass $M^2_{\pi\pi}$, for $\pi^+\pi^-\gamma$, $\mu^+\mu^-\gamma$ and $\pi^+\pi^-\pi^0$ Monte Carlo samples.

distributions describing the signal and background sources. This fitting and subtracting technique is similar to the one applied for 2001 Small Angle analysis, but the new one exploits a more refined procedure.[3]

The list of systematic errors for $a_\mu^{\pi\pi}$, evaluated with the Small Angle analysis using 2002 data, is shown in Tab. 4.3.

As stated above, an updated version of the generator, `Babayaga@NLO` [108], gives a Bhabha cross section which is 0.7% lower than the value from the previous version, while the calculated uncertainty is improved from 0.5% to 0.1%. The experimental uncertainty on the luminosity is 0.3%, dominated now by systematics on the angular acceptance.

The differential $\pi^+\pi^-\gamma$ cross section is then obtained from the observed count after subtracting the residual background, correcting for the selection efficiency and the integrated luminosity, see Eq. 4.7. In order to correct for the resolution effects, the differential cross section is unfolded using the Bayesian approach [109]. The unfolding procedure does not introduce any additional error to a_μ.

The a_μ dispersion integral has been evaluated in the range between 0.35 and 0.95 GeV^2

$$a_\mu^{\pi\pi} = \frac{1}{4\pi^3}\int_{s_{min}=0.35}^{s_{max}=0.95} ds\ \sigma^{bare}_{\pi\pi(\gamma)}(s)\,K(s), \tag{4.9}$$

where $\sigma^{bare}_{\pi\pi}$ is the bare cross section, inclusive of FSR and with vacuum polarization effects removed [110]. The obtained result is

$$a_\mu^{\pi\pi} = (387.2 \pm 0.5_{\rm stat} \pm 2.4_{\rm exp} \pm 2.3_{\rm th}) \times 10^{-10}. \tag{4.10}$$

This result has been compared to those one from the scan in the range $0.630 < \sqrt{s} < 0.958$ GeV

[3] The same technique, specifically adjusted and performed with 2006 sample, is applied also in the off-peak analysis, and it will be described in Sec. 5.4.

Experimental sources	
Reconstruction Filter	-
Background subtraction	0.3 %
Trackmass/Miss. Mass	0.2 %
π/e-ID	-
Tracking	0.3 %
Trigger	0.1 %
Unfolding	-
Acceptance ($\theta_{\pi\pi}$)	0.2 %
Acceptance (θ_{π})	-
Software Trigger (L3)	0.1 %
Luminosity $(0.1_{\mathrm{th}} \oplus 0.3_{\mathrm{exp}})\%$	0.3 %
$\sqrt{s}$ dep. of H	0.2 %
Total exp systematics	0.6 %
Theoretical sources	
Vacuum Polarization	0.1 %
FSR resummation	0.3 %
Rad. function H	0.5 %
Total theory systematics	0.6 %

Tab. 4.3: List of systematic errors on $a_{\mu}^{\pi\pi}$ extracted from Small Angle analysis with 2002 data sample. A "-" sign denotes that the error is considered negligible.

Analysis	$a_\mu^{\pi\pi}(0.630 < \sqrt{s} < 0.958\ \text{GeV}) \times 10^{-10}$
Small Angle 2002	$356.7 \pm 0.4_{\text{stat}} \pm 3.0_{\text{sys}}$
SND	$361.5 \pm 1.7_{\text{stat}} \pm 2.9_{\text{sys}}$
CMD-2	$361.0 \pm 2.0_{\text{stat}} \pm 4.7_{\text{sys}}$

A fit for the best value gives 359.2 ± 2.1 with $\chi^2/\text{ndof} = 1.24/2$ corresponding to a confidence level of 54.5%. The values of $a_\mu^{\pi\pi}$ shows a reasonable agreement, confirming, once included in the computation of a_μ^{SM}, the discrepancy between the theoretical predicted value and the direct measurement.
The result on $|F_\pi(s)|^2$ is compared with the results from the energy scan experiments at Novosibirsk, CMD-2 [115] and SND [116], see Fig. 4.9(a) and Fig. 4.9(b). For a given energy scan experiment, whenever there are several data points falling in one 0.01GeV^2 bin, the values are averaged. The comparison shows a slope between the KLOE and the CMD-2 and SND results.

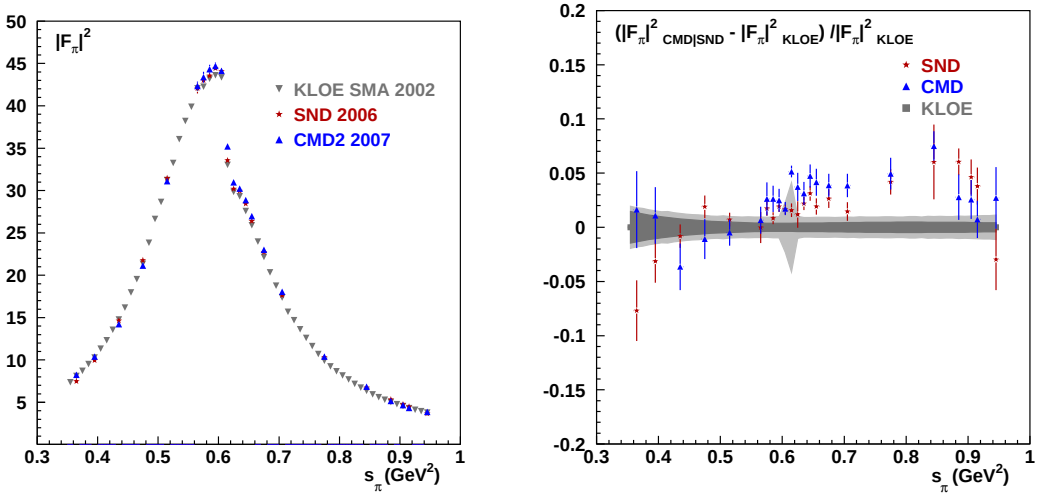

(a) (b)

Fig. 4.9: (a) $|F_\pi(s)|^2$ for the CMD-2 2007 data [115], for the SND 2006 data [116] and the KLOE data itself. Only statistical errors are shown. (b) Fractional difference between data points from CMD-2 or SND and KLOE. For CMD-2 and SND only statistical errors are shown. The dark grey band gives the statistical error for KLOE, the light grey band combines the statistical and systematic error (added in quadrature).

The discrepancy, taking as a reference the KLOE measurement, goes from ca. -5%, below the ρ-peak, up to $+5\%$, for high energies. The agreement on $a_\mu^{\pi\pi}$ is caused by a "compensation" effect, which balances the disagreement. However the trend in the $|F_\pi(s)|^2$ fractional difference must be investigate, possibly also extending the energy range covered by KLOE, since both the scan experiments reach the $\pi^+\pi^-$-threshold (not visible in Fig. 4.9(a) and Fig. 4.9(b)). This situation makes the measurements selecting events with the ISR-photons emitted at large polar angle of great relevance. Especially the analysis based on the off-peak data allows both (*i*) a fundamental cross check on the previous KLOE measurements, and (*ii*) the possibility to reach

the threshold with an accuracy which is competitive to that one of CMD-2 and SND results.
As stated in Sec. 2.4 also the BaBar collaboration is performing the measurement the two pion channel cross section $\sigma(e^+e^- \to \pi^+\pi^-)$, using the Radiative Return method. Preliminary results are shown in [73]. The result of this analysis is really waited, since it will provide further checks and improvements on the determination of $|F_\pi(s)|^2$ and $a_\mu^{\pi\pi}$, in the energy range from the threshold up to 4 GeV^2.

4.3 Analysis with photon emitted at large polar angle

4.3.1 2002 data sample

In order to cover the energy region below 0.35 GeV^2, for which most precise measurement come from the SND and CMD-2 collaborations, KLOE has performed a first analysis selecting events with the ISR-photon emitted at large polar angle using 2002 on-peak data.
We have actively contributed to the Large Angle analysis based on 2002 data essentially in: (*i*) developing a kinematic fit to reject the $\pi^+\pi^-\pi^0$ background; (*ii*) evaluating the vertexing efficiency; (*iii*) studying the systematic uncertainty due to the sQED description of the FSR event, using of the forward-backward asymmetry, which arises from the interference between ISR-LO photon events with FSR-LO events.
While at large photon angle the background from $e^+e^-\gamma$ and $\mu^+\mu^-\gamma$ events is reduced by requesting the photon to be between 50° and 130° – for both processes, the preferred photon emission direction is along the beam-line – this is not the case for $\phi \to \pi^+\pi^-\pi^0$ decays, since the direction of the π^0 occurs mainly at central values of θ, i.e. the polar angle with respect to the beam line. $\pi^+\pi^-\pi^0$ events heavily populate the region at low s_π, as can be seen in Fig. 4.3.1, where the Large Angle geometrical selection and the `ppgtag` pre-filter cut, rejecting $\pi^+\pi^-\pi^0$ events (see Sec. 5.2 and [117]), have been applied.

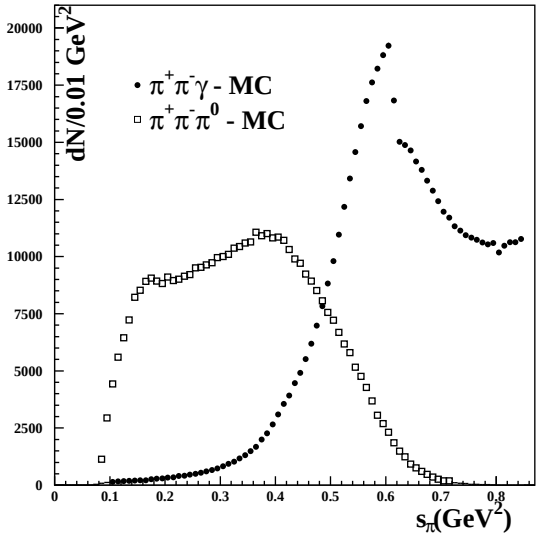

Fig. 4.10: Event distribution after the acceptance cut, $50° < \theta_{\pi,\gamma} < 130°$, and a pre-filter cut, for $\pi^+\pi^-\gamma$ and $\pi^+\pi^-\pi^0$ Monte Carlo samples, normalized to the integrated luminosity of the 2002 data (~ 240 pb^{-1}).

The possibility to have the kinematic closure of the event allows a set of dedicated cuts for the $\pi^+\pi^-\pi^0$ rejection.
As mentioned before, we have worked out a *kinematic fit* under the $\pi^+\pi^-\pi^0$ hypothesis, with the aim to reject events using the $\chi^2_{\pi\pi\pi}$ of the fit. The procedure uses as inputs the curvature, the cotangent of the polar angle θ and the azimuthal angle ϕ of the two tracks and the three components of the momentum of the two photons. In the case of more than two photons, the fit is repeated for each pair, and the minimum value of $\chi^2_{\pi\pi\pi}$ is chosen. The twelve input quantities are constrained by four-momentum conservation and by the invariant mass of the two photons, which is required to be close to the π^0 mass. In total one obtains five constraints. The covariance matrix of the twelve inputs is also passed to the fit and the least-squares method is used for the minimization. In Fig. 4.11(a) the distribution of $\chi^2_{\pi\pi\pi}$ is shown for the Monte Carlo samples

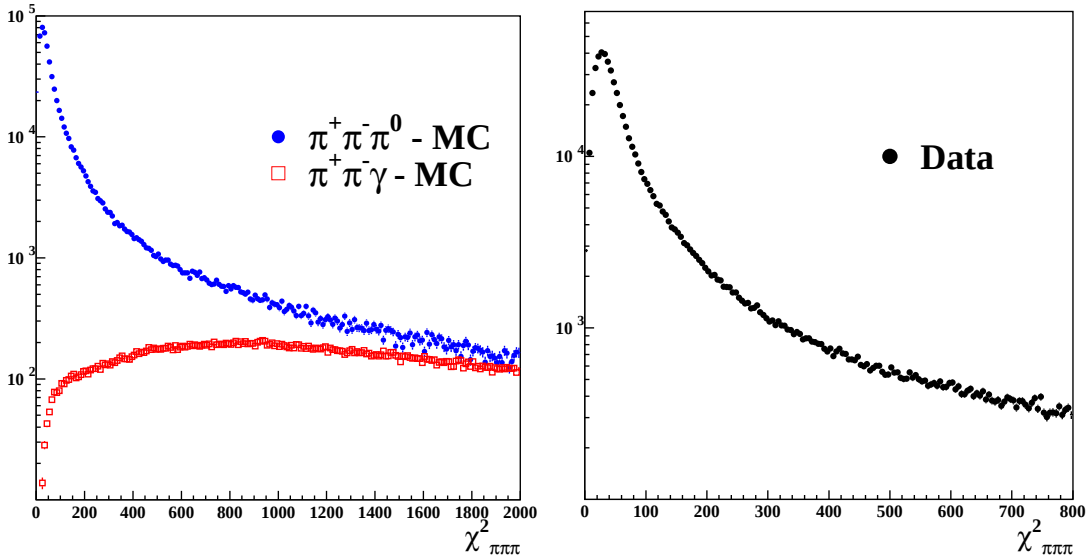

(a) (b)

Fig. 4.11: (a) $\chi^2_{\pi\pi\pi}$ distribution for $\pi^+\pi^-\pi^0$ and $\pi^+\pi^-\gamma$ Monte Carlo events normalized to the integrated luminosity of the data sample. (b) $\chi^2_{\pi\pi\pi}$ distribution for the 2002 data sample.

of $\pi^+\pi^-\pi^0$ and $\pi^+\pi^-\gamma$ events, both normalized to the integrated luminosity. The fit allows to clearly distinguish between the signal and the $\pi^+\pi^-\pi^0$ background, given also by the fact that only about 20% of signal events enter the fit, which is performed only in the presence of two (or more) photons. In Fig. 4.11(b) the distribution of $\chi^2_{\pi\pi\pi}$ for data is presented. Event with $\chi^2_{\pi\pi\pi} < 200$ are rejected, providing a rejection power of ca. 40% and a signal inefficiency smaller than 2%.
The Ω-*angle*

$$\Omega = \mathrm{acos}\left(\frac{\vec{p}_{\mathrm{miss}} \cdot \vec{p}_{\gamma}}{|\vec{p}_{\mathrm{miss}}||\vec{p}_{\gamma}|}\right), \tag{4.11}$$

defined as the angle between the tagged photon and the missing momentum of the tracks is the main cut to reject $\pi^+\pi^-\pi^0$ events. In the case of more than one photon in the event, the smallest Ω-angle is considered as that one generated by the γ_{ISR}. The distribution of Ω-angle peaks at zero for signal – since the ISR-photon is emitted along the missing momentum direction – and is off-zero for multi-photon events. Therefore it is a very powerful tool to separate signal from

$\pi^+\pi^-\pi^0$ events, as can be seen in Fig. 4.12, where the Ω-angle distribution is plotted for $\pi^+\pi^-\gamma$ (in red) and $\pi^+\pi^-\pi^0$ (in yellow) Monte Carlo events. It is visible that the $\pi^+\pi^-\pi^0$ distribution is much broader than the one for signal. The width of the $\pi^+\pi^-\gamma$ peak in Fig. 4.12 is not only due to resolution effects but also to NLO signal events. At high values of s_π this effect becomes larger, because of the increasing number of low energy NLO events. To take into account this

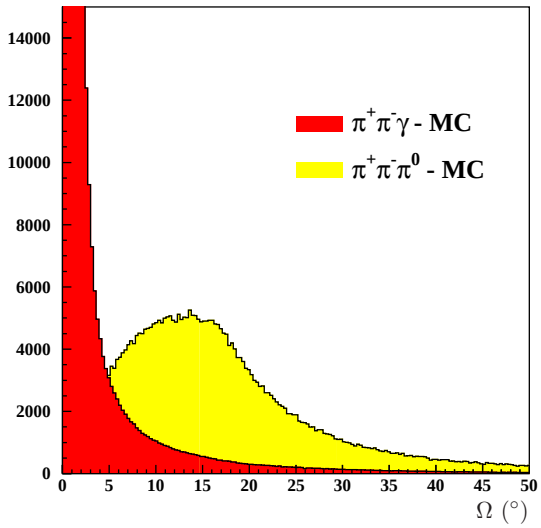

Fig. 4.12: Distribution of Ω-angle, for $\pi^+\pi^-\gamma$ (in red) and $\pi^+\pi^-\pi^0$ events (in yellow), both from Monte Carlo.

broadening, a s_π-dependent cut has been applied for the Ω-angle. The applied cut provides a rejection power of more than 90% of the $\pi^+\pi^-\pi^0$ events, and a signal loss of few percent at threshold up to a maximum of $\sim 10\%$ at high s_π.

The χ^2 and Ω-angle cuts do not reduce the irreducible background, as this has exactly the same signature as the signal. There are three sources of irreducible background for the large photon polar angle selection: (*i*) leading order final state radiation, Fig. 4.13(a), (which actually corresponds to the diagram in Fig. 4.2); (*ii*) $\phi \to \rho\pi \to \pi^+\pi^-\gamma$, Fig. 4.13(b) and (*iii*) the radiative ϕ decay to $\pi^+\pi^-\gamma$ through the scalar meson: $\phi \to (f_0(980) + f_0(600))\gamma \to \pi^+\pi^-\gamma$, Fig. 4.13(c). These must be precisely described by the Monte Carlo simulation in order to be subtracted. Also the interference among them must be taken into account.
The contribution from $\phi \to \rho\pi \to \pi^+\pi^-\gamma$ is actually small [38]. The KLOE analysis on the $\phi \to \pi^0\pi^0\gamma$ state [111] has measured an upper limit for the decay chain $\phi \to \rho^0\pi^0\gamma \to \pi^0\pi^0\gamma$ and under the assumption that the decay $\phi \to \rho^\pm\pi^\mp\gamma \to \pi^\pm\pi^\mp\gamma$ has a similar order of magnitude, this contribution is negligible for $s_\pi > 0.5$ GeV^2, and Monte Carlo simulations support this ansatz.
The scalar mesons contribution consists of $f_0(980)\gamma$ and in $f_0(600)\gamma$ events. This radiative decay proceeds with a photon angular distribution $f(\theta) \sim (1 + \cos^2(\theta))$, therefore its effect is much more relevant in the Large Angle analysis than in the Small Angle one. Since the properties of the scalar are still very active field of research, the prediction of their contribution is not straightforward. Moreover due to the fact that the amplitude of this process generates interference pattern with FSR amplitude, events involving $f_0(980)$ or $f_0(600)$ mesons cannot be simply removed by subtraction. KLOE has analyzed the $\pi^+\pi^-\gamma$ final state at large photon

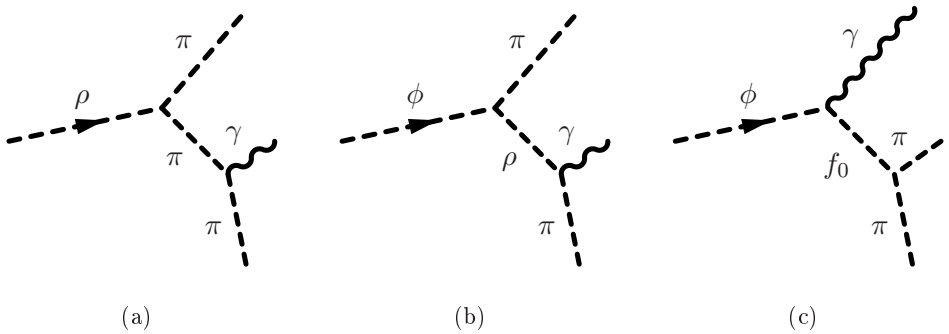

Fig. 4.13: Irreducible background sources for 2002 data sample requiring photon tagging. Leading order final state radiation (a) (this corresponds to the diagram in Fig. 4.2); $\phi \to \rho\pi \to \pi^+\pi^-\gamma$ (b); the radiative ϕ decay to $\pi^+\pi^-\gamma$ through scalar meson: $\phi \to (f_0(980) + f_0(600))\gamma \to \pi^+\pi^-\gamma$.

polar angle ($45° < \theta_{\pi,\gamma} < 135°$) using the 2001-2002 data sample (~ 350 pb^{-1}) to evaluate the properties of the scalar mesons [112]. Fitting the $f_0(980)$ mass spectrum,[4] it has been possible to achieve a good agreement between data and Monte Carlo prediction between 400 and 1000 MeV in invariant mass (see Fig. 4.14). The decay $\phi \to f_0(980)\gamma$ features a specific E_γ^3 behaviour,

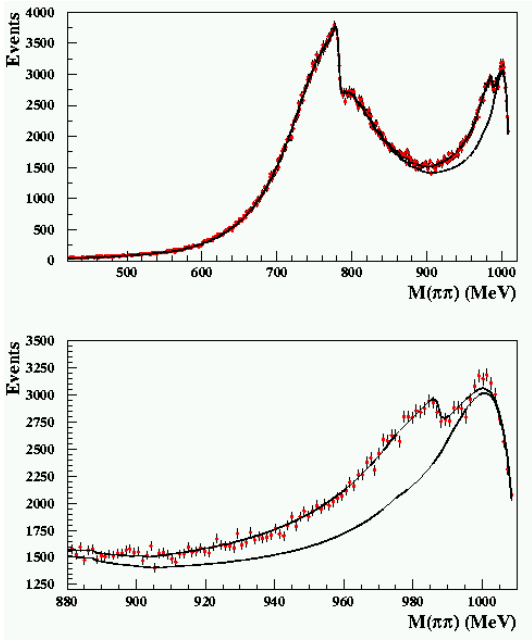

Fig. 4.14: Spectrum in $M_{\pi\pi}$ for $\pi^+\pi^-\gamma$ Large Angle events: the bump around 980 MeV shows the evidence for $\phi \to f_0\gamma \to \pi^+\pi^-\gamma$. The upper and the lower curves correspond to data fits, assuming the ϕ decays into $f_0\gamma$ through a charged kaon loop, and the background parametrization, respectively. The lower plot shows an enlarged view of the f_0 signal, [112]

causing the extension of the mass spectrum not only close to its own mass but extended down

[4] The model used is based on the "kaon loop amplitude" [113].

to the $\pi^+\pi^-$-threshold. Several models have been proposed to parametrize the dynamics of the decay $\phi \to (f_0(980) + f_0(600))\gamma \to \pi^+\pi^-\gamma$ and the interference with $e^+e^- \to \pi^+\pi^-(\gamma_{\rm FSR})$. The model dependence in the description of this process is under control for $s_\pi > 0.5$ GeV^2, but gets very large uncertainty below this value. Moreover, at the threshold region the contribution of $e^+e^- \to \rho^\pm\pi^\mp\gamma \to \pi^\pm\pi^\mp\gamma$ irreducible background can not be neglected anymore.
It has therefore be taken the decision, that the Large Angle analysis for 2002 on-peak data can be used for a precision measurement only for $s_\pi > 0.5$ GeV^2. We have also contribute in testing the description of the FSR photon events of the Monte Carlo generator used in the analysis.
Fig. 4.15 shows the fraction of $\pi^+\pi^-\gamma_{\rm FSR}$ for 2002 data after the Large Angle acceptance cuts. The contamination of these events can reach 30% depending on the energy on the second photon.[5] The model inserted in the Monte Carlo PHOKHARA generator, to describe FSR events, is the sQED.

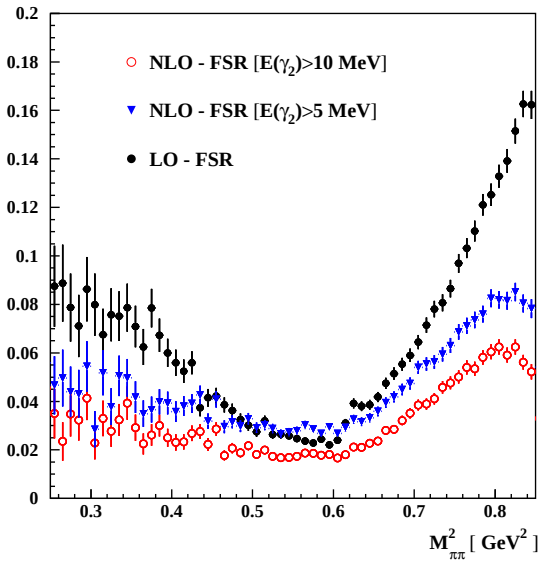

Fig. 4.15: Fraction of leading-order (full circles in black) and next-to-leading order FSR at large photon angles, as a function of $M^2_{\pi\pi}$. The FSR-NLO contribution is estimated requiring for the second photon an energy above 5 MeV in one case (blue triangles) and above 10 MeV (red triangles) in the other case.

In this approach pions are treated as point-like particles and then the total FSR amplitude is multiplied by the pion form factor, according to the Kühn-Santamaria parametrization. The validity of the model has been checked by means of the interference between ISR and FSR, which gives rise to a *Forward-Backward asymmetry* (*F-B*)

$$\mathcal{A}_{\rm FB}(s_\pi) = \frac{N_{\pi^\pm}(\theta > 90^\circ) - N_{\pi^\pm}(\theta < 90^\circ)}{N_{\pi^\pm}(\theta > 90^\circ) + N_{\pi^\pm}(\theta < 90^\circ)}, \tag{4.12}$$

and a *charge asymmetry* [133] of the pion tracks. Comparing data and Monte Carlo, it is possible to set an upper limit on the validity of the model, at least in the region where the irreducible background, especially from scalar mesons, is negligible. In Fig. 4.16(b) it is possible to appreciate the agreement between the sQED model inserted into PHOKHARA represented by the blue triangles, and data 2006, red circles. The use of off-peak data is motivated by the fact that they are almost

[5] Acceptance cuts require also at least one photon having an energy above 50 MeV.

completely free from effects due to scalar mesons, which instead are present in the 2002 data, as can be seen in the black in Fig. 4.16(a).

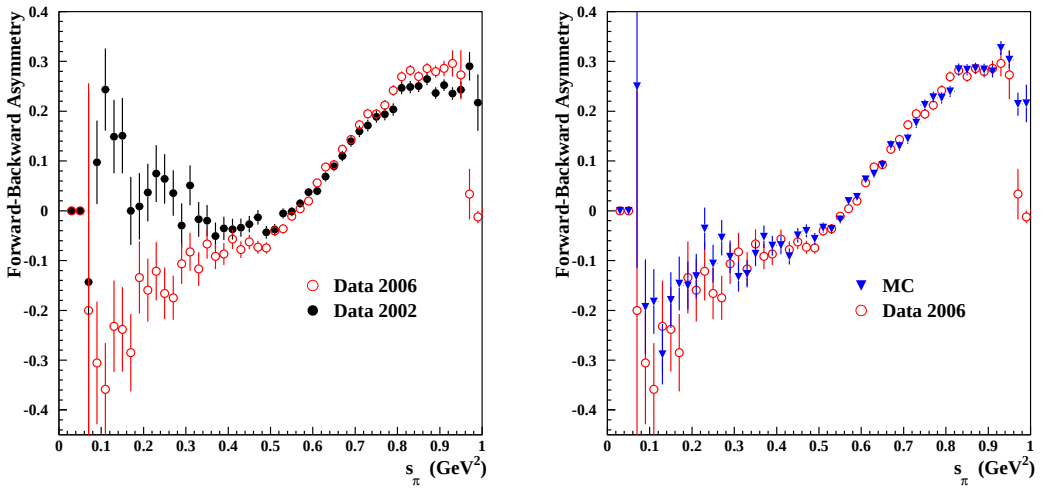

(a) (b)

Fig. 4.16: (a) Forward-Backward asymmetry for 2002 data (full black circles) and 2006 data (open red circles). (b) Forward-Backward asymmetry for 2006 data (open red circles) and Monte Carlo (blue triangles).

The Large Angle analysis 2002 data is very close to be finalized, and a preliminary result of pion form factor is available. As mentioned above, even though the $\pi^+\pi^-$-threshold is kinematically reachable, the spectrum has been evaluated in the limited range $0.5 < s_{\gamma^*} < 0.85$ GeV^2.[6] In Fig. 4.17 the comparison between the pion form factors from the Large Angle analysis 2002 data and the Small Angle analysis 2001 data [62] is shown. The red band represents the systematic error due to the scalar mesons correction, while the blue points correspond to the 2001 Small Angle analysis, and contains only statistical errors. The systematic errors are shown in Tab. 4.4. A Preliminary evaluation of $a_\mu^{\pi\pi}$ has been performed, giving the value

$$a_\mu^{\pi\pi}(0.5 - 0.85\ \text{GeV}^2) = (252.5 \pm 0.6_{\text{stat}} \pm 5.1_{\text{styst}}) \times 10^{-10}. \tag{4.13}$$

A detailed explanation of the analysis with large photon polar angle with 2002 data can be found in the Ph.D. thesis of D. Leone [114].

The observation that for on-peak data the irreducible background from ϕ-decay into scalar mesons, as well as the background from $\phi \to \rho\pi$, makes a precision measurement of the $e^+e^- \to \pi^+\pi^-$ cross section impossible has lead to the decision that a major data sample needs to be taken off-resonance, i.e. for $\sqrt{s} = 1$ GeV. The analysis of this off-peak data will be described in the following chapters and is the major topic of this work.

[6] The energy is indicated as s_{γ^*}, i.e. the momentum transferred by the virtual photon. The passage from the invariant mass of the hadronic system $M^2_{\pi\pi} \equiv s_\pi$ to the invariant mass of the virtual photon $M^2_{\gamma^*} \equiv s_{\gamma^*}$ will be described in Sec. 6.4.

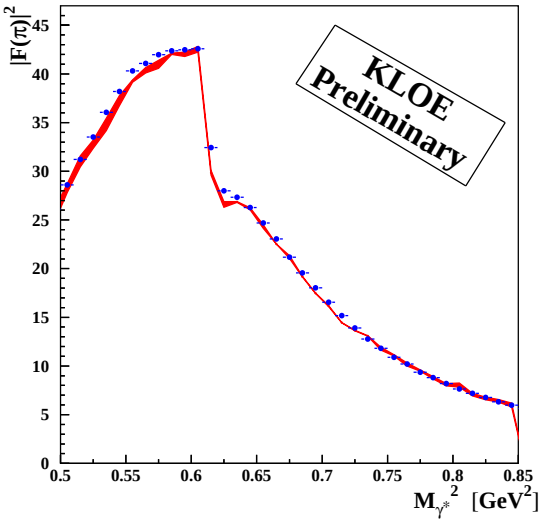

Fig. 4.17: Pion form factor from 0.5 to 0.85 GeV^2 obtained at Large Angle (red band) compared with the one obtained from Small Angle with 2001 data [62]. The red band represents the systematic error introduced by the subtraction of the scalar mesons. $M^2_{\gamma^*}$ stays for the invariant mass of the virtual photon.

	Flat in s_π	0.4 GeV^2	0.6 GeV^2	0.85 GeV^2
Trigger	0.1%			
Filfo	0.1%			
Tracking	0.2%			
Vertex	0.2%			
Particle ID	0.3%			
Acceptance	0.3%			
Kinematic fit	0.2%			
Trackmass cut	0.2%			
Ω-angle cut	0.1%			
$\mu^+\mu^-\gamma$ and $\pi^+\pi^-\pi^0$ subtraction		0.2%	<0.1%	0.3%
FSR correction		0.4%	0.2%	∼1%
Total		0.8%	0.6%	1.2%

Tab. 4.4: List of the systematic errors for $|F_\pi(s)|^2$ extracted from $\sigma(e^+e^- \to \pi^+\pi^-\gamma)$ with photon tagging. The systematic error of the subtraction of the scalar mesons background is not reported.

5. SIGNAL SELECTION AND BACKGROUND SUBTRACTION

In this section, a description of the *Large Angle off-peak* analysis will be presented in details. We start with a description of the fine tuning procedure of track parameters, which has been performed in order to obtain a high precision measurement. The $\pi^+\pi^-\gamma$ signal selection and the fit procedure to subtract the background will be also described.
The data sample used in the analysis corresponds to the 233 pb^{-1} collected in 2006 at $\sqrt{s} =$ 1 GeV. The integrated luminosity of the Monte Carlo samples correspond to 1400 pb^{-1} for $\pi^+\pi^-\gamma$ and $\mu^+\mu^-\gamma$ channels (scale factor 6) and 225 pb^{-1} for $\pi^+\pi^-\pi^0$ one.

5.1 Calibration of tracking parameters

5.1.1 Tracking fine calibration on data

Fine calibration for charged tracks in data have been worked out and the accuracy of the data-Monte Carlo agreement has been checked.
Normally the track calibration is performed by means of calibration runs, acquired twice per week during the data taking (see Sec. 3.3.2 and, for more details, [119]). Further offline studies, especially dedicated to the hadronic cross section analyses, have been developed and resulted in a fine calibration of the momenta of the charged tracks. This calibration is based on $e^+e^- \to \pi^+\pi^-$ collinear events. The trackmass variable, $M_{\rm trk}$ see Eq. 4.6, is used to check the procedure, by looking at the value of the charged pion peak.
To select collinear events, the following requirements have been applied:[1]

1. track quality criteria:
   - a cut on the radial position of the first hit in the drift chamber: $\rho_{\rm FH} < 50$ cm;
   - a cut on the radial position and the z-position of the extrapolated point of closest approach (PCA) between the track and the interaction point: $\rho_{\rm PCA} < 8$ cm and $|z_{\rm PCA}| < 12$ cm;
   - a cut on the z-component and on the transverse component of the track momentum, to reject spiralizing track: $|p_z| > 90$ MeV or $|p_T| > 160$ MeV;
   - both of tracks should be identified as pions by the $\pi - e$ PID likelihood function [106, 107];
   - both of the tracks are required to be at large polar angle, i.e. $50^\circ < \theta_{\rm trk} < 130^\circ$

[1] The events have fulfilled data quality criteria and the streaming conditions for the stream of charged radiative events, See. 5.2.

2. to ensure the collinarity of the tracks, the following requirements are imposed

   - $s_\pi > 0.95$ GeV^2;
   - $\Delta\phi = \pi - |\phi_{\pi^+} - \phi_{\pi^-}| < 0.5°$;
   - $\Delta\theta = \pi - |\theta_{\pi^+} + \theta_{\pi^-}| < 0.5°$;
   - $\Delta p = |\vec{p}_{\pi^+}| - |\vec{p}_{\pi^-}| < 5$ MeV;

where s_π is the invariant mass of the $\pi^+\pi^-$-system, ϕ and θ are the azimuthal and the polar angles, respectively, and $\vec{p}$ is the track momentum. All the quantities are referred to Center-of-Mass (CM) system of the colliding beams. Because of the collinearity, Δp, $\Delta\theta$ and $\Delta\phi$ must be peaked at zero. By fitting with gaussian functions, one can test the track calibration and check for possible miscalibrations.
For $\Delta\theta$ and $\Delta\phi$ the mean values of the fits are in agreement with 0°, proving an excellent calibration. For Δp the value of the peak is shifted by about 300 KeV. For collinear events with momenta of ca. 500 MeV, this would correspond to a systematic miscalibration well below 1%. However, to get the best possible accuracy, fine corrections have been applied since a precise knowledge of tracking and of trackmass variable is crucial (*i*) for the signal selection (see Sec. 5.2) and (*ii*) for the residual background subtraction (Sec. 5.4).
The main sources of the deviation on momenta is caused by the z-component, as can be seen in Fig. 5.1(c). To investigate this discrepancy, two kinematic quantities have been worked out for $e^+e^- \to \pi^+\pi^-$ events.[2]

The first variable, called δp, is evaluated in the CM-system of the beams and represents the difference between the modulus of the expected momentum and the observed modulus. It assumes as fixed parameters the $\sqrt{s}$ and the charged pion mass. It can be formulated as:

$$\delta p^\pm = \sqrt{\left(\frac{\sqrt{s}}{2}\right)^2 - m_\pi^2} - |\vec{p}^{\,\pm}_{\rm CM}|, \tag{5.1}$$

where $|\vec{p}^{\,\pm}_{\rm CM}|$ is the modulus of the track momentum in the CM-system of the beams for positive or negative pion. If the tracks are well calibrated, $\delta p^\pm$ is equal to zero. The values of δp^+ and δp^- are shown in Fig. 5.2(a) and in Fig. 5.2(b), respectively. Positive tracks show a tiny miscalibration, of the order 200 KeV, in the variable δp^+.

In the laboratory system (LAB) the beams are colliding with a small boost towards the center of the DAΦNE dual ring (see Sec. 3.1). In Fig. 5.3 a schematic picture of the spatial quantities involved in the bunch crossing is drawn. This boost, $\vec{p}_b$, is assumed to be precisely known when evaluating the variables in the CM-system of the beams, like in Eq. 5.1. It is useful to develop another variable, in the LAB frame, which can also give information on the direction of the tracks. This can be inferred from the angle between the track momentum, $\vec{p}_{\rm trk}$ (shown in blue in Fig. 5.3), and the boost impressed to the collision in LAB-system, $\vec{p}_b$ (shown in red in Fig. 5.3). So one can obtains the difference between the expected and the observed value of the angle between $\vec{p}_b$ and $\vec{p}_{\rm trk}$, named α and indicated as a green arc in Fig. 5.3. The second variable, called $\delta\alpha^\pm$, is therefore given by:

$$\delta\alpha^\pm = E_{e^+e^-} \cdot E_{\rm trk} - \frac{s}{2} - \vec{p}_{\rm b} \cdot \vec{p}^{\,\pm}_{\rm LAB}, \tag{5.2}$$

[2] A further cut in $|M_{\rm trk} - m_\pi| < 20$ MeV is applied to select pions. Since the correction and the precision of the fit on $M_{\rm trk}$ peaks are much smaller than the window of 20 MeV this cut on trackamss, this does not cause any bias on the calibration method.

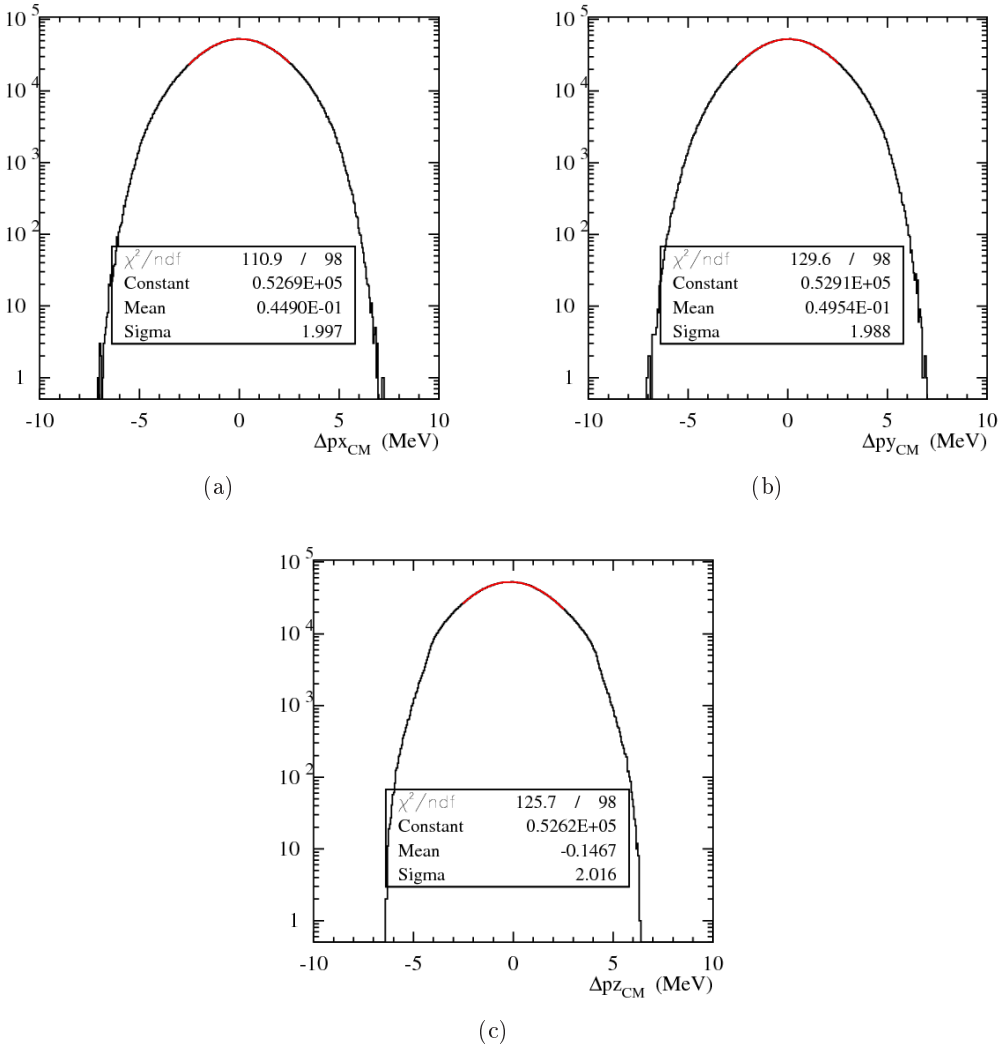

Fig. 5.1: Components along the x, y and z direction of Δp.

where $E_{e^+e^-}$ is the total energy of the beams and $\vec{p}_b$ is the boost impressed to the collision in the LAB-system. In the case of perfectly calibrated tracks, $\delta\alpha^{\pm}$ is equal to zero. $\delta\alpha^{+}$ and $\delta\alpha^{-}$ are drawn in Fig. 5.4(a) and in Fig. 5.4(b) , respectively. Positive tracks show a small miscalibration of the order of 1.3°.

Using δp and $\delta\alpha$ together gives the possibility to check the calibration of the tracks, for each charge separately, in the LAB and in the beam CM-system.[3] As said above, the miscalibration is found to be well below 1%. However, to reduce all sources of systematics, we have developed *fine tuning corrections*.

The corrections are evaluated is such a way to minimize δp and $\delta\alpha$ and they are applied to each momentum component for positive and negative tracks, in the following way:

[3] The variable Δp, $\Delta\theta$ and $\Delta\phi$ are then used as a check of the tuning procedure. Variables obtained by not fully closing the kinematics do not allow for separate corrections for positive or negative charge of the tracks.

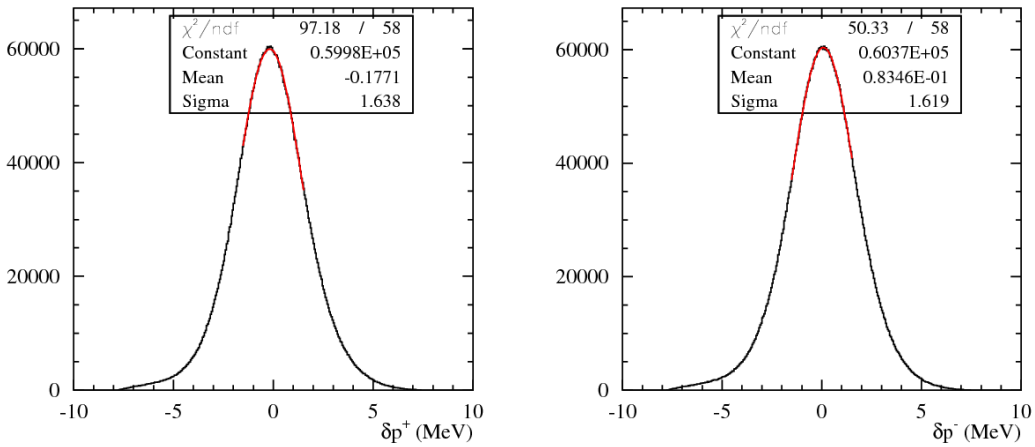

(a) (b)

Fig. 5.2: Difference between expected and observed momentum modulus for collinear events in the collision CM-system, δp^+ (a) and δp^- (b). A small miscalibration is visible, especially for the positive track (a), of the order of 200 KeV.

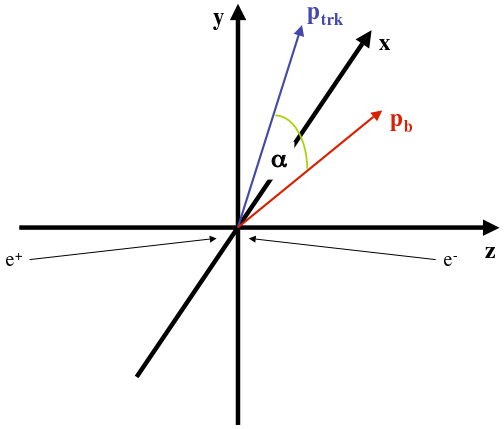

Fig. 5.3: Schematic picture of the spatial variables involved in $\delta\alpha$. The directions of the colliding e^+e^- beams are reported and the boost present in the collision is drawn in red. The boost occurs in the x-y plane. The momentum direction of one of the two collinear tracks is represented by the blue arrow. The angle between $\vec{p}_{\rm b}$ and $\vec{p}_{\rm trk}$, i.e. α, is sketched by the green arch.

1. positively charged track:
   - $p^+_{x,y} = p^+_{x,y} \cdot (1. - 4. \times 10^{-4})$
   - $p^+_z = p^+_z + |p^+_z| \cdot 6. \times 10^{-4}$;
2. negatively charged track:
   - $p^-_{x,y} = p^-_{x,y} \cdot (1. + 3. \times 10^{-4})$

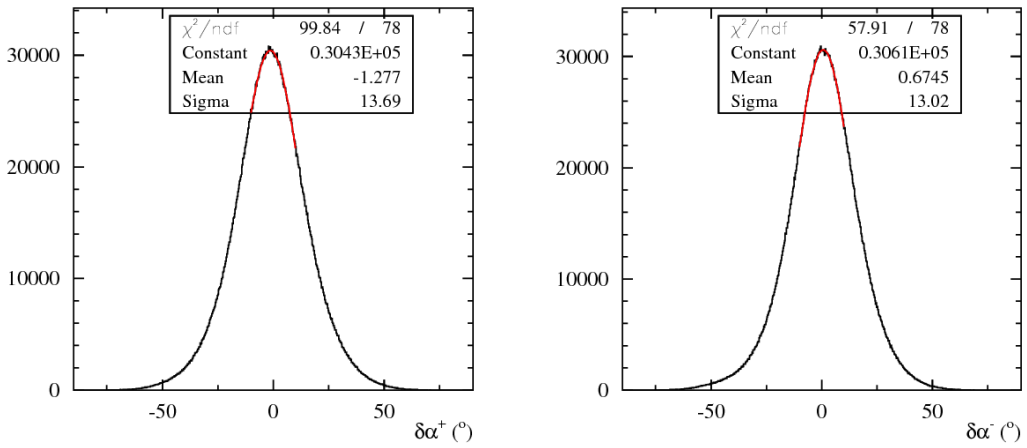

(a) (b)

Fig. 5.4: Difference between the expected and observed values of the angle between the track direction and the boost direction of the collision in the LAB system, for positive (a) and negative (b) track. The positive track shows a small miscalibration of ca. 1.3°.

$$- \; p_z^- = p_z^- + |p_z^-| \cdot 5. \times 10^{-4}$$

One can see the small order of magnitude of the corrections, $\mathcal{O}(10^{-4})$ in momentum, which shows the goodness of the default track calibration performed during the data taking.
In Fig. 5.5 and in Fig. 5.6 the δp and $\delta\alpha$ distributions are shown for the positive and negative tracks after the corrections. It is possible to appreciate the improved calibration of the tracks: $\delta p^{+,-}$ have a mean value around ca. 30 KeV; and $\delta\alpha$ are below 0.2° or, for the negative track, even smaller.

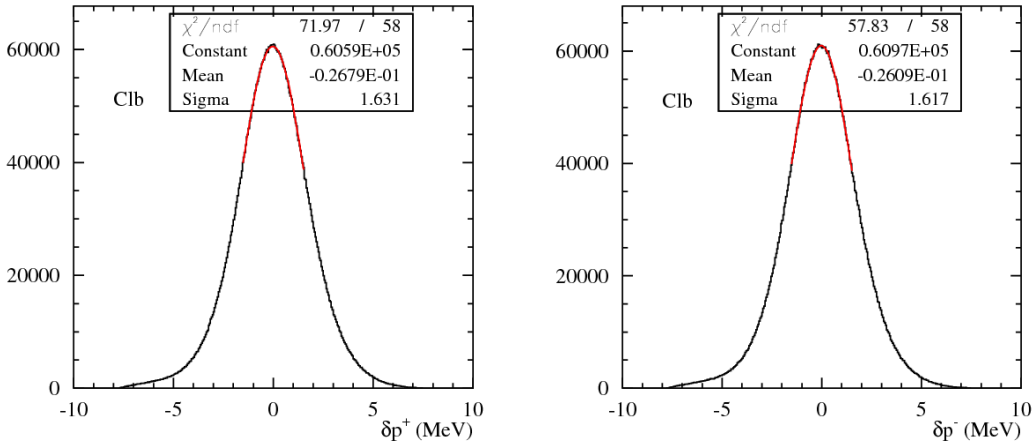

(a) (b)

Fig. 5.5: Distribution of δp^+ (a) and δp^- (b) track, after the calibration.

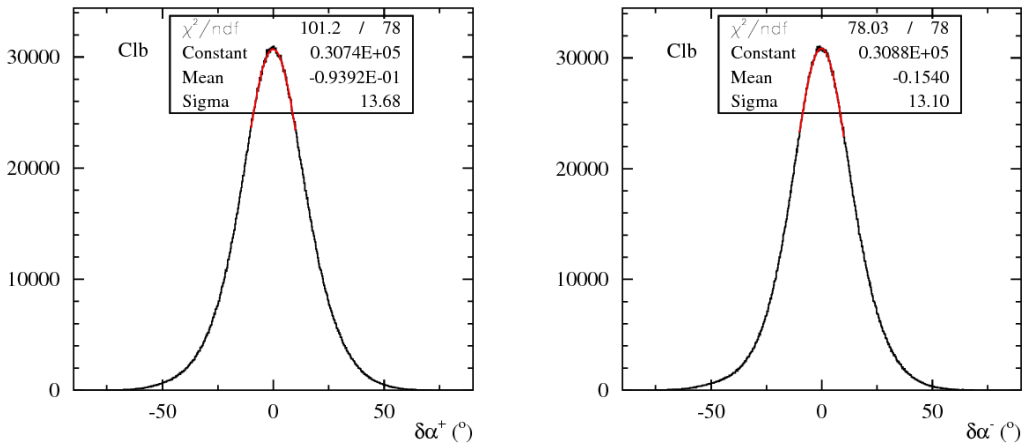

(a) (b)

Fig. 5.6: Difference between expected and observed direction for collinear events, Eq. 5.2, after the calibration.

Quantity	before the calibration	after the calibration
δp^+	-177 KeV	-27 KeV
δp^-	-83 KeV	-26 KeV
$\delta\alpha^+$	-1.3°	-0.1°
$\delta\alpha^-$	0.7°	-0.1°

Tab. 5.1: Table of the variables $\delta p^{+,-}$ and $\delta\alpha^{+,-}$ before and after the fine calibrations.

In Tab. 5.1 the comparison between $\delta p^{+,-}$ and $\delta\alpha^{+,-}$ before and after the fine calibrations is shown.

The effect of the corrections has been checked looking at the trackmass shape: fitting the peak of the $\pi^+\pi^-\gamma$ events with a gaussian function, one can see whether its value corresponds to $m_\pi = 139.57$ MeV [1]. The fit is performed both inclusively in s_π, see Fig. 5.7(a), and for different slices in s_π, see Fig. 5.7(b). In Fig. 5.7(b) the red and the blue circles represent the mean values of $M_{\rm trk}$ without and with the fine calibration, respectively. The good agreement between the mean value of the fit, $\bar{M}^{\pi\pi\gamma}_{\rm trk}$, after the calibrations and m_π is evident. Fig. 5.7(b) also proves that the corrections, which have been evaluated using collinear events requiring the pion system invariant mass to be bigger than 0.95 GeV^2, work well also at lower energy.

The ρ-ω interference region of the $\pi^+\pi^-\gamma$ mass spectrum can provide a further check on the track calibration: by fitting it with two Breit-Wigner functions it is possible to extract the mass of the ω meson, to be compared with the PDG value $m_\omega = 782.65 \pm 0.12$ MeV [1]. The fit is performed in a range of 100 MeV (see Fig. 5.8(a)), which has been shifted in steps of 0.5 MeV (see Fig. 5.8(b)) to test the stability of the result. One obtains $m_\omega = 782.4 \pm 0.2$MeV which is in good agreement, within one standard deviation, with the world average value cited above.[4] Without the calibration one would obtain m_ω values of about 3 MeV far from the PDG value.

[4] The ±0.2 MeV error corresponds to the maximum deviation of the values obtained, shown in Fig. 5.8(b).

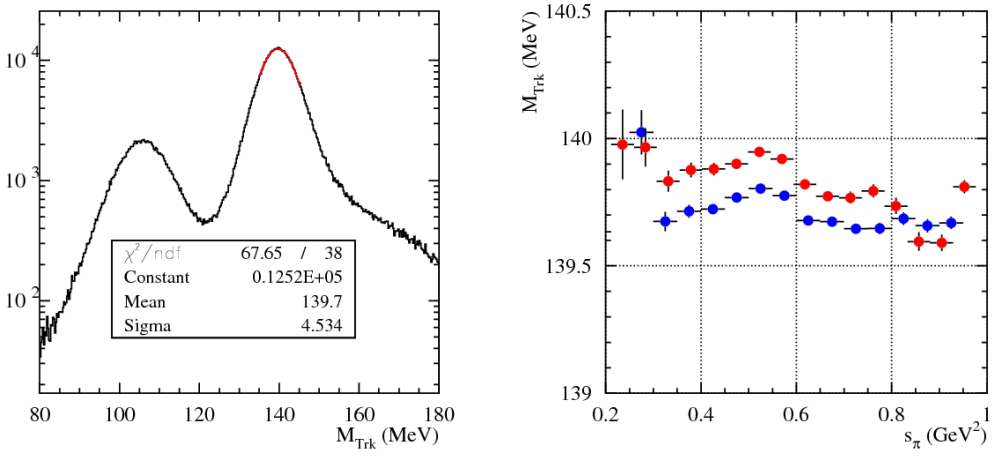

(a) (b)

Fig. 5.7: (a) Fit on the $\pi^+\pi^-\gamma$ peak of trackmass distribution inclusive in s_π. (b) The mean values of $M_{\rm trk}$ as found in the fit for different regions of s_π. The red circles represent the values without applying the calibration, the blue circles the mean values after the fine calibration procedure.

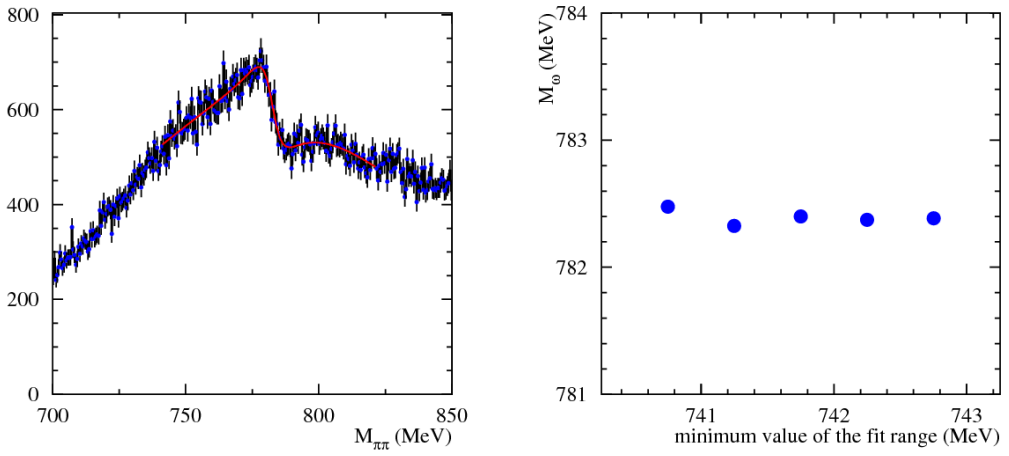

(a) (b)

Fig. 5.8: (a) Fit of two Breit-Wigner distributions to the mass spectrum of $\pi^+\pi^-\gamma$ events performed to extract the ω mass. In (b) the stability of the result changing the range of the fit is shown. On the x-axis the low edge of the fit range is reported.

5.1.2 Monte Carlo shifting and smearing

In the previous chapter the fine tracking calibration for data has been discussed. To optimize data-Monte Carlo agreement small corrections on the Monte Carlo momenta are applied as well. For 2001 the Monte Carlo samples (see Sec. 4.2.1, and [62]) a tuning procedure had been developed.[5] These corrections could be applied also for the 2002 sample (see Sec. 4.2.2 and [63],

[5] Detailed explanation on the procedure can be found within the Ph.D. thesis of B. Valeriani [107].

for the Small Angle analysis, and Sec. 4.3.1 and [114], for the Large Angle analysis). For the 2006 data sample, which is discussed here, a new Monte Carlo fine tuning procedure is however needed.
Signal, $\pi^+\pi^-\gamma$, and background, $\mu^+\mu^-\gamma$ and $\pi^+\pi^-\pi^0$ samples are corrected by shifting and smearing the track momenta. A check of the procedure is performed on the basis of the data-Monte Carlo agreement in trackmass distribution by looking at positions and widths of the trackmass peak. To cover the whole phase space range, the data-Monte Carlo comparison is performed for different values of s_π and polar angle, θ.
The *shift* is applied to each spatial component of momentum for each charge. The expression for the shifting is

$$p_i^{+,-} \to p_i^{+,-}/\zeta^{+,-}(\theta, \phi, s_\pi), \tag{5.3}$$

where

$$\zeta^{+,-}(\theta, \phi, s_\pi) = c_\theta^{+,-}(\theta) \cdot c_\phi^{+,-}(\phi) \cdot (1.001) \begin{cases} -(5.2\ s_\pi) \times 10^{-4} & \text{if } s_\pi < 0.6\ \text{GeV}^2 \\ -(5.8\ s_\pi) \times 10^{-4} & \text{if } s_\pi \geq 0.6\ \text{GeV}^2, \end{cases}$$

with

$$c_\theta^{+,-}(\theta) = (1. - 2.5 \times 10^{-5}) \cdot (1. - 0.25/|\vec{p}^{\,+,-}| \cdot \theta^{\,+,-}),$$

and

$$c_\phi^{+,-}(\phi) = (1. - 2.5 \times 10^{-5}) \cdot \begin{cases} 1 + (0.2 \times 10^{-6} \cdot \phi^2 + 0.25 \times 10^{-5}\phi - 0.25 \times 10^{-2})/(2. \cdot |\vec{p}^{\,+}|) \\ 1 - (0.2 \times 10^{-6} \cdot \phi^2 + 0.25 \times 10^{-5}\phi + 0.52 \times 10^{-2})/(2. \cdot |\vec{p}^{\,-}|), \end{cases}$$

where θ and ϕ are the polar and the azimuthal angle of the considered track in the LAB system. The trackmass mean values, $\bar{M}_{\rm trk}^{\pi\pi\gamma}$, obtained from the gaussian fit for the $\pi^+\pi^-\gamma$ peak as a function of the $\pi^+\pi^-$-system invariant mass are shown: in Fig. 5.9(a) the corrections have not been applied while in Fig. 5.9(b) the result after the procedure is shown. The red circles are referred to the data distribution and the black squares to the Monte Carlo ones. In the lower plots the fractional difference are reported. The data-Monte Carlo agreement is improved from 0.4% to 0.1%.
In Fig. 5.10(a) and Fig. 5.10(b) $\bar{M}_{\rm trk}$ as a function of the polar angle of positive and negative track, respectively, are shown. The fit is performed in the range $[135 - 145]$ MeV, around the $\pi^+\pi^-\gamma$ peak. Similar check has been done also for $\mu^+\mu^-\gamma$ and $\pi^+\pi^-\pi^0$ Monte Carlo samples. It is possible to appreciate the good data-Monte Carlo agreement, resulting in a discrepancy always below 0.3% in the whole phase space. Similar good agreement is also found for $\mu^+\mu^-\gamma$ and $\pi^+\pi^-\pi^0$ peaks.

The *smearing* procedure is applied to obtain better agreement in the trackmass widths, which have been found narrower for Monte Carlo than for data of ca. 15% (see Fig. 5.11(a)). Each component, i, of the momentum of the track ($p_i^\pm$) is smeared according to

$$p_i^{+,-} \to p_i^{+,-} \cdot smear^{+,-}$$

– if $s_\pi < 0.3\ \text{GeV}^2$

$$smear^{+,-} = \begin{cases} 1 - 0.005\ x & \text{for 1/20 of the events} \\ 1 - 0.0013\ x & \text{else} \end{cases}$$

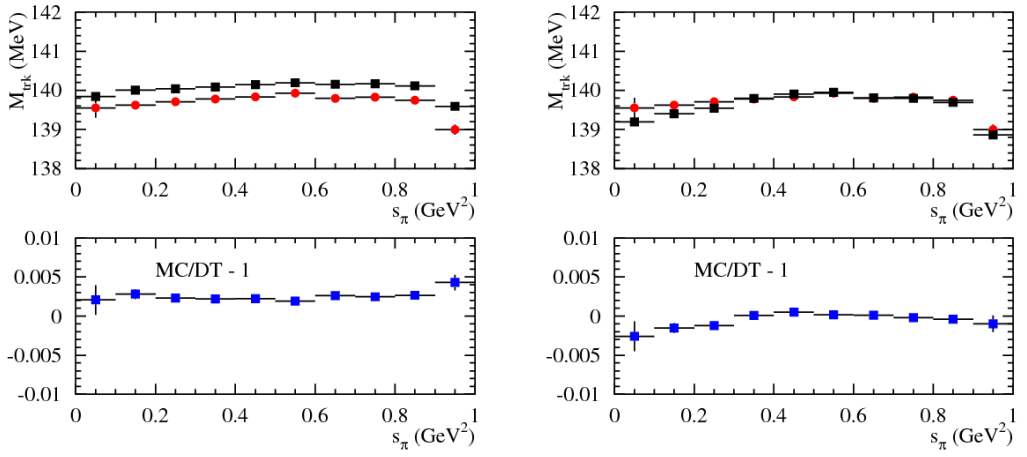

Fig. 5.9: Data-Monte Carlo agreement in trackmass value as a function of s_π for the $\pi^+\pi^-\gamma$ peak before and after the Monte Carlo fine corrections, in (a) and in (b) respectively. In the upper plots the mean value of the gaussian fits for different values of the hadron invariant mass are reported. In red circles, data and, in black squares, Monte Carlo are shown. In the lower plots the relative difference MC/DT − 1 is shown.

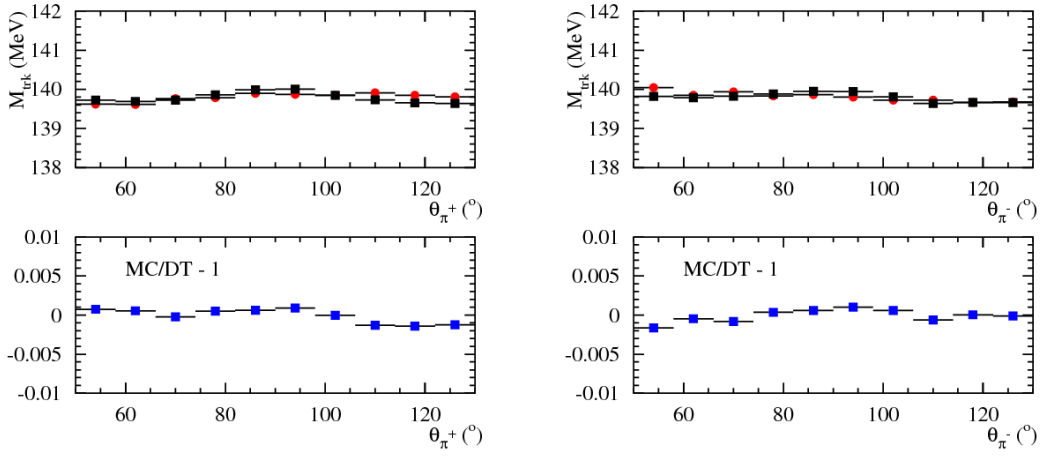

Fig. 5.10: Data-Monte Carlo agreement in trackmass mean value as a function of polar angle for positive (a) and negative (b) track. The upper plots report the mean value of the gaussian fits of the $\pi^+\pi^-\gamma$ peak for different values of $\theta_{\pi^\pm}$: red circles for data and black squares for Monte Carlo. In the lower plots the fractional difference MC/DT − 1 are shown.

– if $0.3 \leq s_\pi < 0.8$ GeV^2

$$smear^{+,-} = \begin{cases} 1 - 0.007\ x & \text{for 1/20 of the events} \\ 1 - 0.0018\ x & \text{else} \end{cases}$$

– if $s_\pi > 0.8$ GeV^2

$$smear^{+,-} = \begin{cases} 1 - 0.007\ x & \text{for 1/20 of the events} \\ 1 - 0.0023\ x & \text{else,} \end{cases}$$

where x is a random Gaussian distributed variable with mean 0 and sigma 1.

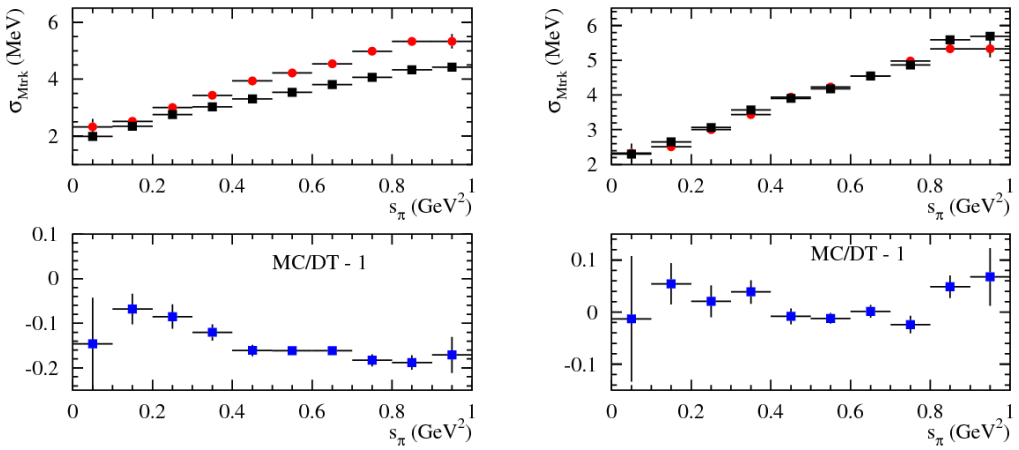

Fig. 5.11: Data-Monte Carlo agreement in trackmass widths as a function of s_π for $\pi^+\pi^-\gamma$ peak before, in (a), and after, in (b), the smearing procedure. In the upper plots the widths of the gaussian fits for different values of the hadron invariant mass are shown: in red circles for data and in black squares for Monte Carlo. In the lower plots the fractional difference MC/DT – 1 is reported. Note the different scale of the left and of the right plots.

In Fig. 5.11(a) the data-Monte Carlo comparison of the $\pi^+\pi^-\gamma$ peak widths as a function of s_π before the smearing procedure is shown, and in Fig. 5.11(b) the data-Monte Carlo comparison after the smearing. For the peaks and the widths evaluation, all the Monte Carlo samples are included, properly corrected and normalized to the data integrated luminosity. The agreement at the level of 5%, and compatible with zero within the errors in the whole energy range, guarantees low systematic uncertainty concerning the $M_{\rm trk}$ selection cuts (see Sec. 5.3.2), and also an improved precision for the background subtraction fit procedure (see Sec. 5.4).

5.2 Signal selection

The event selection requires two charged tracks with opposite curvatures at large polar angle ($50° < \theta_\pi < 130°$), and at least one photon detected in the barrel of the electromagnetic calorimeter ($50° < \theta_\gamma < 130°$). In the analysis a photon is defined as a cluster in the EMC not associated to any tracks satisfying:

$$(T_{\rm clu} - L/c) < 3 \text{ ns},$$

where $T_{\rm clu}$ is the time of the cluster, and L is the position of the centroid of the energy release in the EMC, i.e. the flying path of the particles coming from the IP. A particle ID method [106]

together with further kinematic cuts, i.e. $M_{\rm trk}$ and Ω-angle, are used to reject $\mu^+\mu^-\gamma$, $e^+e^-\gamma$ and $\pi^+\pi^-\pi^0$ events. Residual background is then subtracted using a sophisticated fit procedure, which will be described in Sec. 5.4.
The signal is selected according to:

- the event has to satisfy the *calorimeter trigger*, see Sec. 3.2.3, i.e. at least two trigger sectors should have been fired in the barrel;
- the event has to pass the *offline reconstruction filter*. The purpose of this filter is to identify background events on the base of the calorimeter cluster reconstruction before they enter the pattern recognition and tracking fit algorithms, cutting out cosmic rays, machine background and Bhabha events at small polar angles from machine background;[6]
- both of the tracks of the event have to fulfill the following requirements:
  * the radial position of the *first hit* in the drift chamber, $\rho_{\rm FH}$, has to be within 50 cm from the beam line;
  * the extrapolated point of closest approach of the track to the interaction point has to have $\rho_{\rm PCA} = \sqrt{x^2_{\rm PCA} + y^2_{\rm PCA}} < 8$ cm and $|z_{\rm PCA}| < 12$ cm. This cut is useful to clean the sample from for machine background;
  * to reject tracks spiralizing in the drift chamber, cuts on transverse and longitudinal momentum components are applied: $|p_T| > 160$ MeV or $|p_z| > 90$ MeV;
  * a cut on module of the track momentum, $|\vec{p}| > 200$ MeV, is also applied;
- a pre-filter, called `ppgtag` (for more details see [117]), which consists of cuts in the plane $\Delta E_{\rm miss}$ vs. $M_{\rm trk}$.[7] The cut on missing energy is -220 MeV $< \Delta E_{\rm miss} < 120$ MeV and the cut on trackmass is 80 MeV $< M_{\rm trk} < 400$ MeV. More than 90% of $\pi^+\pi^-\pi^0$ events are rejected by this pre-filter.
- The cuts in acceptance are
$$50^\circ < \theta_\pi < 130^\circ,$$
for both of the tracks, and at least one photon with
$$50^\circ < \theta_\gamma < 130^\circ,$$
and energy $E_\gamma > 20$ MeV has to be present in the event. A cut on the invariant mass of the hadron system is also applied, requiring $s_\pi < 0.85$ GeV^2, to reject collinear events $e^+e^- \to \pi^+(\mu^+)\pi^-(\mu^-)$. The cuts on track and on photon polar angles represent the *Large Angle acceptance* cuts.

In Fig. 5.12 the spectrum is shown after having applied the previously mentioned acceptance cuts.

[6] Bhabha events with electrons and positrons emitted at large polar angles are retained for measuring the integrated luminosity

[7] Where $\Delta E_{\rm miss} = \sqrt{E^2_{\rm miss} - |\vec{P}^2_{\rm miss}|}$, with $E_{\rm miss} = \sqrt{s} - \sqrt{|\vec{p}_{\pi^+}|^2 + m^2_{\pi^\pm}} - \sqrt{|\vec{p}_{\pi^-}|^2 + m^2_{\pi^\pm}}$ and $|\vec{P}_{\rm miss}|^2 = |\vec{p}_b - \vec{p}_{\pi^+} - \vec{p}_{\pi^-}|^2$.

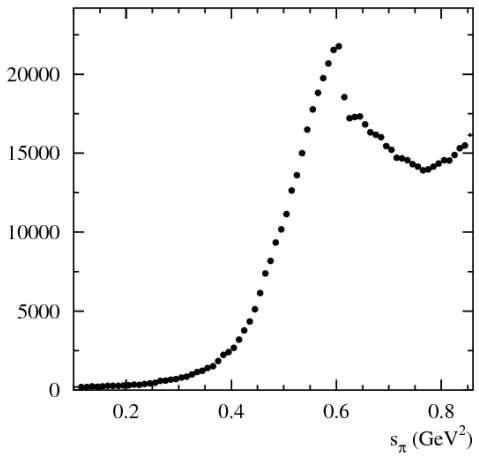

Fig. 5.12: Spectrum of the data sample after the signal selection and before the residual background subtraction

5.3 Background rejection

Main background sources are due to $\mu^+\mu^-\gamma$, $e^+e^-\gamma$ and $\pi^+\pi^-\pi^0$ events. Reducing the $\sqrt{s}$ from m_ϕ (on-peak data sample) down to 1 GeV (off-peak data) strongly reduces the cross section for the $\phi \to \pi^+\pi^-\pi^0$ process of about 95% [118]. The major efforts are thus devoted to the rejection of $\mu^+\mu^-\gamma$ and $e^+e^-\gamma$ events.

5.3.1 Particle identification

A $\pi - e$ *particle identification* (*PID*) method based on a likelihood estimator using information of value, position and time of the energy release in the electromagnetic calorimeter is applied. The likelihood function used is the same as the one applied in the Small Angle analysis, see Sec. 4.2, and for the Large Angle analysis with 2002 data; see Sec. 4.3 and [106, 107] for more details. In the analysis at least one track has to be recognized as a pion – in the following this requirement will be called "`or`-configuration" of the $\pi - e$ PID likelihood. In Fig. 5.13(a) the $Log\mathcal{L}$ distribution of the positive vs. negative track is shown, events inside the red square on the lower left, corresponding to $Log\mathcal{L}_+ < 0$ and $Log\mathcal{L}_- < 0$ (i.e. both of the tracks identified as electrons), are rejected. The signal loss caused by this cut is lower than 1% for s_π below 0.4 GeV^2, and negligible at higher energies. The rejection power for $e^+e^-\gamma$ events is bigger than 95% for $s_\pi > 0.5$ GeV^2 and of about 85% for lower $s_\pi$values.

5.3.2 Trackmass

The *trackmass* variable is used to reject $\mu^+\mu^-\gamma$ and $\pi^+\pi^-\pi^0$ events. This variable, $M_{\rm trk}$, is obtained by imposing the four-momentum conservation on events with two charged particles, having the same mass, and one photon ($e^+e^- \to x^+x^-\gamma$) via the relation

$$(\sqrt{W} - \sqrt{|\vec{p}_+|^2 + M_{\rm trk}} - \sqrt{|\vec{p}_-|^2 + M_{\rm trk}})^2 - |\vec{p}_+ + \vec{p}_-|^2 = 0, \qquad (5.4)$$

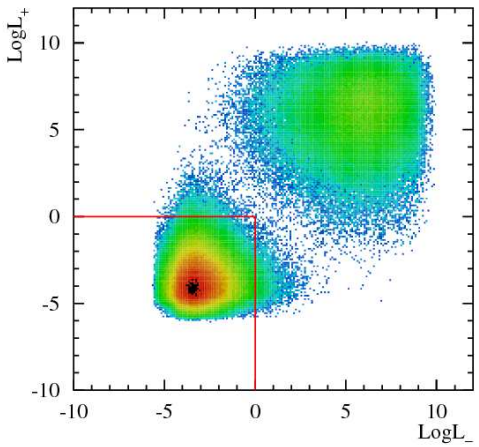

Fig. 5.13: Distribution of $Log\mathcal{L}$ of the positive vs. the negative tracks. Events inside the red square, corresponding to $Log\mathcal{L}_+ < 0$ and $Log\mathcal{L}_- < 0$, are rejected in the analysis. These events are predominantly Bhabha events.

where W is the energy squared of the colliding bunches including the boost provided to the beams in the LAB system. The trackmass variable peaks at m_π for $\pi^+\pi^-\gamma$ and at m_μ for $\mu^+\mu^-\gamma$ events; for $\pi^+\pi^-\pi^0$ events a broader distribution is found which peaks at ca. 180 MeV. Because of the reduced $\sqrt{s}$ and of the `ppgtag` pre-filter the $\pi^+\pi^-\pi^0$ yield is almost negligible. Indeed its trackmass peak is not visible under the radiative tail of the $\pi^+\pi^-\gamma$ events, see Fig. 5.14(a).[8]
In Fig. 5.14(b) the data distribution of $M_{\rm trk}$ vs. s_π is shown. The events have passed the Large Angle acceptance and the `ppgtag` pre-filter, which causes the "arch" edge at the higher left part of the scatter plots. The red lines represent the analysis cuts. The lower cut

$$M_{\rm trk} > 120 \text{ MeV},$$

is applied to reject $\mu^+\mu^-\gamma$ events, which get the maximun yield below this line, see Fig. 5.15(b). To reject the residual $\pi^+\pi^-\pi^0$ events, the following cuts are applied:

$$M_{\rm trk} < 200 \text{ MeV},$$

and

$$M_{\rm trk} < \left(150 + 4s_\pi^2\,(1+s_\pi^2) \times 10^{-4}\right) \text{ MeV}. \tag{5.5}$$

Fig. 5.15(c) shows how $\pi^+\pi^-\pi^0$ events are situated above the $M_{\rm trk}(s_\pi)$ cut. For the events in Fig. 5.15, neither the `ppgtag` pre-filter nor Large Angle acceptance have been applied.
Depending on s_π the trackmass cut rejects $\mu^+\mu^-\gamma$ events by 80% - 90%, see Fig. 5.16(b). $\pi^+\pi^-\pi^0$ events, which have passed the `ppgtag` pre-filter, are further reduced by about 50%, see Fig. 5.16(c). The effect of the cuts on signal $\pi^+\pi^-\gamma$ is visible in Fig. 5.16(a): signal events are rejected by less than 1%.

[8] The trackmass radiative tail is due to events with more than one radiated photon, namely $e^+e^- \to x^+x^-\gamma(\gamma)$

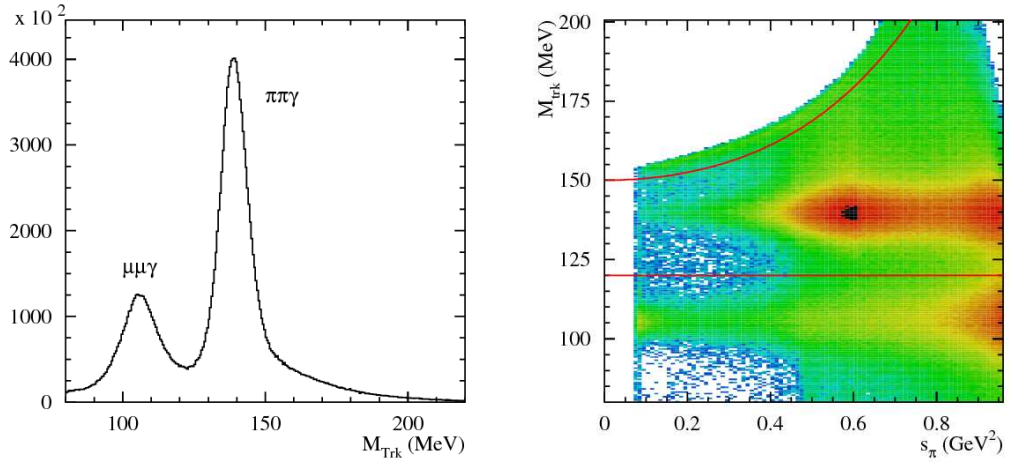

Fig. 5.14: Trackmass distribution for data sample after Large Angle acceptance cut and `ppgtag` filter: (a) inclusive in the two pions invariant mass and (b) $M_{\rm trk}$ vs. s_π. Is possible to see the $\pi^+\pi^-\gamma$ and $\mu^+\mu^-\gamma$ peaks, while the very small $\pi^+\pi^-\pi^0$ contribution is hidden under the $\pi^+\pi^-\gamma$ radiative tail, on the right of the m_π-peak. The red lines represent the cuts applied: regions outside the area shown are rejected.

Systematics on trackmass cut

The systematic uncertainties due to trackmass enters essentially in two points of the analysis, namely: (*i*) in the estimation procedure (it will be described in Sec. 5.4) and (*ii*) in the signal selection cut.
To evaluate the systematic uncertainty of the trackmass cut a data-Monte Carlo *double ratio* check is applied.[9] It consist in

- shifting each single cut (*shifted cut*) with respect to the value used in the analysis (*standard cut*), leaving unchanged all the others. The shift is about 1σ of the resolution of the variable in which the cut is applied;
- running the full selection procedure on data, and the Monte Carlo $\pi^+\pi^-\gamma$, $\mu^+\mu^-\gamma$, $e^+e^-\gamma$ and $\pi^+\pi^-\pi^0$ samples;
- subtracting the residual background events from the data sample, according to the background subtraction procedure, explained in Sec. 5.4, and build the ratio between data and $\pi^+\pi^-\gamma$ Monte Carlo in the shifted cut over the standard cut conditions;
- performing the double ratio of the spectra, data over $\pi^+\pi^-\gamma$ Monte Carlo

$$R_{\rm cut}(s_\pi) = \frac{(dN^{\rm data}/dN^{\rm MC})|_{\rm shifted\ cut}}{(dN^{\rm data}/dN^{\rm MC})|_{\rm standard\ cut}}(s_\pi), \tag{5.6}$$

  where $dN^{\rm data,MC}$ is the number of events binned in s_π and $dN^{\rm data}$ is the background subtracted event yield.

[9] This approach will be used also to estimate the systematic errors of the other selection cuts.

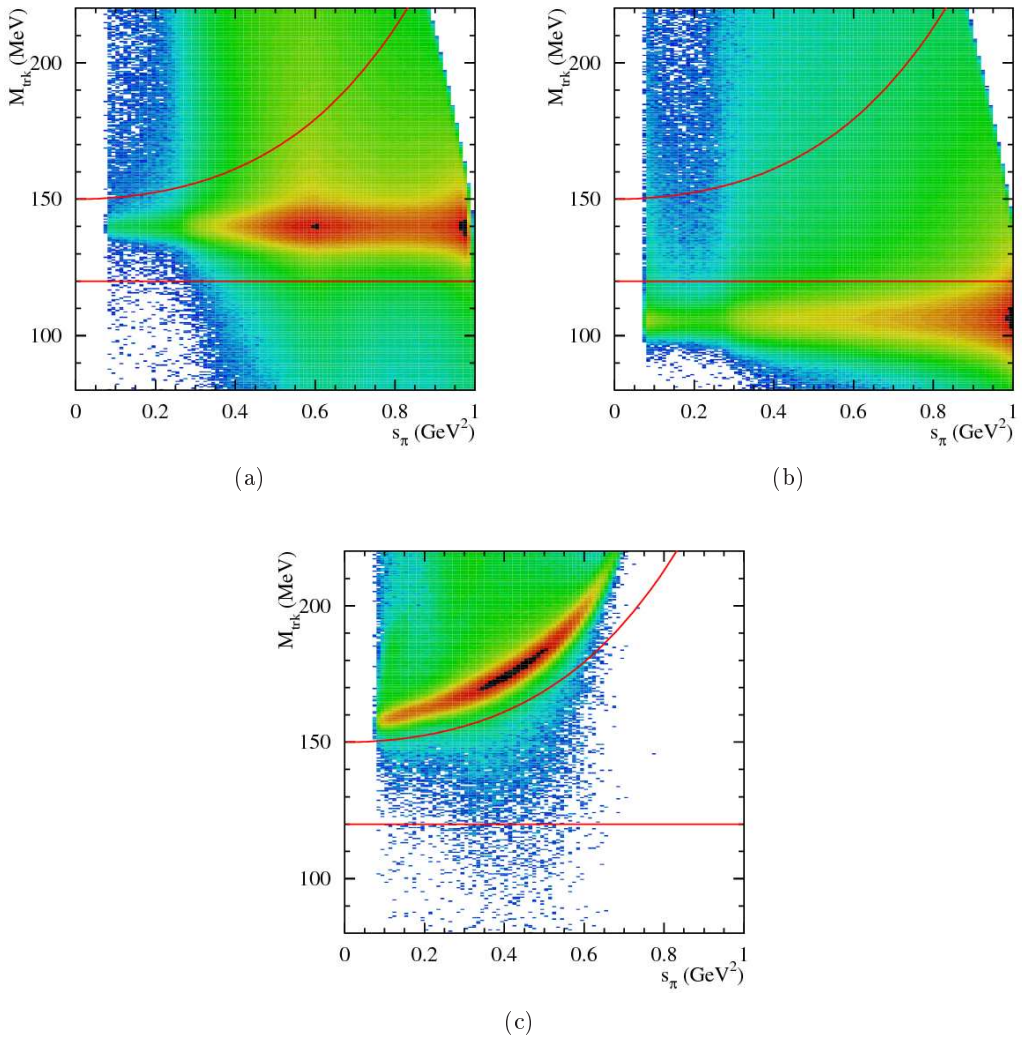

Fig. 5.15: Monte Carlo Trackmass distributions inclusive in acceptance and without any cuts applied. The plots are in logarithmic scale on the entries(z-) axis. (a) Monte Carlo $\pi^+\pi^-\gamma$, (b) Monte Carlo $\mu^+\mu^-\gamma$ and (c) Monte Carlo $\pi^+\pi^-\pi^0$.

By means of this double ratio it is possible to check both the changing of the spectrum caused by modifying a specific selection cut and, at the same time, the data-Monte Carlo agreement in that cut.

In Fig. 5.17(a) the resolution of the trackmass variable is shown, obtained from the difference between the generated and the reconstructed value using Monte Carlo $\pi^+\pi^-\gamma$ sample. In the reconstructed quantities the smearing and the shifting of momenta, described in Sec. 5.1.2, have been applied. The distribution is fitted with two Gaussian functions, shown in red. The first Gaussian fit has a standard deviation $\sigma \simeq 3$ MeV, which is taken as the resolution of the trackmass variable, since the other Gaussian function is needed for a small fraction of events.

First a shift of ± 3.5 MeV is applied to the upper trackmass cut, while the lower is leaved

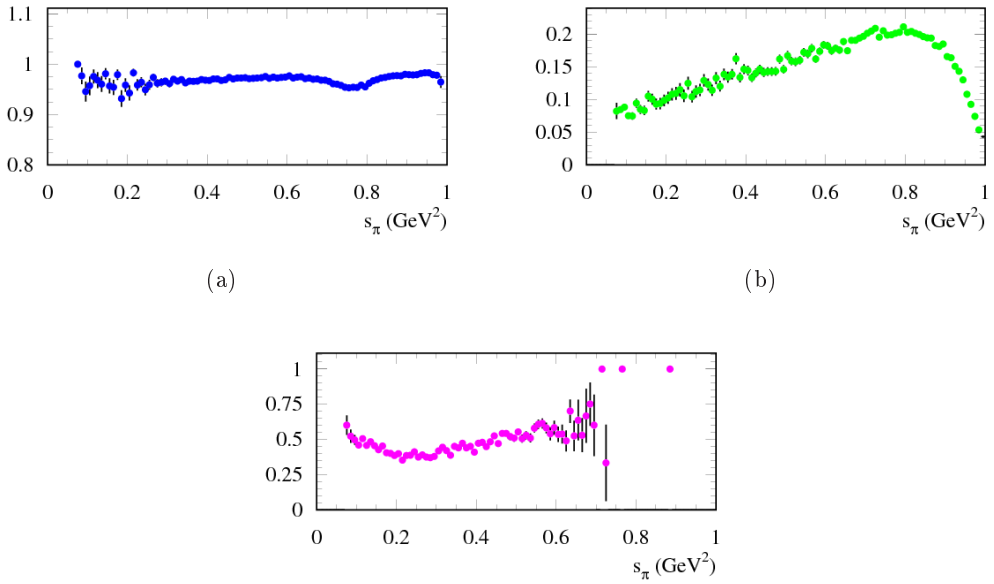

Fig. 5.16: In (a), effect of the trackmass cut on $\pi^+\pi^-\gamma$ events is shown. (b) depicts the percentage of $\mu^+\mu^-\gamma$ events surviving the cut and in (c) the percentage referred to $\pi^+\pi^-\pi^0$ events is presented. About 1×10^7 Monte Carlo events have been used to evaluate the ratios.

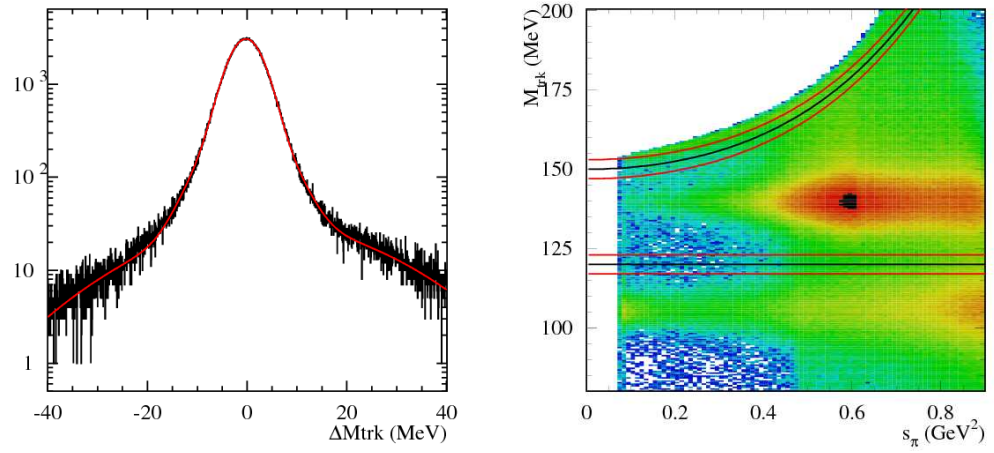

Fig. 5.17: In (a), the resolution of trackmass variable, estimated as the difference between the reconstructed and the "true" values of the $\pi^+\pi^-\gamma$ Monte Carlo sample, is shown. The reconstructed quantities take into account the tuning and the smearing procedure described in Sec. 5.1.2. In (b), the $M_{\rm trk}$ vs. s_π distribution from data is shown. The black lines describe the standard analysis cuts, while the red ones the shifted cuts applied to estimate the systematic error.

unchanged. After that the lower cut is shifted while the upper cut is untouched.[10] In Fig. 5.17(b) the standard cuts, described by the black curves, and the shifted ones, in red, are shown on the data distribution of $M_{\rm trk}$ vs. s_π.
The results of the double ratios are shown in Fig. 5.18(a) and in Fig. 5.18(b), for the upper cuts and to the lower cut shifted, respectively. The discrepancies from 1 are very small, suggesting a small systematic uncertainty, especially in the region between 0.4 and 0.8 GeV^2. To take into account the no constant behaviour of the double ratio in s_π, a fit with a third order polynomial functions is performed for each ratio, represented by the red lines.

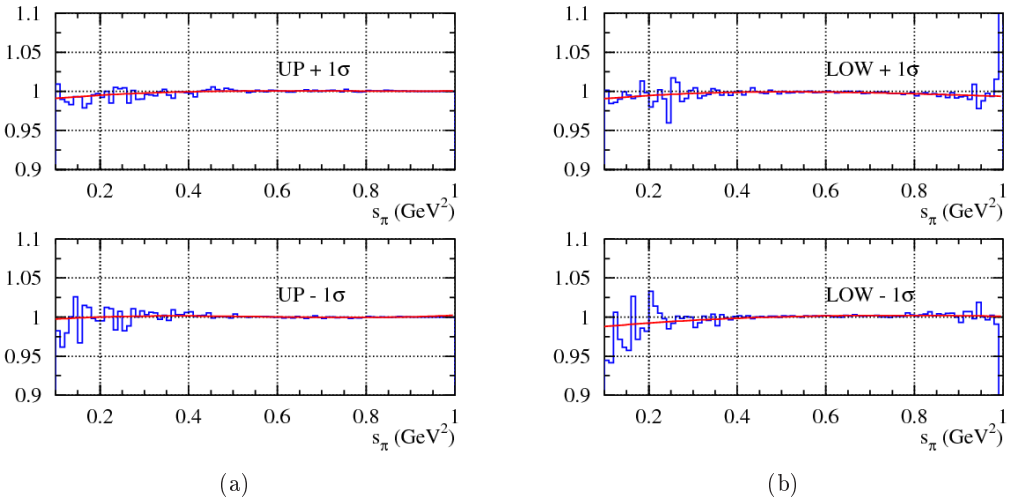

Fig. 5.18: Double ratio results for shifting the upper, (a), and the lower trackmass cut, (b). The red curves represents the third power functions used to fit the double ratios.

As systematic error associated to the trackmass cut the maximum deviation from 1 of the four fitting functions, which are used to fit the double ratios, is taken, see Fig. 5.19. The error reaches up to ca. 1% close to the $2m_\pi$-threshold and decreases down to 0.1% on the ρ-peak.
The uncertainty is very small thanks to: (*i*) the good data-Monte Carlo agreement, obtained after the fine calibration and tuning of track parameters, see Sec. 5.1.1 and Sec. 5.1.2; and (*ii*) the relatively loos cuts are applied in the analysis. Cutting far away from steep slopes in the variable shapes, where the variation of the spectrum is smooth over the variable interval, allows to get small systematic uncertainty, cutting on that specific variable.

5.3.3 Ω-angle

For ISR events with one photon, which represent the dominant part of the ISR spectrum, the emitted photon and the missing momentum of the track have the same direction. Exploiting this information, together with the photon detection, it is possible to reject background from

[10] As described above the trackmass cuts correspond to

upper : $M_{\rm trk} < \left(150 + 4s_\pi^2\,(1+s_\pi^2) \times 10^{-4}\right)$ MeV and $M_{\rm trk} < 200$ MeV;

lower : $M_{\rm trk} > 120$ MeV.

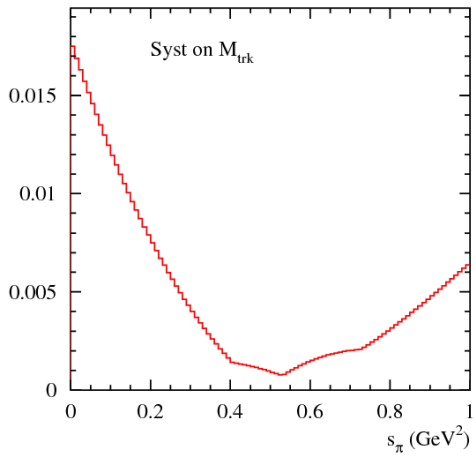

Fig. 5.19: Maximum deviation from one among the four fitting functions shown in Fig. 5.18(a) and Fig. 5.18(b).

$\pi^+\pi^-\pi^0$ events, for which the direction of the photons produced by the π^0 decay is uniformly distributed.
The Ω-*angle* is defined as the angle between the track missing momentum and the momenta of the detected photon. In the case of more than one photon presented in the event, all the combinatorial combinations are built and the smallest value of Ω-angle is chosen:

$$\Omega = \min(\Omega_i)$$

$$\Omega_i = \text{acos}\left(\frac{\vec{p}_{\text{miss}} \cdot \vec{p}_{\gamma,i}}{|\vec{p}_{\text{miss}}||\vec{p}_{\gamma,i}|}\right), \tag{5.7}$$

where $\vec{p}_{\text{miss}}$ stands for the track missing momentum and $\vec{p}_{\gamma,i}$ is the momentum of the i^{th} photon. The Ω-angle distribution peaks at zero for signal events while it is off-zero for events with higher photon multiplicity, as can be seen in Fig. 5.20 for $\pi^+\pi^-\gamma$ and $\pi^+\pi^-\pi^0$ Monte Carlo samples. The plot shows events normalized to the same integrated luminosity after the Large Angle acceptance cuts and `ppgtag` pre-filter.
The spread of the $\pi^+\pi^-\gamma$ peak is not only due to resolution, but mainly to the NLO events. Since at high values of s_π the amount of NLO-ISR processes are comparable with respect to the LO events, a s_π-dependent cut is applied (see Fig. 5.21(a))

$$\Omega < (5 + e^{6.5 s_\pi})^\circ, \tag{5.8}$$

to preserve signal events at large values of s_π. A further cut on the fixed value of $\Omega < 90^\circ$ is imposed.
The inefficiency of the cut imposed on signal events is negligible, as can be seen in Fig. 5.22(a). The drop at $s_\pi > 0.9$ GeV^2 is due to the rejection of NLO-ISR and NLO-FSR events, see Fig. 4.2, whose amount increases at high energy.[11] In Fig. 5.22(b) the percentage of $\pi^+\pi^-\pi^0$ events which survive the Ω-angle cut (after passing the `ppgtag` pre-filter and trackmass cuts) is shown. The

[11] This region is however out of the energy range of our measurement.

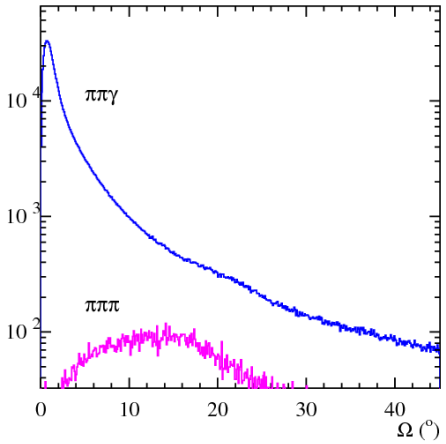

Fig. 5.20: Distributions of the Ω-angle for $\pi^+\pi^-\gamma$ blue histogram, and $\pi^+\pi^-\pi^0$ pink histogram, from Monte Carlo samples. The events shown have passed the `ppgtag` pre-filter and Large Angle acceptance cuts. They are inclusive in s_π and normalized to the same integrated luminosity. The signal is peaked at small values of Ω-angle, while background events from $\pi^+\pi^-\pi^0$ are situated at higher value.

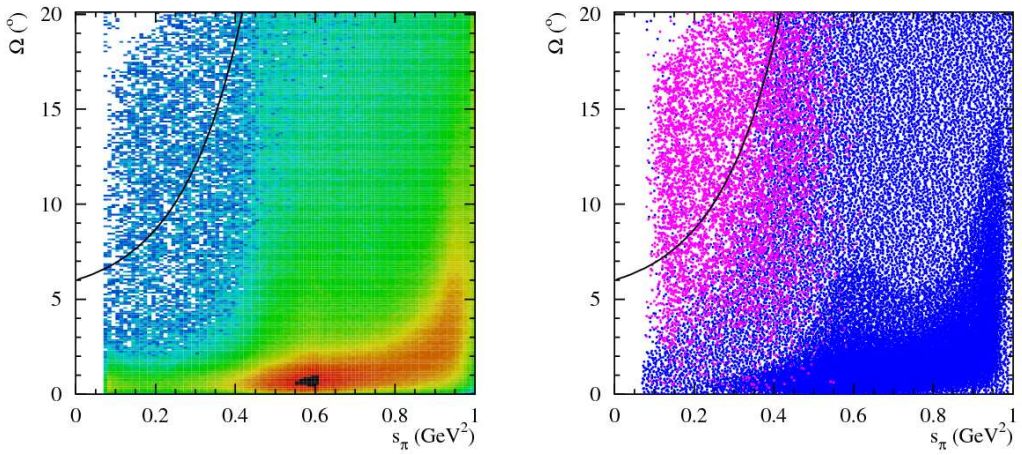

Fig. 5.21: Ω-angle distribution for the data sample, in (a), and for $\pi^+\pi^-\gamma$ (blue dots) and $\pi^+\pi^-\pi^0$ (pink dots) Monte Carlo samples, in (b), after Large Angle acceptance cut and the `ppgtag` pre-filter. The events are normalized to the integrated luminosity of the data sample. The spreading for the signal events at high s_π due to NLO-ISR processes is visible. The black line represents the cut applied, see Eq. 5.8.

rejection power on $\pi^+\pi^-\pi^0$ goes from ca. 75%, for low energy, down to 0.15%, at $s_\pi \simeq 0.6$ GeV^2. Above 0.65 GeV^2 the $\pi^+\pi^-\pi^0$ contamination is negligible.

The Ω-angle can not distinguish among different kind of ISR processes, thus it does not help in further rejecting $\mu^+\mu^-\gamma$ or $e^+e^-\gamma$ events.

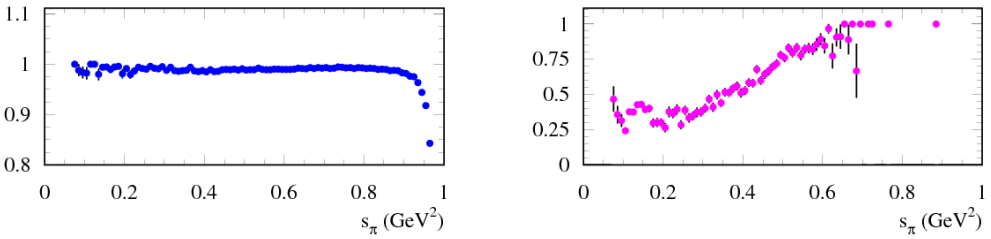

(a) (b)

Fig. 5.22: (a) Efficiency of Ω-angle for $\pi^+\pi^-\gamma$ events; (b), percentage of residual $\pi^+\pi^-\pi^0$ events surviving the cut. The ratios have been evaluated using 1×10^7 Monte Carlo events.

Systematics on Ω-angle cut

The same "double ratio approach" used for $M_{\rm trk}$, see Sec. 5.3.2 and Eq. 5.6, is applied to evaluate the systematic uncertainty on the Ω-angle cut.
To take into account the broadening of the Ω-angle distribution with the increasing of the energy, see Fig. 5.21, the root mean square as a function of s_π has been evaluated, $rms(s_\pi)$. Thus, to obtain $(dN^{\rm data}/dN^{\rm MC})|_{\rm shifted\ cut}$, the standard cut in Ω-angle is moved of $\pm rms(s_\pi)$. In Fig. 5.23 the blue circles represent the values of the rms evaluated in slices of s_π. The red line shows a linear fit.

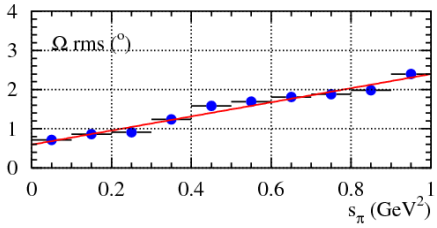

Fig. 5.23: The values of the Ω-angle rms evaluated in slices of s_π are shown, together with the linear fit, in red.

Fig. 5.24 shows the Ω-angle vs. s_π distribution for data. Superimposed to the spectrum, in black, the standard cut applied in the analysis, see Eq. 5.8, and, in red, the cut shifted by $+rms(s_\pi)$ and $-rms(s_\pi)$ are drawn.
The double ratio results are shown in Fig. 5.25: in the upper plot the shifting of the standard Ω-angle cut by $+rms(s_\pi)$ and the lower plot by $-rms(s_\pi)$. The shifts affect the spectrum only below 0.4 GeV^2, while at higher energy the deviation from 1 is negligible. The low statistics, denoted by the scattering of the histograms, also plays a role at the low energy values, however a small trend in the ratios is visible. To consider that, a third power polynomial function fit is applied, indicated by the red lines, from the threshold up to 0.4 GeV^2, while above that energy a linear fit is used. The maximum deviation from 1 between the two fitting functions is taken as the systematic error, see Fig. 5.26. The systematic uncertainty is negligible above 0.4 GeV^2 and it reaches ca. 2% at the $2m_\pi$-threshold. Thanks to the good data-Monte Carlo agreement and to

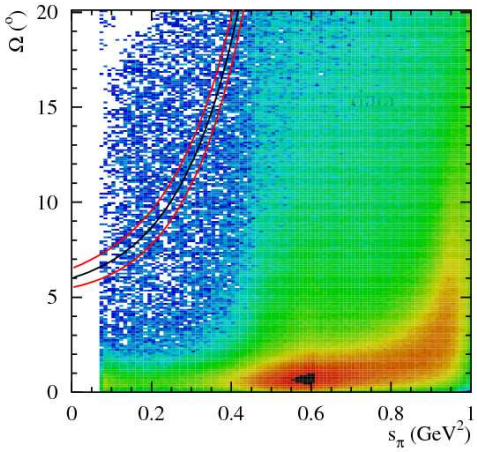

Fig. 5.24: The Ω-angle vs. s_π distribution for data sample is shown. The black line represents the standard cut applied in the analysis, see Eq. 5.8, and the red ones the standard cut shifted by $\pm rms(s_\pi)$.

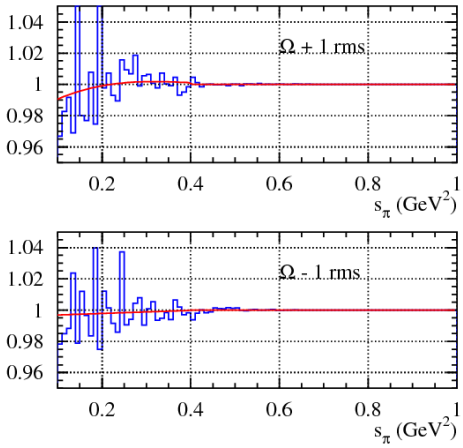

Fig. 5.25: Double ratio results shifting the Ω-angle cut by adding, in the upper plot, or subtracting, in the lower one, 1 $rms(s_\pi)$.

the little $\pi^+\pi^-\pi^0$ contamination in the off-peak data, it is possible to keep small the uncertainty due to the Ω-angle cut. The almost $\pi^+\pi^-\pi^0$ free data sample permits to apply a much looser cut in the Ω-angle with respect to the one applied for 2002 on-peak data. This avoids a considerable signal lost (which is an issue at the $\pi^+\pi^-$-threshold) and allows to apply the cut only in a region where the tails of the signal distributions are smooth.

5.4 Residual background subtraction

After the selection cuts, the main background sources are

– $e^+e^- \to \mu^+\mu^-\gamma(\gamma)$

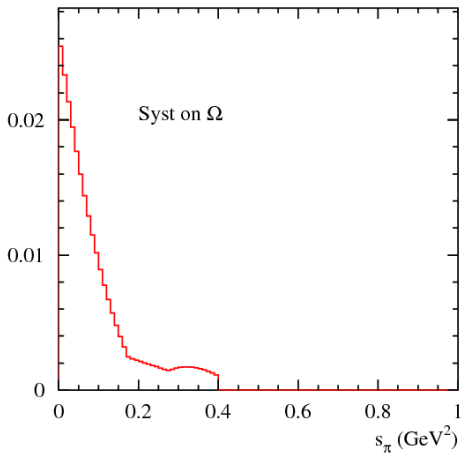

Fig. 5.26: Double ratio results for shift in upper, (a), and in lower trackmass cut, (b). In (c) the maximum deviation is shown.

- $e^+e^- \to \pi^+\pi^-\pi^0$
- $e^+e^- \to e^+e^-\gamma(\gamma)$

Their combined $M_{\rm trk}$ shapes from Monte Carlo in slices of s_π together with the signal one are fitted to the data $M_{\rm trk}$ shape, to estimate their relative contributions. The weights, $w_{ch}(j)$, are used as free normalization parameters in the fit, for each channel ch in each $j^{\rm th}$ slice in s_π. The fit procedure follows the method described in [120], using the `HBOOK` [121] routine `HMCMLL` with small modifications (see [122, 123]).
The main difference with respect to [120] is that all the three background processes are treated simultaneously in the same fitting procedure. This is possible thanks to the increased Monte Carlo statistics which allows to enlarge the fitting range up to $180-220$ MeV in the $M_{\rm trk}$ variable. So one can include the full peak of the $\pi^+\pi^-\gamma$ events in $M_{\rm trk}$.
The following Monte Carlo samples are used in the fitting procedure:

- 1400 pb^{-1} of $\pi\pi\gamma(\gamma)$ events, with both ISR and FSR at NLO;
- 1400 pb^{-1} of $\mu\mu\gamma(\gamma)$ events, with both ISR and FSR at NLO;
- 225 pb^{-1} of $\pi^+\pi^-\pi^0$ events.

$e^+e^-\gamma$ events are obtained directly from data, asking for both of the tracks to be recognized as electrons (the area delimited by the red square in Fig. 5.13). In the following this will be called "`nor`-configuration" of the $\pi - e$ PID.
Monte Carlo distributions are adjusted using the corrections described in Sec. 5.1.2 to give better agreement to data.
The fit is performed after the data sample has been corrected for the `FILFO` efficiency, see Sec. 6.1.1. To increase the sensitivity, the fit is performed without the cuts in $M_{\rm trk}$, shown in Fig. 5.14. This allows to include the full peak of $\mu^+\mu^-\gamma$, around 110 MeV, and to be more inclusive in $\pi^+\pi^-\pi^0$ events. All the other selection cuts are applied.

The fit procedure is performed in two steps. The first one is dedicated to obtain the $e^+e^-\gamma$ background contamination, evaluating $w_{ee\gamma}$, while in the second one $w_{\mu\mu\gamma}$ and $w_{\pi\pi\pi}$ are determined.

Step A. $e^+e^-\gamma$ contribution

The fit is performed for 23 slices in s_π (each slice of 0.04 GeV^2) between 0.08 and 1.0 GeV^2. In the standard analysis at least one track has to be identified as a pion:

"`or`" of the $\pi - e$ PID likelihood
$$Log\mathcal{L}_+ > 0 \ \cup \ Log\mathcal{L}_- > 0$$

According to this requirement, the background due to $e^+e^-\gamma$ channel corresponds to those events where one track is recognized as an electron and the other as a pion:

"`xor`" of the $\pi - e$ PID likelihood
$$(Log\mathcal{L}_+ < 0 \ \cap \ Log\mathcal{L}_- > 0) \ \cup \ (Log\mathcal{L}_+ > 0 \ \cap \ Log\mathcal{L}_- < 0)$$

Requiring the `xor`-configuration in the data sample gives higher sensitivity to $e^+e^-\gamma$ events, because it reduces the amount of the other channels and leaves the number of radiative Bhabha unchanged.[12] As already said, radiative Bhabha are selected directly from data events, applying the `nor`-configuration of the $\pi - e$ likelihood function, while for the Monte Carlo samples no PID requirement is applied. Thus fitting $e^+e^-\gamma$, $\pi^+\pi^-\gamma$, $\mu^+\mu^-\gamma$ and $\pi^+\pi^-\pi^0$ trackmass shapes to the data one provides precise estimation of $e^+e^-\gamma$ amount and, consequently, of $w_{ee\gamma}(j)$. The other channels are included, at this step, only to contribute to the overall shape of $M_{\rm trk}$, and the obtained weights relative to $\mu^+\mu^-\gamma$ and $\pi^+\pi^-\pi^0$ are not considered further in the analysis. Their correct values will be evaluated in the step B of the background fit procedure, which will be explained in the following.
Some technical details on the fitting procedure:

1. s_π in $[(0. - 0.36)$ GeV$^2]$: bin-width of 5.0 MeV in $M_{\rm trk}$
   - $s_\pi > 0.08$ GeV^2 $\pi^+\pi^-\gamma$, $\mu^+\mu^-\gamma$ and $\pi^+\pi^-\pi^0$ Monte Carlo samples and $e^+e^-\gamma$ events fitted to data;
2. s_π in $[(0.4 - 0.56)$ GeV$^2]$: bin-width of 2.5 MeV in $M_{\rm trk}$
   - $\pi^+\pi^-\gamma$, $\mu^+\mu^-\gamma$ and $\pi^+\pi^-\pi^0$ Monte Carlo samples and $e^+e^-\gamma$ events fitted to data;
3. s_π in $[(0.60 - 1.)$ GeV$^2]$: bin-width of 1. MeV in $M_{\rm trk}$
   - $s_\pi < 0.64$ GeV^2 $\pi^+\pi^-\gamma$, $\mu^+\mu^-\gamma$ and $\pi^+\pi^-\pi^0$ Monte Carlo samples and $e^+e^-\gamma$ events fitted to data;
   - $s_\pi > 0.68$ GeV^2 $\pi^+\pi^-\gamma$ and $\mu^+\mu^-\gamma$ Monte Carlo samples and $e^+e^-\gamma$ events fitted to data.

The $\pi^+\pi^-\pi^0$ contribution in $M_{\rm trk}$ vanishes above 0.65 GeV^2, therefore above this value the fit is performed for only 3 sources. The result on the $e^+e^-\gamma$ weights will be shown in Tab. 5.2, together with the weights relative to $\mu^+\mu^-\gamma$ and $\pi^+\pi^-\pi^0$.

[12] A check on the equivalence between ($e^+e^-\gamma$ | `xor`) and ($e^+e^-\gamma$ | `or`) has been done applying the two PID requests to the Bhabha Monte Carlo sample, proving this assumption.

Step B. $\mu^+\mu^-\gamma$ and $\pi^+\pi^-\pi^0$ contributions

The fit is performed for 22 slices in s_π (each slice of 0.04 GeV^2) between 0.12 and 1. GeV^2. As in the step A, all the selection cuts except for the cuts in trackmass are applied to the data sample. Differently from the procedure in step A, the `or`-configuration of the $\pi - e$ likelihood is now required. Again Monte Carlo is used for the $\pi^+\pi^-\gamma$, $\mu^+\mu^-\gamma$ and $\pi^+\pi^-\pi^0$ channels while $e^+e^-\gamma$ events are obtained from data. Then all the channels are fit together to the data $M_{\rm trk}$ shape. For Bhabha events the normalization parameters are fixed to $w_{ee\gamma}(j)$, which have been evaluated in step A, and the $e^+e^-\gamma$ events, properly weighted, are added to the other samples.

1. s_π in $[(0. - 0.36)$ GeV$^2]$: bin-width of 5.0 MeV in $M_{\rm trk}$
   - $s_\pi > 0.12$ GeV^2 $\pi^+\pi^-\gamma$, $\mu^+\mu^-\gamma$ and $\pi^+\pi^-\pi^0$ Monte Carlo samples fitted to data and $e^+e^-\gamma$ added (with weight parameters obtained in step A);
2. s_π in $[(0.4 - 0.56)$ GeV$^2]$: bin-width of 2.5 MeV in $M_{\rm trk}$
   - $\pi^+\pi^-\gamma$, $\mu^+\mu^-\gamma$ and $\pi^+\pi^-\pi^0$ Monte Carlo samples fitted to data and $e^+e^-\gamma$ added (with weight parameters obtained in step A);
3. s_π in $[(0.60 - 1.)$ GeV$^2]$: bin-width of 1. MeV in $M_{\rm trk}$
   - $s_\pi < 0.64$ GeV^2 $\pi^+\pi^-\gamma$, $\mu^+\mu^-\gamma$ and $\pi^+\pi^-\pi^0$ Monte Carlo samples fitted to data and $e^+e^-\gamma$ added (with weight parameters obtained in step A);
   - $s_\pi > 0.68$ GeV^2 $\pi^+\pi^-\gamma$ and $\mu^+\mu^-\gamma$ Monte Carlo samples fitted to data and $e^+e^-\gamma$ (with weight parameters obtained in step A).

The weights $w_{ch}(j)$ $(j = 1, 2, ...25)$ obtained from the background fit procedure for each slice in s_π are shown in Tab. 5.2, together with the errors on each weight value and the χ^2/ndof of the fit for both the two steps. For step A in the first two slices, and in the first three slices for step B, the fit has not been performed, because of the low statistics. At these energy values the weights are set on a fixed value.
In Fig. 5.32,5.33 and in Fig. 5.34,5.35 the trackmass shapes after the fit procedure are shown, for step A and for step B, respectively.

A fit for each *ch* background channel using polynomial functions, $f_{ch}(s_\pi)$, is performed to smoother the values of the weights, $w_{ch}(j)$. For the $\mu^+\mu^-\gamma$ and $e^+e^-\gamma$ samples a third power polynomial function is used, while for the $\pi^+\pi^-\pi^0$ a linear fit is applied. With the polynomial functions obtained, it is possible to rebin the weights for smaller intervals of s_π:

$$w_{ch}(j) \rightarrow w'_{ch}(k) = f_{ch}(s^*_\pi),$$

where j is the index of the 25 slices in s_π of 0.04 GeV^2 width, used in step A and B, and k is the index of the new s_π slicing. We chose to increase the slicing in s_π from $j = 1, 2, ...25$ to $k = 1, 2, ...50$ of 0.02 GeV^2 widths in s_π. The new weights are obtained by sampling the polynomial functions $f_{ch}(s_\pi)$.
The weights $w'_{ch}(k)$ obtained from the fit function $f_{ch}(s_\pi)$ for each background channel ($\mu^+\mu^-\gamma$, $e^+e^-\gamma$ and $\pi^+\pi^-\pi^0$) are reported in Tab. 5.3 together with the errors. Since the number of slices for $w'_{ch}(k)$ is doubled with respect to that one for $w_{ch}(j)$, the same $\delta w_{ch}(j)$ goes to two

s_π slice (GeV^2)	$w_{\mu\mu\gamma} \pm \delta w_{\mu\mu\gamma}$	$w_{ee\gamma} \pm \delta w_{ee\gamma}$	$w_{\pi\pi\pi} \pm \delta w_{\pi\pi\pi}$	χ^2/ndof step A	χ^2/ndof step B
$0.00 - 0.04$	1.000 ± 0.000	0.0500 ± 0.0000	1.000 ± 0.000	–	–
$0.04 - 0.08$	1.000 ± 0.000	0.0500 ± 0.0000	1.000 ± 0.000	–	–
$0.08 - 0.12$	1.000 ± 0.000	0.0419 ± 0.0044	1.000 ± 0.000	9.13/10	–
$0.12 - 0.16$	0.980 ± 0.028	0.0807 ± 0.0099	0.991 ± 0.085	23.75/12	66.32/12
$0.16 - 0.20$	0.920 ± 0.030	0.1311 ± 0.0131	1.081 ± 0.088	6.55/12	41.81/12
$0.20 - 0.24$	0.957 ± 0.032	0.1244 ± 0.0126	0.708 ± 0.128	2.64/11	9.77/11
$0.24 - 0.28$	0.974 ± 0.031	0.0602 ± 0.0075	0.774 ± 0.177	7.28/11	9.77/11
$0.28 - 0.32$	1.030 ± 0.030	0.0388 ± 0.0060	0.847 ± 0.088	17.67/12	19.75/11
$0.32 - 0.36$	0.964 ± 0.027	0.0523 ± 0.0058	0.819 ± 0.110	14.41/12	22.07/12
$0.36 - 0.40$	0.932 ± 0.023	0.0336 ± 0.0043	1.035 ± 0.070	42.12/30	13.42/12
$0.40 - 0.44$	0.949 ± 0.021	0.0501 ± 0.0045	1.385 ± 0.080	40.42/32	46.76/30
$0.44 - 0.48$	0.972 ± 0.019	0.0557 ± 0.0028	1.388 ± 0.100	34.08/32	83.08/32
$0.48 - 0.52$	0.973 ± 0.018	0.0527 ± 0.0013	1.557 ± 0.112	71.78/34	83.08/32
$0.52 - 0.56$	0.988 ± 0.017	0.0382 ± 0.0011	0.962 ± 0.210	34.34/34	54.24/32
$0.56 - 0.60$	1.000 ± 0.016	0.0400 ± 0.0010	2.174 ± 0.281	119.86/101	93.73/34
$0.60 - 0.64$	0.982 ± 0.015	0.0337 ± 0.0008	3.095 ± 0.597	118.21/106	113.66/34
$0.64 - 0.68$	0.998 ± 0.014	0.0318 ± 0.0007	0.000 ± 0.000	140.81/116	224.89/101
$0.68 - 0.72$	0.978 ± 0.012	0.0308 ± 0.0006	0.000 ± 0.000	138.55/126	282.00/117
$0.72 - 0.76$	0.963 ± 0.011	0.0315 ± 0.0005	0.000 ± 0.000	169.17/137	217.17/127
$0.76 - 0.80$	0.959 ± 0.010	0.0305 ± 0.0005	0.000 ± 0.000	142.64/137	257.77/137
$0.80 - 0.84$	0.979 ± 0.009	0.0302 ± 0.0005	0.000 ± 0.000	145.91/137	280.86/137
$0.84 - 0.88$	0.958 ± 0.008	0.0299 ± 0.0004	0.000 ± 0.000	153.42/137	159.82/137
$0.88 - 0.92$	0.935 ± 0.007	0.0289 ± 0.0004	0.000 ± 0.000	132.74/132	171.13/137
$0.92 - 0.96$	0.930 ± 0.005	0.0279 ± 0.0004	0.000 ± 0.000	114.66/107	155.03/137
$0.96 - 1.00$	0.886 ± 0.005	0.0256 ± 0.0004	0.000 ± 0.000	162.30/77	104.09/137

Tab. 5.2: Weights for each background source obtained from the background fit procedure.

consecutive values of $w'_{ch}(k)$, k and $k+1$, contained in the same j. Where the fit has not been performed the biggest value among all the $\delta w_{ch}(j)$ is considered.

The upper plots of Fig. 5.27(a), (b) and (c) show the results of the background fit procedure, $w_{ch}(j)$ (red circles), together with the fitting functions, $f_{ch}(s_\pi)$ (blue line). The error bars correspond to the errors reported in Tab. 5.2.

The smallness of $w_{ee\gamma}$ weights is due to the fact that selecting $e^+e^-\gamma$ events by means of the `nor`-configuration of the $\pi - e$ PID increases the Bhabha yield relatively to the other channels by about a factor 20 with respect to the `or`-configuration, which is applied in the analysis. Thus a roughly factor 1/20 must be recovered in the weights.

For $\mu^+\mu^-\gamma$, $\pi^+\pi^-\gamma$ and $\pi^+\pi^-\pi^0$ the value of w_{ch} is a direct test of how well the Monte Carlo prediction works: if the value of w_{ch} is equal to 1 this implies that the luminosity scaled Monte Carlo is excellent. From Tab. 5.2 one sees that the simulation, even if is rather well reproducing the data, needs to be adjusted of some few percent.

The lower plots, in Fig. 5.27(a), (b) and (c), show the sampling of $f_{ch}(s_\pi)$ to extract $w'_{ch}(k)$ in each of the k^{th} slice in s_π. The distance between $f_{ch}(s_\pi)$ and $w_{ch}(j)$ is used as an estimator for the systematics, as it will be explained below.

Once the normalization parameters $w'_{ch}(k)$ are obtained in each k^{th} slice, they are applied on an event-by-event basis as weights for each sample (Monte Carlo and $e^+e^-\gamma$) in the standard selection, where all the analysis cuts are applied, including the cuts in trackmass. The bin width in s_π for the analysis is 0.01 GeV^2, which is half the number of the slices for $w'_{ch}(k)$, so each weight of the k^{th} slice in s_π is applied to the two consecutive bins contained in that specific interval.

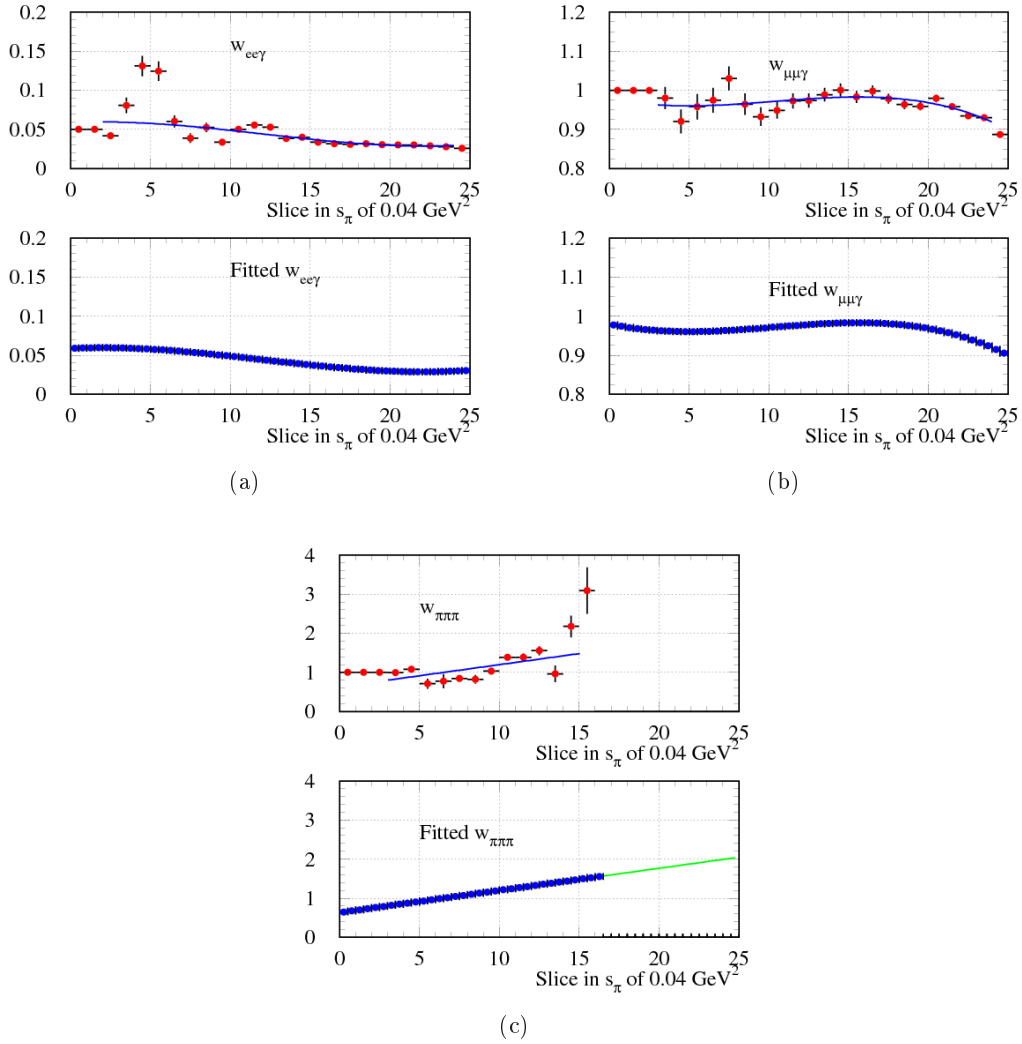

Fig. 5.27: (Upper plots) Weights for $e^+e^-\gamma$ (a), $\mu^+\mu^-\gamma$ (b) and $\pi^+\pi^-\pi^0$ (c) samples ($w_{ee\gamma}(j)$, $w_{\mu\mu\gamma}(j)$ and $w_{\pi\pi\pi}(j)$, where $j = 1, 2, ...25$) obtained from the fit procedure, red points, are shown together with the fitting functions used to smoothing, blue curves. (Lower plots) The same functions, $f_{ch}(s_\pi)$, sampled in 50 points to obtain the parameters ($w'_{ee\gamma}(k)$, $w'_{\mu\mu\gamma}(k)$ and $w'_{\pi\pi\pi}(k)$, where $k = 1, 2, ...50$) used to reweight the s_π spectra for $\mu^+\mu^-\gamma$ $e^+e^-\gamma$ and $\pi^+\pi^-\pi^0$.

The fraction of background events is obtained as

$$f_{\rm tot} \equiv N_{\rm bkg}/N_{\rm tot} = \frac{w'_{\mu\mu\gamma}\cdot N_{\mu\mu\gamma} + w'_{ee\gamma}\cdot N_{ee\gamma} + w'_{\pi\pi\pi}\cdot N_{\pi\pi\pi}}{N_{\rm tot}}, \tag{5.9}$$

for each bin of s_π relative to the number of data events $N_{\rm tot}$ found in the bin. The data spectrum is then corrected in each bin with the factor $(1 - f_{\rm tot})$:

$$N_{s_\pi} = N_{\rm tot}\cdot(1 - f_{\rm tot}). \tag{5.10}$$

The statistical error of the combined background fraction in each bin i of s_π is calculated by

$$(\delta f_i)^2 = \left(\frac{w'_{\mu\mu\gamma,i}\cdot\delta N_{\mu\mu\gamma,i}}{N_{\mathrm{dat},i}}\right)^2 + \left(\frac{w'_{\mu\mu\gamma,i}\cdot N_{\mu\mu\gamma,i}\cdot\delta N_{\mathrm{dat},i}}{N^2_{\mathrm{dat},i}}\right)^2 + \left(\frac{w'_{ee\gamma,i}\cdot\delta N_{ee\gamma,i}}{N_{\mathrm{dat},i}}\right)^2 + \left(\frac{w'_{ee\gamma,i}\cdot N_{ee\gamma,i}\cdot\delta N_{\mathrm{dat},i}}{N^2_{\mathrm{dat},i}}\right)^2 + \left(\frac{w'_{\pi\pi\pi,i}\cdot\delta N_{\pi\pi\pi,i}}{N_{\mathrm{dat},i}}\right)^2 + \left(\frac{w'_{\pi\pi\pi,i}\cdot N_{\pi\pi\pi,i}\cdot\delta N_{\mathrm{dat},i}}{N^2_{\mathrm{dat},i}}\right)^2 . \quad (5.11)$$

The different values for the integrated luminosity for data and Monte Carlo events are taken into account properly in the procedure.
In Fig. 5.28(a) the s_π spectra for data (black circles), signal $\pi^+\pi^-\gamma$ (empty blue circles), $\mu^+\mu^-\gamma$ (green circles), $e^+e^-\gamma$ (red circles) and $\pi^+\pi^-\pi^0$ (pink circles) are shown. The sum of all background sources is represented by the blue points. The peculiar trend of $e^+e^-\gamma$ events, which dramatically drops down below 0.4 GeV^2, is due to the large angle geometrical acceptance selection. In Fig. 5.28(b) the relative amount of background over data events, i.e. the f_{tot} value of Eq. 5.9, is shown. In Fig. 5.29 the ratios between each background source, *ch*, and selected

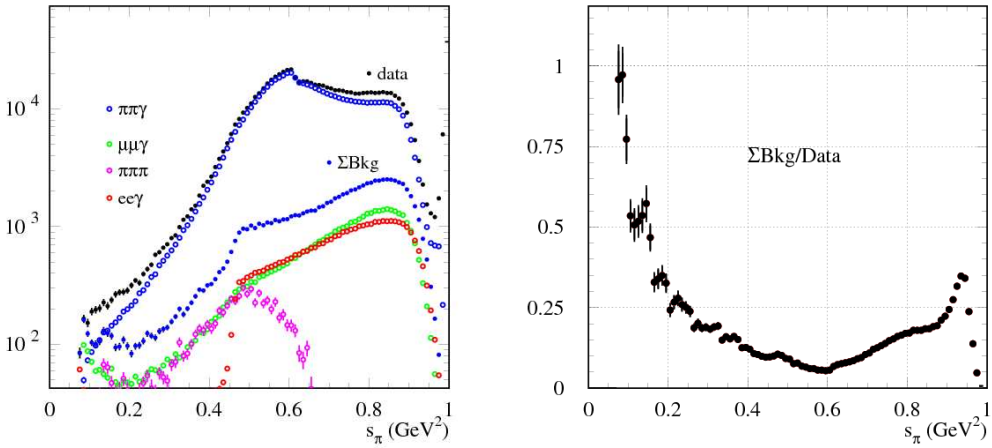

(a) (b)

Fig. 5.28: Plot of the s_π spectra for different channels after the background fit procedure, in (a). Ratio between the sum of all the background sources over data is shown in (b).

data events, $f_{ch} = (w'_{ch}\cdot N_{ch})/N_{\mathrm{tot}}$, is shown: .

Systematic error on the background fit procedure

The statistical error due to the background fit and subtraction procedure is evaluated according to Eq. 5.11. This evaluation is performed separately for each background source. For each background channel two contributions are considered:

– the first one, $\delta^{\mathrm{wgt}}_{\mathrm{syst}}$, concerns the reliability of the weights. This contribution is evaluated in two cases. (*i*) In the s_π regions where the fit on M_{trk} shapes has not been performed,

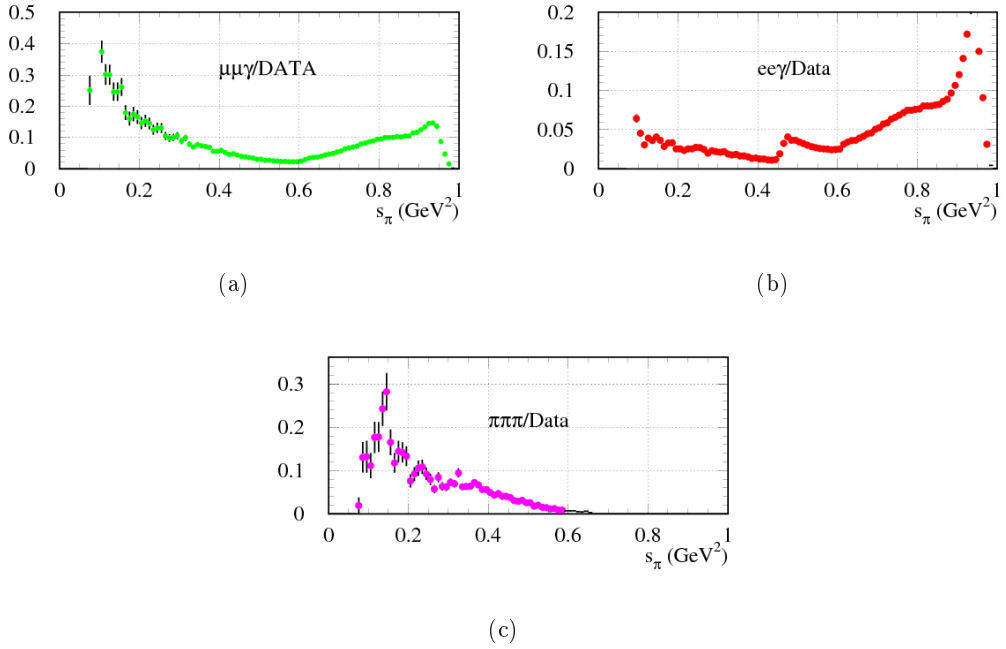

(a) (b) (c)

Fig. 5.29: Fraction of background sources with respect to the data events after the analysis cuts described in Sec. 5.2.

because of the small statistics (see Tab. 5.2) and the weights are obtained only from the fit functions $f_{ch}(s_\pi)$ (see Tab. 5.3). It means that $w_{ch}(j)$'s assume a fixed value. This happens below 0.12 GeV^2 for the $\mu^+\mu^-\gamma$ and $\pi^+\pi^-\pi^0$ samples. (*ii*) The fit looks unstable for $e^+e^-\gamma$ events, in the s_π slices where the $w_{ee\gamma}(j)$ weights are dramatically scattering (below 0.52 GeV^2). To estimate $\delta^{\rm wgt}_{\rm syst}$, the distance between the function $f_{ch}(s_\pi)$ and the weights w_{ch} for each slice of s_π is computed;

– the second contribution to the systematic error, $\delta^{\rm func}_{\rm syst}$, concerns the stability of the fit functions $f_{ch}(s_\pi)$. It is estimated by changing the s_π range to obtain $f_{ch}(s_\pi)$. In this way, different $f^j_{ch}(s_\pi)$ ("blue lines" in Fig. 5.27) are evaluated for each background channel ch. The difference $|f_{ch}(s_\pi) - f^j_{ch}(s_\pi)|$ is then computed in the whole s_π range.

The systematic uncertainty for each channel is therefore:

$$\delta_{ch,\rm syst} = (\delta^{\rm wgt}_{ch,\rm syst} + \delta^{\rm func}_{ch,\rm syst}) \cdot \frac{N_{ch}}{N_{\rm data}}, \tag{5.12}$$

where N_{ch} is the number of events of the $ch^{\rm th}$ background sources in bin of 0.01 GeV^2 of s_π and $N_{\rm data}$ the number of data which passed all the selection cuts and after the background subtraction, see Eq. 5.10, in the same binning.
In Fig. 5.30 the systematic uncertainties for each background samples are shown. The total systematic uncertainty is given by

$$\delta_{\rm bkg,syst} = \delta_{\mu\mu\gamma,\rm syst} + \delta_{ee\gamma,\rm syst} + \delta_{\pi\pi\pi,\rm syst}. \tag{5.13}$$

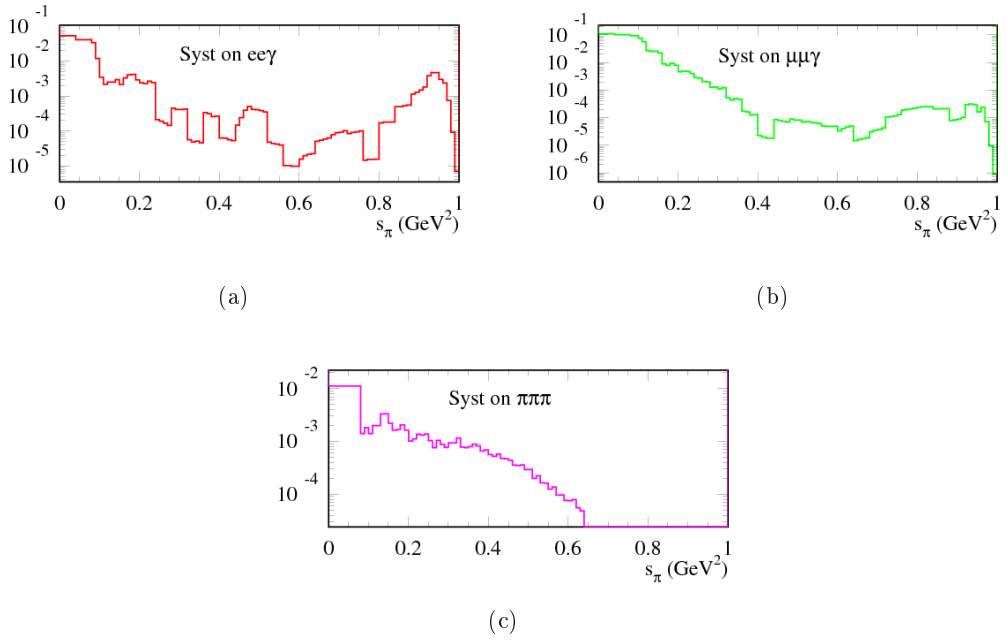

(a) (b)

(c)

Fig. 5.30: Systematic uncertainties for the different background sources.

To consider the systematic uncertainty in each bin 0.01 GeV^2 of the spectrum a smoothing procedure on $\delta_{\mathrm{bkg,syst}}$ is applied. The result is shown in Fig. 5.31, which is then taken as the systematic uncertainty. The uncertainty is actually negligible above 0.4 GeV^2, where it is smaller

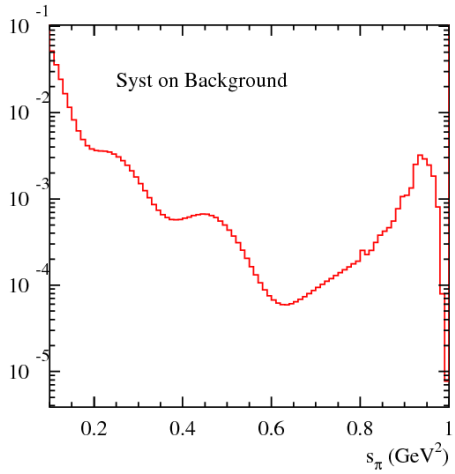

Fig. 5.31: Total systematic uncertainties due to the background fit procedure.

than 0.1%. Below 0.2 GeV^2 the large value is mainly caused by the uncertainty of the weights, estimated with the difference between the function $f_{ch}(s_\pi)$ and the weights $w_{ch}(j)$. The main reason of the increase of the error at the threshold can be referred to the low statistics, which makes it difficult to estimate, with similar precision as at higher energies, the background event

yield.

s_π slice (GeV^2)	$w'_{\mu\mu\gamma} \pm \delta w'_{\mu\mu\gamma}$	$w'_{ee\gamma} \pm \delta w'_{ee\gamma}$	$w'_{\pi\pi\pi} \pm \delta w'_{\pi\pi\pi}$
$0.00 - 0.02$	0.977 ± 0.040	0.0587 ± 0.0004	2.12 ± 1.80
$0.02 - 0.04$	0.973 ± 0.040	0.0591 ± 0.0004	1.89 ± 1.80
$0.04 - 0.06$	0.970 ± 0.040	0.0593 ± 0.0200	1.69 ± 1.80
$0.06 - 0.08$	0.967 ± 0.040	0.0594 ± 0.0200	1.51 ± 1.80
$0.08 - 0.10$	0.965 ± 0.040	0.0594 ± 0.0044	1.35 ± 1.80
$0.10 - 0.12$	0.963 ± 0.040	0.0593 ± 0.0044	1.22 ± 1.80
$0.12 - 0.14$	0.962 ± 0.028	0.0591 ± 0.0099	1.10 ± 0.08
$0.14 - 0.16$	0.961 ± 0.028	0.0588 ± 0.0099	1.01 ± 0.08
$0.16 - 0.18$	0.960 ± 0.030	0.0584 ± 0.0131	0.94 ± 0.08
$0.18 - 0.20$	0.960 ± 0.030	0.0579 ± 0.0131	0.88 ± 0.08
$0.20 - 0.22$	0.960 ± 0.032	0.0573 ± 0.0126	0.85 ± 0.12
$0.22 - 0.24$	0.960 ± 0.032	0.0566 ± 0.0126	0.83 ± 0.12
$0.24 - 0.26$	0.961 ± 0.031	0.0559 ± 0.0075	0.82 ± 0.17
$0.26 - 0.28$	0.961 ± 0.031	0.0551 ± 0.0075	0.83 ± 0.17
$0.28 - 0.30$	0.962 ± 0.030	0.0543 ± 0.0060	0.85 ± 0.08
$0.30 - 0.32$	0.963 ± 0.030	0.0533 ± 0.0060	0.88 ± 0.08
$0.32 - 0.34$	0.965 ± 0.027	0.0524 ± 0.0058	0.92 ± 0.11
$0.34 - 0.36$	0.966 ± 0.027	0.0514 ± 0.0058	0.97 ± 0.11
$0.36 - 0.38$	0.968 ± 0.023	0.0503 ± 0.0043	1.03 ± 0.07
$0.38 - 0.40$	0.969 ± 0.023	0.0493 ± 0.0043	1.10 ± 0.07
$0.40 - 0.42$	0.971 ± 0.021	0.0481 ± 0.0045	1.17 ± 0.08
$0.42 - 0.44$	0.972 ± 0.021	0.0470 ± 0.0045	1.25 ± 0.08
$0.44 - 0.46$	0.974 ± 0.019	0.0459 ± 0.0028	1.33 ± 0.10
$0.46 - 0.48$	0.976 ± 0.019	0.0447 ± 0.0028	1.42 ± 0.10
$0.48 - 0.50$	0.977 ± 0.018	0.0436 ± 0.0013	1.50 ± 0.11
$0.50 - 0.52$	0.978 ± 0.018	0.0424 ± 0.0013	1.59 ± 0.11
$0.52 - 0.54$	0.979 ± 0.017	0.0413 ± 0.0011	1.67 ± 0.21
$0.54 - 0.56$	0.980 ± 0.017	0.0402 ± 0.0011	1.76 ± 0.21
$0.56 - 0.58$	0.981 ± 0.016	0.0391 ± 0.0010	1.84 ± 0.28
$0.58 - 0.60$	0.982 ± 0.016	0.0380 ± 0.0010	1.91 ± 0.28
$0.60 - 0.62$	0.982 ± 0.015	0.0369 ± 0.0008	1.99 ± 0.59
$0.62 - 0.64$	0.982 ± 0.015	0.0359 ± 0.0008	2.05 ± 0.59
$0.64 - 0.66$	0.982 ± 0.014	0.0349 ± 0.0007	2.11 ± 1.80
$0.66 - 0.68$	0.982 ± 0.014	0.0340 ± 0.0007	0.00 ± 1.80
$0.68 - 0.70$	0.981 ± 0.012	0.0331 ± 0.0006	0.00 ± 1.80
$0.70 - 0.72$	0.979 ± 0.012	0.0323 ± 0.0006	0.00 ± 1.80
$0.72 - 0.74$	0.978 ± 0.011	0.0316 ± 0.0005	0.00 ± 1.80
$0.74 - 0.76$	0.975 ± 0.011	0.0309 ± 0.0005	0.00 ± 1.80
$0.76 - 0.78$	0.973 ± 0.010	0.0303 ± 0.0005	0.00 ± 1.80
$0.78 - 0.80$	0.970 ± 0.010	0.0298 ± 0.0005	0.00 ± 1.80
$0.80 - 0.82$	0.966 ± 0.009	0.0293 ± 0.0005	0.00 ± 1.80
$0.82 - 0.84$	0.962 ± 0.009	0.0290 ± 0.0005	0.00 ± 1.80
$0.84 - 0.86$	0.957 ± 0.008	0.0287 ± 0.0004	0.00 ± 1.80
$0.86 - 0.88$	0.952 ± 0.008	0.0286 ± 0.0004	0.00 ± 1.80
$0.88 - 0.90$	0.945 ± 0.007	0.0286 ± 0.0004	0.00 ± 1.80
$0.90 - 0.92$	0.939 ± 0.007	0.0287 ± 0.0004	0.00 ± 1.80
$0.92 - 0.94$	0.931 ± 0.005	0.0289 ± 0.0004	0.00 ± 1.80
$0.94 - 0.96$	0.923 ± 0.005	0.0292 ± 0.0004	0.00 ± 1.80
$0.96 - 0.98$	0.914 ± 0.005	0.0297 ± 0.0004	0.00 ± 1.80
$0.98 - 1.00$	0.904 ± 0.005	0.0303 ± 0.0004	0.00 ± 1.80

Tab. 5.3: Weights for each background source obtained from the sampling of $f_{ch}(s_\pi)$ for each channels.

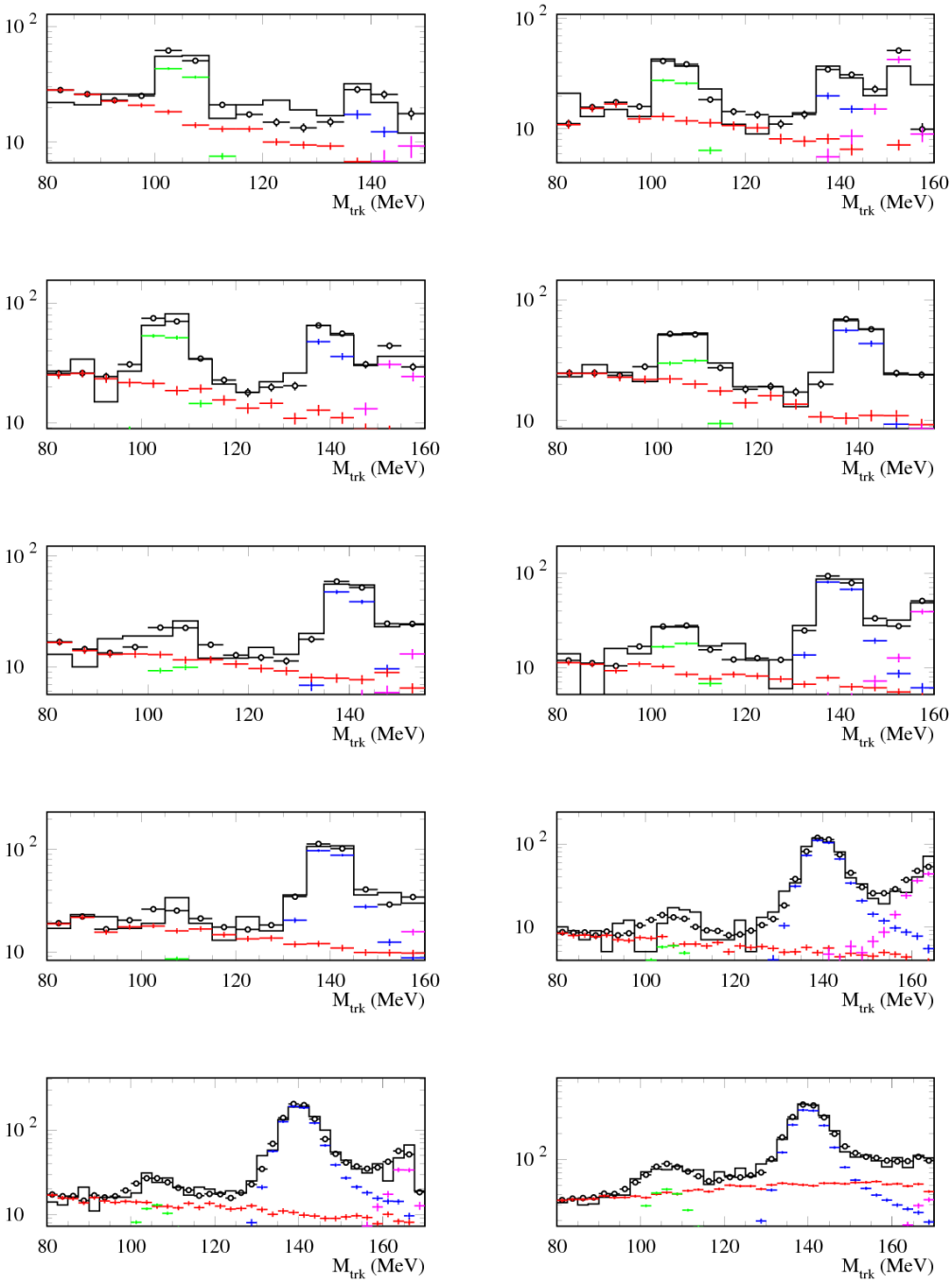

Fig. 5.32: Trackmass shapes in slices of s_π after step A of the fitting procedure described in Sec. 5.4. The black histogram represents the data sample, with the `xor`-configuration of the $\pi - e$ PID. The blue circles represent the $\pi^+\pi^-\gamma$ Monte Carlo sample, the green circles the $\mu^+\mu^-\gamma$ one and the pink circle the $\pi^+\pi^-\pi^0$ events. In red circles the $e^+e^-\gamma$ events selected applying the `nor`-configuration of the $\pi - e$ PID to the data sample. The empty black circles indicate the sum of all Monte Carlo sources and of the $e^+e^-\gamma$ channel. It is possible to appreciate the good agreement with the data histogram. The order of the slicing, each slice in s_π of 0.04 GeV^2, is from left to right from the top to the bottom with s_π in the range $[0.08 - 0.48]$ GeV^2.

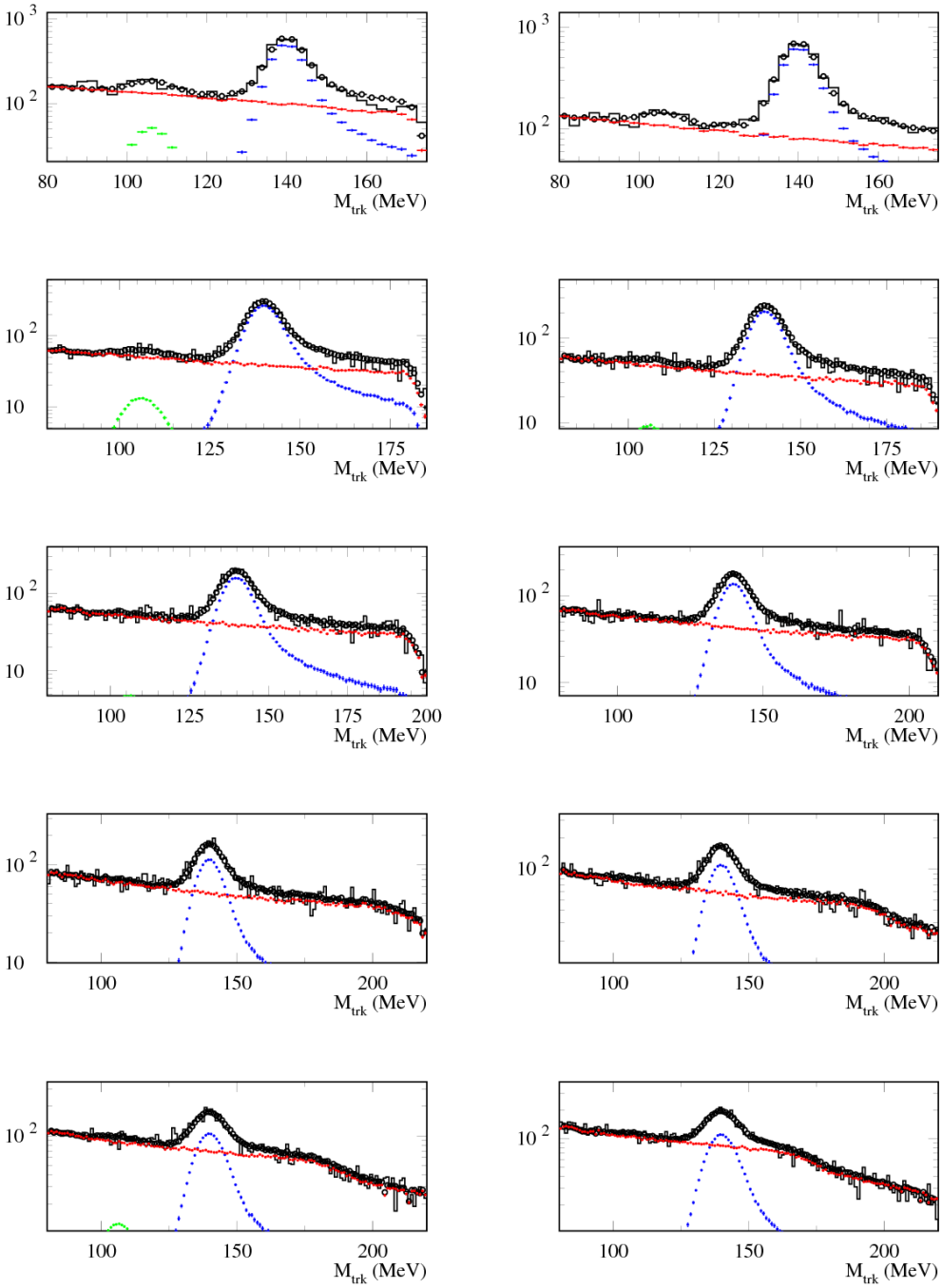

Fig. 5.33: Trackmass shapes in slices of s_π after step A of the fitting procedure. The color codes is the same of the previous figure: black histogram represents the data sample, the blue circles the $\pi^+\pi^-\gamma$ Monte Carlo, the green circles the $\mu^+\mu^-\gamma$, the pink circle the $\pi^+\pi^-\pi^0$ events and the red circles the $e^+e^-\gamma$ events. The empty black circles are the sum of the signal plus the background events after the weighting. The order of the slicing is again from left to right from the top to the bottom with s_π in the range $[0.52 - 0.88]$ GeV^2.

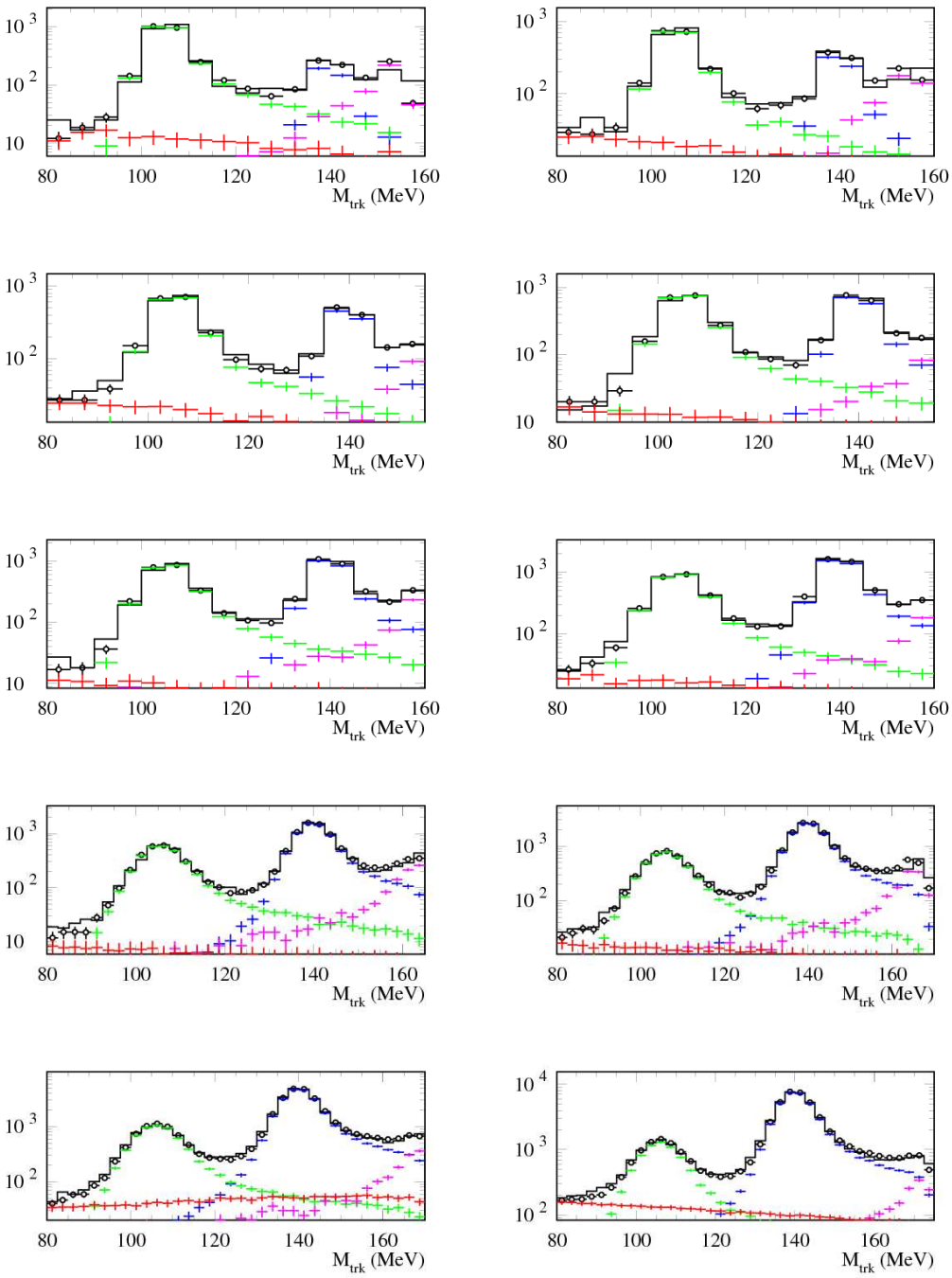

Fig. 5.34: Trackmass shapes in slices of s_π after step B of the fitting procedure described in Sec. 5.4. The black histogram represents the data sample, with the `or`-configuration of the $\pi - e$ PID. The blue circles represent the $\pi^+\pi^-\gamma$ Monte Carlo sample, the green circles the $\mu^+\mu^-\gamma$ one and the pink circle the $\pi^+\pi^-\pi^0$ events. The red circles represent the $e^+e^-\gamma$ events directly obtained from step A. The empty black circles indicate the sum of all Monte Carlo sources and of the $e^+e^-\gamma$ channel. It is possible to appreciate the good agreement with the data histogram. The order of the slicing, each slice in s_π of 0.04 GeV^2, is from left to right from the top to the bottom with s_π in the range $[0.12 - 0.52]$ GeV^2.

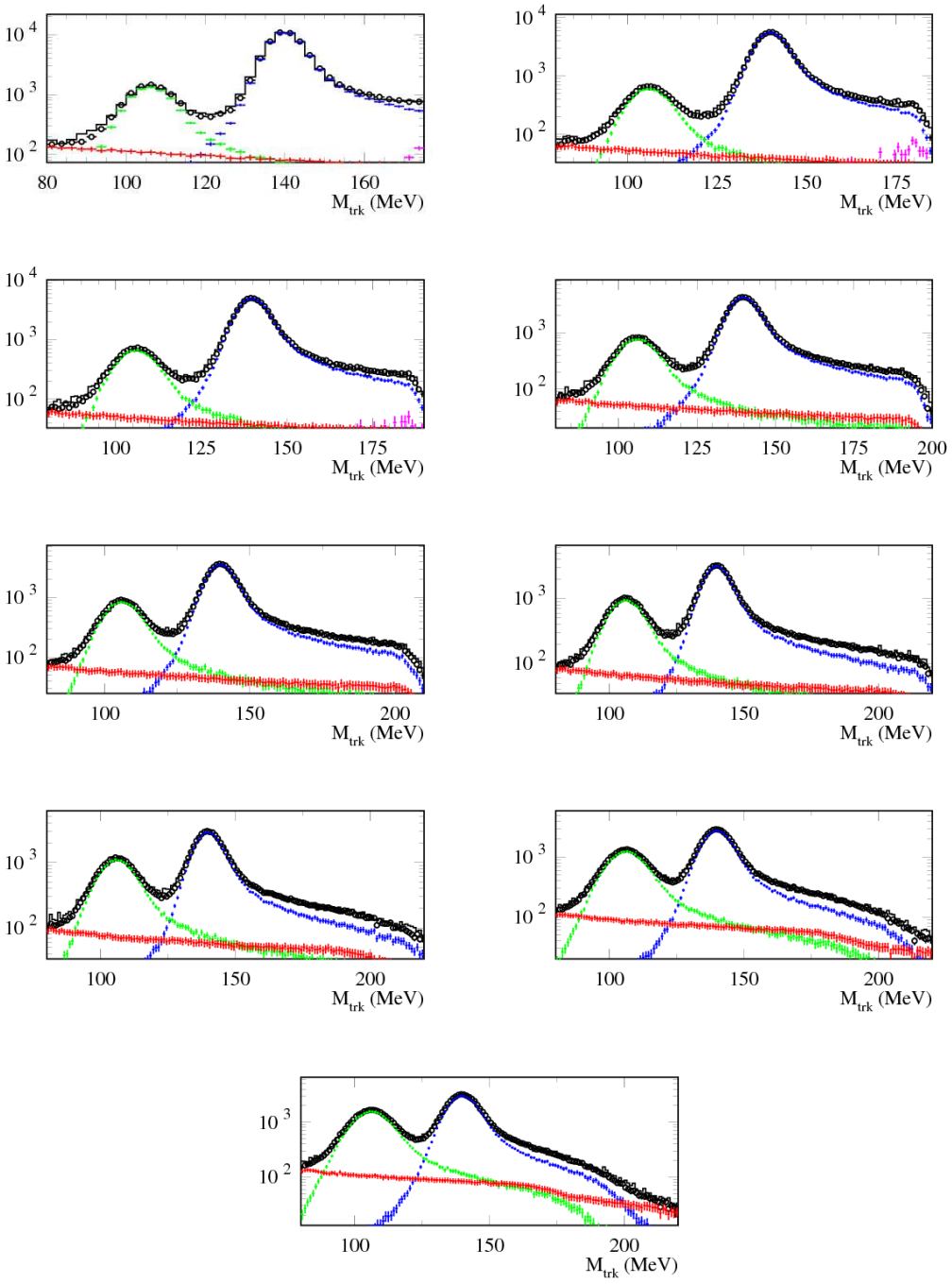

Fig. 5.35: Trackmass shapes in slices of s_π after step B of the fitting procedure. The color codes is the same of the previous figure: black histogram represents the data sample, the blue circles the $\pi^+\pi^-\gamma$ Monte Carlo, the green circles the $\mu^+\mu^-\gamma$, the pink circle the $\pi^+\pi^-\pi^0$ events and the red circles the $e^+e^-\gamma$ events. The empty black circles are the sum of the signal plus the background events after the weighting. The order of the slicing is again from left to right from the top to the bottom with s_π in the range $[0.56 - 0.88]$ GeV^2.

6. EFFICIENCIES EVALUATION AND $|F_\pi(s)|^2$ EXTRACTION

In Fig. 6.1 the analysis flow is shown, where all the steps needed in the Eq. 6.1 and Eq. 6.2 are listed. We will discuss in the following the individual analysis steps of Fig. 6.1.

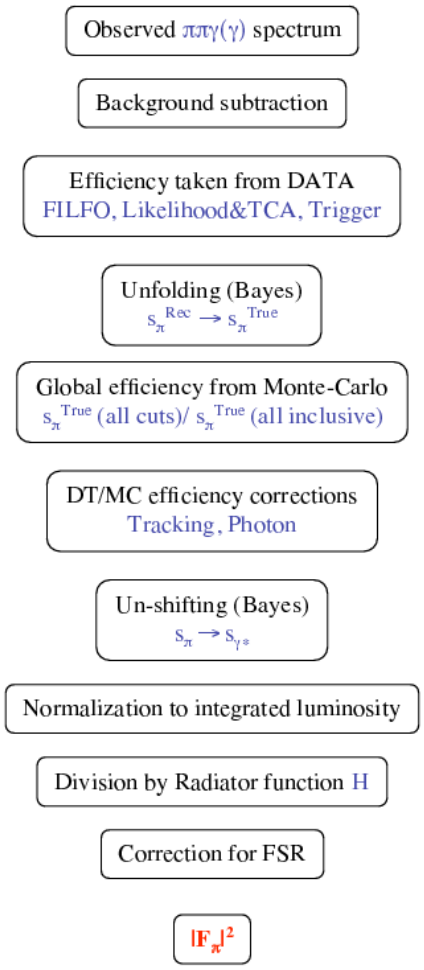

Fig. 6.1: Analysis flow for the Large Angle off-peak analysis.

In Fig. 6.2 the event yield of $e^+e^- \rightarrow \pi^+\pi^-\gamma(\gamma)$ events after signal selection and background subtraction is presented.

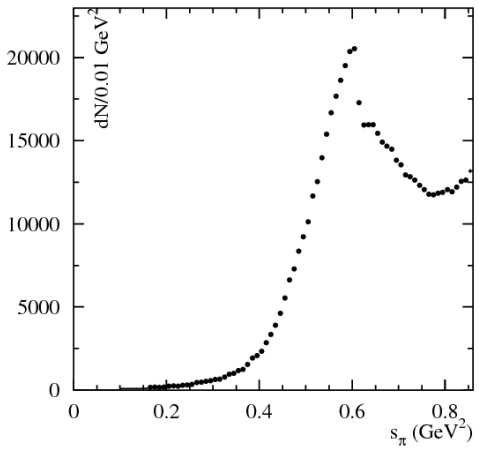

Fig. 6.2: Data $e^+e^- \to \pi^+\pi^-\gamma$ spectrum after the background subtraction.

The pion from factor is connected to the $\sigma(e^+e^- \to \pi^+\pi^-)$ cross section via the relation

$$|F_\pi(s)|^2 = \frac{3s}{\pi\alpha^2\beta^3}\sigma_{e^+e^-\to\pi^+\pi^-}(s). \tag{6.1}$$

The cross section can be extracted from radiative events by means of the relation

$$\frac{d\sigma_{\pi\pi}}{ds_\pi} = \frac{\Delta N_{\rm obs} - \Delta N_{\rm bkg}}{\Delta s_\pi} \cdot \frac{1}{\varepsilon \cdot \varepsilon_{\rm glob}\Delta\varepsilon} \cdot \frac{1}{\int \mathcal{L}\, dt} \cdot \frac{1}{H(s_\pi, s)\cdot\delta_{\rm rad}}. \tag{6.2}$$

In Eq. 6.2, $\Delta N_{\rm obs} - \Delta N_{\rm bkg}$ represents the observed spectrum after the residual background subtraction, binned in the hadronic system invariant mass, Δs_π, equal to 0.01 GeV^2; ε represents the correction for the efficiencies evaluated directly from data control samples; $\varepsilon_{\rm glob}$ indicates the effective global efficiency taken from Monte Carlo; $\Delta\varepsilon$ possible corrections for data-Monte Carlo differences in the individual efficiencies; $\int \mathcal{L}\, dt$ is the integrated luminosity of the 2006 data sample, corresponding to 233 pb^{-1}; $H(s_\pi, s)$ is the radiator function and $\delta_{\rm rad}$ further radiative corrections.

6.1 Efficiencies obtained directly from data sample

The correction for the efficiencies are applied using an *effective global efficiency* approach: the factor $\varepsilon_{\rm glob}$ is evaluated by means of the Monte Carlo signal sample and includes all the efficiencies. Each single efficiency is then separately evaluated, and corrections are applied for the differences between data and the simulation. However, the efficiencies for `FILFO`, trigger and $\pi - e$ likelihood are evaluated directly from data, thus they do not enter $\varepsilon_{\rm glob}$ and do not require any further correction.

6.1.1 `FILFO` (offline background filter) efficiency

The `FILFO` filter identifies background events, such a reconstructed Bhabha, cosmic ray events and machine background events, at a very early stage of data taking and rejects them before

they enter the CPU-consuming pattern recognition and track fitting algorithms (see Sec. 3.3.2 and [32]). The offline background filter has been completely rewritten and as a consequence brought the systematic uncertainty was reduced to a negligible level, and moreover the efficiency was significantly increased. This is achieved by retaining an unbiased downscaled sample during the data taking and the deactivation of the `BHABREJ` subfilter [124]. Fig. 6.3 shows the efficiency obtained in this way.

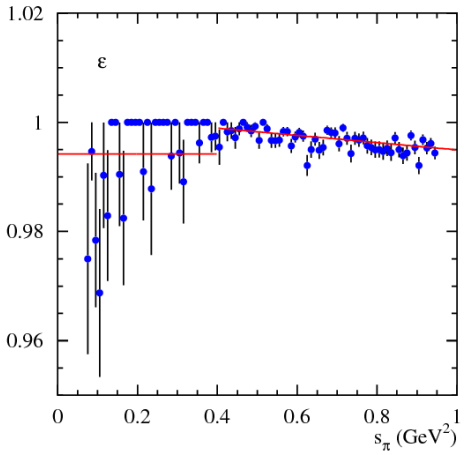

Fig. 6.3: Efficiency of the `FILFO` reconstruction filter for pions. The red lines represent the functions used to fit the efficiency.

Instead of applying a bin-by-bin correction of the spectrum, the efficiency is fitted with two linear functions, visible as red lines in Fig. 6.3. In the range $[0. - 0.4]$ GeV^2 the mean value of the efficiency is taken and, for $s_\pi > 0.4$ GeV^2, a first power function is used:

$$f_{\varepsilon_{\mathrm{FILFO}}}(s_\pi) = a_0 + a_1 \cdot s_\pi.$$

The efficiency for `FILFO` filter is very high, always well above 99%.

Systematic error on the `FILFO` efficiency

The systematic uncertainty on `FILFO` efficiency has been evaluated for the two energy ranges separately. In the range $[0. - 0.4]$ GeV^2, where the mean value is taken, the systematic error is given by the average distance between the mean value and the efficiency values, i.e. the distance between the red line and the blue circles shown in Fig. 6.3.
In the range $[0.4 - 1]$ GeV^2, where the linear fit is performed, the uncertainty is estimated as the sum in quadrature of the errors of the fit parameters a_0 and a_1 are taken: $(\delta^{\mathrm{FILFO}}_{\mathrm{syst}})^2 = \delta^2_{a_0} + \delta^2_{a_1}$.
In Fig. 6.4 the systematic uncertainty due to the `FILFO` efficiency is shown.

6.1.2 $\pi - e$ likelihood and track to cluster association efficiency

In the analysis, each track is extrapolated to the calorimeter and at least one cluster is searched within a sphere of radius $|\vec{r}_{\mathrm{ext}} - \vec{r}_{\mathrm{clu}}| < 90$ cm, where $\vec{r}_{\mathrm{ext}}$ represents the coordinates of the extrapolated impact point of the track in the calorimeter and $\vec{r}_{\mathrm{clu}}$ is the position of the cluster

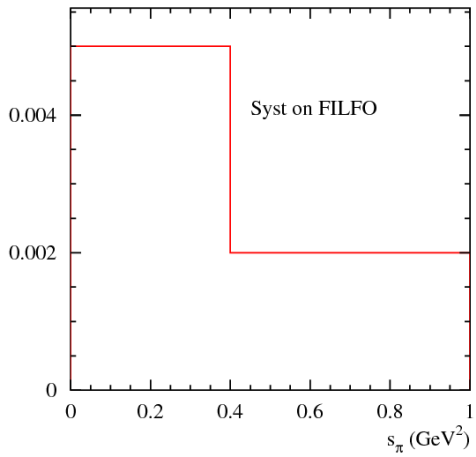

Fig. 6.4: Systematic uncertainty on `FILFO` efficiency. The two values are due to the different fit functions used in and to the two systematic evaluation methods, as explained in the test.

centroid. If there is more than one cluster inside this sphere, the most energetic one is associated to the track.
At least one track has to be recognized as a pion, as written in Sec. 5.2, which means that at least one track must have an associated cluster with $\log \mathcal{L}_\pi/\mathcal{L}_e > 0$.
The single $\pi^\pm$ efficiency, is defined as the probability to find an associated cluster in the calorimeter with $\log \mathcal{L}_\pi/\mathcal{L}_e > 0$, conditioned to the presence of another track recognized to be a $\pi^\mp$. The efficiency is evaluated from a data control sample with the following requirements:

- two tracks of opposite sign satisfying the same conditions on point of closest approach and first hit as applied in the analysis;
- $50° < \theta_\pm < 130°$;
- $|M_{\rm trk} - m_\pi| < 2.5$ MeV, to obtain a clean sample of $\pi^+\pi^-\gamma$;
- cut in Ω-angle as in Eq. 5.7.

The single pion efficiency, $\varepsilon_{\rm like}(\theta_{\pi^\pm}, p_{\pi^\pm})$, is evaluated in 8 slices of polar angle between 50° and 130° and in 30 bins of momentum modulus $p_{\pi^\pm}$ between 200 and 500 MeV, for positive and negative track. The efficiencies as a function of polar angle and momentum can be seen in Fig. 6.5 and in Fig. 6.6 for positive and negative tracks, respectively.

The likelihood efficiency as a function of s_π is obtained by *mapping* these single pion efficiencies with the kinematics generated from simulation. This allows to extract the likelihood efficiency as a function of s_π using the measured values of $\varepsilon_{\rm like}(\theta_{\pi^\pm}, p_{\pi^\pm})$, i.e

$$\varepsilon_{\rm like}(\theta_{\pi^\pm}, p_{\pi^\pm}) \rightarrow \varepsilon_{\rm like}(s_\pi).$$

The same cuts applied in the analysis are used in the Monte Carlo $\pi^+\pi^-\gamma$ events to extract $\varepsilon_{\rm like}(s_\pi)$. For a given bin in s_π (width $= 0.01$ GeV^2), the likelihood efficiency is an average over

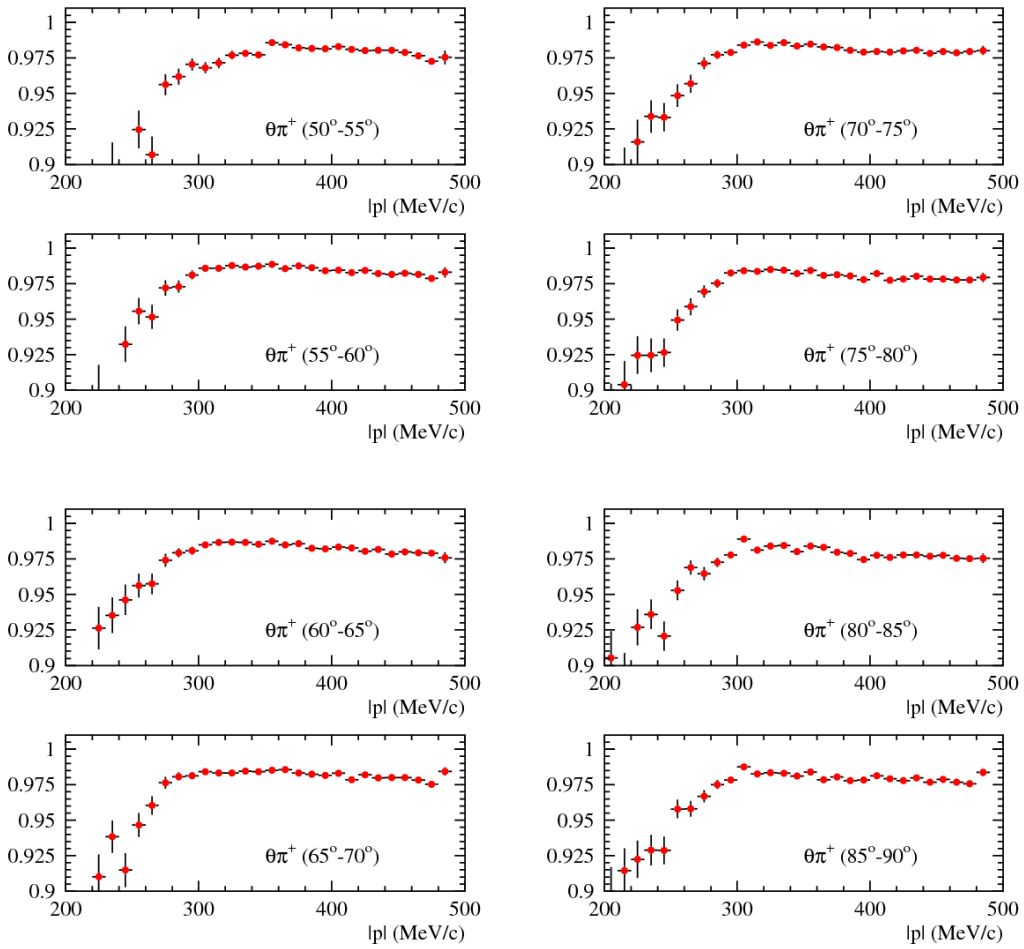

Fig. 6.5: PID likelihood single particle efficiency for π^+ as a function of polar angle and momentum.

the n different phase space configurations $(\theta_{\pi^+}, p_{\pi^+}, \theta_{\pi^-}, p_{\pi^-})$ contributing to that bin:

$$\varepsilon_{\text{like}}(s_\pi) = \frac{1}{N} \sum_{k=1}^{n} \nu_k \; \varepsilon_k, \tag{6.3}$$

where N is the number of Monte Carlo events used to compute the frequency ν_k of a certain k configuration. In the analysis the `or`-configuration of the $\pi - e$ PID likelihood is used, thus the efficiency parameter, ε_k, to be put in the expression of the mapping, is:

$$\varepsilon_k = 1 - \left[1 - \varepsilon_{\text{like}}^{\text{data}}(\theta_{\pi^+}, p_{\pi^+})\right] \left[1 - \varepsilon_{\text{like}}^{\text{data}}(\theta_{\pi^-}, p_{\pi^-})\right]. \tag{6.4}$$

Inserting Eq. 6.4 in Eq. 6.3 one gets $\varepsilon_{\text{like}}^{\text{data}}(s_\pi)$.
In Fig. 6.7 the efficiency of the `or`-configuration of the $\pi - e$ likelihood as a function of s_π is shown. The result is close to 100%, which means that the probability of misidentifying both of the tracks is very small. The drop for low values of s_π is mainly due to track to cluster association, which is more inefficient for low momentum tracks.

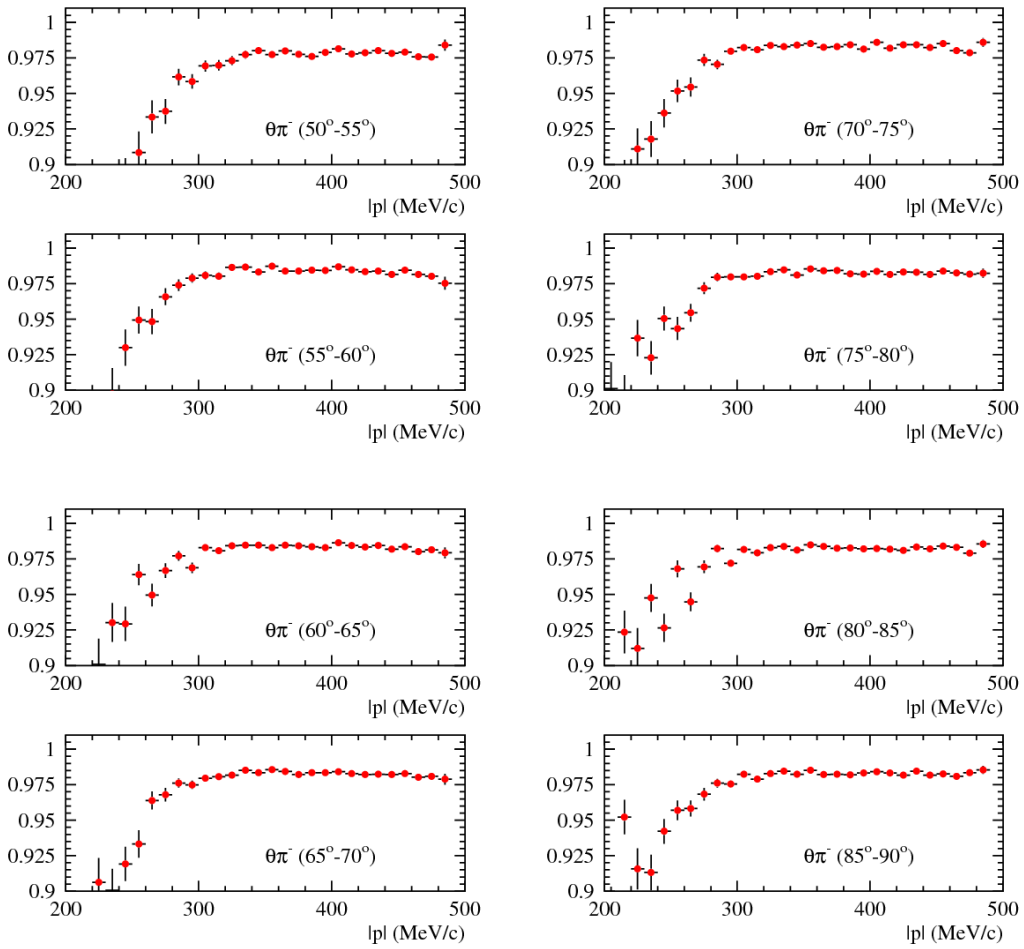

Fig. 6.6: PID likelihood single particle efficiency for π^- as a function of polar angle and momentum.

A test of the likelihood efficiency evaluation has been done using a fully Monte Carlo based procedure, i.e. obtaining the single pion efficiency values, $\varepsilon_{\rm like}(\theta_{\pi^\pm}, p_{\pi^\pm})$, from $\pi^+\pi^-\gamma$ Monte Carlo and then extracting the $\varepsilon_{\rm like}(s_\pi)$ according to Eq. 6.3. The result of this "full Monte Carlo based" procedure is in very good agreement with the one from data, as it can be seen in Fig. 6.8. Monte Carlo is also used to estimate the systematic uncertainty, as it will be explained below.

A further check has been performed using $\pi^+\pi^-\gamma$ Monte Carlo. The single pion ("mapping") method has been compared with the "direct" method. The latter consists in looking directly at the $\pi - e$ PID efficiency for a certain value of s_π. Then $\varepsilon_{\rm like}^{\pi\pi\gamma\ {\rm map}}(s_\pi)$ and $\varepsilon_{\rm like}^{\pi\pi\gamma\ {\rm dir}}(s_\pi)$ are compared for each bin of s_π. In Fig. 6.9 the ratio between the two methods is shown, proving an excellent agreement.

The values of $\varepsilon_{\rm like}^{\rm data}(s_\pi)$ shown in Fig. 6.7 are used as bin-by-bin corrections of the spectrum.

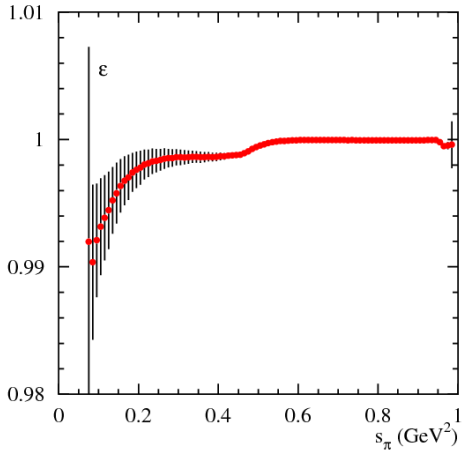

Fig. 6.7: PID likelihood efficiency as a function of the $\pi^+\pi^-$-system invariant mass.

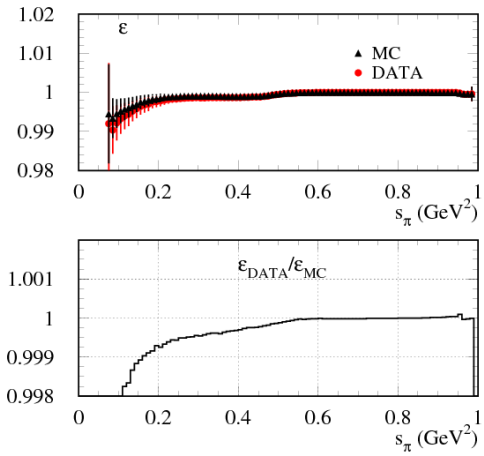

Fig. 6.8: PID likelihood efficiency as a function of the $\pi^+\pi^-$-system invariant mass evaluated from data, red circles, and from $\pi^+\pi^-\gamma$ Monte Carlo, black circles. The lower plots shows the relative difference.

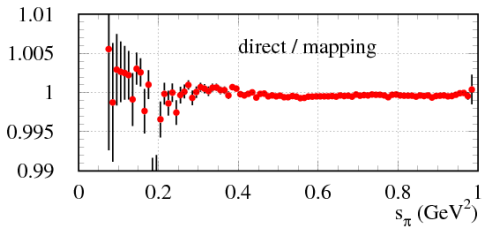

Fig. 6.9: Ratio between PID likelihood efficiencies evaluated by means of the single pion efficiency (mapping) and the direct method using $\pi^+\pi^-\gamma$ Monte Carlo sample.

Systematic error on the $\pi - e$ PID efficiency

The main cut applied to select the $\pi^+\pi^-\gamma$ sample in the $\pi - e$ PID efficiency evaluation is the cut on trackmass: $|M_{\rm trk} - m_\pi| < \Delta_{M_{\rm trk}}$ MeV, which, in the standard configuration, is $\Delta_{M_{\rm trk}} = 2.5$ MeV. The systematic uncertainty is thus estimated changing $\Delta_{M_{\rm trk}}$ according to the resolution in $M_{\rm trk}$(see Fig. 5.17(a)). The window has been opened up to 7.5 MeV, which correspond to about 1σ. The ratio

$$(\varepsilon_{\rm like}|\Delta'_{M_{\rm trk}})/(\varepsilon_{\rm like}|\Delta_{M_{\rm trk}})$$

is then evaluated, where $\Delta_{M_{\rm trk}}$ corresponds to the standard value $\Delta_{M_{\rm trk}} = 2.5$ MeV and $\Delta'_{M_{\rm trk}}$ corresponds to the modified window.
In Fig. 6.10 two examples of the ratio are shown. They are fitted by a third order polynomial

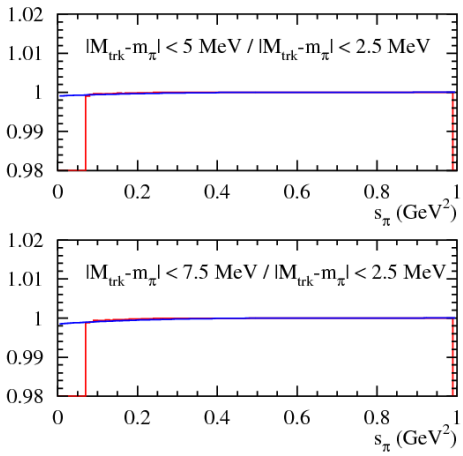

Fig. 6.10: Ratios between PID likelihood efficiencies using different cut in trackmass around m_π.

functions, represented by the red lines, in order to consider the behaviour as a function of s_π. As the systematic errors the maximum deviation from 1 among different ratios is taken, see Fig. 6.11. The `or`-configuration of the PID provides an high efficiency always above 99% and also guarantees a very small systematic uncertainty, smaller than 0.1% in the whole energy range. Actually, as already said, the only source of inefficiency comes from the association between the found cluster in the EMC and the track.

6.1.3 Trigger efficiency

In the 2006 data sample only the calorimeter trigger is used. An event, to be acquired, has to fire at least two *trigger sectors*, see Sec. 3.2.3. The fired sectors can be located either both in the barrel, or in the two endcaps (not in the same) or one in the barrel and the other in one of the two endcaps. However, because of the large angle acceptance cuts, the trigger sectors in the endcaps are not involved in this analysis.
Since one cluster can consist of more than one trigger sector, it may happen that one single particle can trigger the event. In this case one has a so-called "self triggering" particle, e.g. pion or photon.
The trigger efficiency, $\varepsilon_{\rm trg}$, is evaluated using ca. 50 pb^{-1} of data. Signal Monte Carlo is used only for testing and for evaluating the systematic uncertainty.

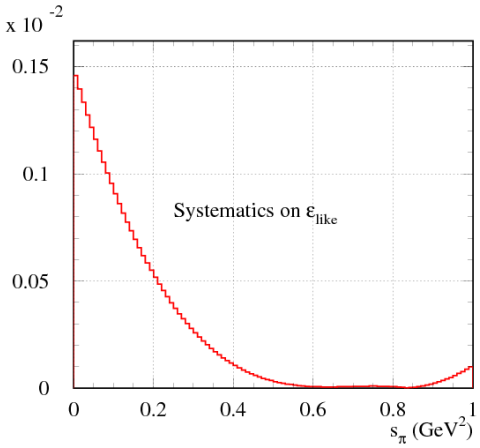

Fig. 6.11: Maximum deviation from 1 among the ratios computed varying the window around m_π in trackmass.

To evaluate the single particle efficiency (for π^+, π^- and γ) and to obtain an unbiased sample of the considered particle, two particles are required to trigger the event, then the trigger sectors fired by the remaining one are counted. An example is sketched in Fig. 6.12, where a π^- and a γ have triggered the event unbiasing the π^+, whose efficiency is measured.

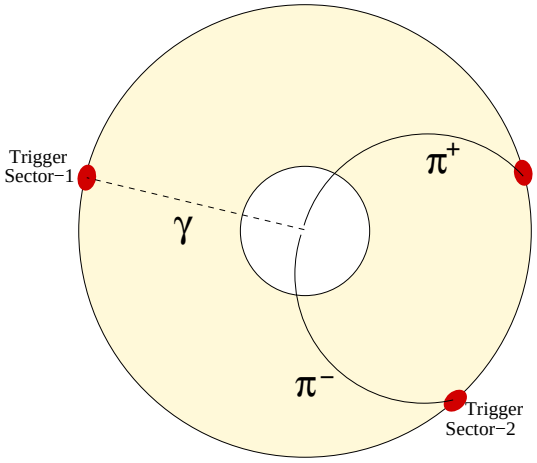

Fig. 6.12: Schematic representation of the single particle trigger efficiency. In this example a π^- and a γ are triggering the event providing an unbiased sample for π^+, whose probability of firing trigger sectors is measured.

The single particle efficiency, $\varepsilon_{\rm trg}(\theta_{\pi^+,\pi^-,\gamma}, p_{\pi^+,\pi^-,\gamma})$, is evaluated in 8 slices between 50° and 130° of polar angle and in 10 bins between 200 and 500 MeV for the pion momentum and in 10 bins between 50 and 500 MeV for the photon energy. The single particle efficiency can be seen in Fig. 6.13 for the positive pion, in Fig. 6.14 for the negative pion and in Fig. 6.15 for the photon. The trigger efficiency is very close to 100% for the photon, while for $\pi^\pm$ it is well above 97% in $|90° - \theta_{\pi^\pm}| < 30°$. At lower polar angles, $30° < |90° - \theta_{\pi^\pm}| < 40°$, the bending of the low momentum tracks in the magnetic field, causes a drop in the efficiency, as can be see in

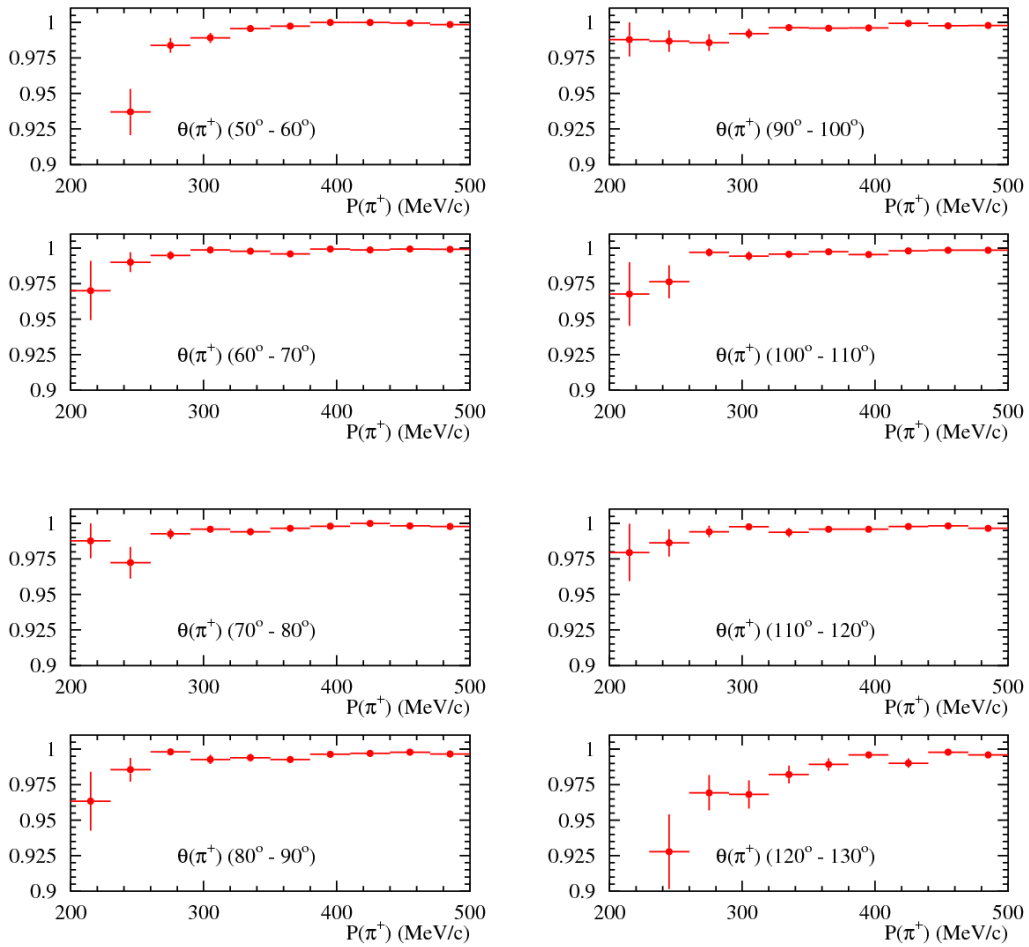

Fig. 6.13: Efficiency of firing at least one trigger sector for unbiased π^+ sample as a function of momentum in slices of polar angle.

Fig. 6.13 and Fig. 6.14. This drop is due to the less efficient performance of the barrel-endcaps intersections, where the bent tracks enter the calorimeter.

The trigger efficiency as a function of s_π is obtained applying the same mapping method used for the likelihood efficiency. The passage

$$\varepsilon_{\rm trg}(\theta_{\pi^+,\pi^-,\gamma}, p_{\pi^+,\pi^-,\gamma}) \rightarrow \varepsilon_{\rm trg}(s_\pi),$$

is performed taking the kinematic from Monte Carlo $\pi^+\pi^-\gamma$ events using

$$\varepsilon_{\rm trg}(s_\pi) = \frac{1}{N}\sum_{k=1}^{n} \nu_k \; \varepsilon_k, \tag{6.5}$$

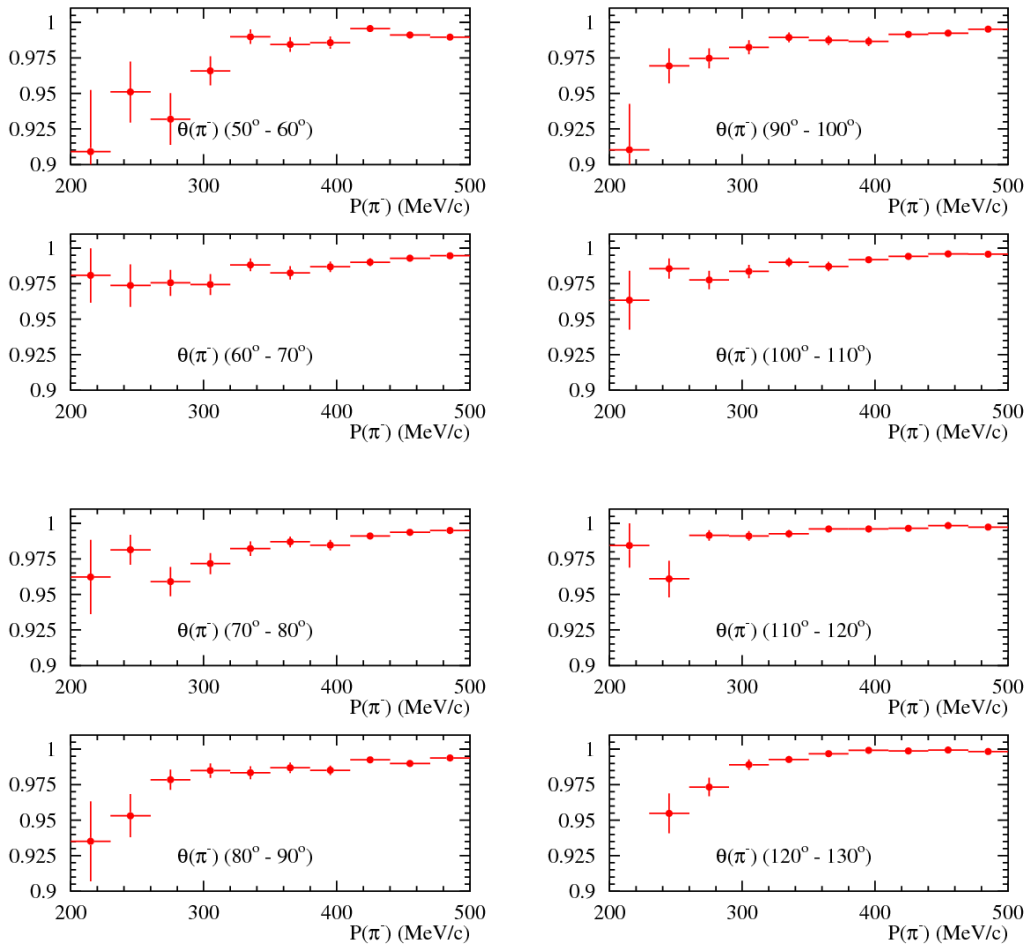

Fig. 6.14: Efficiency of firing at least one trigger sector for unbiased π^- sample as a function of momentum in slices of polar angle.

which is the analogous of Eq. 6.3. The parameter ε_k is given by

$$\begin{aligned}\varepsilon_k = 1 &- P_0^{\pi^+}(\theta,p)P_0^{\pi^-}(\theta,p)P_0^{\gamma}(\theta,p)\\ &- P_1^{\pi^+}(\theta,p)P_0^{\pi^-}(\theta,p)P_0^{\gamma}(\theta,p)\\ &- P_0^{\pi^+}(\theta,p)P_1^{\pi^-}(\theta,p)P_0^{\gamma}(\theta,p)\\ &- P_0^{\pi^+}(\theta,p)P_0^{\pi^-}(\theta,p)P_1^{\gamma}(\theta,p)\end{aligned} \tag{6.6}$$

where $P^j_{0(1)}(\theta,p)$ is the probability for the particle j (i.e. π^+, π^- or γ), at polar angle θ and momentum p, to fire 0 (1 and only 1) trigger sectors, evaluated with the single particle method described above. Inserting $\varepsilon_k^{\rm data}$, see Eq. 6.6, in Eq. 6.5 one gets $\varepsilon_{\rm trg}^{\rm data}(s_\pi)$. The trigger efficiency as a function of s_π is shown in Fig. 6.16. The efficiency is very close to 100%. The inefficiency is essentially due to the tracks, as explained before, since the photon is always firing at least one trigger sector. The $\pi^+\pi^-\gamma$ spectrum is corrected bin-by-bin for the result shown in Fig. 6.7.
A comparison between trigger efficiency evaluated from data, giving $\varepsilon_{\rm trg}^{\rm data}(\theta_{\pi^+,\pi^-,\gamma},p_{\pi^+,\pi^-,\gamma})$,

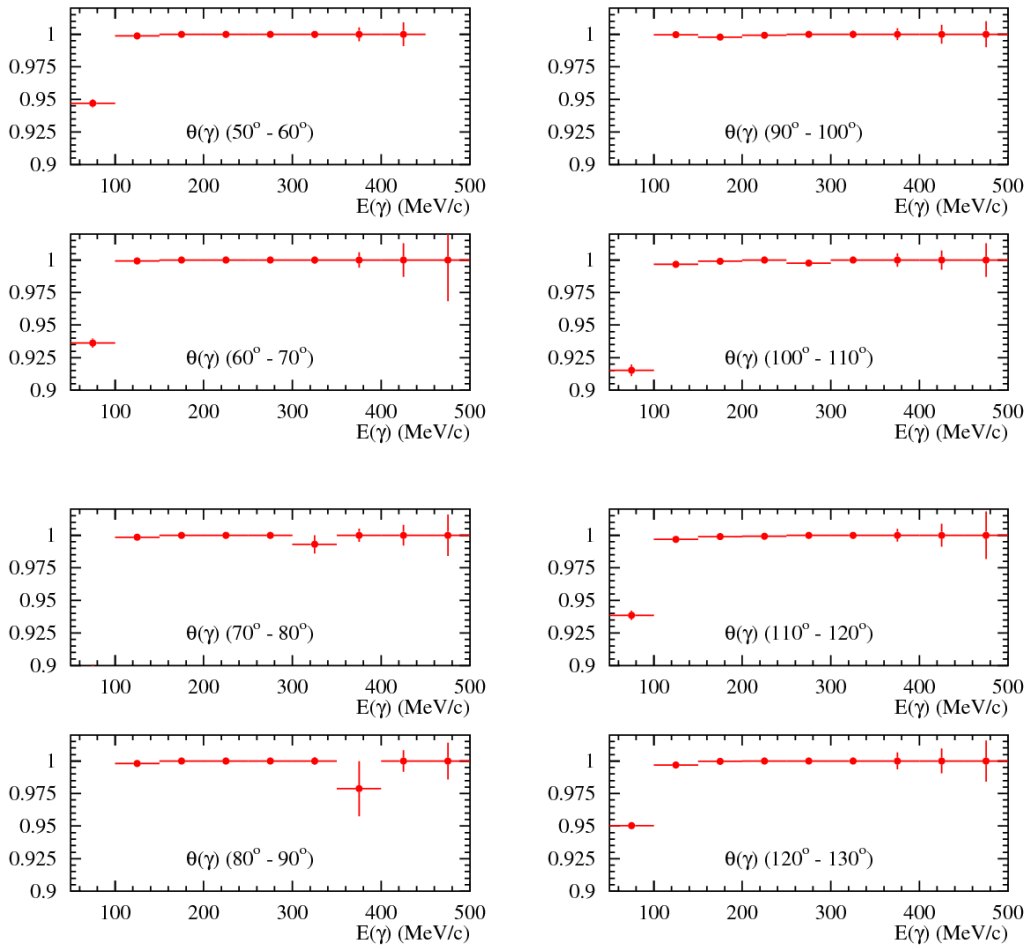

Fig. 6.15: Efficiency of firing at least one trigger sector for unbiased γ sample as a function of momentum in slices of polar angle.

and from $\pi^+\pi^-\gamma$ Monte Carlo sample, $\varepsilon_{\rm trg}^{\rm MC}(\theta_{\pi^+,\pi^-,\gamma}, p_{\pi^+,\pi^-,\gamma})$, has been performed. The ratio $\varepsilon_{\rm trg}^{\rm data}(s_\pi)/\varepsilon_{\rm trg}^{\rm MC}(s_\pi)$, evaluated after the mapping described by Eq. 6.5 and Eq. 6.6, is ca. 1×10^{-4} over the whole energy range.

Systematic error on the trigger efficiency

The evaluation of the systematic uncertainty is performed by comparing the single particle method, described above and indicated as "mapping", with the "direct" efficiency evaluation, using in both cases the $\pi^+\pi^-\gamma$ Monte Carlo sample. The direct method consists in looking at how many Monte Carlo events, for a certain bin of s_π, have fired at least two trigger sectors. The systematics is evaluated performing the ratio between $\varepsilon_{\rm trg}^{\pi\pi\gamma\ \rm dir}(s_\pi)$ and $\varepsilon_{\rm trg}^{\pi\pi\gamma\ \rm map}(s_\pi)$, where $\varepsilon_{\rm trg}^{\pi\pi\gamma\ \rm map}(s_\pi)$ is given by Eq. 6.5 and Eq. 6.6. In the upper plot of Fig. 6.17 the comparison between the two methods is shown. The ratio is fitted by a third order polynomial function, see the red line in the lower plot of Fig. 6.17, in order to keep the dependence on s_π of the systematic uncertainty.

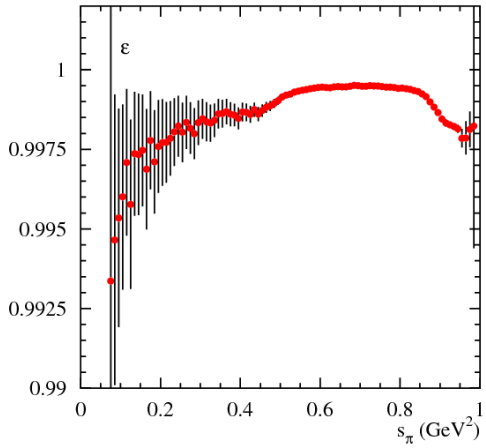

Fig. 6.16: Trigger as a function of the $\pi^+\pi^-$-system invariant mass.

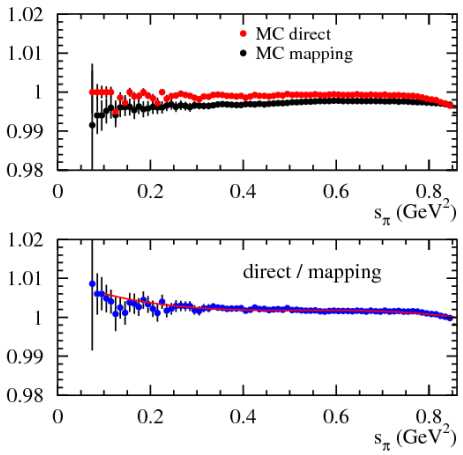

Fig. 6.17: The upper plot shows the comparison between the trigger efficiency evaluated with the single particle method, black circles, and the direct method, red circles. In the lower the ratio between the two, together with a fit function, is shown.

The systematic uncertainty, shown in Fig. 6.18, is then given by the deviation of the polynomial function from 1. The systematics reaches about 0.7% at the threshold region and, in the rest of the energy range, it is well below 0.3%.

6.2 Unfolding for detector resolution

The correction for the detector resolution (often also called *unfolding*) in s_π takes place right after the correction for those efficiencies which are directly evaluated from data control samples and before correcting for the effective global efficiency (see Fig. 6.1). As this implies the passage from *reconstructed events*, which take into account the effects of the detector, to the *generated*

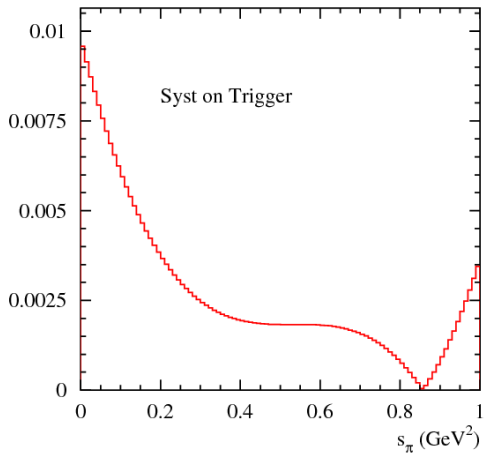

Fig. 6.18: Systematic uncertainty on trigger efficiency, given by the deviation from 1 of the function used to fit the ratio $\varepsilon_{\rm trg}^{\pi\pi\gamma\ {\rm dir}}(s_\pi)$ over $\varepsilon_{\rm trg}^{\pi\pi\gamma\ {\rm map}}(s_\pi)$, shown in Fig. 6.17.

(*true*) events,

$$s_\pi^{\rm rec} \rightarrow s_\pi^{\rm true},$$

subsequent corrections have to be performed in $s_\pi^{\rm true}$.
The number of events in a bin i of $s_\pi^{\rm true}$ can be related to the spectrum of observed events in bins j of $s_\pi^{\rm rec}$ via

$$N_i^{\rm true} = \sum_{j=1} P(N_i^{\rm true}|N_j^{\rm rec}) \cdot N_j^{\rm rec}, \tag{6.7}$$

where the sum runs over all bins of the reconstructed quantity $s_\pi^{\rm rec}$. The problem then consists in finding the quantity $P(N_i^{\rm true}|N_j^{\rm rec})$, which describes the bin-to-bin migration of events due to the reconstruction (and thus the detector resolution). This quantity determines the contribution of an observed event in bin j of $s_\pi^{\rm rec}$ to the bin i in $s_\pi^{\rm true}$.
Two methods have been used to evaluate $P(N_i^{\rm true}|N_j^{\rm rec})$:

1. Evaluating $P(N_i^{true}|N_j^{rec})$ directly from a sample of $\pi^+\pi^-\gamma$ Monte Carlo events, using the normalization condition

$$\sum_{i=1}^{n_{\rm true}} P(N_i^{\rm true}|N_j^{\rm rec}) = 1.$$

   This method assumes that each observed event must come from one or more bins of the true values of s_π. Then the correction reduces to a *matrix multiplication* of $P(N_i^{\rm true}|N_j^{\rm rec})$ with the vector of the observed spectrum in bins of $s_\pi^{\rm rec}$. However, a bias can be introduced due to the parametrization of $|F_\pi(s)|^2$ used in the Monte Carlo generation.

2. Evaluating $P(N_i^{\rm true}|N_j^{\rm rec})$ using Bayes' theorem [125]. This approach reduces the bias due to the parametrization for $|F_\pi(s)|^2$ used by defining $P(N_i^{\rm true}|N_j^{\rm rec})$ as

$$P(N_i^{\rm true}|N_j^{\rm rec}) = \frac{P(N_j^{\rm rec}|N_i^{\rm true}) \cdot P_0(N_i^{\rm true})}{\sum_{l=1}^{n_{\rm true}} P(N_j^{\rm rec}|N_l^{\rm true}) \cdot P_0(N_l^{\rm true})},$$

where the *initial probability* $P_0(N_l^{\text{true}})$ is changed in an iterative procedure to become more and more consistent with the distribution of N_i^{true}. Both $P_0(N_l^{\text{true}})$ and the *response matrix* $P(N_j^{\text{rec}}|N_i^{\text{true}})$ are obtained from a Monte Carlo production of $\pi^+\pi^-\gamma$ events.[1]

In Fig. 6.19, the probability matrix $P(N_i^{\text{true}}|N_j^{\text{rec}})$ from Monte Carlo is shown. The high precision of the KLOE drift chamber results in an almost diagonal matrix.

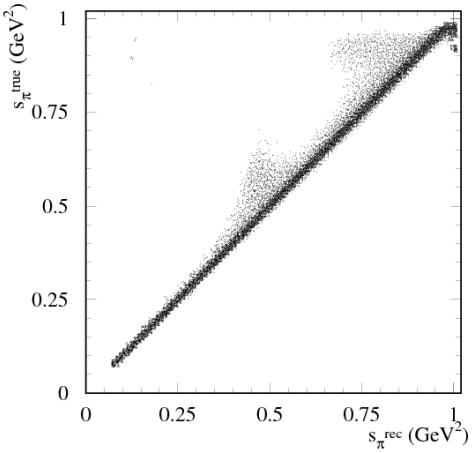

Fig. 6.19: The probability matrix $P(N_i^{\text{true}}|N_j^{\text{rec}})$ (*smearing matrix*) which represents the correlation between generated (true) and reconstructed values for s_π. The axis of the entries is in logarithmic scale.

Both methods give rather similar results. A smoothing of the spectrum to be unfolded is applied to avoid fluctuations caused by statistical limitations. The smoothing is performed only in the regions below 0.5 GeV^2 and between 0.7 and 0.95 GeV^2, and not in the region of the ρ-ω interference. The Bayesian method is applied in the analysis, while the matrix multiplication method is used to evaluate the systematic error.
Fig. 6.20 shows the outcome of the Bayes method, compared to the original input spectrum. The Bayesian approach with its iterative procedure, is less prone to introduce a bias from the $|F_\pi(s)|^2$ parametrization. It has also been verified that the outcome of the procedure does not depend on the χ^2-like cutoff value used to terminate the iteration loop.

Systematic error on the unfolding procedure

As an estimate of the systematic uncertainty due to the unfolding effect the absolute value of the difference between the two methods is taken. This gives a significant contribution only near the ρ-ω interference region, where the smallness of the width of the ω meson introduces strong variations in the shape of $|F_\pi(s)|^2$. In Fig. 6.21(b) the ratios between the unfolded over the input spectra are shown. The blue circles are referred to the Bayesian approach, while the red ones correspond to the matrix approach. It can be seen as the deviation between the two methods affects only the region within $[0.55 - 0.64]$ GeV^2.

[1] The code which is used in the procedure can be find in the authors' webpage [126]

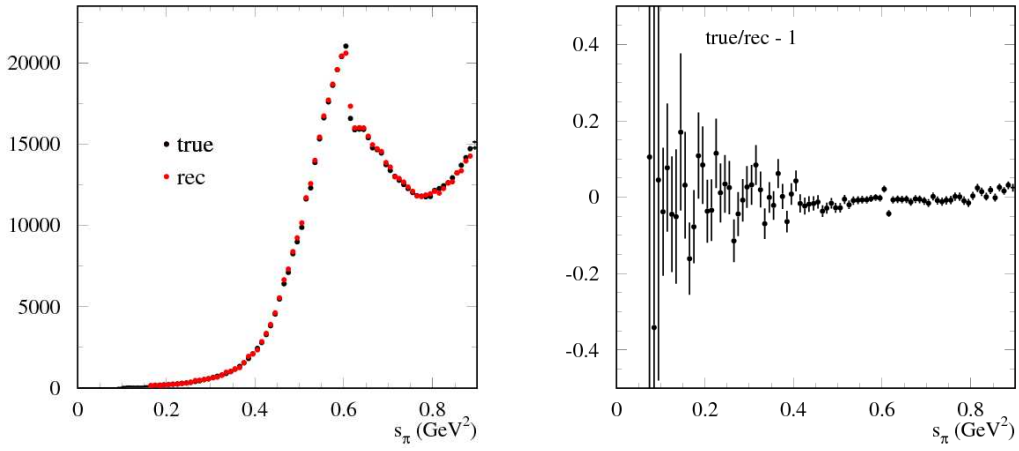

(a) (b)

Fig. 6.20: Left: input spectrum (red) in bins of s_π^{rec} and unfolded spectrum for Bayesian method (black) in bins of s_π^{true}. Right: relative difference between the unfolded spectrum (true) and the input one (rec).

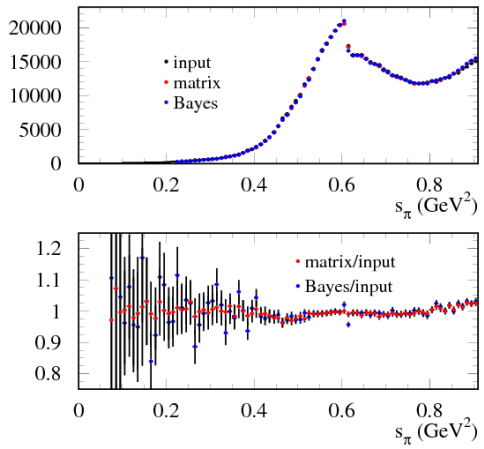

Fig. 6.21: In (a), the superimposition of the s_π input spectrum, in black, and those one unfolded by the Bayesian and by the matrix approaches, in blue and red circles respectively, is shown. In (b) the ration between the unfolded spectra over the input ones is drawn.

In Fig. 6.22 the systematic uncertainty, given by the absolute difference of the ratio

$$\frac{s_\pi^{\text{Bayes}} / s_\pi^{\text{input}}}{s_\pi^{\text{matrix}} / s_\pi^{\text{input}}},$$

in the ρ-ω interference region, is shown.
The unfolding has a negligible effect on the integral on $a_\mu^{\pi\pi}$, as it moves the major part of events between neighbouring bins.

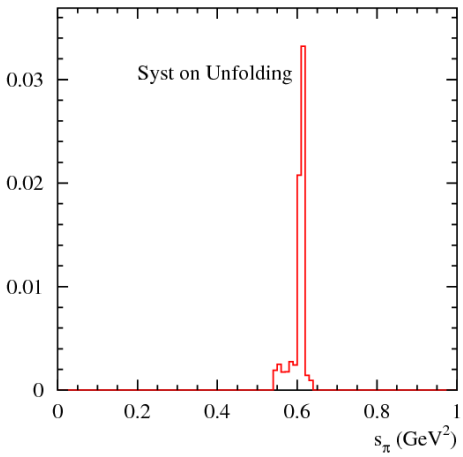

Fig. 6.22: Systematic uncertainty due to the unfolding procedure.

6.3 Effective global efficiency

The *global effective efficiency* approach consists in performing the ratio

$$\varepsilon_{\rm glob} = \frac{(dN_{\pi^+\pi^+\gamma}\,|\,\text{all analysis cuts})/(ds_\pi^{\rm true})}{(dN_{\pi^+\pi^+\gamma}\,|\,\text{full inclusive})/(ds_\pi^{\rm true})}. \tag{6.8}$$

Due to the fact that the unfolding for detector resolution effects has been already applied the $\pi^+\pi^-$-system invariant mass at Monte Carlo generated level, $s_\pi^{\rm true}$, is considered. By means of the full set of analysis cuts, we take into account:

– corrections for the geometrical acceptance:

$$50^\circ < \theta_\pi < 130^\circ \;;\; 50^\circ < \theta_\gamma < 130^\circ \;;\; E_\gamma > 20 \text{ MeV};$$

– signal loss due to selection cuts:

$$120 \text{ MeV} < M_{\rm trk} < M_{\rm trk}(s_\pi) \text{ as in Eq. 5.5; } \Omega < \Omega(s_\pi) \text{ as in Eq. 5.8;}$$

– signal loss due to data quality requests on momentum:

$$|p_T| > 160 \text{ MeV or } ; \; |p_z| > 90 \text{ MeV } ; \; |\vec{p}| > 200 \text{ MeV};$$

– corrections for tracking efficiency according to the request of

$$\rho_{\rm PCA} = \sqrt{x^2_{\rm PCA} + y^2_{\rm PCA}} < 8 \text{ cm } ; \; |z_{\rm PCA}| < 12 \text{ cm};$$

The $\pi^+\pi^-\gamma$ spectrum obtained after all selection cuts (Sec. 5.2), after the background subtraction (Sec. 5.4) and the unfolding procedure (Sec. 6.2) is then corrected by the global effective efficiency.

The value of $\varepsilon_{\rm glob}$ is shown in Fig. 6.23(a). The slope is mainly due to the large angle geometrical acceptance cuts, which are also the main source of the event loss.
In Fig. 6.23(b) the efficiency of the analysis cuts, i.e. after trackmass and Ω-angle efficiencies, is shown. The ratio is performed using as normalization sample the signal Monte Carlo events. It is worth to notice the high efficiency achieved for signal events achieved. The small dip just below 0.8 GeV^2 is due to the $M_{\rm trk}$ cut, as it can be seen already in Fig. 5.16.

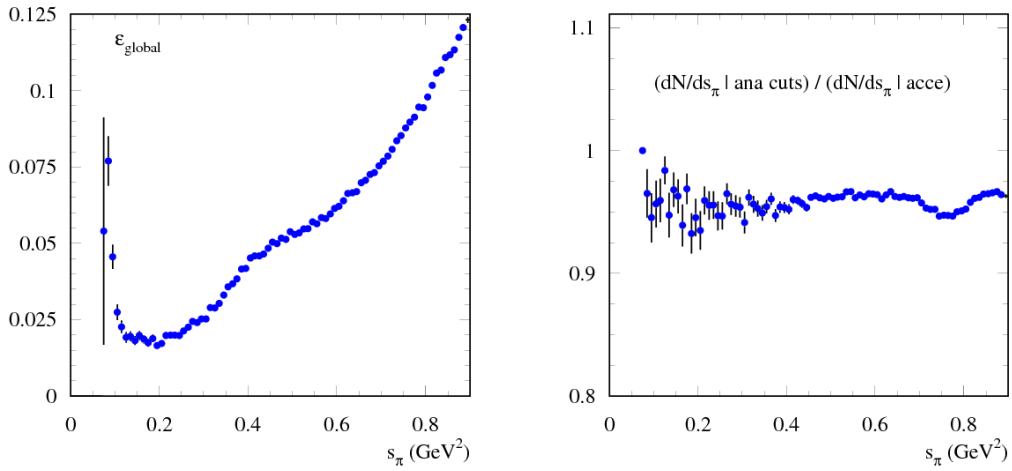

(a) (b)

Fig. 6.23: Effective global efficiency (a), according to the ratio of Eq. 6.8 and the cuts described in the text. In (b), efficiency of the analysis cuts (trackmass and Ω angle) normalized to events after Large Angle acceptance.

Systematic error on the acceptance efficiency

The geometrical acceptance is taken from Monte Carlo and included in the effective global efficiency approach.[2]
The evaluation of the systematic error introduced by the acceptance cuts is performed again by means of the double ratio approach, see Sec. 5.3.2 and Sec. 5.3.3. The double ratio has been performed moving separately the cuts on the pion polar angle and on the photon polar angle.
Varying the pion polar angle one can perform the double ratio

$$R_{\theta_\pi}(s_\pi) = \frac{(dN^{\rm data}_{\theta_\pi}/dN^{\rm MC}_{\theta_\pi})|_{\theta_\pi \pm 2^\circ}}{(dN^{\rm data}_{\theta_\pi}/dN^{\rm MC}_{\theta_\pi})|_{\theta_\pi}}(s_\pi), \tag{6.9}$$

where $\theta_\pi \pm 2^\circ$ stands for the standard cut on θ_π moved by 2°. Concerning the photon polar angle one has

$$R_{\theta_\gamma}(s_\pi) = \frac{(dN^{\rm data}_{\theta_\gamma}/dN^{\rm MC}_{\theta_\gamma})|_{\theta_\gamma \pm 5^\circ}}{(dN^{\rm data}_{\theta_\gamma}/dN^{\rm MC}_{\theta_\gamma})|_{\theta_\gamma}}(s_\pi), \tag{6.10}$$

[2] The asymmetric distribution of the pion polar angle, caused by the interference between FSR and ISR events (see Eq. 4.12), vanishes in the case of symmetric cuts on the pion polar angle.

where again $\theta_\gamma \pm 5°$ is referred to the the standard cut on θ_γ moved by 5°.
The quantity of the shifts – i.e. $\pm 2°$ for pions and $\pm 5°$ for photons – have been chosen according to the resolutions on θ_π and θ_γ. These are obtained from the difference between the generated value and the reconstructed one using Monte Carlo $\pi^+\pi^-\gamma$ sample, as shown in Fig. 6.24.

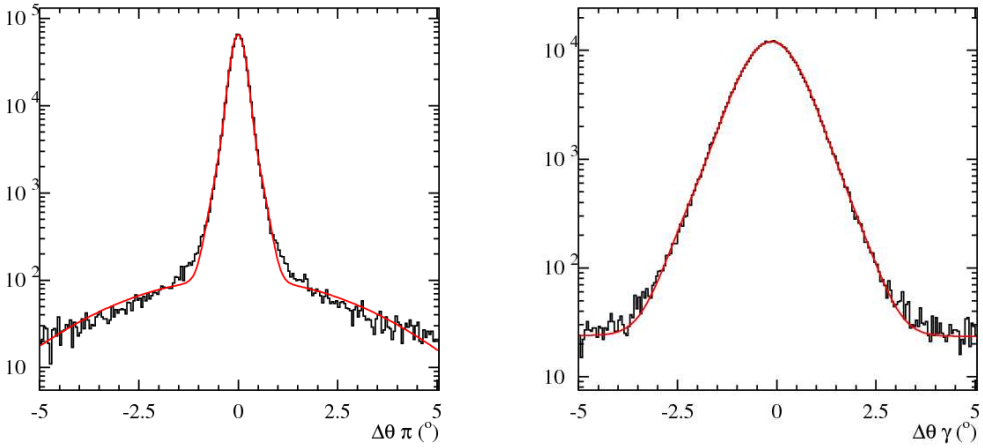

(a) (b)

Fig. 6.24: Resolutions on θ_π, in (a), and θ_γ, in (b).

The resolution on θ_π, shown in Fig. 6.24(a), has been fitted by three Gaussian distributions, to correctly describe also the tails. The third Gaussian function is required by less than 1% of the events, thus only the first two are taken into account, obtaining a σ of ca. 0.1° and 0.3° respectively, giving a global resolution of ca. 0.5°. The shift applied on θ_π then corresponds to 4σ.
The same evaluation has been performed for θ_γ, see Fig. 6.24(b), giving an estimated σ of about 1.5°. Thus, shifting the photon polar angle of 5° corresponds to ca. 3 times of the resolution.
Like the systematic uncertainty evaluation for $M_{\rm trk}$ and Ω-angle cuts, the spectra $dN^{\rm data}$ and $dN^{\pi\pi\gamma}$ in bin of 0.01 GeV^2 is s_π are extracted after having applied all the analysis cuts and after having subtracted the background events from $dN^{\rm data}$. Each of the four double ratios – two for $\theta_\pi \pm 2°$ and two for $\theta_\gamma \pm 5°$ – is fitted by a third order polynomial function, to reproduce the behaviour in s_π. The maximum deviation from 1 for each θ_π and θ_γ cut is taken, see Fig. 6.25(a) for the pion and Fig. 6.25(b) for the photon polar angle cuts, respectively.
The systematic error on the acceptance cut is given by the maximum deviation from 1 between $R(s_\pi)|_{\theta_\pi \pm 2°}$ and $R(s_\pi)|_{\theta_\gamma \pm 5°}$, as it is shown in Fig. 6.26. The uncertainty reaches ca. 2% at the $2m_\pi$-threshold, and dramatically drops down to ca. 0.5% in the higher energy range.

6.3.1 Tracking efficiency

The tracking efficiency takes into account not only the pure efficiency of the reconstruction algorithm, but also the effects due to the pion decay and nuclear interactions.[3]

[3] If only the tracking reconstruction algorithm efficiency was considered, the tracking efficiency would be actually 100%, since given some hits in the DC the pattern recognition procedure is almost always able to find a track, see Sec. 3.3.4.

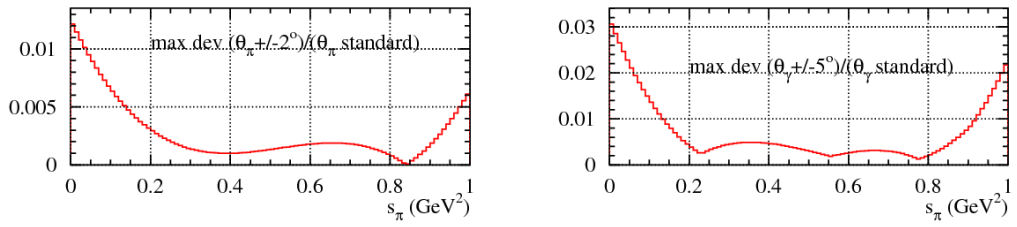

(a) (b)

Fig. 6.25: Maximum deviation from 1 of the two double ratios for the pion polar angle, $R(s_\pi)|_{\theta_\pi \pm 2^\circ}$, in (a), and of the two double ratios for the photon polar angle, $R(s_\pi)|_{\theta_\gamma \pm 5^\circ}$, in (b).

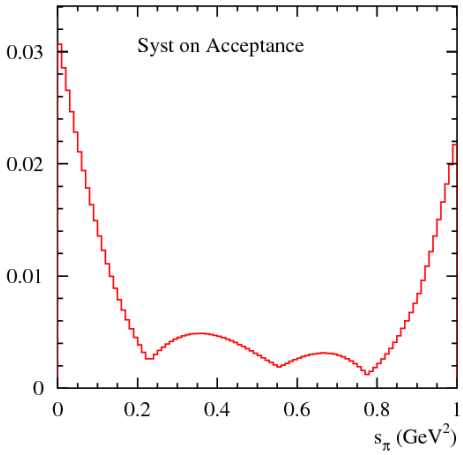

Fig. 6.26: Systematic uncertainty due to the acceptance cut as a function of s_π.

The efficiency of reconstructing the pion track is measured per single charge, both with Monte Carlo and data samples, conditioned to the presence of a tagging track of opposite sign. The efficiency to find the pion track of a given sign is parametrized as a function of momentum and polar angle slices of the expected track.
A sample of ca. 50 pb^{-1} of data and of effective 300 pb^{-1} of Monte Carlo is analyzed.[4] The efficiency is evaluated directly from signal events selected from these samples.
The selected events consist in

- at least one *tagging track*, satisfying the following requests:
  - the polar angle $50^\circ < \theta_{\rm tag} < 130^\circ$;
  - the radial position of the first hit in the drift chamber $\rho_{\rm FH} = \sqrt{x_{\rm FH}^2 + y_{\rm FH}^2} < 30$ cm and of the last hit $\rho_{\rm LH} = \sqrt{x_{\rm LH}^2 + y_{\rm LH}^2} > 180$ cm;

[4] The Monte Carlo signal sample has been produced with a scale factor of 6 in cross section with respect to data, giving in this way $L_{\pi\pi\gamma} = 6 \times L_{\rm data}$.

  * the extrapolated point of closest approach to the interaction point with $\rho_{\rm PCA} = \sqrt{x^2_{\rm PCA} + y^2_{\rm PCA}} < 8$ cm and with $|z_{\rm PCA}| < 7$ cm;
  * an associated cluster (after extrapolating the track to the calorimeter and looking for a cluster within a sphere of radius = 90 cm) recognized as a pion by the $\pi - e$ PID function, i.e. $\log \mathcal{L}_\pi/\mathcal{L}_e > 0.3$;

- 1 and only 1 photon with
  * the polar angle $50° < \theta_\gamma < 130°$;
  * the energy $E_\gamma > 50$ MeV;
- cut on track and photon missing quantity
  * the missing mass, $M_{\rm miss}$, evaluated using the 4-momentum conservation on momenta of the photon and the tagging track (having imposed the mass of the pion to the tagging track), must satisfy $|M_{\rm miss} - m_\pi| < 20$ MeV.

An event is defined efficient, when a fitted track with opposite charge with respect to the tagging one is found. The *expected track* to be considered an "efficient" track has to satisfy the following conditions:

* the radial position of the first hit: $\rho_{\rm FH} < 50$ cm;
* the position of the point of closest approach: $\rho_{\rm PCA} < 8$ cm and $|z_{\rm PCA}| < 12$ cm.

These conditions correspond to the same requests applied in the analysis.
The single track efficiency is evaluated for 6 bins from 200 MeV to 500 MeV in the expected track momentum and in 4 slice in polar angle within $|90° - \theta_{\rm exp}| < 40°$, both for data, $\varepsilon^{\rm data}_{\rm trk}(\theta_{\pi^\pm}, p_{\pi^\pm})$, and for Monte Carlo, $\varepsilon^{\rm MC}_{\rm trk}(\theta_{\pi^\pm}, p_{\pi^\pm})$. The results are shown in Fig. 6.27 and in Fig. 6.28 for positive and negative track, respectively. Data are represented by red and Monte Carlo by black circles.
For each slice of $\theta_{\pi^\pm}$ the ratio of the tracking efficiencies from data and Monte Carlo as a function of $p_{\pi^\pm}$ is computed:

$$c(\theta_{\pi^\pm}, p_{\pi^\pm}) = \frac{\varepsilon^{\rm data}_{\rm trk}(\theta_{\pi^\pm}, p_{\pi^\pm})}{\varepsilon^{\rm MC}_{\rm trk}(\theta_{\pi^\pm}, p_{\pi^\pm})}, \tag{6.11}$$

represented by the blue circles in the lower plots of Fig. 6.27 and Fig. 6.28 for the positive and negative track, respectively. The ratios result to be almost flat for the considered momentum range and in each slice of polar angle a linear fit is performed, whose value, $\zeta(\theta_{\pi^\pm})$, is used to obtain $\varepsilon_{\rm trk}(s_\pi)$. In Fig. 6.27 and Fig. 6.28 the linear fit is reported by the red line and the fit results are also indicated.
The tracking efficiency as a function of s_π is obtained by mapping these single pion efficiencies with generated kinematics from Monte Carlo. For a given bin in s_π (width = 0.01 GeV^2), the tracking efficiency is an average over the n different configurations of $(\theta_{\pi^+}, p_{\pi^+}, \theta_{\pi^-}, p_{\pi^-})$ contributing to that bin:

$$\varepsilon_{\rm trk}(s_\pi) = \frac{1}{N} \sum_{k=1}^{n} \nu_k \; \varepsilon_k, \tag{6.12}$$

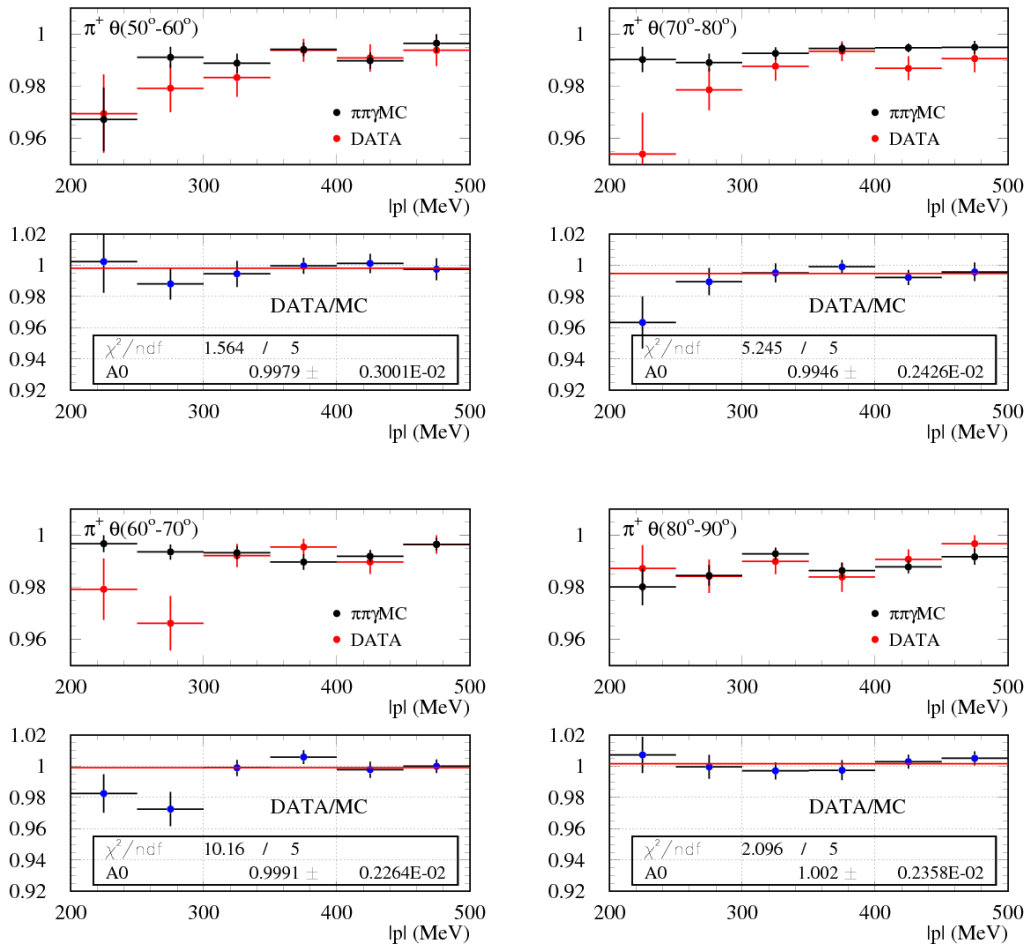

Fig. 6.27: Single track efficiency for π^+ sample as a function of momentum in slices of polar angle. Data are represented in red points and Monte Carlo in black points. Ratios between the efficiencies from data and from simulation are also shown, for each slice in polar angle. The red straight line is the linear fit performed to obtain the correction factors $\zeta(\theta_{\pi^+})$ used to evaluate the data efficiency as a function of s_π, $\varepsilon_{\rm trk}^{\rm data}(s_\pi)$.

where N is the number of Monte Carlo events used to compute the frequency ν_k of the occurrence of a certain k configuration.
To evaluate the efficiency per event for the Monte Carlo sample, i.e. to perform the passage

$$\varepsilon_{\rm tk}^{\rm MC}(\theta_{\pi^\pm}, p_{\pi^\pm}) \rightarrow \varepsilon_{\rm trk}^{\rm MC}(s_\pi),$$

the input, ε_k, to Eq. 6.12 is

$$\varepsilon_k = \varepsilon_{\rm trk}^{\rm MC}(\theta_{\pi^+}, p_{\pi^+})\varepsilon_{\rm trk}^{\rm MC}(\theta_{\pi^-}, p_{\pi^-}). \tag{6.13}$$

To get the efficiency for data as a function of s_π

$$\varepsilon_{\rm trk}^{\rm data}(\theta_{\pi^\pm}, p_{\pi^\pm}) \rightarrow \varepsilon_{\rm trk}^{\rm data}(s_\pi)$$

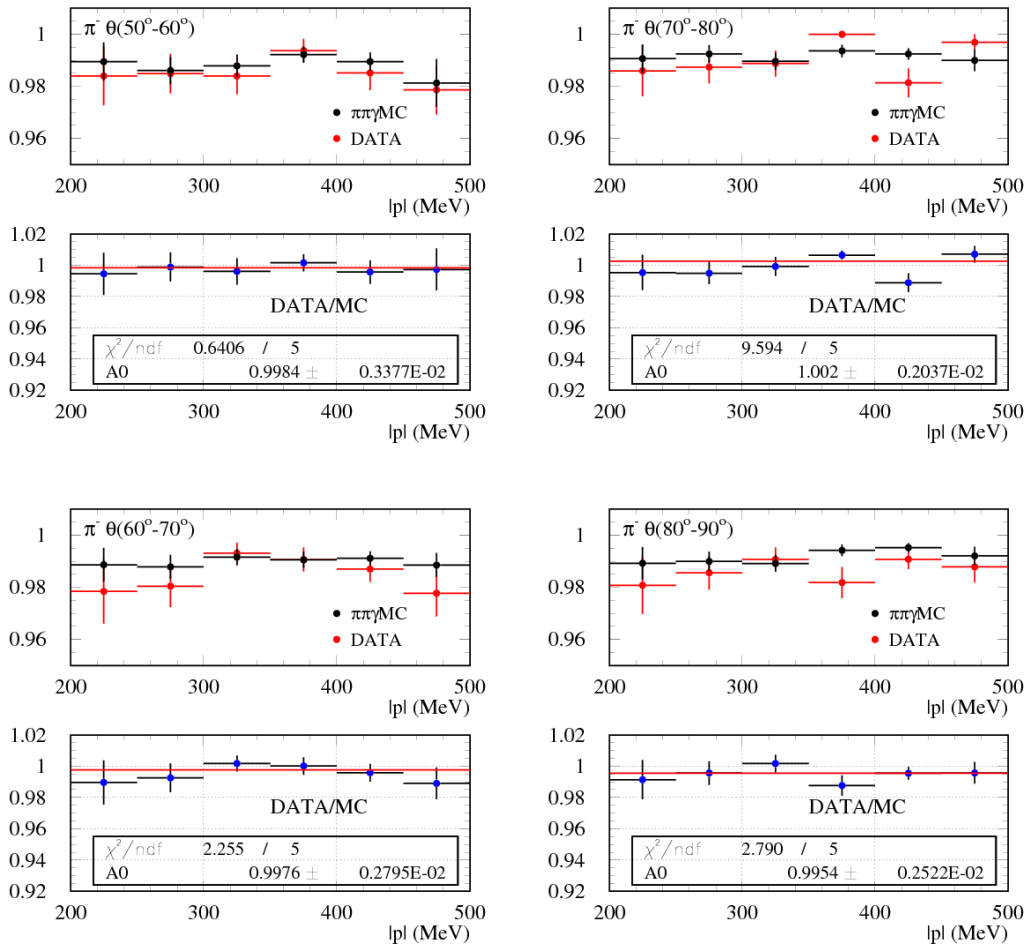

Fig. 6.28: Single track efficiency for π^- sample as a function of momentum in slices of polar angle. Data are represented in red points and Monte Carlo in black points. Ratios between the efficiencies from data and from simulation are also shown, for each slice in polar angle. The red straight line is the linear fit performed to obtain the correction factors $\zeta(\theta_{\pi^-})$ used to evaluate the data efficiency as a function of s_π, $\varepsilon_{\rm trk}^{\rm data}(s_\pi)$.

the correction factors, $\zeta(\theta_{\pi^\pm})$, are used, which have been obtained by fitting the data-Monte Carlo ratio (see Fig. 6.27 and Fig. 6.28). The parameter ε_k is given by:

$$\varepsilon_k = \zeta(\theta_{\pi^+})\varepsilon_{\rm trk}^{\rm MC}(\theta_{\pi^+}, p_{\pi^+}) \cdot \zeta(\theta_{\pi^-})\varepsilon_{\rm trk}^{\rm MC}(\theta_{\pi^-}, p_{\pi^-}). \tag{6.14}$$

The choice of using in both the two evaluations $\varepsilon_{\rm trk}^{\rm MC}(\theta_{\pi^\pm}, p_{\pi^\pm})$ from Monte Carlo – properly corrected by $\zeta(\theta_{\pi^\pm})$ in the case of data – is motivated by the bigger statistics of the simulation with respect to the data one. In Fig. 6.29(a) the results for $\varepsilon_{\rm trk}^{\rm data}$ is shown. In Fig. 6.29(b) data (red points) and Monte Carlo (black points) comparison (upper plot) and the ratio (lower plot) are presented. It is worth to notice the good agreement between experimental sample and simulation, giving a correction on $\Delta\varepsilon$ due to tracking (see Eq. 6.2) of ca. 0.3%.

Since in the effective global efficiency approach the tracking reconstruction is included in $\varepsilon_{\rm glob}$, the spectrum is bin-by-bin corrected by the data–Monte Carlo difference for the tracking

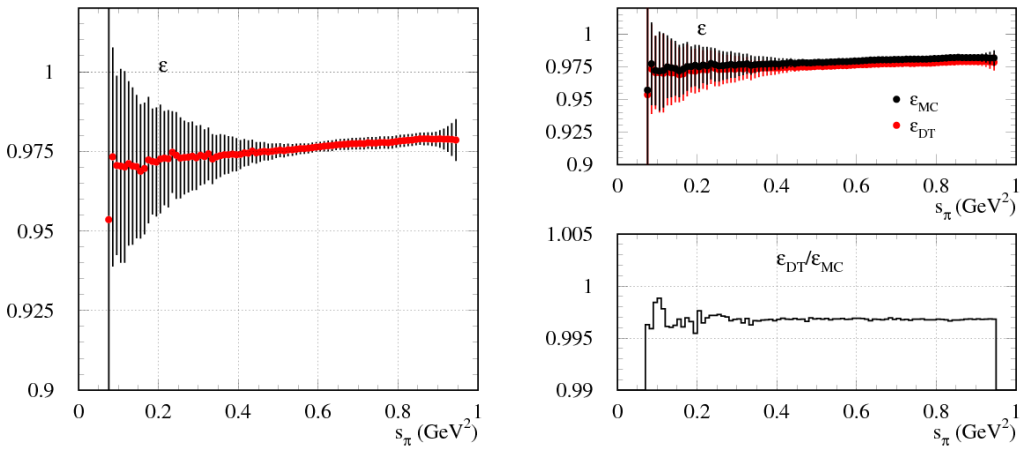

(a) (b)

Fig. 6.29: In (a) the tracking efficiency for data, evaluated according to Eq. 6.14 is shown. The comparison between data and Monte Carlo is visible in (b, upper) and the data–Monte Carlo ratio is drawn in (b, lower). The spectrum is bin-by-bin corrected by this ratio.

efficiency. The data-Monte Carlo discrepancy is mainly due to a not perfect simulation of split and spiralizing tracks in the simulation. An example of this kind of events is shown in Fig. 6.30 where a front and a side view of the KLOE detector are drawn. To reduce the presence of

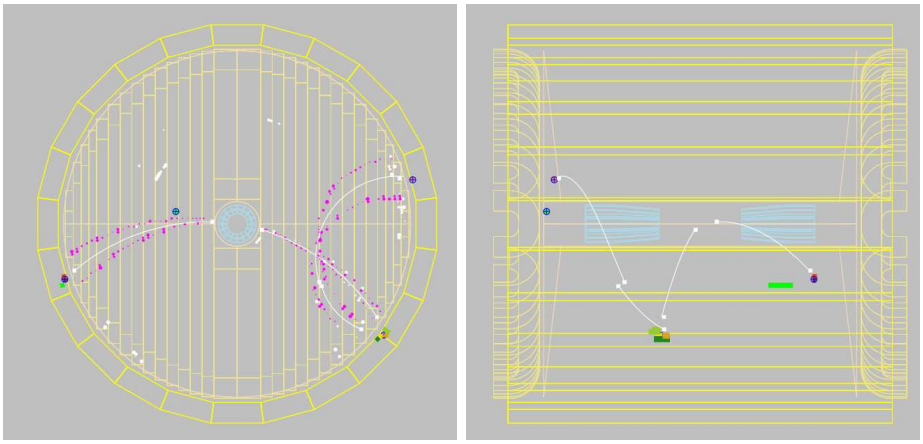

(a) (b)

Fig. 6.30: A front (a) and side (b) view of the KLOE detector of a typical data event where a split track is present. This kind of events are not precisely reproduced by Monte Carlo.

these events, which happen essentially only for low momentum tracks, a cut $|\vec{p}_{trk}| > 200$ MeV is applied. This cut introduces an inefficiency for signal event of ca. 15%.
Several test have been performed to verify the result on the tracking efficiency. Possible influences from the trigger efficiency and from the presence of residual $\mu^+\mu^-\gamma$ and $\pi^+\pi^-\pi^0$ events have been checked.
In addition to the conditions described above, the tagging track has been required also to trigger

the event. This is fulfilled by ca. 30% of the events. The "self triggering" requirement causes a negligible change of ca. 0.1% on $\varepsilon_{\rm trk}(s_\pi)$, coherently on data and Monte Carlo, leaving unchanged the agreement between the two.
Defining α as the angle between the missing momentum – with respect to the tagging track and the detected photon – and the found expected track momentum (see Fig. 6.31), one can cut on that variable to reject possible residual $\pi^+\pi^-\pi^0$ events. The 3π sample is already strongly reduced by the cut on missing mass ($|M_{\rm miss} - m_\pi| < 20$ MeV), resulting in about 10^{-3} less event than signal. Even if a-priori there is no reason to expect a different tracking efficiency between the $\pi^+\pi^-\gamma$ and the $\pi^+\pi^-\pi^0$ samples, since the tracks are generated by the same kind of charged particle, cuts on α, from 5° to 20°, have been applied to test this hypothesis. Only negligible differences in absolute efficiency are found, which leaves unchanged the data-Monte Carlo ratios.

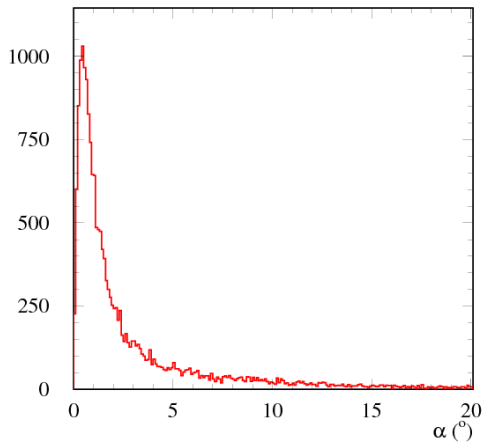

Fig. 6.31: Angle between the missing momentum, from the tagging track and the photon, and the candidate track found for data sample.

Systematic error on the tracking efficiency

The main cause of inefficiency consists in the fact that the candidate track does not satisfy one of the following conditions

* $\rho_{\rm FH} < 50$ cm;
* $\rho_{\rm PCA} < 8$ cm;
* $|z_{\rm PCA}| < 12$ cm.

To evaluate the systematic uncertainty of the tracking efficiency each of the conditions listed above has been moved, keeping the others unchanged. The systematic uncertainty is then obtained from the ratio

$$(\varepsilon^{\rm data}_{\rm trk}|cut'_{(\rho_{\rm FH},\rho_{\rm PCA},|z_{\rm PCA}|)})/(\varepsilon^{\rm data}_{\rm trk}|cut_{(\rho_{\rm FH},\rho_{\rm PCA},|z_{\rm PCA}|)}), \qquad (6.15)$$

where the efficiency values $\varepsilon_{\rm trk}$ are obtained directly from the data sample, and *cut* indicates the conditions on first hit and point of closest approach applied to evaluate the efficiency, while *cut′* stays for the shifted requests, either on the point of closest approach or on the first hit. Each ratio is fitted with a third order polynomial function.
The radial position of the first hit inside the drift chamber is moved from a minimal value of 45 cm to a maximum of 60 cm. The values of the ratios

$$(\varepsilon^{\rm data}_{\rm trk}|_{\rho_{\rm FH}<45})/(\varepsilon^{\rm data}_{\rm trk}|_{\rho_{\rm FH}<50}) \text{ and } (\varepsilon^{\rm data}_{\rm trk}|_{\rho_{\rm FH}<60})/(\varepsilon^{\rm data}_{\rm trk}|_{\rho_{\rm FH}<50}),$$

are shown in the upper and lower plot of Fig. 6.32.

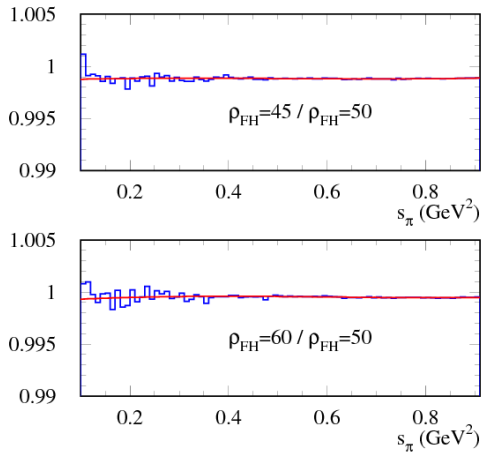

Fig. 6.32: Ratio between the tracking efficiency varying the radial position of the first hit. The red lines represent the polynomial functions used to fit the ratio.

The conditions on the point of closest approach have been moved from 6 cm to 10 cm, for $\rho_{\rm PCA}$, and from 10 cm to 14 cm, for $|z_{\rm PCA}|$. In Fig. 6.33 and Fig. 6.34 the ratios

$$(\varepsilon^{\rm data}_{\rm trk}|_{\rho_{\rm PCA}<6})/(\varepsilon^{\rm data}_{\rm trk}|_{\rho_{\rm PCA}<8}) \text{ and } (\varepsilon^{\rm data}_{\rm trk}|_{\rho_{\rm PCA}<10})/(\varepsilon^{\rm data}_{\rm trk}|_{\rho_{\rm PCA}<8})$$

and

$$(\varepsilon^{\rm data}_{\rm trk}|_{|z_{\rm PCA}|<10})/(\varepsilon^{\rm data}_{\rm trk}|_{|z_{\rm PCA}|<12}) \text{ and } (\varepsilon^{\rm data}_{\rm trk}|_{|z_{\rm PCA}|<14})/(\varepsilon^{\rm data}_{\rm trk}|_{|z_{\rm PCA}|<12})$$

are reported.
The systematic error is evaluated as the maximum deviation from 1 between each of the two rations on $\rho_{\rm FH}$, $\rho_{\rm PCA}$ and $|z_{\rm PCA}|$. The total uncertainty for the tracking efficiency, shown in Fig. 6.35, is obtained by adding in quadrature the three maximum deviations. The systematic errors is about 0.3% in the whole s_π range.

6.3.2 Photon efficiency

The calorimeter photon efficiency has been measured using a sample of $\pi^+\pi^-\pi^0$ events, selected from data requiring two opposite charged tracks from the IP, and requiring the missing mass around the mass of π^0. One of the two photons from the neutral pion decay is detected, as a *tagging photon*, and the event is defined efficient if another neutral cluster is found within a cone

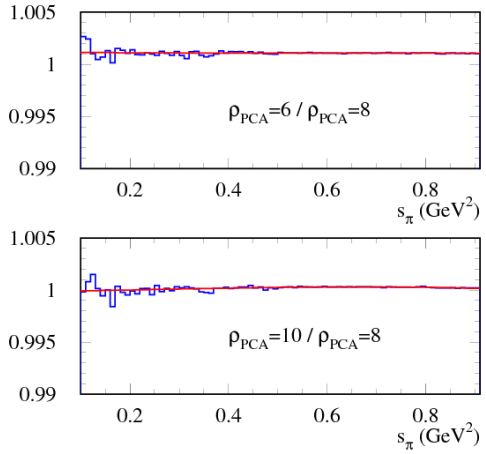

Fig. 6.33: Ratio between the tracking efficiency varying the radial position of the extrapolated point of closest approach of the track to the interaction point. The red lines represent the polynomial functions used to fit the ratio.

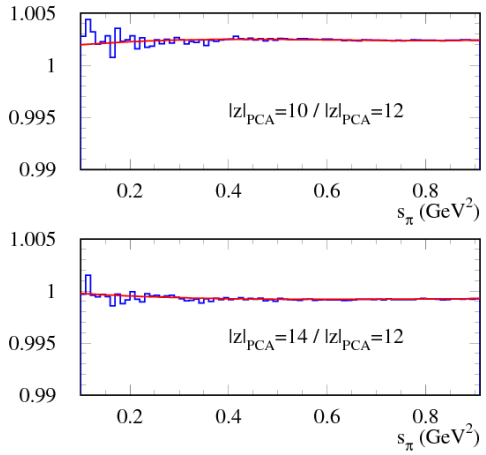

Fig. 6.34: Ratio between the tracking efficiency varying the longitudinal position of the point of closest approach. The red lines represent the polynomial functions used to fit the ratio.

around the expected direction. The efficiency is evaluated in bins of polar angle of the expected energy. Using the mapping procedure, the result as a function of the pion invariant mass, $\varepsilon_\gamma(s_\pi)$, is obtained. For a detailed explanation of the procedure see [127].
The calorimeter efficiency for photon detection is already included in the effective global efficiency, therefore the relevant quantity is the data-Monte Carlo ratio. The ratio as a function of s_π is shown in Fig. 6.36. Data and Monte Carlo samples are in excellent agreement in the energy range considered in the analysis described in this work, delimited by the red line, set at $s_\pi = 0.85$ GeV^2. However the $\pi^+\pi^-\gamma$ spectrum is bin-by-bin corrected by $\varepsilon_\gamma^{\rm data}/\varepsilon_\gamma^{\rm MC}$.

Due to the very high efficiency and the extremely good data-Monte Carlo agreement, we consider the systematic uncertainty on the photon detection efficiency as negligible.

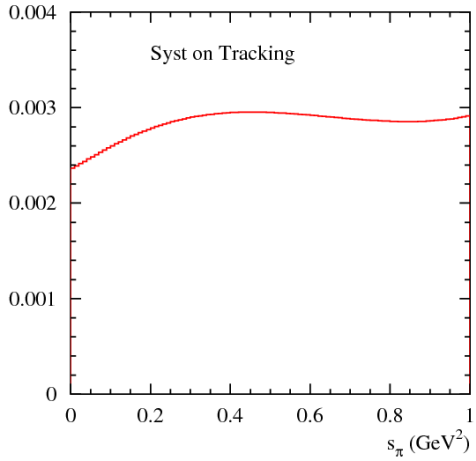

Fig. 6.35: The maximum deviation from 1 of the ratios, see Eq. 6.15, for each condition is shown: ρ_{FH} in green, ρ_{PCA} in red and $|z_{\mathrm{PCA}}|$ in violet. To evaluate the total systematic uncertainty, shown in black, the three contributions are added in quadrature.

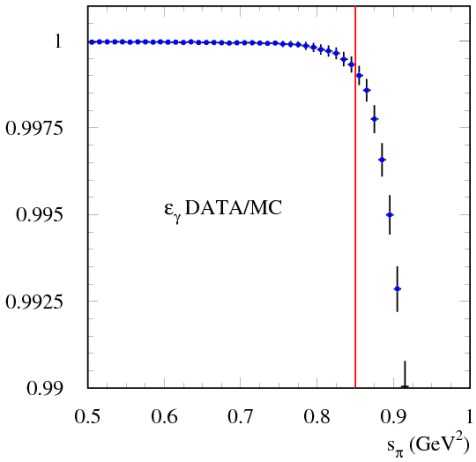

Fig. 6.36: Photon efficiency as a function of s_π.

6.4 Correction for final state radiation events

The transition from s_π to s_{γ^*} is performed using a special version of the PHOKHARA Monte Carlo generator [128]. This version of the generator allows to distinguish between photons radiated in the initial state from photons emitted in the final state. The presence of final state radiation shifts the observed value of s_π (evaluated from the momenta of the two charged pion tracks in the events) away from the value of the invariant mass squared of the virtual photon produced in the collision. The shift occurs only in one direction, $s_{\gamma^*} \geq s_\pi$, as can be seen in the spectra reported in Fig. 6.38.

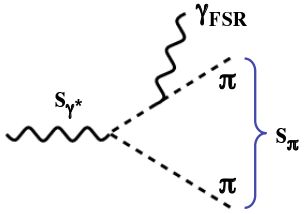

Fig. 6.37: Graphical description of the shifting in the $\pi^+\pi^-$-system invariant mass, from s_{γ^*} to s_π, due to the photon emission by a pion.

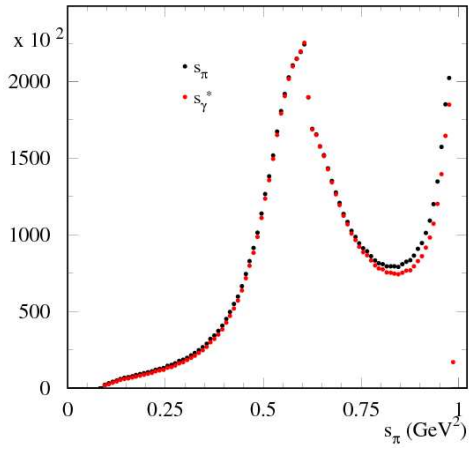

Fig. 6.38: The spectra of s_{γ^*} in red points, and of s_π, in black points.

To find out to which bin of s_{γ^*} an event with a measured value of s_π belongs, a population matrix and a probability matrix, shown in Fig. 6.39(a) and Fig. 6.39(b) respectively, have been constructed. The method, based on a matrix multiplication is similar to that one used to evaluate the systematic error of the unfolding procedure (see Sec. 6.2). In this way one can *un-shift* the spectrum performing the passage

$$s_\pi \longrightarrow s_{\gamma^*}.$$

In order to be as much as possible inclusive in NLO-FSR events, the energy range considered is broader than that one chosen for the result: the un-shifting is performed in the range $[0. - 1.02]$ GeV^2 instead of $[0. - 0.85]$ GeV^2 considered in the measurement.
The spectrum is unshifted after having corrected by acceptance effects (included in the effective global efficiency). Thus the $s_\pi \longrightarrow s_{\gamma^*}$ procedure is fully inclusive for the polar angle. The presence of FSR events is of the order of several percent, as can be seen in Fig. 6.40, where the un-shifting correction is reported by the ratio between s_π and s_{γ^*}. At low values of the pion system invariant mass, the relative increase of final state radiation effects due to events with the emission of two photons, one photon from ISR and the other one from FSR (NLO-FSR), is larger than 15%.

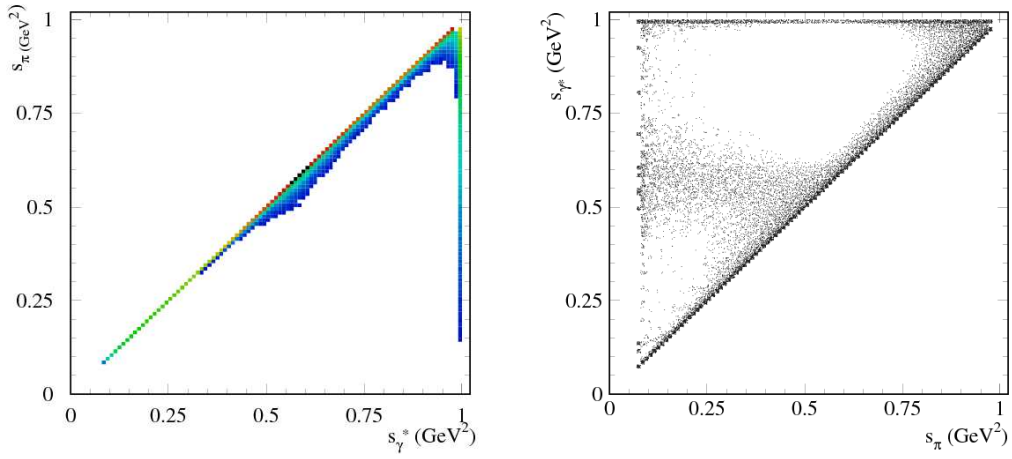

(a) (b)

Fig. 6.39: In (a) the population matrix used in the unshifting procedure is shown. In (b) the probability matrix used to unshift the s_π spectrum.

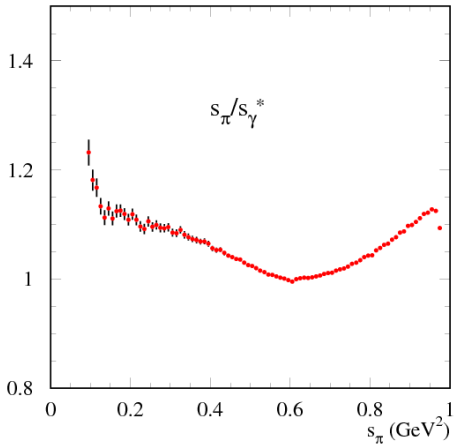

Fig. 6.40: In (b), unshifting correction due to final state radiation on the spectrum (obtained from Monte Carlo).

6.5 Luminosity

The absolute normalization of the data spectrum is obtained by dividing to the integrated luminosity. The luminosity is measured with the KLOE detector itself looking at Bhabha events at large polar angles, $55° < \theta_{e^\pm} < 125°$ (*Very Large Angle Bhabha, VLAB*). At the energy equal to 1 GeV, the cross section for such events is ~ 440 nb, big enough to make the statistical error completely negligible. The integrated luminosity, L, is provided by:

$$L = \frac{N_{\rm obs} - N_{\rm bkg}}{\sigma_{\rm eff}}, \tag{6.16}$$

where $N_{\rm obs}$ is the number of candidate Large Angle Bhabha events, $N_{\rm bkg}$ is the number of background events and $\sigma_{\rm eff}$ is the effective cross section for the KLOE VLAB selection cuts. The effective cross section is evaluated with the `Babayaga` Monte Carlo generator [129] – including QED radiative corrections with the parton shower approach – interfaced with the KLOE detector simulation `GEANFI` [130]. Detailed explanation of the measurement can be found in [131].
An updated version of the generator, `Babayaga@NLO` [108] is used for the luminosity evaluation. In this version the new predicted cross section decreases by 0.7% [5] and the theoretical uncertainty improves from 0.5% to 0.1% with respect to the older version.
Concerning the experimental systematic error, differently from 2001 data taking, the hardware veto of cosmic rays is not applied anymore. This implies a negligible inefficiency in the analysis of VLAB events. However the new hardware set also causes an increasing of the background process $e^+e^- \to \pi^+\pi^-$, which needs to be subtracted from data, giving a relative correction of 0.5%.

The relative systematic error on the luminosity measurement is: $\delta_{\rm th} \oplus \delta_{\rm exp} = 0.3\%$. Specific studies on the luminosity evaluation dedicated to 2006 data sample will be performed soon in order to cross check this uncertainty.

6.6 Radiative corrections

As shown in Eq. 6.2 to obtain the cross section $\sigma(e^+e^- \to \pi^+\pi^-)$, the radiator function, $H(s_{\gamma^*}, s)$, has to be taken into account and radiative correction, $\delta_{\rm rad}$, are required.

6.6.1 The radiator function

The radiative differential cross section $d\sigma(e^+e^- \to \pi^+\pi^- + \gamma_{\rm ISR}(\gamma_{\rm ISR}))(s_{\gamma^*}, \theta_\gamma)/ds_{\gamma^*}$ and the total cross section for the process $e^+e^- \to \pi^+\pi^-$, in the absence of photons from final state radiation, are related by a theoretical radiator function, $H(s_{\gamma^*}, s, \theta_\gamma)$, via the equation [133, 134]

$$\frac{d\sigma(e^+e^- \to \pi^+\pi^- + \gamma_{\rm ISR}(\gamma_{\rm ISR}))(s_{\gamma^*}, \theta_\gamma)}{ds_{\gamma^*}} \cdot s = H(s_{\gamma^*}, s, \theta_\gamma) \times \sigma(e^+e^- \to \pi^+\pi^-)(s_{\gamma^*}). \quad (6.17)$$

Here s_{γ^*} is the squared of the momentum transferred, identical to the squared of the virtual photon invariant mass (and, in absence of FSR, equal to s_π), s is the squared Center-of-Mass energy of the DAΦNE collider, and θ_γ is the polar angle of the photon or the photon polar angle obtained from the two pion system (in the case that there is more than one photon).
The dimensionless quantity H describes the emission of soft, virtual and hard photons in the initial state.
Using $\sigma_{\pi\pi}(s_{\gamma^*}) = \frac{\pi\alpha^2}{3s_{\gamma^*}}\beta_\pi^3|F_\pi(s_{\gamma^*})|^2$, it is possible to rewrite Eq. 6.17 as[6]

$$\frac{d\sigma_{\pi\pi\gamma(\gamma)}(s_{\gamma^*}, \theta_\gamma)}{ds_{\gamma^*}} = \frac{H(s_{\gamma^*}, s, \theta_\gamma)}{s} \times \frac{\pi\alpha^2}{3s_{\gamma^*}}\beta_\pi^3|F_\pi(s_{\gamma^*})|^2. \quad (6.18)$$

Exploiting Eq. 6.18 and the `PHOKHARA` Monte Carlo generator, which contains ISR processes up to the next-to-leading order [134], one can obtain the H-function. Setting $|F_\pi(s_{\gamma^*})|^2 = 1$

[5] For a comparison of the Bhabha cross section with other generators see [131].

[6] $\beta_\pi = \sqrt{1 - \frac{4m_\pi^2}{s_{\gamma^*}}}$.

in the generator (and switching off the vacuum polarization of the intermediate photon in the generator), $H(s_{\gamma^*}, s, \theta_\gamma)$ becomes

$$H(s_{\gamma^*}, s, \theta_\gamma) = s \cdot \frac{3 s_{\gamma^*}}{\pi \alpha^2 \beta_\pi^3} \cdot \frac{d\sigma_{\pi\pi\gamma(\gamma)}(s_{\gamma^*}, \theta_\gamma)}{d s_{\gamma^*}} \Big|^{\mathrm{MC}}_{|F_\pi(s_{\gamma^*})|^2=1}. \tag{6.19}$$

If the case that the width of the bins ds_{γ^*} is chosen identical for the measured differential cross section $\frac{d\sigma_{\pi\pi\gamma(\gamma)}}{ds_{\gamma^*}}$ and for the quantity $\frac{d\sigma_{\pi\pi\gamma(\gamma)}}{ds_{\gamma^*}}\Big|^{\mathrm{MC}}_{|F_\pi(s_{\gamma^*})|^2=1}$ obtained from Monte Carlo, the division by H automatically allows the transition from a differential to an absolute cross section.
In the analysis H is evaluated for $0° < \theta_\gamma < 180°$, since the spectrum has been already corrected by acceptance cuts. The radiator function is shown in Fig. 6.41

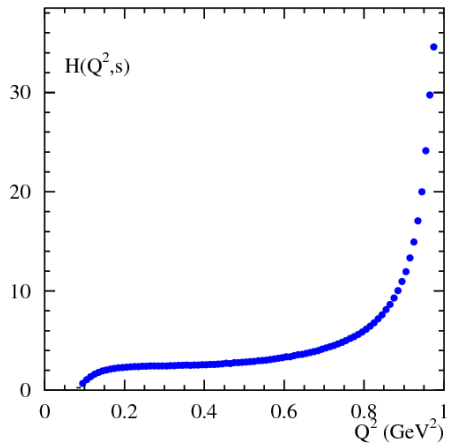

Fig. 6.41: The radiator $H(s_{\gamma^*}, s)$, inclusive in θ_γ, in bins of 0.01 GeV^2 in s_{γ^*}. The value used for s in the Monte Carlo production is $s = 999.85$ (GeV)^2, corresponding to the mean value of DAΦNE energy for data collected in 2006.

Systematic error of the radiator function

The error quoted by the authors of PHOKHARA on the ISR part of the generator is 0.5%, mainly due to missing diagrams like non-factorizable two-photon exchange contributions.
Possible experimental systematic uncertainty to the radiator function, due to the spread of $\sqrt{s}$ during the 2006 running period of DAΦNE, results to be less than 3×10^{-4} and is flat in the whole energy range. Thus this source of error is considered negligible and only the quoted theoretical 0.5% is taken into account.

6.6.2 Final state radiation

The presence of events with final state radiation in the data sample affects the analysis

– in the M_{trk} distributions. The missing FSR-NLO terms and the model dependence might affect the data-Monte Carlo agreement in the M_{trk} cut (see Sec. 5.2) and the background

fitting procedure (see Sec. 5.4). However, thanks to the fine tuning of tracking parameters, described in Sec. 5.1.2, the Monte Carlo trackmass distributions reproduce very well the data ones. The systematic uncertainty relative to this cut has already been taken into account;

– in the un-shifting procedure. The correction due to the passage from s_π to s_{γ^*} is of the order of several percent, see Fig. 6.40. The presence of a second photon from FSR, which is not included in the PHOKHARA Monte Carlo code, could cause some effect [33]. No sizable effects are expected for other higher order corrections.

FSR events are described by means of the sQED approach. A test of this model dependence can be done exploiting the interference between ISR and FSR events. In ISR events the $\pi^+\pi^-$ system is in an odd charge conjugation state, while in the FSR events the $\pi^+\pi^-$ system is in an even charge conjugation state. The interference of the two generates a forward-backward asymmetry:

$$\mathcal{A}_{\rm FB}(s_{\gamma^*}) = \frac{N_{\pi^\pm}(\theta > 90^\circ) - N_{\pi^\pm}(\theta < 90^\circ)}{N_{\pi^\pm}(\theta > 90^\circ) + N_{\pi^\pm}(\theta < 90^\circ)}. \tag{6.20}$$

Comparing $\mathcal{A}_{\rm FB}(s_{\gamma^*})$ obtained from data and from the simulation one can perform a test on the model inserted in the generator. The comparison is shown in Fig. 4.16(b). An overall agreement $\leq 5\%$ is found. To obtain an estimation of the systematic uncertainty due to the modelling of FSR events, one multiplies this 5% discrepancy with the total contribution of FSR events in the cross section, obtained by performing the ratio $s_{\gamma^*}/s_{\gamma^*}$ visible in Fig. 6.40. The uncertainty on the sQED model inserted in the simulation can be seen in Fig. 6.42. The increase of the

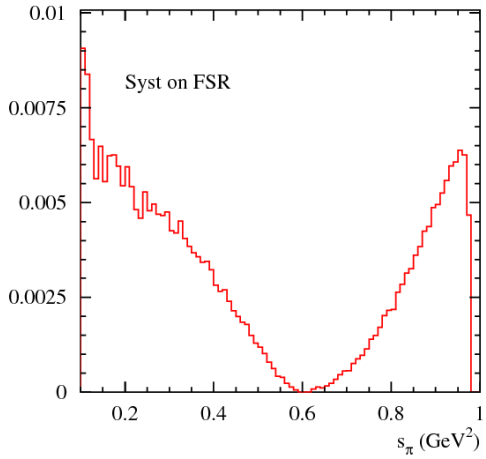

Fig. 6.42: Systematic uncertainty due to the FSR description, based on the sQED approach.

systematic error is due to the increasing of the relative amount of NLO events in the spectrum.

6.6.3 Vacuum polarisation

In order to obtain the *bare* cross section, needed to evaluate $a_\mu^{\pi\pi}$ (see Eq. 2.23 and Eq. 4.9), vacuum polarization effects must be subtracted. This is done by correcting the cross section for

the running of $\alpha_{\rm em}$ as follows:

$$\sigma^{bare} = \sigma^{dressed} \left(\frac{\alpha_{\rm em}(0)}{\alpha_{\rm em}(s)} \right)^2 \equiv \sigma^{dressed}/\delta(s). \tag{6.21}$$

where the running of $\alpha_{\rm em}$, neglecting the contribution from the top quark (see Sec. 2.5 and Eq. 2.30), can be written as [135]:

$$\alpha_{\rm em}(s) = \frac{\alpha_{\rm em}(0)}{1 - \Delta\alpha^{lep}_{\rm em}(s) - \Delta\alpha^{\rm had}_{\rm em}(s)} \tag{6.22}$$

The leptonic contribution can be calculated analytically, while the hadronic contribution comes from a dispersion integral, which includes the hadronic cross section itself in the integrand:[7]

$$\Delta\alpha^{\rm had}_{\rm em}(s) = -\frac{\alpha_{\rm em}(0)s}{3\pi} Re \int_{4m_\pi^2}^{\infty} ds' \frac{R(s')}{s'(s' - s - i\epsilon)}. \tag{6.23}$$

Therefore, the correct procedure has to be iterative and it should include the same data that must be corrected. However, since the correction is at the few percent level, the $\Delta\alpha_{\rm had}(s)$ is evaluated using $\sigma_{\rm had}(s)$ values previously measured previously [110].

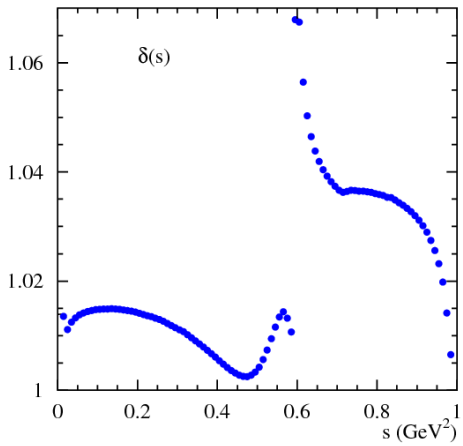

Fig. 6.43: Correction factor $\delta_{\rm VP}(s)$: $\sigma^{bare}(s) = \sigma^{dressed}(s)/\delta_{\rm VP}(s)$, obtained from [110].

Fig. 6.43 shows the correction $\delta_{\rm VP}(s)$ applied to the $\pi^+\pi^-$ cross section. This correction avoids double-counting of higher order terms in the dispersion integral for $a_\mu^{\pi\pi}$, and it is not applied to the pion form factor $|F_\pi(s)|^2$.

[7] $R(s) \equiv \sigma^{had}_{bare}(s)/\frac{4\pi\alpha(0)^2}{3s}$

7. RESULTS AND FUTURE PERSPECTIVES

7.1 Extraction of the pion form factor

The Large Angle off-peak analysis represents the ultimate KLOE $\sigma(e^+e^- \to \pi^+\pi^-)$ cross section measurement. The data collected at $\sqrt{s} = 1$ GeV provide indeed a sample free from ϕ-decays background, especially from ϕ-decays into scalar mesons, whose presence causes a big systematic uncertainty at energies below 0.5 GeV^2 for the Large Angle analysis based on on-peak ($\sqrt{s} = m_\phi$) data. Moreover, selecting events with ISR-photons emitted at large polar angle, allows to cover the energy region below 0.35 GeV^2, while this possibility is kinematically forbidden when requiring the small angle geometrical acceptance.
The extraction of $|F_\pi(s)|^2$ has been performed following the analysis flow shown in Fig. 6.1.
The differential $\pi^+\pi^-\gamma$ cross section is obtained from the observed number of events, $N_{\rm obs}$, after subtracting the residual background, $N_{\rm bkg}$, unfolding for the detector resolution, correcting for the efficiencies, $\epsilon(s_\pi)$, and normalizating to the integrated luminosity L, as discussed in previous sections:

$$\frac{d\sigma_{\pi\pi\gamma}}{ds_\pi} = \frac{N_{\rm obs} - N_{\rm bkg}}{\Delta s_\pi} \cdot \frac{1}{\varepsilon(s_\pi) \cdot L}. \tag{7.1}$$

After the unshifting procedure – which allows to pass from the hadron final state invariant mass, s_π, to the momentum carried by the virtual photon, s_{γ^*} – the differential cross section is divided by the radiator function (provided by the PHOKHARA Monte Carlo program) to obtain the measured total cross section $\sigma_{\pi\pi(\gamma)}(s)$ according to the Eq. 6.17.
The pion form factor is extracted from the total cross section $\sigma_{\pi\pi(\gamma)}(s)$ by subtracting final state radiation processes under the assumption of pointlike pions and – to be inclusive by the effects from vacuum polarization (see Sec. 6.6.3) – the sample is not corrected by the factor $\delta_{\rm VP}$:

$$|F_\pi(s)|^2 = \frac{3}{\pi}\frac{s}{\alpha_{\rm em}^2\beta_\pi^3}\sigma_{\pi\pi(\gamma)}\left(1 - \eta_{\rm FSR}\right), \tag{7.2}$$

where s is the squared of the momentum transferred by the virtual photon, $\beta_\pi = \sqrt{1 - \frac{4m_\pi^2}{s}}$ and $\eta_{\rm FSR}$ describes the FSR contribution in the pointlike-pion approach [136].
In Fig. 7.1 the result for the pion form factor (inclusive for vacuum polarisation, and undressed from pionic final state radiation) is shown. Only statistical errors are shown in the plot. The spectrum is presented in the energy range between 0.1 and 0.85 GeV^2, where s indicates the invariant mass of the virtual photon.
The systematic uncertainties are reported in Tab. 7.1. Above 0.2 GeV^2 the total systematic uncertainty is well below 1% (if one excludes the errors due to the unfolding for the detector resolution, which however does not enter strongly in the evaluation on $a_\mu^{\pi\pi}$, as said in Sec. 6.2). Only at the $\pi^+\pi^-$-threshold the uncertainty reaches a value of ca. 5%. The main sources of error at the threshold are the analysis cuts (i.e. geometrical acceptance, cuts on $M_{\rm trk}$ and on Ω-angle)

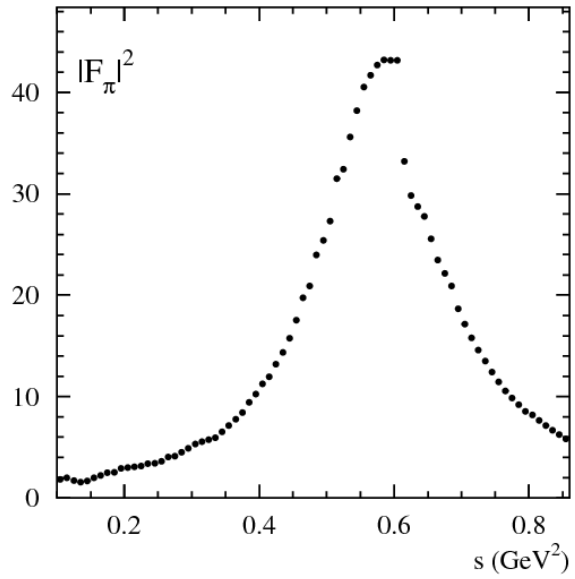

Fig. 7.1: $|F_\pi(s)|^2$ as a function of s. Only statistical errors are reported.

and the background subtraction procedure, which can not be determined with similar precision as at higher energies due to the low statistics. The small number of events makes it difficult to keep under control (at the permil level) the effects caused by the analysis cuts or to evaluate in a robust way the estimation of the background event yield, see Sec. 5.4. However, it must be stressed that already for slightly bigger energies – i.e. already at 0.15 GeV^2 (just ca. 0.07 GeV^2 above the $\pi^+\pi^-$-threshold) – all the systematic uncertainties drop well below 1%, making this work the first KLOE measurement of the pion form factor below 0.35 GeV^2 with an accuracy better than 1%.

7.1.1 Comparison with other KLOE result and Novosibirsk experiments

As the KLOE analysis is a binned analysis in bins of s with a width of 0.01 GeV^2, it is not sensitive to structures in the spectrum, which are smaller than the bin width. This is not the case for experiments at the VEPP-2M collider in Novosibirsk, which use an energy scan instead of the radiative return to measure the cross section as a function of the very precisely known collider energy. To compare the KLOE result on $|F_\pi(s)|^2$ with the results from CMD-2 and SND, trapezoidal integration has been used to average the energy scan experiment's data by integrating over the width of the bin whenever more than one value was found to be inside a bin of 0.01 GeV^2 width, then dividing the result for the bin width of 0.01 GeV^2.
In Fig. 7.2(a) the pion form factor obtained in this work (indicated as KLOE Off Peak in the figure) is shown, compared to the most recent KLOE published result [63] (Small Angle analysis based on 2002 data) and to those one from CMD-2 [115] and SND [116].[1]
The fractional differences on the $|F_\pi(s)|^2$, using the result of this work as reference, are shown in

[1] The years associated to the name of the experiments at Novosibirsk report the year of the publication.

	Energy range (GeV^2)				
	< 0.2	$[0.2-0.3]$	$[0.3-0.5]$	$[0.5-0.7]$	$[0.7-0.85]$
Acceptance	2%	0.4%			
Trackmass cut	1.5%	0.5%	0.2%		0.5%
Ω-angle cut	2%	0.2%	-		
Background	4%	0.5%	0.1%		0.3%
Unfolding	-			3%	-
Filfo	0.5%		0.2%		
Trigger	0.7%	0.2%		-	
$\pi - e$ ID	0.1%	-			
Tracking	0.3%				
FSR correction	0.5%	0.2%	-		0.3%
Total	5.2%	0.9%	0.6%	3% (0.6% w/o unfolding)	0.8%

Tab. 7.1: List of the systematic errors for $|F_\pi|^2$ for different energy ranges. A "-" sign denotes that the error is considered as negligible.

Fig. 7.2(b). The dark grey band gives the statistical error of our measurement and the light grey one combines the statistical and systematic uncertainties (added in quadrature). The increasing of the systematic uncertainty on the ρ-peak is due to the unfolding for the detector resolution procedure.
The previous KLOE results on $|F_\pi(s)|^2$ (see Fig. 4.9(b)) show a relative trend in the fractional difference with the energy scan experiments: the relative discrepancy with CMD-2 and SND results show a discrepancy up to the 5% at higher energies. Thus, one of the aims of the Large Angle off-peak analysis is also to cross check the Small Angle on-peak analysis.
The two KLOE results are in good agreement with each other, while the difference with Novosibirsk experiments is confirmed by the off-peak data analysis. For energy above the ρ-peak a maximum deviation of ca. 5% is observed. Below 0.35 GeV^2, due to the dramatic increase of the uncertainties – particularly the statistical error is dominating –, it is not possible to immediately define whether the slope is present. However the pion form factor from KLOE is slightly higher than the ones from SND and CMD-2, which is also confirmed by the value of $a_\mu^{\pi\pi}$ at low energies, as will be shown below.[2]

The discrepancy between the pion form factor is still an open issue.

[2] The BaBar experiment is also analyzing ISR events to measure the $\sigma(e^+e^- \to \pi^+\pi^-)$ cross section, and a preliminary result has been shown [73]. The BaBar new measurement would provide a further relevant contribution for a better comprehension of the pion form factor.

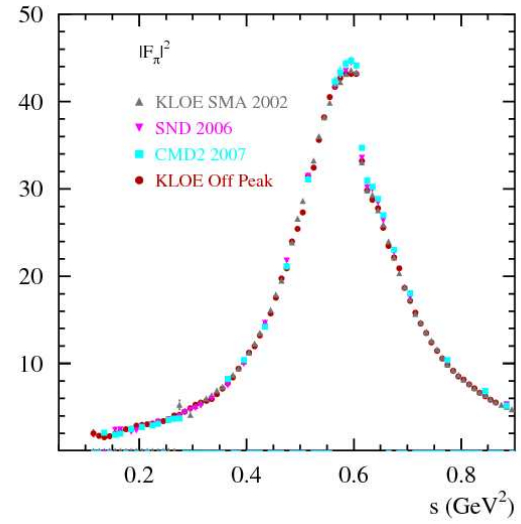

(a)

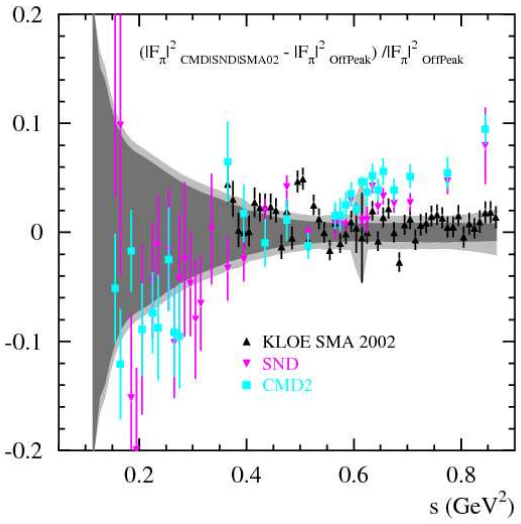

(b)

Fig. 7.2: The comparison among $|F_\pi(s)|^2$ result from KLOE, SND and CMD-2 is shown. The pion form factor result based on 2006 KLOE data is still preliminary. In (b) the relative difference among the different pion factor evaluations with respect to the one obtained by the KLOE Large Angle analysis with off-peak data presented in this work. For CMD-2 and SND only statistical errors are shown. The dark grey band gives the statistical error for KLOE, the light grey band combines the statistical and systematic error (added in quadrature).

KLOE has performed four completely independent analyses, using different data samples (on-peak data collected in 2001 and in 2002, and off-peak data taken in a dedicated DAΦNE run in 2006), selecting two different phase space regions (either looking at event with ISR-photon emit-

ted at small polar angle or selecting event tagging the photon at large polar angle) and applying different selection tools, see Tab. 4.1. The good agreement among all the KLOE measurements is a solid cross check for each of the KLOE analyses.
Searching for possible reason of this discrepancy on $|F_\pi(s)|^2$ one may argue that it can be caused by the radiator function, H. This theoretical function is the only tool which enters the different KLOE analyses without modifications (apart the value of the energy of the collider, needed as an input, which is different for the on-peak and the off-peak analysis). However, it is quite unlikely that this could be the reason of the discrepancy between the pion form factor, since the theoretical uncertainty, claimed by the authors, is 0.5%, well below the discrepancy between the KLOE and the SND and CMD-2 results, making it a very robust instrument for ISR measurements. Moreover the PHOKHARA Monte Carlo generator, which is used by KLOE and includes the H function, has been compared to other Monte Carlo generators, and a good agreement has been found. A further test on the radiator function $H(s)$ can be performed experimentally by measuring the $\sigma(e^+e^- \to \mu^+\mu^-\gamma)$ cross section. This measurement is in progress.
A possible explanation for the difference in $|F_\pi(s)|^2$ between KLOE and the Novosibirsk experiments could come from the description of FSR events, which strongly depends on the model inserted in the Monte Carlo generator. In the PHOKHARA generator the FSR events are treated within the sQED approach. The reliability of the simulation has been tested comparing the data-Monte Carlo agreement in the Forward-Backward asymmetry, which arises from the interference between ISR-LO and FSR-LO events, see Sec. 6.6.2. An agreement better than 5% has been found, which, multiplied for the amount of FSR events in the data spectrum, gives an uncertainty of few permil. Higher radiative corrections (Next-to-Next-to-Leading Order) for FSR events, which are not present in the Monte Carlo generators and may be needed at the achieved experimental accuracy, could represent a possible source of discrepancy between the pion form factor results. However, higher order effect should cause a minimal impact on $|F_\pi(s)|^2$, and a-priori they can not modify the spectra of some percent.

7.2 Evaluation of $a_\mu^{\pi\pi}$

As seen, at the very $2m_\pi$-threshold the systematic uncertainty gets larger, reaching about 5%. This increase of the error is mainly due to the difficulty of keeping under control the selection cuts and the background subtraction procedure with low statistic.[3] As a consequence of that, in order to have an accuracy on $a_\mu^{\pi\pi}$ of the order of 1%, the dispersion integral has been evaluated in the range between 0.25 and 0.85 GeV^2. To underline the relevance of this measurement we point out that this range gives about 80% of the total value of $a_\mu^{\pi\pi}$, which corresponds to ca. 60% of the total hadronic contribution to $a_\mu^{\rm had}$. The Large Angle off-peak analysis thus provides the bigger contribution to the muon anomaly with respect to all the other KLOE measurements, and reaches, for the first time at KLOE, with a precision at the percent level energies below 0.35 GeV^2.
The dispersion integral is

$$a_\mu^{\pi\pi} = \frac{1}{4\pi^3} \int_{s_{min}=0.25}^{s_{max}=0.85} \mathrm{d}s \; \sigma^{bare}_{\pi\pi(\gamma)}(s)\, K(s), \tag{7.3}$$

[3] For this reason some more data with DAΦNE operating at $\sqrt{s} = 1$ GeV, would be really welcome.

where $\sigma^{bare}_{\pi\pi(\gamma)}(s)$ corresponds to the cross section with vacuum polarization effects removed, see Sec. 6.6.3. The cross section is inclusive of FSR. The kernel function $K(s)$ is evaluated at the central value of each bin.
Our preliminary result is:

$$a_\mu^{\pi\pi}(0.25 < s < 0.85\ \mathrm{GeV}^2) = (426.7 \pm 0.9_{\mathrm{stat}} \pm 2.8_{\mathrm{exp}} \pm 2.5_{\mathrm{theo}}) \times 10^{-10} \tag{7.4}$$

The statistical errors of the value of $\sigma_{\pi\pi}$ for different energies are summed quadratically, while the systematic uncertainties are summed linearly in the integration. The total fractional error of our $a_\mu^{\pi\pi}$ results to be 0.9%.

7.2.1 Comparison with the other KLOE results and CMD-2

The evaluation of $a_\mu^{\pi\pi}$ in the range between 0.35 and 0.85 GeV^2 allows to compare the preliminary result obtained in this work with the KLOE latest published result [63].

KLOE Analysis	$a_\mu^{\pi\pi}(0.35 < s < 0.85\ \mathrm{GeV}^2) \times 10^{-10}$
LA 2006	$375.0 \pm 0.7_{\mathrm{stat}} \pm 2.3_{\mathrm{exp}} \pm 2.2_{\mathrm{theo}}$
SA 2002	$379.6 \pm 0.4_{\mathrm{stat}} \pm 2.4_{\mathrm{exp}} \pm 2.2_{\mathrm{theo}}$

The two values are in agreement within the errors (0.7σ). This provide a reliable cross check of the two KLOE analyses.
The CMD-2 collaboration has also evaluated $a_\mu^{\pi\pi}$ at low energies, in the range between 390 and 520 MeV [115]. To compare it with the KLOE off-peak result we also have computed the dispersion integral in the same energy range.

Analysis	$a_\mu^{\pi\pi}(390 < s < 520\ \mathrm{MeV}) \times 10^{-10}$
KLOE LA 2006	$47.8 \pm 0.9_{\mathrm{stat}} \pm 0.6_{\mathrm{syst}}$
CMD-2	$46.2 \pm 1.0_{\mathrm{stat}} \pm 0.3_{\mathrm{syst}}$

The KLOE result is higher of ca. 1.5σ. This discrepancy is also visible in Fig. 7.2.

7.3 Conclusions

The *Radiative Return* method has been used to analyze the large photon polar angle acceptance region using a data sample of ∼230 pb^{-1} collected by KLOE in 2006 at $\sqrt{s} = 1$ GeV. The pion form factor has been measured down to the $\pi^+\pi^-$-threshold.
The analysis presented in this work represents the most accurate hadronic cross section measurement performed so far at KLOE and it is the only one measuring $|F_\pi(s)|^2$ down to the threshold with high precision. The improvement given to $a_\mu^{\pi\pi}$ is of big relevance, since it adds ca. 15% to the previous KLOE measurements (performed selecting events with ISR-photons at small polar angles) and it provides ca. 80% of the total value of $a_\mu^{\pi\pi}$, with an accuracy better than 1%.

Fine calibration corrections have been applied to the momenta of the charged tracks for data, and a tuning and smearing procedure has been developed for the Monte Carlo samples to get

the best possible agreement between data and simulation. After the selection cuts, the residual background from radiative Bhabha events, $\mu^+\mu^-\gamma$ and $\pi^+\pi^-\pi^0$ events has been estimated using a procedure in which the Monte Carlo distributions with free normalization parameters are fitted to the data distribution. The systematic error associated to the background subtraction is about 0.5% in the region between 0.35 and 0.7 GeV^2, and reaches ca. 4% at the $2m_\pi$-threshold. The systematic uncertainty on the analysis cuts and on the background subtraction could be strongly reduced if more statistics at the threshold was available. However, further data taking with DAΦNE operating off the ϕ-resonance peak are not scheduled for the time being. The efficiencies of the analysis selection have been evaluated directly from data control samples, except for the acceptance, the tracking and calorimeter efficiencies, in which the signal Monte Carlo sample has been used.
For each analysis cut the associated systematic error has been estimated. The total systematic uncertainty on the ρ-peak is 0.6%, neglecting the contribution from the unfolding for the detector resolution procedure, which however distorts only negligibly the $\pi^+\pi^-\gamma$ spectrum. At the $\pi^+\pi^-$-threshold the systematic uncertainty is of the order of some percents, which is anyhow competitive with the result obtained by CMD-2.
The pion form factor obtained in this work has been compared with the latest published result from KLOE (i.e. the Small Angle analysis based on 2002 data sample) and with the CMD-2 and SND results. A good agreement between the KLOE results is found in the whole energy range ([0.35 - 0.85] GeV^2), while the relative trend with respect to the Novosibirsk scan experiments is confirmed, giving a discrepancy of about 5% at 0.8 GeV^2.
Although the different trend visible in the comparison between the pion form factor results, the $a_\mu^{\pi\pi}$ values from ISR and from energy scan measurements are in agreement within 1 standard deviation. A compensation effect seems to play a role between the two methods. The fact that for low energy regions the KLOE result is higher, giving a bigger contribution to $a_\mu^{\pi\pi}$ than SND and CMD-2, is compensated at the ρ-peak and at the higher energies, where the situation is reversed. The disagreement between the $|F_\pi(s)|^2$ result is something which still needs to be investigate by all the collaborations.

Since the result obtained in this work is still preliminary, it has not been yet included into any official computation of $a_\mu^{\text{theo(SM)}}$. An estimation of the impact of this analysis on the discrepancy between the direct measurement and the theoretical prediction of $(g-2)_\mu$ is however presented in the following.
We use our new result in the range $[0.25 - 0.85]$ GeV^2 and we combine it with the results from other data sets [190]. The total contribution given by the $\pi^+\pi^-$-channel results to be:

$$a_\mu^{\pi\pi} = (504.04 \pm 3.9) \times 10^{-10}.$$

Including all the other hadronic contributions [45], the ones from QED [20] and from Weak interaction [30], one obtains:

$$a_\mu^{\text{theo(SM)}} = (11\,659\,178.6 \pm 6.0) \times 10^{-10}.$$

Comparing this value to the world average experimental value,

$$a_\mu^{\text{exp}} = (11659208.0 \pm 6.3) \times 10^{-10}.$$

one gets: $\Delta a_\mu = a_\mu^{\text{exp}} - a_\mu^{\text{theo(SM)}} = (29.4 \pm 8.7)$, which corresponds to ca. 3.4σ. Therefore, the Large Angle off-peak result confirms both the difference between the direct measurement of $(g-2)_\mu$ and its theoretical predicted value and the order of magnitude of Δa_μ.

To conclude, one may say that the anomaly of the muon magnetic moment could really represent a "narrow open window" where to peer for New Physics.

7.4 Future perspectives

The future perspectives of the hadronic cross section measurements at KLOE are the following: (*i*) finalize the Large Angle analysis based on 2002 data, improving the knowledge of the scalar mesons; (*ii*) proceed in the publication of the off-peak Large Angle analysis, which has been described in this work, and perform the $\sigma(e^+e^- \to \pi^+\pi^-)$ cross section measurement at small angle acceptance with the off-peak sample; (*iii*) to perform the measurement of $R(s)$ using 2002 on-peak and 2006 off-peak data.

7.4.1 Improvement of the Large Angle on-peak analysis and knowledge of scalar mesons

During the development of the pion form factor measurement at large photon polar angles using on-peak data collected in 2002, the difficulties arising from the presence of the scalar mesons has become more and more evident. A restriction of the energy range to [0.5 - 0.85] GeV^2 was a consequence of that. However this analysis based on on-peak data reveals itself to be a good field where to explore the nature of the scalars mesons.
The KLOE collaboration has already published an analysis of the decay $\phi \to f_0(980)\gamma \to \pi^+\pi^-\gamma$ [137] using the mass spectrum to evaluate the f_0 parameters, see Fig. 4.14. A continuation of this work was started in [114], the same measurement can be performed applying a complementary method, i.e. evaluating the mass and the coupling constants of the scalar mesons via the data-Monte Carlo comparison of the Forward-Backward asymmetry. The mass spectrum is then exploited as a check of the accuracy of the parameters tuned via the (F-B) asymmetry. For this approach, an evolution of the standard `PHOKHARA` Monte Carlo has been worked out.[4] This new generator contains:

- Initial + Final State Radiation at the Next-to-Leading Order;
- the scalar meson contribution $f_0(980)$ and $f_0(600)$ is described according to a more sophisticated version of the kaon loop model, with respect to the one inserted in the previous versions;
- the decay $\phi \to \rho^\pm\pi^\mp \to \pi^+\pi^-\gamma$ according to the Vector Meson Dominance model.

As a consequence of more precise studies of the scalar mesons, the possibility to extend the spectrum of the Large Angle on-peak analysis down to 0.3 GeV^2 has been discussed. Even if the $2m_\pi$-threshold can not be reached, a broader energy range could provide a further cross check for the other KLOE analyses and an improved investigation on the nature of the scalar mesons.

7.4.2 Off-peak data

This analysis is complete and an official publication is in progress. Few further checks can still be performed.

[4] This version of the `PHOKHARA` generator is based on the latest official version of the generator [188] where a new model for f_0 and $\rho\pi$ has been inserted, [189]

A more precise understanding of final state radiation, based on the extension of the sQED, can be useful to reduce the systematics uncertainty associated with these processes, especially at low energies, where the FSR-NLO increases.
The Forward-Backward asymmetry evaluated from off-peak data follows the behavior of the $\pi^+\pi^-\gamma$ ISR+FSR prediction (see Fig. 4.16(b)), indicating that the sample collected in 2006 is almost free from the scalar mesons contribution, matching the expectations and the motivations of collecting data off the ϕ-resonance peak. However, dedicated studies on the presence of background from the $e^+e^- \to f_0(980)\gamma \to \pi^+\pi^-\gamma$ and from $e^+e^- \to \rho^\pm\pi^\mp \to \pi^+\pi^-\gamma$ using the latest evolution of the PHOKHARA Monte Carlo are still to be precisely done. Those effect are expected to be of the 1% level in the precision of the F-B asymmetry.
Further check, as stated in Sec. 6.5, on the systematic error related to the luminosity evaluation can be performed. The reported value of 0.3% in the systematic uncertainty exploits the fact that, since the 2002 on-peak data sample, the cosmic ray veto is not applied; however background correction and reconstruction efficiency for VLABs should be specifically checked for the off-peak data. Dedicated studies on this topic have been started, even so no sizable deviations are expected.
To reduce the systematic uncertainty associated to the selection cuts and to the background subtraction procedure at the very $\pi^+\pi^-$-threshold, it would of fundamental help to collect more data with DAΦNE operating at $\sqrt{s} = 1$ GeV. However, for the time being further data taking at off-resonance are not included in the near future physics program.

7.4.3 Measurement of $R(s)$ via the small angle analysis

An alternative approach to evaluate $a_\mu^{\pi\pi}$ is to normalize the $\pi^+\pi^-\gamma$ cross section to the $\mu^+\mu^-\gamma$ events, instead of using the absolute integrated luminosity. This means that one directly measures the ratio $R(s)$, which is then put into the dispersion integral (see Eq. 2.23).
The analysis, selecting events with ISR-photons emitted at small polar angles using 2002 on-peak data, is in progress. This approach has the important advantage to cancel out several systematic uncertainties:

- the error due to the luminosity evaluation, both from the theoretical evaluation of the Bhabha cross section and from the experimental measurement, is cancelled out, since the knowledge of the luminosity is not required anymore;
- the uncertainty related to the radiator function, $H(s_{\gamma^*}, s)$ is cancelled out, as the initial state radiation process is identical for both $\pi^+\pi^-\gamma$ and $\mu^+\mu^-\gamma$ events;
- the theoretical uncertainty associated to the computation of the vacuum polarization $\delta_{\rm VP}(s)$ is also vanishing, because this dose not depend on the final state.

Removing these three sources of errors, the total theoretical uncertainty in the Small Angle analysis could be reduced from 0.9% down to less than 0.5%.
The statistics collected, either in 2002 or in 2006 data taking, is sufficient to perform the $R(s)$ measurement. This analysis has been developing in parallel with the Small Angle on-peak 2002 and with the Large Angle off-peak one.
The main variables used to separate pions from muons, in the $R(s)$ measurement at KLOE, consists in $M_{\rm trk}$, see Fig. 7.4.3. The black histogram represents the data events, the blue and the green ones report the two Monte Carlo samples, $\pi^+\pi^-\gamma$ and $\mu^+\mu^-\gamma$ respectively. Since the tails

from the two channels overlap, due to resolution effects, the region between 115 and 130 MeV is excluded, to avoid difficulties in distinguishing the two processes. The main limitation, for the

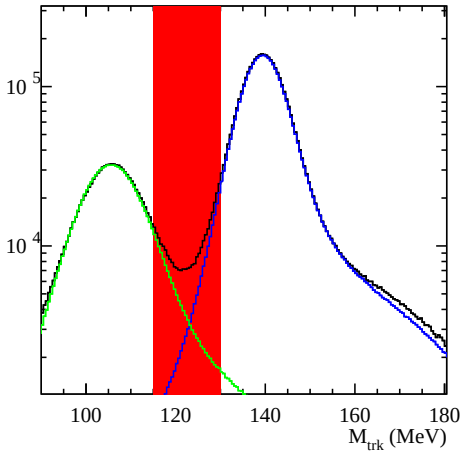

Fig. 7.3: The trackmass distributions for data (black histogram), for $\pi^+\pi^-\gamma$ (blue histogram) and $\mu^+\mu^-\gamma$ (green histogram) Monte Carlo samples are reported. The events falling into the region in the red shadow do not enter in the analysis.

time being, stays in the precise understanding of the selection efficiencies for the $\mu^+\mu^-\gamma$ events. A step forward has been done removing the request of a vertex close to the interaction point,[5] taking out in such a way a source of systematic uncertainty, which was not well under control, especially for the $\mu^+\mu^-\gamma$ events.
Another difficulty stays in developing a precise $\pi - \mu$ PID able to separate with high efficiency pions from muons. A tentative approach has been made in developing a neural network procedure, but still further work has to be done on this topic. In general, the accuracy reached is still not good enough to get an experimental error smaller than 1% level.
The $R(s)$ measurement selecting ISR-photon at small polar angle would provide the most precise evaluation of $a_\mu^{\pi\pi}$ performed at KLOE for energies above 0.35 GeV^2.
The muon sample can be also used to check the radiator function H: by comparing the $\mu^+\mu^-\gamma$ cross sections from data and from Monte Carlo, one can test the reliability of the H function inserted in the `PHOKHARA` generator and to obtain a cross check for the pion form factor measurement.

KLOE has been very successful in measuring the pion form factor exploiting the Radiative Return method, proving this technique to be a reliable new method for high precision measurements. Via the analysis presented in this thesis and the upcoming ones, the KLOE experiment has been giving extremely significant contribution to the "$(g-2)_\mu$ puzzle".

[5] This choice which has been taken also by the Small Angle analysis and the Large Angle off-peak analysis, as presented in this work, following the "suggestion" of the R-measurement analysis.

BIBLIOGRAPHY

[1] C. Amsler et al. (Particle Data Group), *Rev. of Part. Phys. B* **667** (2008)

[2] G.W. Bennet et al., (Muon (g-2) Coll.), *Phys. Rev. Lett. D* **73**, 072003 (2006)

[3] P.A.W. Dirac, *Proc. Roy. Soc. A* **126**, 360 (1928)

[4] P. Kusch, *Science* **123**, 207 (1956)

[5] P. Kusch, *Phys. Today* **19**, 23 (1966)

[6] J.S. Schwinger, *Phys. Rev.* **73**, 416 (1948)

[7] J.E. Nafe, E.B. Nelson, I.I. Rabi, *Phys. Rev.* **71**, 914 (1947)

[8] D.E. Nagle et al., *Phys. Rev.* **72**, 971 (1947)

[9] G. Breit, *Phys. Rev.* **72**, 984 (1947)

[10] P. Kusch and H.M. Foley, *Phys. Rev.* **73**, 421 (1948)

[11] H.R. Crane et al., *Phys. Rev.* **91**, 475 (1953)

[12] H.R. Crane et al., *Sci. Amer.* **218**, 72 (1968)

[13] V.B. Berestetskii, *Zh. Eksp. Teor. Fiz.* **30**, 788 (1956)

[14] G. Charpak, *Phys. Rev. Lett.* **6**, 128 (1961)

[15] F.J.M. Farley et al., *Nuovo Cim.* **45**, 281 (1966)

[16] J. Bailey et al., *Phys. Rev. Lett. B* **28**, 287 (1968)

[17] J. Bailey et al., *Nuovo Cim. A* **9**, 369 (1972)

[18] J. Bailey et al. (CERN Muon Storage Ring Coll.), *Phys. Lett. B* **67**, 225 (1977)

[19] J. Bailey et al. (CERN-Mainz-Daresbury Coll.), *Nucl. Phys. B* **150**, 1 (1979)

[20] M. Passera, *Phys. Rev. D* **75**, 013002 (2007)

[21] C.M. Sommerfield, *Phys. Rev.* **107**, 328 (1957)

[22] C.M. Sommerfield, *Ann. Phys. (N.Y.)* **5**, 26 (1958)

[23] A. Petermann, *Helv. Phys. Acta* **30**, 407 (1957)

[24] A. Petermann, *Nucl. Phys.* **5**, 677 (1958)

[25] S. Laporta and E. Remiddi, *Phys. Lett. B* **356**, 390 (1995)

[26] S. Laporta and E. Remiddi, *Phys. Lett. B* **379**, 283 (1996)

[27] S. Laporta, *Nuovo Cim. A* **106**, 675 (1993)

[28] S. Laporta and E. Remiddi, *Phys. Lett. B* **301**, 440 (1993)

[29] T. Aoyama et al., *hep-ph/0806.3390* (2008)

[30] A. Czarnecki, B. Krause and W.J. Marciano, *Phys. Lett. D* **52**, 2619 (1995)

[31] A. Czarnecki, W.J. Marciano and A. Vainshtein, *Phys. Lett. D* **73**, 11901 (2006)

[32] S. Müller, *Messung des Wirkungsquerschnitts* $\sigma(e^+e^- \to \pi^+\pi^-)$ *mit dem KLOE Detektor*, PhD Thesis, Universität Karlsruhe (TH) (2004)

[33] F. Jegerlehner, *Springer Tracts in Mod. Phys. The Anomalous Magnetic Moment of the Muon*, Springer (2007)

[34] G.J. Gounaris and J.J. Sakurai, *Phys. Rev. Lett.* **21**, 244 (1968)

[35] J.H. Kühn and A. Santamaria, *Z. Phys. C* **48**, 445 (1990)

[36] G. Rodrigo and J.H. Kühn, *Eur. Phys. Jour. C* **25**, 215 (2002)

[37] H. Czyż and A. Grzelińska and J.H. Kühn and G. Rodrigo, *Eur. Phys. Jour. C* **33**, 333 (2004)

[38] H. Czyż and A. Grzelińska and J.H. Kühn and G. Rodrigo, *Phys. Lett. B* **611**, 116 (2005)

[39] H. Burkhardt and B. Pietrzyk, *Phys. Rev. D* **72**, 057501 (2005)

[40] S.J. Brodsky and E. De Rafael, *Phys. Rev.* **168**, 1620 (1967)

[41] B.E. Lautrup and E. De Rafael, *Phys. Rev.* **174**, 1835 (1968)

[42] S. Eidelman, *Status of* $(g_\mu-2)/2$ *in Standard Model* talk given at the *ICHEP 2006, XXXIII International Conference on High Energy Physics*, Moscow (Russia) 2006

[43] S. Eidelman, *SM prediction for Muon* $(g_\mu-2)/2$, talk given at the *Tau08,* 10^{th} *International Workshop on Tau Lepton Physics*, BINP Novosibirsk, September 2008

[44] M. Davier, S. Eidelman, A. Höcker and Z. Zhang, *Eur. Phys. Jour. C* **31**, 503 (2003)

[45] K. Hagiwara et al, *Phys. Rev. B* **649**, 173 (2007)

[46] J. Bijnes and J. Prades, *Mod. Phys. Lett. A* **22**, 767 (2007)

[47] M. Passera and W.J. Marciano and A. Sirlin, *hep-ph/0809.4062v1* (2008)

[48] M. Passera and W.J Marciano and A. Sirlin, *Phys. Rev. D* **78**, 013009 (2008)

[49] F. Jegerlehner, *Nucl. Phys. B* **164**, 325 (2004)

[50] J.F. de Troconiz and F.J. Yndurain, *Phys. Rev. D* **71**, 073008 (2005)

[51] K. Hagiwara and A.D. Martin and D. Nomura and T. Teubner, *hep-ph/0611102* (2006)

[52] I.B. Vasserman et al., *Sov. Jour. Nucl. Phys.* **30**, 519 (1979)

[53] I.B. Vasserman et al., *Sov. Jour. Nucl. Phys.* **33**, 709 (1981)

[54] S.I. Dolinsky et al., *Phys. Rep.* **202**, 99 (1991)

[55] L.M. Barkov et al. (CMD Coll.), *Nucl. Phys. B* **256**, 365 (1985)

[56] R.R. Akhmetshin et al. (CMD2 Coll.), *Phys. Lett. B* **527**, 161 (2002)

[57] R.R. Akhmetshin et al. (CMD2 Coll.), *Phys. Lett. B* **578**, 285 (2004)

[58] M.N. Achasov et al. (SND Coll.), *Jour. Exp. Theor. Phys.* **101**, 1053 (2005)

[59] M.N. Achasov et al. (SND Coll.), *Jour. Exp. Theor. Phys.* **103** (2006)

[60] A. Quenzer et al. (DM1 Coll.), *Phys. Lett. B* **76**, 512 (1978)

[61] D. Bisello et al. (DM2 Coll.), *Phys. Lett. B* **220**, 321 (1989)

[62] A. Aloisio et al. (KLOE Coll.), *Phys. Lett. B* **606**, 12 (2005)

[63] F. Ambrosino et al. (KLOE Coll.), *Phys. Lett. B* **670**, 285 (2009)

[64] R.R. Akhmetshin et al. (CMD2 Coll.), *Phys. Lett. B* **642**, 203 (2006)

[65] R.R. Akhmetshin et al. (CMD2 Coll.), *Phys. Lett. B* **595**, 101 (2004)

[66] B. Aubert et al. (BaBar Coll.), *Phys. Lett. D* **70**, 072004 (2004)

[67] B.Aubert et al. (BaBar Coll.), *Phys. Lett. D* **71**, 052001 (2004)

[68] B. Aubert et al. (BaBar Coll.), *Phys. Lett. D* **76**, 012008 (2007)

[69] B. Aubert et al. (BaBar Coll.), *Phys. Lett. D* **76**, 092005 (2007)

[70] B. Aubert et al. (BaBar Coll.), *Phys. Lett. D* **73**, 052003 (2006)

[71] R. Alemany, M. Davier and A. Höcker A., *Eur. Phys. Jour. C* **2**, 123 (1998)

[72] V. Cirigliano, G. Ecker and H. Neufeld, *Jour. High En. Phys.* **0208**, 002 (2002)

[73] M. Davier, *Precision measurement of* $e^+e^- \to \pi^+\pi^-(\gamma)$ *cross section with the ISR method*, talk given at the *Tau08,* 10^{th} *International Workshop on Tau Lepton Physics*, BINP Novosibirsk, September 2008

[74] M. Benayoum, *Eur. Phys. Jour. C* **55**, 199 (2008)

[75] M. Steinhauser, *Phys. Lett. B* **429**, 158 (1998)

[76] J.H. Kühn and M. Steinhauser, *Phys. Lett. B* **437**, 425 (1998)

[77] F. Jegerlehner, *Nucl. Phys. Proc. Suppl.* **162**, 22 (2006)

[78] Tevatron EW Working Group, *arXiv:0808.1089*

[79] R. Barate et al., *Phys. Lett. B* **565**, 61 (2003)

[80] `http://lepewwg.web.cern.ch/LEPEWWG/plots/summer2008/`

[81] Tevatron EW Working Group, *arXiv:0808.0147*

[82] M. Grünewald et al., *Phys. Rept.* **427**, 257 (2006)

[83] LEP EW Working Group, *arXiv:0808.1089*

[84] W.J. Marciano, *:hep-ph/0411179*

[85] F.V. Flores-Baez et al, *Phys. Rev. D* **76**, 096010 (2007)

[86] M. Benayoun et al., *Eur. Phys. Jour. C* **55**, 199 (2008)

[87] G. Altarelli and G. Isidori, *Phys. Lett. B.* **337**, 141 (1994)

[88] R.W. Schiel and J.P. Ralston, Phys. Lett. B 657 (2007) 43.

[89] J. Wess and B. Zumino, *Nucl. Phys. B* **70**, 39 (1974)

[90] VV. AA., `http://www.susy07.uni-karlsruhe.de/presusy.php`, lectures at *PreSUSY07 school*, Karlsruhe, July 2007

[91] J.R. Ellis et al., *Nucl. Phys. B* **238**, 453 (1984)

[92] S. Ferrara and E. Remiddi, *Phys. Lett. B* **53**, 347 (1974)

[93] J.L. Lopez, D.V. Nanopoulos and X. Wang, *Phys. Rev. D* **49**, 366 (1994)

[94] S.P. Martin and J.D. Wells, *Phys. Rev. D* **67**, 015002 (2003)

[95] D. Stöckinger, *Jour. Phys. G: Nucl. Part. Phys.* **34**, 45 (2007)

[96] M. Czakon and W.J. Marciano, *Phys. Rev. D* **64**, 0103014 (2001)

[97] KLOE Coll., *Nucl. Instr. and Meth. A* **488**, 51-73 (2002)

[98] KLOE Coll., *Nucl. Instr. and Meth. A* **482**, 364-386 (2002)

[99] KLOE Coll., *LNF96/043 (IR)* (1995)

[100] KLOE Coll., *Nucl. Instr. and Meth. A* **534**, 403-433 (2004)

[101] M. Incagli, *KLOE Memo* **147**, 51-73 (2001)

[102] S. Binner, J.H. Kühn and K. Melnikov, *Phys. Lett. B* **459**, 279 (1999)

[103] S. Spagnolo, *Eur. Phys. Journ. C* **6**, 637 (1999)

[104] A. Denig et al, *KLOE Note* **192** (2004) http://www.lnf.infn.it/kloe/pub/knote/kn192.ps

[105] S. Eidelman and F. Jegerlehner, *Z. Phys. C* **67**, 585 (1995)

[106] B. Valeriani, *KLOE Memo* **295** (2004)

[107] B. Valeriani, *Messung des Pion-Formfaktors mittels Radiadive Return an dem KLOE Experiment*, PhD Thesis, Universität Karlsruhe (TH) (2005)

[108] G. Balossini et al., *Nucl. Phys. B* **758**, 227 (2006)

[109] G. D'Agostini, *Nucl. Instrum. Meth. A* **362**, 487 (1995)

[110] $\Delta\alpha_{\rm had}(s)$ provided by F. Jegerlehner.
URL http://www-com.physik.hu-berlin.de/~fjeger/alphaQEDn.uu

[111] A. Aloisio et al. (KLOE Coll.), *Phys. Lett. B* **537**, 21 (2002)

[112] A. Aloisio et al. (KLOE Coll.), *Phys. Lett. B* **634**, 148 (2006)

[113] N.N Achasov and V.I Ivanchenko, *Nucl. Phys. B* **315**, 465 (1989)

[114] D. Leone, *Measurement of the hadronic cross section $\sigma(e^+e^- \to \pi^+\pi^-)$ with the KLOE detector using Radiative Return with tagged photons*, PhD Thesis, Universität Karlsruhe (TH) (2006)

[115] R. R. Akhmetshin et al. (CMD2 Collaboration), *Phys. Lett. B* **648**, 28 (2007)

[116] M.N. Achasov et al. (SND Coll.), *Jour. Exp. Theor. Phys.* **103** (2006)

[117] G. Venanzoni and S. Müller, *KLOE Memo* **305** (2006)

[118] F. Ambrosino et al, *KLOE Memo* **307** (2006)

[119] KLOE Coll., *Nucl. Instr. and Meth. A* **534**, 403-433 (2004)

[120] F. Nguyen, *KLOE Memo* **294** (2004)

[121] R. Brun et al., *CERN Program Library Y250* (1995)

[122] R. Barlow and C. Beeston, *Comp. Phys. Comm.* **77**, 219 (1993)

[123] S. Baker and D. Cousins, *Nucl. Inst. Meth.* **221**, 437 (1984)

[124] M. Moulson and S. Müller, *KLOE Memo* **288** (2004)

[125] G. D'Agostini, *Nucl. Instrum. Meth. A* **362**, 487 (1995)

[126] G. D'Agostini, URL http://www.roma1.infn.it/dagos/bayes_distr.txt

[127] C. Gatti, M. Palutan and T. Spadaro, *KLOE Note* **209** (2004)

[128] H.Czyż et al., private communication

[129] C. M. Carloni Calame et al., *Nucl. Phys. B* **584**, 459 (2000)

[130] F. Ambrosino et al. (KLOE Coll.), *Nucl. Instrum. Meth. A* **534**, 403 (2004)

[131] F. Ambrosino et al. (KLOE Coll.), *Eur. Phys. J. C* **47**, 589 (2006)

[132] G. Balossini et al., *Nucl. Phys. B* **758**, 227 (2006)

[133] S. Binner, J.H. Kühn and K. Melnikov, *Phys. Lett. B* **459**, 279 (1999)

[134] H. Czyż, A. Grzelińska, J. Kühn, G. Rodrigo, *Eur. Phys. J. C* **27**, 563 (2003)

[135] A. Höfer, J. Gluza and F. Jegerlehner, *Eur. Phys. Jour. C* **24**, 51 (2002)

[136] J. S. Schwinger, *Particles, Sources and Fields, Vol.3*, Redwood City, USA Addison-Wesley, 99 (1989)

[137] F. Ambrosino et al. (KLOE Coll.), *Phys. Lett. B* **634**, 148 (2006)

[138] G. Pancheri, O. Shekhovtsova and G. Venanzoni, *Phys. Lett. B* **642**, 342 (2006)

[139] P. Franzini (KLOE Coll.), *arXivid 0802.3009*

[140] N. Cabibbo, *Phys. Rev. Lett.* **10**, 531 (1963)

[141] C. Klopfenstein et al. (CUSB Coll.), *Phys. Lett. B* **130** 444 (1984)

[142] Particle Data Group, *Journ. Phys. G* **33** (2007)

[143] M. Ademollo and R. Gatto, *Phys. Rev. Lett.* **13**, 264 (1964)

[144] A. Sirlin, *Nucl. Phys.* **196**, 83 (1982)

[145] V. Cirigliano et al., *Eur. Phys. Jour. C* **23**, 121 (2002)

[146] T. Alexopolous et al. (KTeV Coll.), *Phys. Rev. D* **70**, 0920072004

[147] A. Lai et al. (NA48 Coll.), *Phys. Lett. B* **604**, 1 (2004)

[148] F. Ambrosino et al. (KLOE Coll.), *Phys. Lett. B* **636**, 166 (2006)

[149] V. Bernard, M. Oertel, E. Passemar and J. Stern, *Phys. Lett. B* **638**, 480 (2006)

[150] M. Jamin, A. Pich and J. Portoles, *Phys. Lett. B* **640**, 176 (2006)

[151] A. Lai et al. (NA48 Coll.), *Phys. Lett. B* **647**, 341 (2007)

[152] O.P. Yushchenko et al., *Phys. Lett. B* **581**, 31 (2004)

[153] C.G. Callan and S.B. Treiman, *Phys. Rev. Lett.* **16**, 153 (1966)

[154] J. Gasser and H. Leutwyler, *Nucl. Phys.* **250**, 465 (1985)

[155] M. Jamin, J.A. Oller and A. Pich, *Phys. Rev. D* **74**, 074009 (2006)

[156] C. Davies, talk at *Lepton-Photon '07*, Daegu, (2007)

[157] W. Marciano, *Phys. Rev. Lett.* **93**, 231803 (2004)

[158] C. Gatti, *Eur. Phys. Jour. C* **45**, 417 2006

[159] K.G Vosburgh et al., *Phys. Rev. D* **6**, 1834 (1972)

[160] F. Ambrosino et al. (KLOE Coll.), *Phys. Lett. B* **632**, 43 (2006)

[161] F. Ambrosino et al. (KLOE Coll.), *Phys. Lett. B* **636**, 15 (2006)

[162] F. Ambrosino et al. (KLOE Coll.), *Phys. Lett. B* **638**, 140 (2006)

[163] F. Ambrosino et al. (KLOE Coll.), *Phys. Lett. B* **566**, 61 (2003)

[164] F. Ambrosino et al. (KLOE Coll.), *Phys. Lett. B* **636**, 173 (2006)

[165] F. Ambrosino et al. (KLOE Coll.), *Phys. Lett. B* **535**, 37 (2002)

[166] F. Ambrosino et al. (KLOE Coll.), *Eur. Phys. Jour. C* **48**, 767 (2002)

[167] F. Ambrosino et al. (KLOE Coll.), *Phys. Lett. B* **538**, 21 (2002)

[168] A. Lai et al. (NA48 Coll.), *Phys. Lett. B* **537**, 28 (2002)

[169] A. Alavi-Harati et al. (KTeV Coll.), *Phys. Rev. D* **67**, 012005 (2003)

[170] F. Ambrosino et al. (KLOE Coll.), *arXivid 0707.2654*

[171] F. Ambrosino et al. (KLOE Coll.), *Phys. Lett. B* **632**, 76 (2006)

[172] F. Ambrosino et al. (KLOE Coll.), *arXivid 0712.3841*

[173] R.J. Ott and T.W. Pritchard, *Phys. Rev. D* **3**, 52 (1971)

[174] F. Ambrosino et al. (KLOE Coll.), *Jour. High Ene. Phys.* **10**, 073 (2008)

[175] F. Ambrosino et al. (KLOE Coll.), *Jour. High Ene. Phys.* **12**, 105 (2007)

[176] E. Follana, et al. (HPQCD/UKQCD Coll.), *arXivid 0706.1726*

[177] P.A. Boyle et al. (RBC/UKQCD Coll.), *arXivid 0710.5136*

[178] V. Cirigliano et al. *Eur. Phys. Jour. C* **23**, 121 (2002)

[179] B. Moussallam and S. Descotes-Genon, *Eur. Phys. Jour. C* **42**, 403 (2005)

[180] V. Cirigliano, Precision tests of the Standard Model with $K_{\ell 3}$ decays, *Proc. of Science for KAON'07* LNF Frascati, May 2007

[181] M.J. Ramsey-Musolf, S. Su and S. Turlin, *Phys. Rev. D* **76**, 095017 (2007)

[182] M. Davier, A. Höcker and Z. Zhang, *Rev. Mod. Phys.* **78**, 1043 (2006)

[183] I.S. Towner and J.C. Hardy, *arXivid 0710.3181*

[184] H. Leutwyler and M. Roos, *Z. Physik* **25**, 91 (1984)

[185] G. Isidori and P. Paradisi, *Phys. Lett. B* **639**, 499 (2006)

[186] G. Isidori and A. Retico, *Jour. High Ene. Phys.* **11**, 001 (2001)

[187] K. Ikado et al. (Belle Coll.), *Phys. Rev. Lett.* **97**, 251802 (2006); B. Aubert et al. (Belle Coll.), *arXivid 0705.1820*

[188] H. Czyż and A. Grzelińska and J.H. Kühn and G. Rodrigo, *arXiv:hep-ph/0702122*, (2007) URL `http://ific.uv.es/~rodrigo/phokhara/`

[189] O. Shekhovtsova and G. Venanzoni, private communication

[190] M. Davier, *Nucl. Phys. Proc. Suppl.* **169**, 288-296 (2007)

ACKNOWLEDGMENTS

Thanks to Prof. Dr. Thomas Müller for being my referent. Without him this Ph.D. would have never been possible.

Thanks to Prof. Dr. Achim Denig for having supervised and advised me, in many many many occasions.

Thanks to the people of the $\pi\pi\gamma$ Group (from the past, the present and the future). Special thanks to Stefan Müller, Debora Leone, Graziano Venanzoni, Federico Nguyen.

Thanks to all from the KLOE collaboration (excluded myself), who did the on line shifts during the 2006 data taking.

Thanks to all the persons (dead, live or alive) who was playing, directing and singing for me, either they were aware of that or not... the $(99.9 \pm 0.1)\%$ were not. From Abbado Claudio to ZZ Top, thanks to all the musicians I was listening to.

Thanks to Who has invented the Music and the Silence... of Science.